Ciemat

Centro de Investigaciones
Energéticas, Medioambientales
y Tecnológicas

Measurement of the Cosmic Ray Anisotropy with AMS-02 on the International Space Station

Medida de la Anisotropía de los Rayos Cósmicos con AMS-02 en la Estación Espacial Internacional

Miguel Molero González

Doctoral Dissertation in Physics

Supervisor: Dr. Jorge Casaus Armentano

Supervisor: Dr. Miguel Ángel Velasco Frutos

Universidad Autónoma
de Madrid

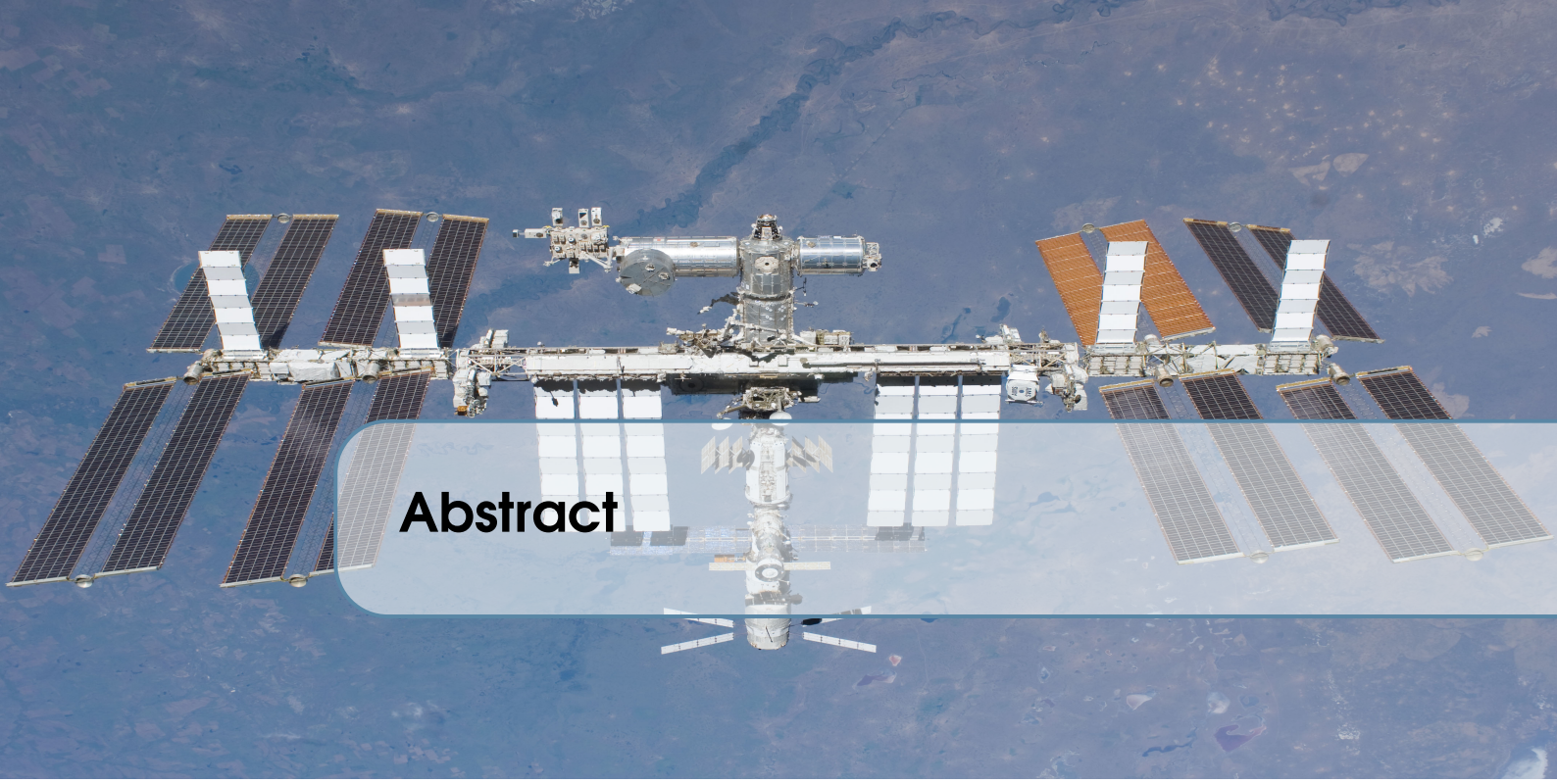

Abstract

The measurement of the charged cosmic ray spectra has provided over the years an important piece of information to understand the acceleration and propagation mechanisms of high energy particles in the cosmos. Among the different types of experiments, space-borne detectors profit from their identification and energy reconstruction capabilities to search for deviations or additional contributions in the fluxes that may challenge the standard paradigm of cosmic rays. In particular, the study of antimatter in space is a very interesting channel since its production is assumed to have a pure secondary origin and, therefore, any excess may constitute a sign of new physical processes.

As of today, AMS-02 has provided the most precise measurements of the individual positron and electron fluxes and of the primary galactic cosmic rays in the GeV-TeV energy range. The positron flux shows a significant excess starting from 25 GeV that cannot be fully explained with the traditional models. The electron flux exhibits a significant excess starting from 42 GeV compared to the lower energy trends, but the nature of this excess is different from the positron one. Protons and light primary nuclei show a progressive hardening above $\sim$ 200 GV. The aforementioned observations challenge the current understanding of the acceleration and propagation mechanisms.

The origin of these features remains unclear, and a plethora of models have been proposed. In the case of positrons, the additional contribution cannot be explained by a pure secondary component and the inclusion of nearby primary sources is necessary, whether of astrophysical (pulsars) or a more exotic (dark matter) origin. The annihilation or decay of dark matter into Standard Model particles may produce an excess of antimatter particles in cosmic rays, thus allowing for an indirect search of dark matter. In the case of protons and light nuclei, the spectral features could also be explained with the inclusion of local sources of high energy cosmic rays or the modification of the current propagation models.

In all the cases, the study of the arrival directions of the individual particle species may help to understand the origin of the observed features and, in particular, allows to explore the impact that nearby sources may imprint in the fluxes.

The determination of the large scale anisotropy, at first order described by a dipole, relies on the construction of an isotropic reference map which is compared with the skymap of measured events. The observation of any deviation of this map from the reference might be regarded as a

signal. Therefore, the precise understanding of the detector dependences when constructing the reference map is crucial in order to account for possible spurious effects.

In this thesis, the techniques developed to construct the isotropic reference map and its application to different cosmic ray species are presented. In particular, results on the dipole anisotropy for electrons, positrons, protons, helium, carbon, and oxygen collected by AMS-02 during its first 8.5 years of operation are reported.

The outline of this thesis corresponds to:

- **Chapter 1** introduces a general review of the cosmic rays as well as observations and challenges to the standard paradigm. This chapter also presents an overview of the anisotropy measurements and motivates the search for anisotropies with AMS-02.
- **Chapter 2** presents the AMS-02 experiment with a description of each subdetector as well as the data acquisition system and Monte Carlo simulation.
- **Chapter 3** provides the framework used for the computation of the fluxes as a function of the energy and direction of the incoming particles. The determination of the directionality of the fluxes requires the definition of a set of coordinate systems and statistical tools to obtain and interpret the possible signal.
- **Chapter 4** describes the application of the framework introduced in chapter 3 to positrons and electrons. The chapter is divided in two parts: the first part describes the standard method used to obtain the intermediate results published in Physical Review Letters; the second one presents the optimization of the analysis based on a template fit to separate positrons and electrons from the proton background.
- **Chapter 5** presents the anisotropy measurement for protons and light primary nuclei helium, carbon, and oxygen. A detailed description of the method for the light primary nuclei is discussed.
- **Appendices** provide additional details of the work presented in this thesis as well as the tables of the numerical results for each cosmic ray species.

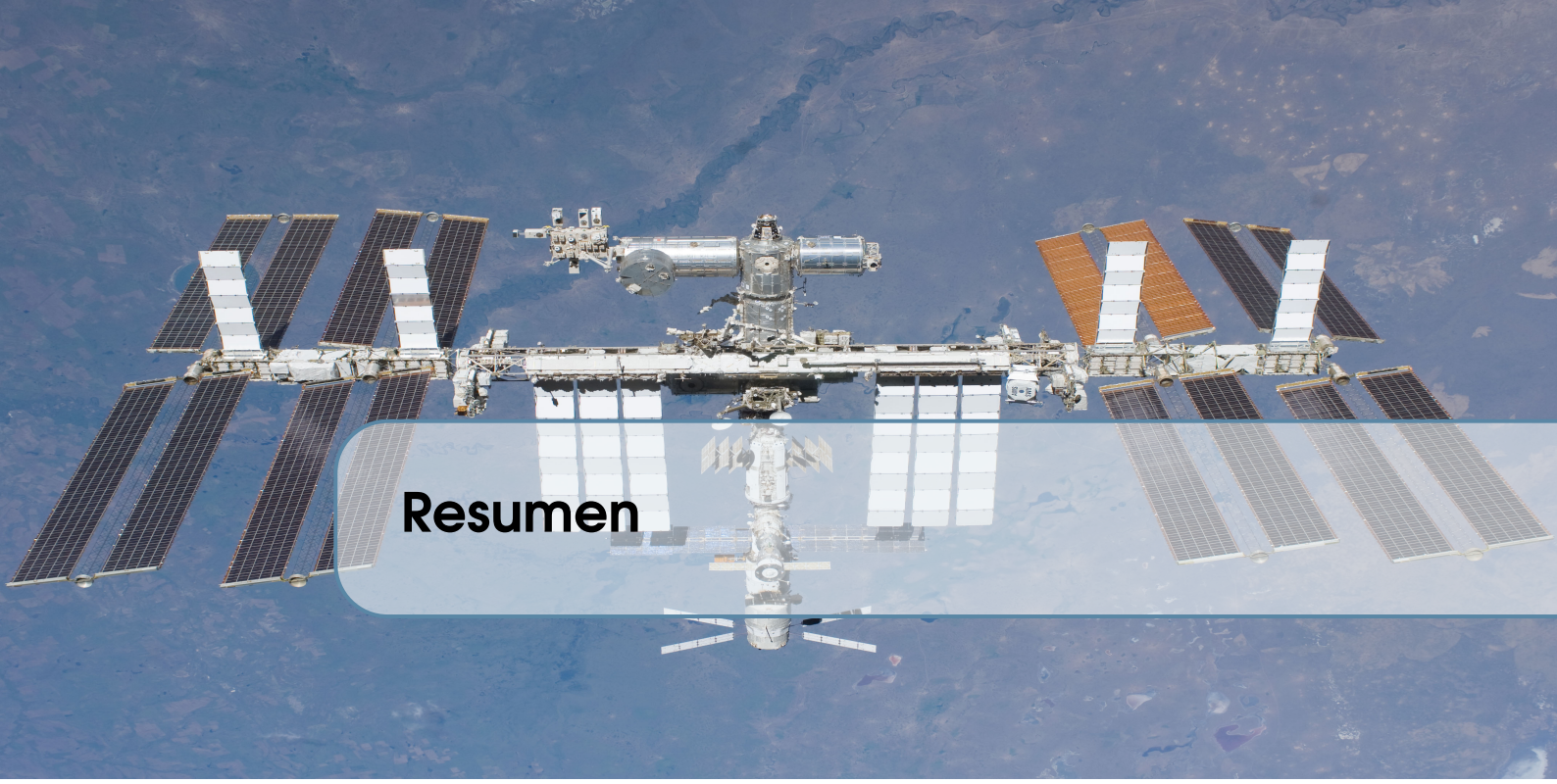

Resumen

La medida de los espectros de los rayos cósmicos cargados ha aportado a lo largo de los años información muy valiosa para entender los mecanismos de aceleración y propagación de las partículas de alta energía en el cosmos. Entre los diferentes tipos de experimentos, los detectores en el espacio se benefician de sus capacidades de identificación y reconstrucción de la energía para buscar desviaciones o contribuciones adicionales en los flujos que podrían desafiar el paradigma estándar de los rayos cósmicos. En concreto, el estudio de la antimateria en el espacio es un canal de particular interés ya que su producción se asume que es de origen secundario y, por tanto, cualquier exceso podría constituir un signo de nuevos procesos físicos.

Hasta la fecha, AMS-02 ha proporcionado las medidas más precisas de los flujos individuales de positrones y electrones, y de los rayos cósmicos primarios en la Galaxia en el rango de energía GeV-TeV. El flujo de positrones muestra un exceso significativo que empieza en 25 GeV que no puede ser explicado con los modelos tradicionales. El flujo de electrones presenta un exceso significativo que empieza en 42 GeV comparado con la tendencia a baja energía, sin embargo, la naturaleza de este exceso es distinta de la de positrones. Los protones y núcleos ligeros primarios muestran una desviación progresiva por encima de $\sim$ 200 GV. Las observaciones mencionadas desafían el actual entendimiento de los mecanismos de aceleración y propagación.

El origen de estas desviaciones permanece incierto y una plétora de modelos han sido propuestos. En el caso de los positrones, la contribución adicional no se puede explicar mediante una componente puramente secundaria y se necesita la inclusión de fuentes cercanas primarias con origen astrofísico (púlsares) o exótico (materia oscura). La aniquilación o la desintegración de la materia oscura en partículas del Modelo Estándar podría producir excesos de antimateria en los rayos cósmicos, permitiendo la búsqueda indirecta de materia oscura. En el caso de los protones y los núcleos ligeros, las características de los espectros se podrían explicar con la inclusión de fuentes locales de rayos cósmicos de alta energía o con la modificación de los modelos actuales de propagación.

En cualquiera de los casos, el estudio de las direcciones de llegada de las especies de partículas individuales podría ayudar a entender el origen de las observaciones y, en concreto, permite explorar el impacto que las fuentes cercanas podrían causar en los flujos.

La determinación de la anisotropía a gran escala, a primer orden descrita por un dipolo, se basa en la construcción de un mapa de referencia isótropo que se compara con el mapa del cielo de sucesos medidos. La observación de cualquier desviación de este mapa respecto a la referencia podría interpretarse como una señal. Por tanto, el entendimiento preciso de las dependencias asociadas a los efectos instrumentales cuando se construye el mapa de referencia es crucial para dar cuenta de posibles efectos espurios.

En esta tesis, se presentan las técnicas desarrolladas para construir el mapa de referencia isótropo y su aplicación a distintas especies de rayos cósmicos. En concreto, se muestran los resultados de la anisotropía dipolar para electrones, positrones, protones, helios, carbonos y oxígenos recogidos por AMS-02 durante sus primeros 8.5 años de operación.

El guion de esta tesis se corresponde con:

- **El Capítulo 1** introduce tanto una revisión general de los rayos cósmicos como de las observaciones y desafíos al paradigma estándar. Asimismo, el capítulo presenta un resumen de las medidas de anisotropía y motiva su búsqueda con AMS-02.
- **El Capítulo 2** presenta el experimento AMS-02 con una descripción detallada de cada subdetector, del sistema de adquisición de datos y de la simulación Monte Carlo.
- **El Capítulo 3** proporciona el marco teórico utilizado para el cálculo de los flujos en función de la energía y la dirección de llegada de las partículas. La determinación de la direccionalidad de los flujos requiere definir una serie de sistemas de coordenadas y herramientas estadísticas para obtener e interpretar la posible señal.
- **El Capítulo 4** describe la aplicación del marco teórico descrito en el capítulo 3 para positrones y electrones. El capítulo se divide en dos partes: la primera describe el método estándar usado para obtener los resultados intermedios que se publicaron en Physical Review Letters; la segunda presenta la optimización del análisis basada en ajustes a patrones para poder separar los positrones y electrones del fondo de protones de contaminación.
- **El Capítulo 5** presenta la medida de la anisotropía para protones y núcleos primarios ligeros (helio, carbono y oxígeno). Una descripción detallada del método es discutida para los núcleos ligeros.
- **Los Apéndices** proporcionan detalles adicionales del trabajo presentado en esta tesis junto con las tablas de los resultados numéricos para cada especie de rayos cósmicos.

List of Selected Publications

The work reported in this thesis has profited to several publications, including peer-reviewed papers and conference reports. This list is not a complete record of the author's publications but rather an abbreviated summary of the works related to the thesis topic.

Physical Review Letters

- M. Aguilar *et al.* [AMS Collaboration], "Towards Understanding the Origin of Cosmic Ray Electrons" Phys. Rev. Lett. **122**, 101101, Mar. 2019
  Link: https://journals.aps.org/prl/abstract/10.1103/PhysRevLett.122.101101
- M. Aguilar *et al.* [AMS Collaboration], "Towards Understanding the Origin of Cosmic Ray Positrons" Phys. Rev. Lett. **122**, 041102, Jan. 2019. ***Editor's Suggestion***
  Link: https://journals.aps.org/prl/abstract/10.1103/PhysRevLett.122.041102

Proceedings

- M.A. Velasco Frutos, J. Casaus, C. Maña, M. Molero, "Anisotropy of Elementary Particle Fluxes in Primary Cosmic Rays Measured with the Alpha Magnetic Spectrometer on the ISS" , Proceedings of the 40th International Conference on High Energy physics (ICHEP2020), Aug. 2020
  Link:https://pos.sissa.it/390/613/
- M.A Velasco, J. Casaus, C. Mana, M. Molero, I. Gebauer, M. Graziani, M. Gervasi, G. La Vacca, P.G Rancoita, "Anisotropy of Cosmic Ray Fluxes Measured with the AMS-02 on the ISS" , Proceedings of the 16th International Conference on Topics in Astroparticle and Underground Physics (TAUP 2019), Sept. 2019
  Link:https://iopscience.iop.org/article/10.1088/1742-6596/1468/1/012083
- M. Molero, J. Casaus, C. Mana, M.A. Velasco, I. Gebauer, M. Graziani, M. Gervasi, G. La Vacca, P.G Rancoita, "Anisotropy of Cosmic Ray Fluxes Measured with the Alpha Magnetic Spectrometer on the ISS", Proceedings of the 2019 Meeting of the Division of Particles and Fields of the American Physical Society (DPF2019),Aug. 2019
  Link: https://arxiv.org/abs/1910.06919
- I. Gebauer, M. Graziani, J. Casaus, M. Molero, C. Mana, M.A. Velasco, M. Gervasi, P.G

Rancoita and G. La Vacca, “Anisotropy of Particle Fluxes in Primary Cosmic Rays Fluxes Measured with the Alpha Magnetic Spectrometer on the ISS” , Proceedings of the XXIX International Symposium on Lepton Photon Interactions at High Energies (LeptonPhoton2019), Aug. 2019
Link: https://pos.sissa.it/367/117/

- I. Gebauer, M. Graziani, J. Casaus, M. Molero, C. Mana, M.A. Velasco, M. Gervasi, P.G Rancoita and G. La Vacca, “Anisotropy of Particle Fluxes in Primary Cosmic Rays Fluxes Measured with the Alpha Magnetic Spectrometer on the ISS” , Proceedings of the 36th International Cosmic Ray Conference (ICRC2019), July. 2019
  Link: https://pos.sissa.it/358/150/
- J. Casaus, C. Mana, M. Molero, M.A. Velasco, I. Gebauer, M. Graziani, S. Zeissler, G. La Vacca, M. Gervasi and P.G Rancoita, “Anisotropy of Elementary Particle Fluxes in Primary Cosmic Rays Measured with AMS on the ISS”, Proceedings of the 39th international Conference on High Energy Physics (ICHEP 2018), July 2018
  Link: https://pos.sissa.it/340/370/pdf

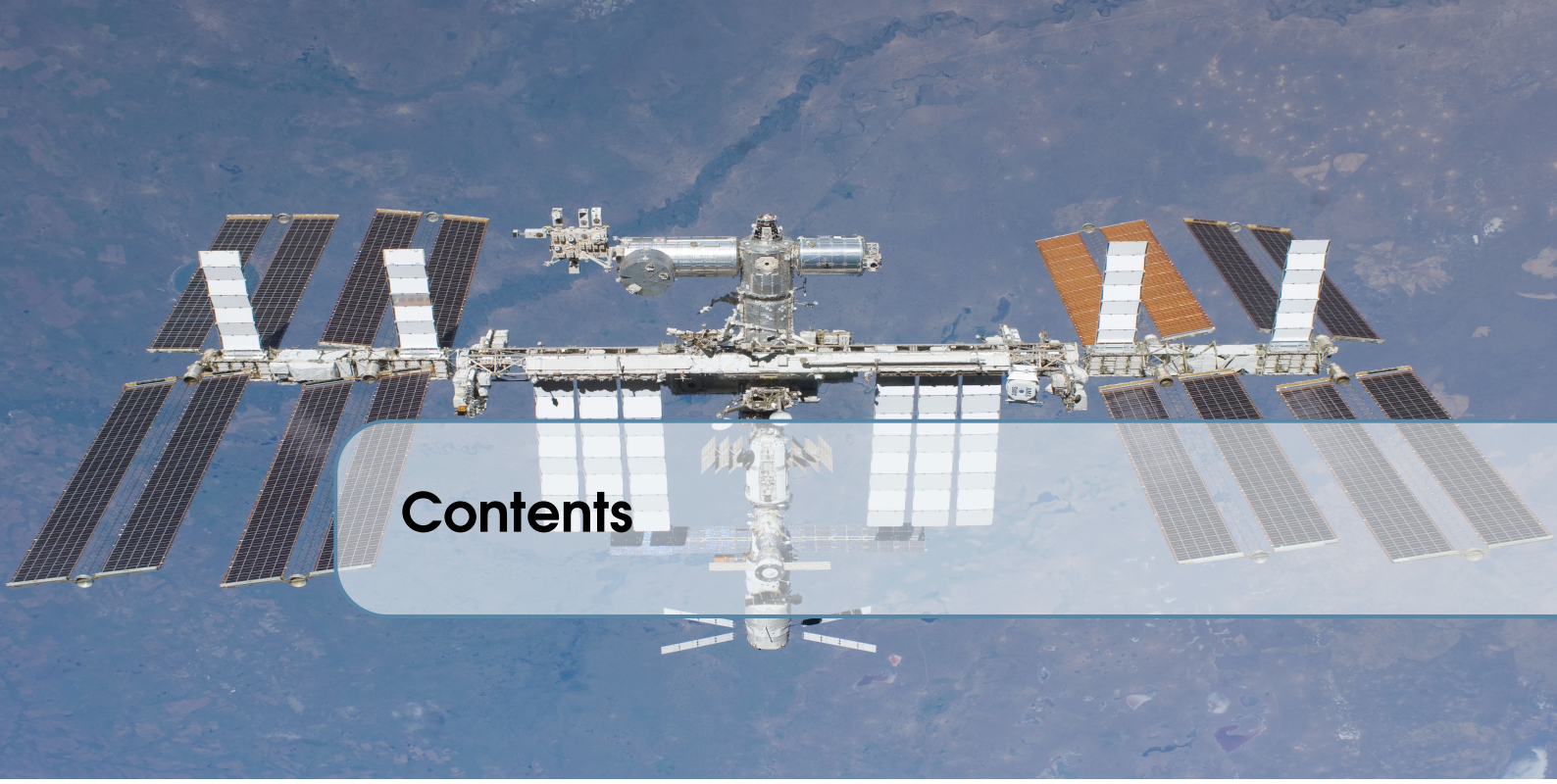

Contents

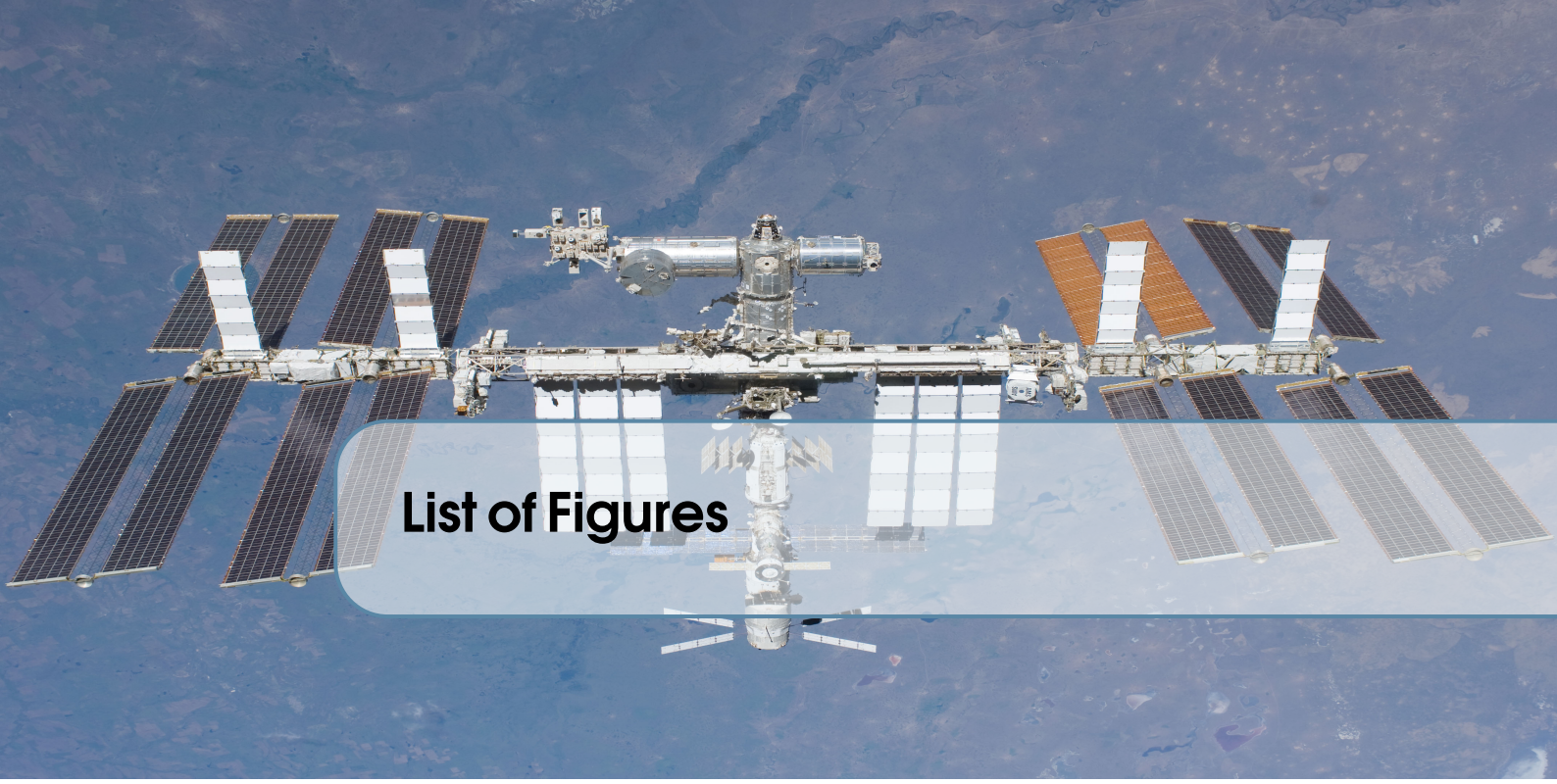

List of Figures

List of Tables

List of Acronyms

ACC Anti-Coincidence Counters
ACE Advanced Composition Explorer
AGASA Akeno Giant Air Shower Array
AGN Active Galactic Nuclei
AMS Alpha Magnetic Spectrometer
ATNF Australian Telescope National Facility
CALET CALorimetric Electron Telescope
CMB Cosmic Microwave Background
CR Cosmic Ray
CRN Cosmic Ray Nuclei
DAMPE Dark Matter Particle Explorer
DAQ Data Acquisition System
DSA Diffusive Shock Acceleration
ECAL Electromagnetic Calorimeter
EVA Extra Vehicular Activities
FE Front-End
Fermi-LAT Fermi Large Area Telescope
FFA Force Field Approximation
FT Fast Trigger
GMF Galactic Magnetic Field
GRB Gamma Ray Burst
GZK Greisen-Zatsepin-Kuzmin
HAWC High Altitude Water Cherenkov
HEAO High Energy Astronomy Observatory
HEALPix Hierarchical Equal Area isoLatitude Pixelation
HESS High Energy Stereoscopic System
HMF Heliosphere Magnetic Field
HT High Threshold

IGRF International Geomagnetic Reference Field
IMF Interplanetary Magnetic Field
ISM Interstellar Medium
ISS International Space Station
KASKADE KArlsruhe Shower Core and Array DEtector
LIS Local Intestellar Medium
LT Low Threshold
MAGIC Major Atmospheric Gamma-ray Imaging Cherenkov Telescope
MC Monte Carlo
MIP Minimum Ionizing Particles
PF Positron Fraction
PAMELA Payload for Antimatter Matter Exploration and Light-nuclei Astrophysics
PMT Photomultiplier Tubes
PWNe Pulsar Wind Nebulae
RICH Ring Imaging Detector
RTI Real Time Information
SAA South Athlantic Anomaly
SHT Super-High Threshold
SM Standard Model
SNR Supernova Remnant
SOHO Solar and Heliospheric Observatory
STD Silicon Tracker Detector
TA Telescope Array
TRD Transition Radiation Detector
TR Transition Radiation
TOF Time of Flight
UHECR Ultra High Energy Cosmic Ray
UTTPS Upgraded Tracker Thermal Pump System
VERITAS Very Energetic Radiation Imaging Telescope Array System

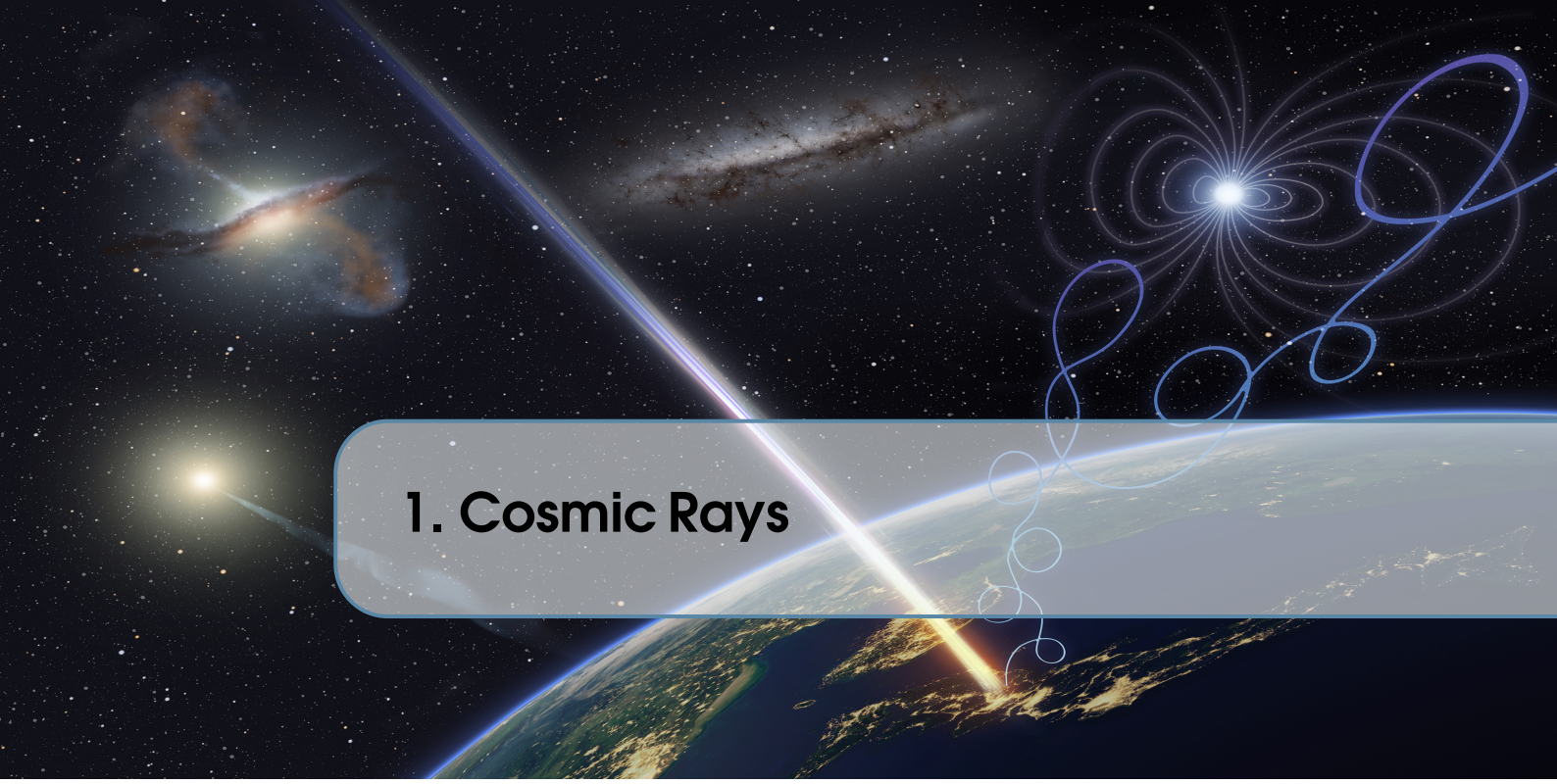

1. Cosmic Rays

"What we know is a drop, what we don't know is an ocean"

— Isaac Newton

1.1 Introduction and History

The history of the experimental study of the cosmic rays (CRs) dates back to the beginning of the 20th century where a large number of experiments were carried out in order to understand the ionization radiation produced in the atmosphere.

After the discovery of spontaneous radioactivity by Becquerel in 1896 [1; 2], it was initially believed that the atmospheric radiation was originated from the radioactive elements coming from the ground. This explanation was generally accepted during the first decade (1900-1910) of the 20th century.

The first hints of radiation of extraterrestrial origin were given by T. Wulf in 1909 [3] and D. Pacini in 1912 [4], who measured the ionization rate at different altitudes. T. Wulf used an electroscope on top of the Eiffel Tower concluding that the intensity measured was higher than the one expected from the ground radiation. D. Pacini measured the ionization rate at a depth of 3 m from the surface also concluding that a certain part of the ionization should come from a different source than the radioactivity of the Earth.

However, those conclusions were not completely accepted until the discoveries of V. Hess in 1912 [5]. During 1911 and 1912 he launched seven balloon flights at an altitude of 5300 m (figure 1.1). The measurements showed an increase of the ionization rate with the altitude, contrary to what was expected from just ground radiation. He concluded that the origin of the measured radiation was most likely extra-terrestrial. The Sun as the radiation source candidate was discarded when a balloon flight was sent during a total eclipse (the moon blocked the Sun radiation) and an increasing rate was still measured. For his discovery, Hess received the Nobel Prize in 1936 [6], although, the term *cosmic rays* was conceived by R. Milikan and G. Cameron in 1926 [7] when they confirmed the measurements of V. Hess.

During the first decade after Hess' discovery, the nature of the cosmic rays was still unclear: were they charged particles or neutral photons? In 1927 J. Clay [8] was the one who tipped the balance in favor of the charged particles. In particular, he measured the ionization rate at different geographical latitudes, finding a smaller rate in the tropics than at high latitudes, the so-called

latitude effect. This was the first indication that the cosmic rays were more efficiently deflected by the Earth's magnetic field in the tropics than in the poles and, therefore, they had to be charged particles.

In 1930, B. Rossi [9] predicted the so-called *East-West effect*, which suggested that if the majority of the cosmic rays had a positive charge the rate would be greater from the geomagnetic West than from the East. This effect was measured by three independent experiments between 1933 and 1934 [10; 11; 12], confirming that cosmic rays were mainly positively charged particles.

Figure 1.1: Victor Hess and his crew in one of the balloons launched during 1911-1912.

During the 1930s and 1940s, a large variety of experiments demonstrated that the cosmic rays observed in the atmosphere were mainly protons and the secondary radiation measured on the ground was composed of a light component of electrons and photons and a heavier component of muons.

Before the existence of particle accelerators, the cosmic rays were used as a source of high energy particles. This led to important advances in the field of nuclear and particle physics, in particular, to the discovery of the positron [13], the muon [14], the pion [15] and the kaon [16].

Nowadays, the synergy between particle physics, cosmic ray astrophysics and gamma-ray astronomy has originated the field of astroparticle physics, which aims to provide information about fundamental physics with the precise study of cosmic radiation.

In this chapter, a general review of the cosmic ray processes (such as origin, acceleration, and propagation) as well as observations and challenges to the standard paradigm will be presented.

1.2 Composition and Energy Spectra

Cosmic rays are charged particles traveling through space, originated from the Sun, from outside the Solar System, and from distant galaxies.

1.2.1 Chemical Composition

The chemical composition of the cosmic rays is mainly protons (86%), helium nuclei (11%), electrons (2%), and heavier nuclei together with a small component of antimatter, positrons, and antiprotons (1%). Figure 1.2 shows the relative elemental abundances of galactic cosmic rays compared to the abundances in the Solar System.

The comparison of both abundances shows some similarities and discrepancies. The peaks corresponding to C, N, O, and Fe, are due to the *odd-even* effect. In general, even-even nuclei (Z and N even) are more stable than odd-even or odd-odd nuclei and, thus they are more abundantly

produced in the stellar nucleosynthesis. The fact that the abundances are similar in both cosmic rays and Solar System supports their origin by thermonuclear reactions in the stars.

The excess in the cosmic rays of Li, Be, B, F, Sc, Ti, V, Cr, and Mn is due to fragmentation (also called spallation) processes when more abundant species interact with the interstellar medium (ISM). The light nuclei Li, Be, and B are produced by the C, N, O whereas the elements from Sc to Mn by the heavier Fe and Ni. In the Solar System, its abundances are suppressed since these elements are not produced during the stellar nucleosynthesis.

Depending on their origin, the cosmic rays are classified in two different types:

- **Primary Cosmic Rays** are stable charged particles accelerated by astrophysical sources that travel through the Galaxy without suffering any fragmentation process with the ISM.
- **Secondary Cosmic Rays** are charged particles produced by the interaction of primary cosmic rays with the ISM or by the decay of unstable species during its propagation.

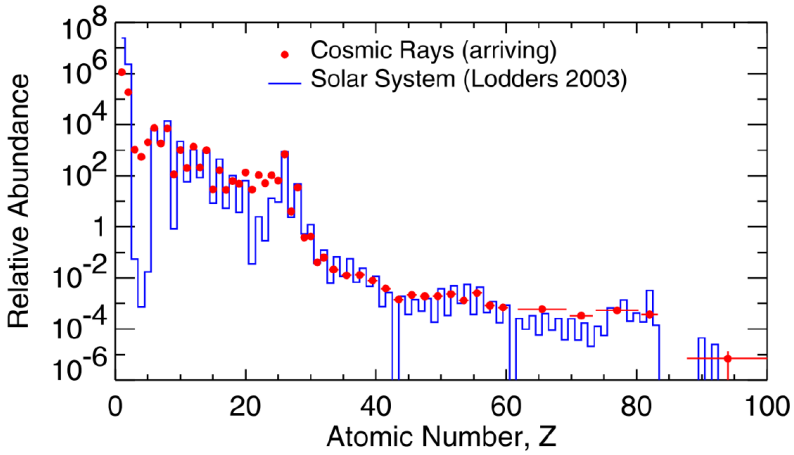

Figure 1.2: Chemical composition of the cosmic rays for $E \leq 1$ GeV/nucleon compared to the abundances in the Solar System for elements with charge from Z = 1 to Z = 100. The abundances are normalized relative to carbon [17].

1.2.2 Energy Spectra

The all particle cosmic rays spectra measured at the Earth covers a very wide range in energy from 10^6 to 10^{20} eV and in intensity from 10^{-28} to 10^4 $m^{-2}sr^{-1}GeV^{-1}s^{-1}$ (figure 1.3). It can be approximately described by a power law

$$\frac{dN(E)}{dE} \propto E^{-\gamma} \tag{1.1}$$

with γ the spectral index. Different features are better displayed in figure 1.4, where the all-particle cosmic ray flux is multiplied by a power of the energy:

- **Knee:** For energies above $\sim$ 3-4 $\times 10^6$ GeV the spectrum gets steeper (softens) from $\gamma \sim 2.7$ to $\gamma \sim 3.1$
- **Second Knee:** For energies above $\sim 10^8$ GeV the spectrum further softens from $\gamma \sim 3.1$ to $\gamma \sim 3.3$
- **Ankle:** For energies above $\sim 5 \times 10^9$ GeV the spectrum hardens from $\gamma \sim 3.3$ to $\gamma \sim 2.7$
- **Suppression:** For energies above $\sim$ 4-5 $\times 10^{10}$ GeV the spectrum suffers a strong suppression with a change in the spectral index from $\gamma \sim 2.7$ to $\gamma \sim 4.2$

The vast majority of the cosmic rays from above a few GeV up to the ankle are believed to have a galactic origin and to be accelerated by the shock waves produced in supernova remnants (SNRs). After being accelerated, they travel through the Galaxy, being randomly deflected by the Galactic

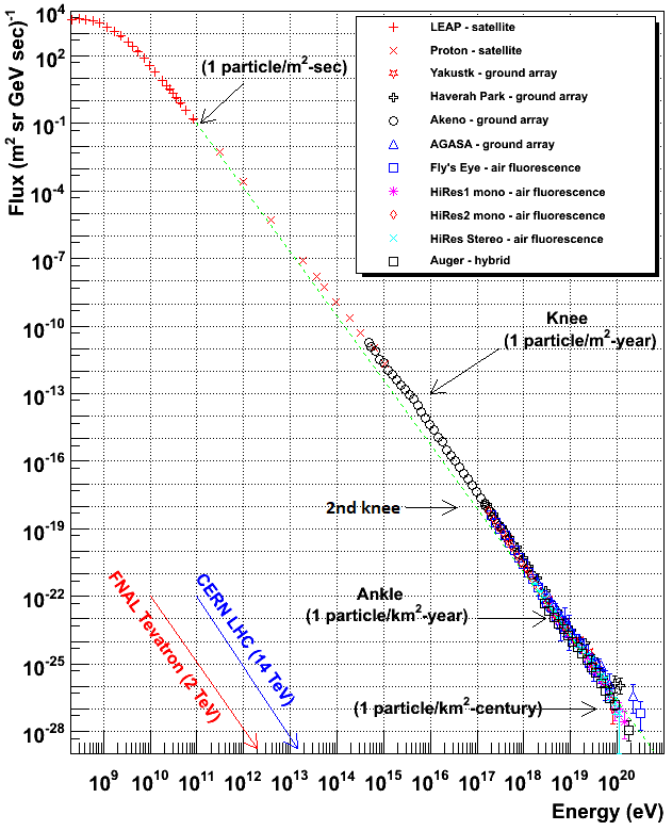

Figure 1.3: The all cosmic rays spectra measured by different experiment indicating the different changes of the spectral index γ [18].

Magnetic Field (GMF) and, finally arrive at the Earth. There are two different explanations for the origin of the knee: it either shows the limit of the maximum energy (cutoff) to which cosmic rays can be accelerated by SNRs in the Galaxy or it reflects the leakage of cosmic rays out of the Galaxy during their propagation due to a less efficient galactic magnetic confinement.

Since both mechanisms depend on the charge of the particle, the energy spectra for individual elements should exhibit different energy cutoffs. This has been confirmed by several experiments from the measurement of the mass composition[19; 20; 21]. Thus, the knee is believed to be caused by the proton spectrum, *proton knee*, and the second knee by heavier nuclei with a bigger contribution from the Fe, *iron knee*.

At the ankle, the component of cosmic rays of extragalactic origin, also named Ultra High Energy Cosmic Rays (UHECRs), starts dominating over the component of galactic cosmic rays, producing a hardening in the spectra. Therefore, at this point, the transition from galactic to extragalactic cosmic rays is believed to occur.

In the highest energy range, a strong suppression is observed originated by the Greisen-Zatsepin-Kuzmin (GZK) mechanism [22]. The UHECRs interact with the photons of the Cosmic Microwave Background (CMB) through inelastic collisions, thus losing energy and producing the observed effect. The controversial detection of cosmic rays with energies above the GZK would necessarily need that their sources are closer than the mean free path associated to this effect [23; 24].

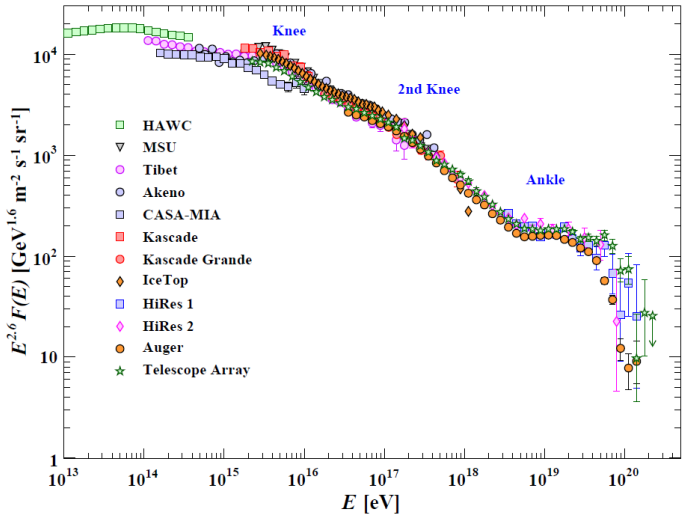

Figure 1.4: The all cosmic rays spectra measured by ground-based experiments with energies from below the knee to above the ankle. The spectra are multiplied by $E^{2.6}$ [25].

1.3 Origin, Acceleration and Propagation

Recent observations have provided enough information to distinguish between two types of accelerators: galactic sources with enough energies to reach the second knee and extragalactic sources which provide energies above the ankle. In both cases, the sources and acceleration mechanisms are a widely debated topic and this section will focus on the description of the current understanding of the galactic cosmic rays.

In this frame, the most accepted candidate as sources of galactic cosmic rays are SNRs [26]. They are astrophysical objects arising from the collapse of a star at the end of its life. When the nuclear fuel runs out inside the star the nuclear energy is not able to contain the gravitational force any longer and the star collapses producing an explosion. In the explosion the stellar material is ejected with a very high energy release to the ISM, typically $\sim 10^{51}$ erg. Assuming two explosions per century the total amount of energy released is $\sim 10^{41}$ erg/s. The CRs density in the Galaxy is approximately $\omega_{CR} \sim 10^{40}$ erg/s and thus, a conversion of 1-10% of the SNR energy would provide enough density of CRs in the Galaxy. The current models of SNRs precisely predict such conversion factors. Other candidates are pulsars and neutron stars in close binary systems, however, the physical mechanisms responsible for the acceleration are still unknown. [1]

The commonly accepted mechanism of acceleration in the SNRs is the diffusive shock acceleration (DSA), based on the studies initially proposed by Fermi [27]. After the explosion, the stellar material is ejected creating a shock wave that propagates into the ISM and the charged particles gain an enormous amount of kinetic energy by means of stochastic scattering on the magnetic turbulences of the shock wave. The main idea is that the particles gain energy by reflecting forth and back in the inhomogeneities of the magnetic turbulences, which in turn act like *magnetic mirrors*. After many interactions, the particles escape the shock wave propagating into the medium. This mechanism predicts a power law energy spectrum $dN/E \propto E^{-\alpha}$ with α between 2.0 and 2.5 [28].

Once the cosmic rays have been accelerated in the source to a certain energy, they propagate through the ISM under the influence of the GMF. The theoretical model used to describe the

[1] In the case of the cosmic rays of extragalactic origin, the accelerators have to provide higher energies and, thus they should come from more violent and energetic phenomena, like Active Galactic Nuclei (AGN) or Gamma-Ray Burst (GRB).

propagation assumes it is a diffusive process that follows the equation [29] (first proposed by Parker [30])

$$\begin{aligned}\frac{\partial \psi_i(\vec{r},p,t)}{\partial t} &= q_i(\vec{r},p,t) + \vec{\nabla}\cdot(D_{xx}\vec{\nabla}\psi_i) + \frac{\partial}{\partial p}\left[p^2 D_{pp}\frac{\partial}{\partial p}\left(\frac{\psi_i}{p^2}\right)\right] + \frac{\partial}{\partial p}\left[\frac{p}{3}(\vec{\nabla}\cdot\vec{v}_c)\psi_i\right] \\ &\quad - \vec{\nabla}\cdot(\vec{v}_c\psi_i) - \frac{\partial}{\partial p}(\dot{p}\psi_i) - \left(\frac{1}{\tau_i^{Frag}} + \frac{1}{\tau_i^{Decay}}\right)\psi_i\end{aligned} \tag{1.2}$$

where $\psi_i(\vec{r},p,t)$ represents the density of momentum p in a space-time coordinate $(\vec{r},t)$ for the ith particle species. The rest of the terms represent:

- **Sources:** The term $q_i(\vec{r},p,t)$ reflects the production mechanism for a given species of particles. In the case of DSA acceleration the energy spectrum is assumed to follow a power law $\partial q/dp \propto p^{-\alpha}$, with α the spectral index of injection.
- **Diffusion:** The GMF can be decomposed in a regular average component, and a turbulent component [31]. The first one follows the distribution of the arms of the galaxy whereas the second one represents the small perturbations of the regular field. The scattering of the cosmic rays with the small random perturbations ($\delta B \ll B$) leads to a diffusive process with a diffusion coefficient D_{xx}. Due to the nature of the perturbation, the coefficient follows a power law $D_{xx} \propto p^{\delta}$, with δ the spectral index of diffusion. Depending on the model of the turbulent fluctuations the value of δ will vary. In particular, two models are commonly used: the Kolmogorov with $\delta = 1/3$ [32] and the Kraichnan [33] with $\delta = 1/2$.
  The cosmic rays propagate from the source to the Earth interacting with the GMF and bending their trajectories. The radius of the curvature (also called *Larmor radius or gyroradius*) is described by the Lorentz force as

$$r = \left(\frac{pc}{Ze}\right)\frac{sin\theta}{Bc} \tag{1.3}$$

  where B (typically between 3-6 μG [34]) is the magnetic field, θ the pitch angle (defined as the angle between the particle velocity vector and the local magnetic field), p the momentum, c the speed of light in vacuum and Ze the charge in electron units. The equation encourages to define the rigidity of the particle as

$$R = \frac{pc}{Ze} \qquad (in\ Volts) \tag{1.4}$$

  such that the direction of the charged particles is bent by the magnetic field according to the rigidity.
- **Re-acceleration:** The scattering of the particles on the magnetic field turbulences induces a stochastic acceleration which is called re-acceleration. The process can be described as a diffusion process with a diffusion coefficient in the momentum space D_{pp}. However, this mechanism only accelerates particles up to a few tens of GeV, the contribution above is negligible.
- **Convection:** The term $\vec{\nabla}\cdot(\vec{v}_c\psi_i)$, with v_c the convection velocity, accounts for the convective transport of the cosmic rays due to the galactic wind. This effect results in energy losses that are negligible above a few tens of GeV.
- **Energy Losses:** The term $\frac{\partial}{\partial p}(\dot{p}\psi_i)$ refers to the energy losses that the cosmic rays suffer during their propagation. Protons and nuclei mainly lose their energy when they ionize the matter in the ISM, following the Bethe-Bloch formula, whereas electrons and positrons lose it more quickly by the emission of synchrotron radiation or by means of the inverse Compton interactions with the photons in the medium.
- **Nuclear Processes:** Finally the τ_i^{Frag} and τ_i^{Decay} express the lifetime for fragmentation and radioactive processes that the cosmic rays may experiment during their propagation.

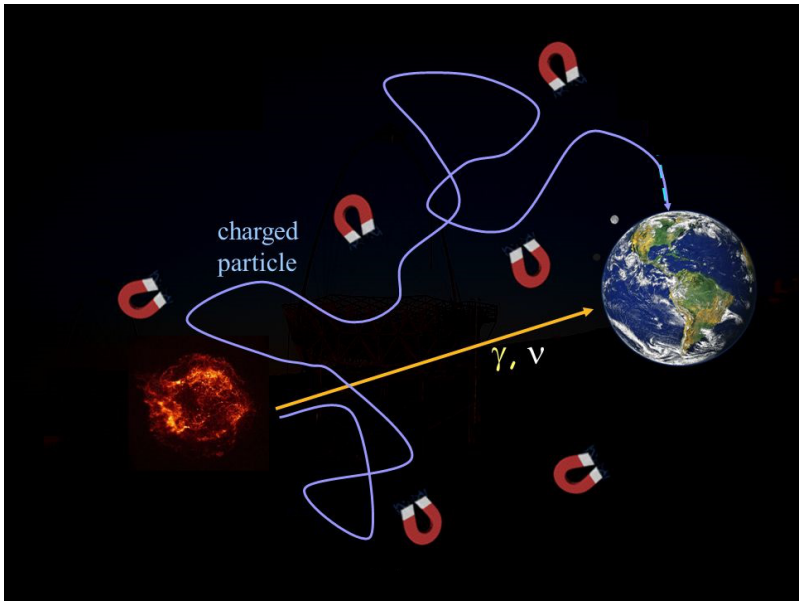

Figure 1.5: Scheme of the cosmic rays propagation where they are accelerated in SNRs and propagate through the GMF following a diffusive process.

Assuming that the propagation is purely diffusive and taking into account that the acceleration has been produced in a SNR by DSA, the spectrum of cosmic rays can be expressed as a power law

$$\frac{dN}{dE} \propto E^{-\alpha-\delta} \tag{1.5}$$

with the contribution of the injection by the source, α, and the diffusion in the GMF, δ.

The diffusion coefficient can be deduced from the secondary-to-primary flux ratio, which is proportional to $E^{-\delta}$. In this sense, the experimental data allows to constrain the value of the spectral index and improve the understanding of the cosmic rays propagation in the Galaxy.

In general, the equation 1.2 can be solved using dedicated software packages such as GALPROP [35], DRAGON [36] or USINE [37].

1.4 Local Environmental Effects

Cosmic rays approaching the Solar System are affected by two phenomena that produce distortions in the Local Interstellar Spectrum (LIS) before reaching the Earth: the solar wind and the Earth's magnetic field.

1.4.1 Solar Modulation

The solar wind is a magnetized plasma composed of low energy protons and electrons ejected by the solar corona to the medium. This magnetized plasma drags out the solar magnetic field lines creating a spiral structure [38] with a large-scale field and small-scale perturbations, known as the Heliosphere Magnetic Field (HMF) or the Interplanetary Magnetic Field (IMF). The interaction of the charged cosmic rays with the solar wind and the subsequent scattering with the small inhomogeneities of the HMF produces a diffusive process known as *solar modulation*. The main effect of the solar modulation is the deceleration of the low energy particles arriving to the Solar System.

As a consequence of the diffusive process, the charged cosmic rays entering the heliosphere can be described by a transport equation. It can be solved numerically or analytically using some

simplifications. In the so-called *force field approximation* (FFA) [39] the solar modulation only depends on the potential ϕ. The solution of the equation connects the flux modulated by the solar wind Φ_{mod} with the local interstellar flux Φ_{LIS} by

$$\Phi_{mod}(E) = \frac{E^2 - m^2c^4}{(E + |Z|e\phi)^2 - m^2c^4} \times \Phi_{LIS}(E + |Z|e\phi) \tag{1.6}$$

where E is the energy at the Heliosphere obtained from the energy in the ISM according to $E = E_{ISM} - |Z|e\phi$. The potential ϕ accounts for the energy losses of the cosmic rays propagating in the Heliosphere. The values of ϕ range between 400 MeV and 1400 MeV depending on the solar activity.

The solar magnetic field does not remain constant in time. In fact, the Sun does not rotate as a rigid body but rather the equator rotates faster than the poles. Therefore, the field lines get twisted and eventually reach the photosphere (visible region of the Sun) accumulating in regions called sunspots.

The Sun follows an 11-year cycle, defined as the time between two solar minima (low number of sunspots) passing through the maximum (high number of sunspots), which indicates the solar activity. During the minimum, the magnetic field can be approximated to a dipole, with the dipole axis almost aligned with the solar rotational axis. In the maximum, this approximation cannot be used anymore and the polarity is reversed. When the dipole is parallel with the rotational axis is referred to as positive polarity (A > 0) whereas when it is anti-parallel as negative polarity (A < 0) (figure 1.6).

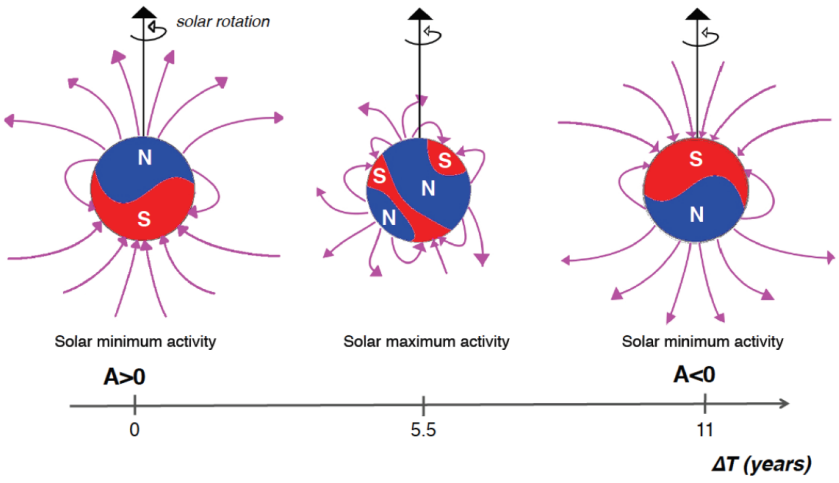

Figure 1.6: Scheme of the solar magnetic field during an 11-year solar cycle starting from a minimum with positive polarity (A > 0) and reaching the next one with negative polarity (A < 0).

The FFA does not include the alternating solar magnetic field polarity which produces a charge sign dependence of the solar modulation, since charged particles will drift to opposite directions when the polarity is reversed [40; 41].

1.4.2 Earth Magnetic Field

The last environment that cosmic rays encounter before arriving to the Earth is the Magnetosphere, where the Earth magnetic field or geomagnetic field dominates the dynamics of the charged particles.

The geomagnetic field is generated by the motion of the metallic fluid of nickel-iron in the outer core of the Earth. Near the surface it can be approximated by a magnetic dipole with moment $M_E = 8 \times 10^{17} Tm^2$, tilted $\sim 11°$ with respect to the Earth's rotational axis and displaced ~ 400 km from the center of the Earth. Far from the surface, the dipole field is extremely distorted by the incoming Solar Wind, as shown in figure 1.7.

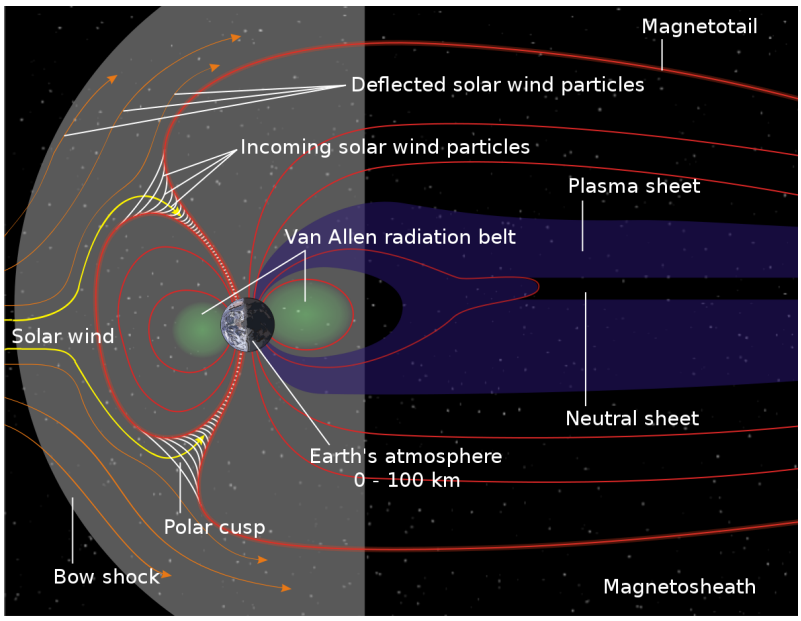

Figure 1.7: Scheme of the magnetosphere structure. The Earth's magnetic field is distorted by the shock wave created by the solar wind. (Credits: NASA, Wikimedia Commons).

In the 1930s Størmer [42] developed a theory based on the definition of a geomagnetic rigidity cutoff, R_c, to explain the motion of charged particles in the geomagnetic field. In this model, only particles above the R_c could penetrate the Earth's magnetic field whereas the others would be deflected or trapped into the geomagnetic field. The rigidity cutoff in the Størmer theory is defined as

$$R_c = \frac{M_E cos^4 \lambda}{r^2 (1 + \sqrt{1 \pm cos^3 \lambda \; cos\phi \; \sin\zeta})^2} \tag{1.7}$$

where λ is the geomagnetic latitude along the dipole, r is the distance from the dipole center, ζ the angle of the incoming particle with respect to the local magnetic zenith, ϕ the azimuthal angle of the incoming particle, and $\pm$ stands for the sign of the particle charge (-1 for positive and +1 for negative). If the incoming particle has $\zeta = 0$ (vertical particles) and normalized units are used, the equation is reduced to

$$R_c \approx \frac{14.5}{(r/r_E)^2} cos^4 \lambda \qquad (in\ GV) \tag{1.8}$$

with r_E the Earth's radius and the cutoff only depends on the geomagnetic latitude. Consequently, R_c is maximum in the geomagnetic equator and vanishes in the magnetic poles.

Within this model, the two effects mentioned in section 1.1 are explained:

- *Latitude Effect:* Due to the dependence of R_c, particles entering the geomagnetic field are more deflected in the equator than in the poles and so the rate of particles is larger at high latitudes.

- *East-West Effect:* As a consequence of the R_c defined in equation 1.7 positive charge particles can penetrate the geomagnetic field more from the West than from the East.

The Størmer geomagnetic cutoff allows understanding many of the effects associated with the interaction of the charged particles with the geomagnetic field. However, the field is not a pure dipole, and also the intensity varies with time. For this reason, a more precise description of the Earth's magnetic field and its annual changes is given by the International Geomagnetic Reference Field (IGRF) [43], which describes the geomagnetic field based on the expansion in spherical harmonics. At first order, the dipole approximation is recovered. The values of the expansion are updated on a 5-year basis, with the IGRF-12 the latest update (2015-2020). Figure 1.8 shows an illustration of the Størmer and IGRF-12 rigidity cutoff as a function of the ISS geographical position.

In addition, some of the particles are trapped by the Earth's magnetosphere creating the Van Allen radiation belts [44]. The Earth has two principal belts extending from an altitude of 640 to 58000 km above the surface: the inner belt is composed of trapped protons and electrons, and the outer belt mainly by electrons.

In particular, the inner Van Allen belt gets closer to the Earth's surface (200 km) over the South Atlantic Ocean, creating the so-called *South Atlantic Anomaly* (SAA) [45]. This region is of special impact for space-borne detectors operating in low Earth orbit since the electronics and the quality of the data can be affected by the high rate of low energetic particles.

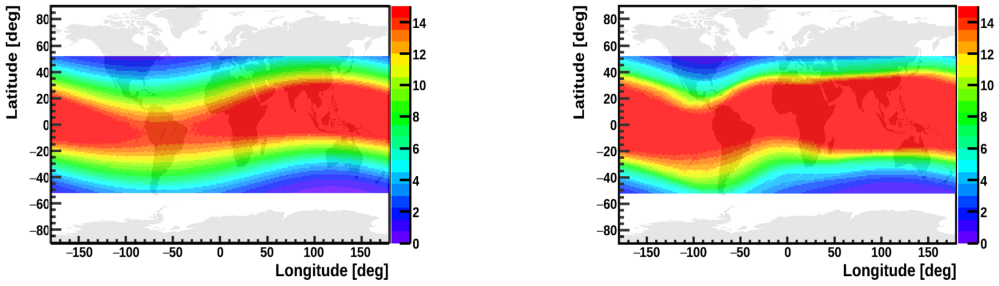

(a) Størmer Rigidity Cutoff (b) IGRF-12 Rigidity Cutoff

Figure 1.8: Values of the Størmer rigidity cutoff (a) and the IGRF-12 rigidity cutoff (b) as a function of the ISS geographical position. The figures correspond to the maximum rigidity cutoff for positive charge particles within the AMS 25º field of view.

1.5 Cosmic Ray Experiments

Due to the characteristics of the cosmic ray flux, which shows a very fast decrease with the energy, two experimental approaches have been used to measure the complete energy range:

- **Indirect Detection:** The secondary particles produced in the atmosphere are measured by ground-based detectors. The large areas of detection allow to cover the highest energy range of the spectrum.
- **Direct Detection:** The incoming particle is measured by detectors in the space, *space-borne*, or balloon flight detectors, *balloon-borne*. Due to the weight constraints in space, the energy range is limited by the size of the detector, currently up to a few hundred TeV.

In general, the combination of both methods allows to characterize the different regions of the energy spectrum.

1.5.1 Indirect Detection

The indirect detection is a method used to measure the secondary particles produced in the interaction of the cosmic rays with the atmosphere. When this happens a cascade of particles, called particle shower, is produced and reaches the ground. By locating an array of detectors at the ground level, *ground-based* detectors, the particle shower can be reconstructed using different techniques, and the energy and nature of the incoming particle can be estimated.

The main advantage of this method is that the surface of detection can be increased by constructing arrays of a great number of detectors with a variable distance between each other. The bigger the surface the more particles will be collected in the highest energy region and, therefore, the precision of the measurement will improve. However, an intrinsic limitation of this technique arises from the particle identification which relies on the models of the atmospheric interaction.

The detectors used for the shower reconstruction can be of different types: scintillator detectors, water Cherenkov detectors, and fluorescence telescopes. Experiments are based on only one of those techniques or in multiple ones (also called hybrid techniques).

Examples of scintillator detectors are the Akeno Giant Air Shower Array (AGASA) [46], the KArlsruhe Shower Core and Array DEtector (KASKADE) [47] and KASKADE-GRANDE [48]; and of water Cherenkov detectors is the High Altitude Water Cherenkov (HAWC) [49] [2].

Among the hybrid ones, it is worth mentioning the Pierre Auger Observatory [53; 54] which uses a combination of water Cherenkov and fluorescence detectors, and the Telescope Array (TA) [55] which uses a combination of scintillators and fluorescence detectors.

1.5.2 Direct Detection

The direct detection is a method used to measure the cosmic rays before they interact with the atmosphere. For this purpose, two type of instruments have been used during the history: balloon-borne and space-borne detectors (this includes particle detectors on satellites or the ISS).

The main advantage of this type of detection is the particle recognition and energy measurement. However, since the instrument has to be flown or launched to space there are some limits in the size which constrain the energy range up to few hundred TeV.

1. **Balloon-Borne Detectors:** Since 1911 the balloon flight detectors have been widely used to provide direct measurements of the cosmic rays due to their ease of construction (less challenging technology was needed) and less expensive cost. Even though the flights lasted for only a few days, the lack of exposure could be compensated with multiple launches of the same instrument. For this reason, nowadays this kind of detector is still in use.
   The modern era of the balloon flight detectors started around 1947 when plastics, suitable for the construction of very big balloons with light-weight skin and able to withstand heavy payloads, became available. From the 1970s on a large number of magnetic spectrometers were flown to study the anti-particles (positrons and antiprotons especially) as well as the nuclei spectra. Some of the more important ones were the High Energy Antimatter Telescope (HEAT) with the measurement of the electron, positron and anti-proton spectra [56; 57]; the Balloon-borne Experiment with Superconducting Spectrometer (BESS) with the measurement of the proton and antiproton spectra [58; 59]; the Cosmic AntiParticle Ring Imaging Cherenkov Experiment (CAPRICE) with the measurement of the electron, positron, proton and antiproton spectra [60; 61; 62]; BESS-polar with the extended measurement of the antiproton spectrum [63]; the Advanced Thin Ionization Calorimeter (ATIC) with the measurement of the electron, proton and nuclei spectra [64; 65]; and the Cosmic Ray

[2] Gamma observatories have also provided measurements of cosmic rays up to a few TeV. Examples of telescope Cherenkov are: the telescope Cherenkov detectors with the Major Atmospheric Gamma-ray Imaging Cherenkov Telescope (MAGIC) [50], the High Energy Stereoscopic System (H.E.S.S.) [51] and Very Energetic Radiation Imaging Telescope Array System (VERITAS) [52]

Energetics and Mass Balloon Experiment (CREAM) with the measurement of proton and nuclei spectra [66].

2. **Space-Borne Detectors:** It was during the 1960s when the first satellite experiments were sent to space to explore the cosmic rays without the atmospheric interaction. In particular, the PROTON satellite program measured the cosmic ray spectra from 100 GeV to 100 TeV [67].
   The next decade initiated the exploration of the outer Solar System with the Voyager program (Voyager 1 and Voyager 2) and made the first survey of the X-ray and gamma-ray part of the electromagnetic spectrum with the High Energy Astronomy Observatory (HEAO 1, HEAO 2 and HEAO 3). The HEAO 3 included a cosmic rays module to measure the composition and energy spectra between beryllium and nickel (Z = 4 to Z = 28) from 0.6 GeV to 35 GeV [68]. During the 1980s the Cosmic Ray Nuclei (CRN) detector measured the elemental composition and energy spectra from Boron to Iron (Z = 5 to Z = 26) for the energy range 40 GeV to 1 TeV [69]. Also, several proposals for a long duration CR observatory in the space were made [70].
   In the 1990s the proposal for a magnetic spectrometer [71], AMS, culminated in the construction of a prototype, AMS-01, to test the performances and operations of a spectrometer in the space. AMS-01 results measured the fluxes for different species of CRs with unprecedented precision, more details in chapter 2.
   The decade of the 2000s was very productive for the field of cosmic rays thanks to the Payload for Antimatter Matter Exploration and Light-nuclei Astrophysics (PAMELA) and Fermi Large Area Telescope (Fermi-LAT) experiments. In particular, PAMELA was the first satellite-based spectrometer dedicated only to the detection of cosmic rays, focusing on the antimatter component (positrons and antiprotons). The acceptance of the detector ($0.002\ m^2 sr$) allowed to reach energies of a few hundred GeV. Even though Fermi-LAT was initially sent to perform gamma-ray observations, the mission has provided over the years very valuable information for the CRs field, corroborating some of the measurements made by PAMELA.
   The last decade has brought several experiments of important relevance classified in two categories depending on the main detection technique:

   - **Calorimeters:** In the space, they profit from their very large acceptances to reach higher energies than other space experiments. However, they mainly consist in an electromagnetic calorimeter and they do not have separation capabilities. Two important calorimeters were launched to space in the last ten years:
     The Dark Matter Particle Explorer (DAMPE) is a space telescope calorimeter for electron, cosmic rays and high energy gamma-ray detection. It was sent to space by China in 2015 being its first space observatory ever, and it continues collecting data up to date. The scientific goals are the measurement of electrons and photons in order to identify possible Dark Matter signatures and the understanding of the origin and propagation mechanisms of high energy cosmic rays by measuring protons and heavy ions. The energy range extends up to 5 TeV for electrons and 100 TeV for protons.
     The CALorimetric Electron Telescope (CALET) is a space telescope calorimeter constructed to perform high precision measurements of the electron spectrum as well as high energy charged cosmic rays. It was launched by the Japan Aerospace Exploration Agency (JAXA) in 2015 and mounted onboard the ISS where it continues collecting data. The scientific objectives include precision measurements of the electron spectrum and the study of the origin and propagation of the high energy charged cosmic rays, performing measurement of cosmic nuclei. The energy range spans up to 5 TeV for electrons, 10 TeV for protons, and 100 TeV for nuclei.

- **Spectrometers:** In the space, they profit from their spectrometer capabilities to identify particles with high precision, in particular, to distinguish matter from antimatter. Their acceptances are smaller than calorimeters and so they reach lower energies of the spectra.
  The Alpha Magnetic Spectrometer (AMS-02) is a large acceptance (0.5 $m^2 sr$) particle physics detector that was installed onboard the International Space Station in May 2011 to carry out a long-term mission of fundamental physics research in space. The scientific goals include indirect searches for dark matter and primordial antimatter, and the origin and propagation of the cosmic rays in the energy range up to a few TeV. The spectrometer capabilities together with the large acceptance of the detector have allowed during the years to provide the most precise measurements of the antimatter channels. More details can be found in chapter 2.

1.6 Galactic Cosmic Ray Spectral Observations

Many observations that are not fully understood have been reported in the whole energy spectrum (figure 1.3). Nevertheless, the main focus of this section will rely on the observations regarding the galactic cosmic rays.

1.6.1 Primaries and Secondaries

The precise measurement of the primary, secondary and secondary-to-primary cosmic ray fluxes constitutes an important piece of information to understand the current acceleration and propagation mechanisms. In particular, their measurement not only allows to improve our knowledge of the different processes but also may reveal additional features that challenge the standard paradigm of cosmic rays.

In fact, the experimental results from PAMELA [72], DAMPE [73], CALET [74] and AMS-02 [75] have shown that the proton flux cannot be described by a single power law and the spectral index progressively hardens above $\sim$ 200 GV (figure 1.9a). Precise measurements of the helium flux by AMS-02 [76] also show a deviation from a single power law in $\sim$ 200 GV but the rigidity dependence is distinctly different (figure 1.9b). The proton-to-helium ratio decreases with the rigidity and can be described from 1.9 GV to 1.8 TV by the function $A + C(R/3.5GV)^{\delta}$ with R the rigidity and, A, C and Δ rigidity independent fit parameters.

AMS-02 has also reported the fluxes for the primaries carbon and oxygen [76] as well as for the secondaries lithium, beryllium, and boron [78]. The results show that primaries He, C, and O have an identical rigidity dependence above 60 GV and secondaries above 30 GV. All fluxes deviate from a single power law above $\sim$ 200 GV, but the rigidity dependence is distinctly different (figure 1.10a). In particular, the differences between the primaries and secondaries are investigated by means of the ratios of Li, Be, and B to C and O, as an example the Boron-to-Carbon flux ratio is shown in figure 1.10b. The ratios are fitted to a single power law function in two non-overlapping rigidity intervals [60.3-192] and [192-3300] GV showing that the secondary cosmic rays harden more than the primaries.

The current observations in the primary and secondary fluxes not only have provided important information to understand better the production and propagation mechanism, but also show new phenomena within the Galaxy which are yet not completely understood. These new features could be explained with the inclusion of local sources of high rigidity cosmic rays [79; 80; 81] or the modification of the current propagation models, usually non-linear models [82; 83; 84]. Therefore, the precise measurement of the cosmic ray fluxes provides, on the one hand, constraints on the propagation models, which may allow to improve the predictions in other relevant channels (such as antimatter), and on the other hand, an additional channel for the exploration of new physics.

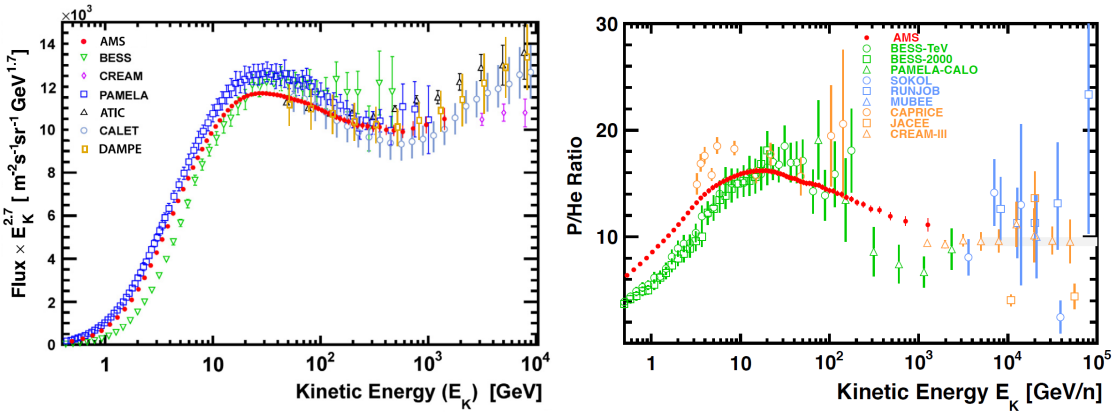

(a) Proton Flux (b) p/He Flux Ratio

Figure 1.9: (a) Proton flux as a function of the kinetic energy for different experiments. Above $\sim$ 200 GV the flux cannot be described by a single power law [77]. (b) Proton-to-helium flux ratio as a function of the kinetic energy for different experiments. The ratio decreases with the rigidity and can be described from 1.9 GV to 1.8 TV by the function $A + C(R/3.5GV)^{\delta}$ with R the rigidity and, A, C and Δ rigidity independent fit parameters [77].

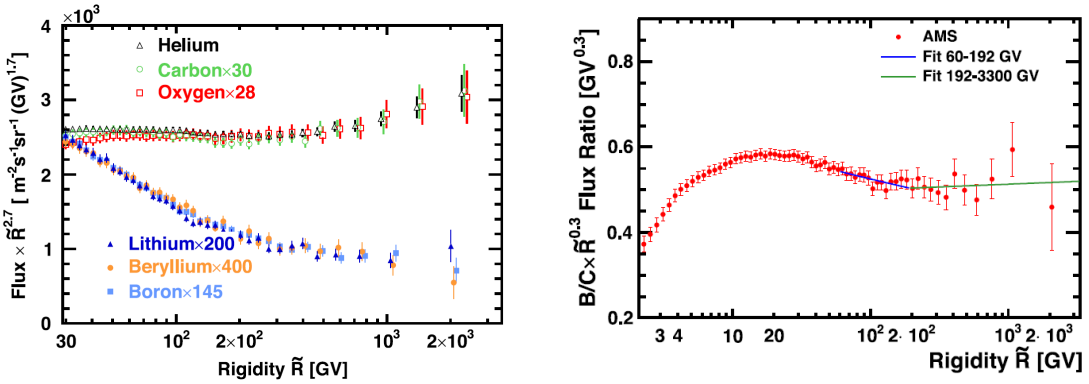

(a) Light Primary and Secondary Fluxes (b) Boron-to-Carbon Flux Ration

Figure 1.10: (a) AMS-02 precise measurements of the light primary (He, C, O) and light secondary (Li, Be, B) fluxes as a function of the rigidity. The rigidity dependence of primary and secondary cosmic rays is distincly different [77] (b) AMS-02 precise measurement of the Boron-to-Carbon flux ratio. The data is fitted to a s single power law function with two non-overlapping intervals [60.3-192] and [192-3300] GV, shown as blue and green respectively. The secondary cosmic rays harden more than the primaries. For display purposes the ratio is scaled by $R^{0.3}$ [77].

1.6.2 Antimatter

The standard paradigm of the cosmic rays predicts that the light antimatter (mainly e^+ and $\bar{p}$) is produced in the interaction of primary protons and nuclei with the ISM. The most abundant particles produced in pp collisions are $\bar{p}$, charged kaons, and charged pions, where the two latter eventually decay into a pair $e^{\pm}$. According to this, the e^- flux has a primary (electrons ejected by SNRs) and a small secondary component, and the e^+ and the $\bar{p}$ fluxes only a pure secondary origin.

The production of heavier antimatter such as anti-helium ($\bar{He}$), anti-carbon ($\bar{C}$), and anti-oxygen ($\bar{O}$) are not expected to come from fragmentation processes and their observation could be a hint of the existence of primordial antimatter domains.

In this sense, the search for antimatter in cosmic rays serves as a channel to test the current

understanding of the production and propagation mechanisms within the Galaxy. In particular, the measurement of the light antimatter channels allows to investigate additional contributions to the expected secondary production.

One of the first observable that was measured in the search for light antimatter was the positron fraction (PF)

$$PF = \frac{\Phi_{e^+}}{\Phi_{e^+} + \Phi_{e^-}} \tag{1.9}$$

since the complete knowledge of the detector's behavior (such as acceptance or efficiencies) would cancel out.

The first measurements of the PF indicated a rise with the energy that was attributed to either an additional contribution of positrons or a reduction of the electrons. The rise was confirmed and attributed to a positron excess by PAMELA [85] and Fermi-LAT [86; 87] with the measurements up to 300 GeV and 200 GeV respectively. AMS-02 has extended the results up to 1 TeV [88] verifying the previous measurements and showing additional features. In particular, it showed that the PF starts rising from $\sim$ 8 GeV until 200 GeV and, then, it drops up to 1 TeV. Figure 1.11a shows a compilation of the PF from different experiments.

AMS-02 has also provided (thanks to the large acceptance and spectrometer capabilities) the precise measurement of the individual positron and electron fluxes to higher energies than previous experiments [89; 88]. The positron flux shows a significant excess starting in $\sim$ 25 GeV followed by a sharp drop-off above $\sim$ 284 GeV. The spectrum is well described by the sum of a secondary component, which dominates at low energies, and a source component, which dominates at high energies, with a finite energy cutoff at 810 GeV (figure 1.11b). The electron flux exhibits a significant excess starting from 42 GeV compared to the lower energy trends, but the nature of this excess is different from the positron flux excess above 25 GeV. Contrary to the positrons the electrons do not present an energy cutoff below 1.9 TeV (figure 1.12a).

The study of the $(e^+ + e^-)$ flux is a complementary measurement mainly carried out by calorimeters or ground-based detectors, since it does not required to distinguish matter from antimatter. Recent results from calorimeters such as Fermi-LAT [86; 87], DAMPE [90] and CALET [91]; and ground-based detectors such as H.E.S.S. [92] have been reported. AMS-02 has also provided results to this channel [93]. Figure 1.12b shows a compilation of the $(e^+ + e^-)$ flux.

The antiproton flux constitutes an additional channel of light antimatter that provides independent information from the positron flux. Recent measurements from BESS-polar [63] and PAMELA [94] showed that the antiproton ratio, as well as the antiproton flux, were consistent with secondary production. AMS-02 results extended the rigidity range with increased precision [95], showing that the functional behavior of the antiproton flux is similar to the proton flux. This result is not expected if cosmic antiprotons are produced only in collisions of cosmic rays with the interstellar medium. Figures 1.13a and 1.13b show the the antiproton-to-proton flux ratio and antiproton flux for the three experiments.

The positron and antiproton observations challenge the standard paradigm of cosmic rays in which antimatter is produced by the interaction of primary protons with the ISM. The origin of these features is still unclear and many models have been proposed.

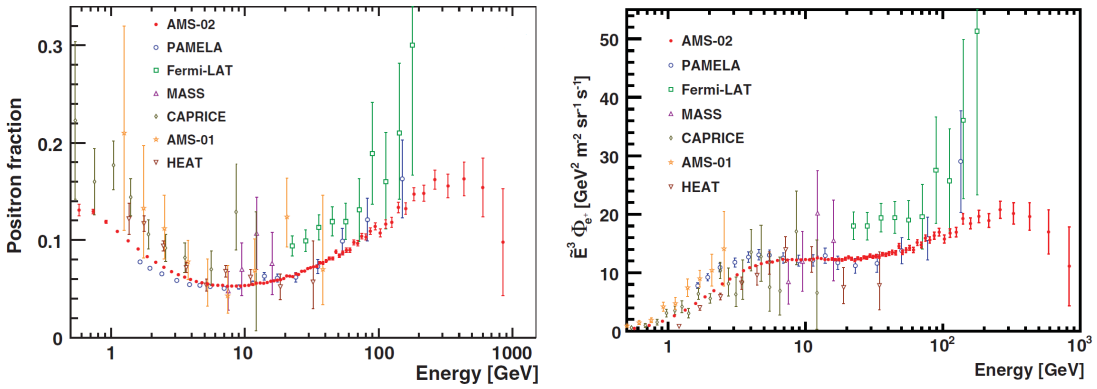

(a) Positron Fraction (b) e^+ Flux

Figure 1.11: Positron fraction [88] (a) and positron flux [89] (b) as a function of the energy for different experiments. The features observed in (a) and (b) suggest an additional contribution of positrons not consistent with a pure secondary production.

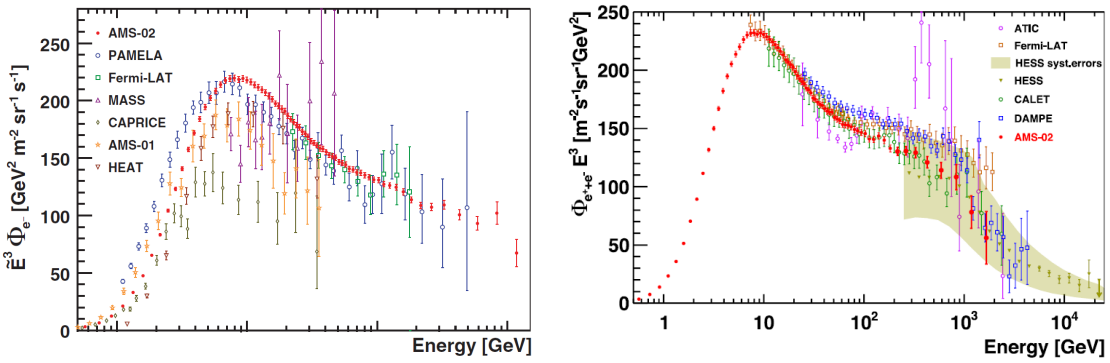

(a) e^- Flux (b) $(e^+ + e^-)$ Flux

Figure 1.12: Electron flux [88] (a) and (positron + electron) flux [89] (b) as a function of the energy for different experiments. The features observed in (a) suggest an additional contribution of electrons with a different origin from the positron flux.

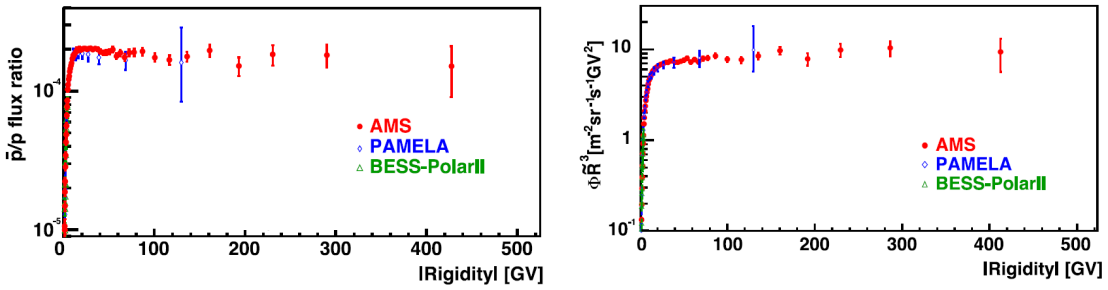

(a) $\bar{p}/p$ Flux Ratio (b) $\bar{p}$ Flux

Figure 1.13: Antiproton-to-proton flux ratio (a) and antiproton flux (b) as a function of the rigidity for different experiments [77]. The features observed in both channels suggest an additional contribution of antiprotons not consistent with a pure secondary production.

Some models include modifications in the cosmic rays propagation [96; 97; 98; 99; 100; 101], but these models not only have to explain the positron and antiproton excesses but also other channels like secondary-to-primary flux ratio. In this sense, the precise measurements of the primary and secondary cosmic rays as well as their ratios allow to constrain propagation parameters needed to better understand the secondary production of antimatter and be more sensitive to the observed features.

Other models require the inclusion of primary sources, typically classified in two scenarios: *astrophysical sources* or *dark matter*.

- **Astrophysical Sources:** The Pulsar Wind Nebulae (PWNe) is one of the astrophysical sources that could explain the rise in the positron flux. Pulsars are magnetized neutron stars rotating very fast that emit beams of electromagnetic cascades out of their magnetic poles. Pairs of $e^{\pm}$ can be injected into the ISM if a fraction of the rotation energy (1-30%) is converted into electromagnetic cascades. The injection follows a power law $dN/dE \propto E^{-\alpha}e^{-E/E_c}$ with an exponential cutoff E_c and the maximum energy attainable depends on the age of the pulsar [102]. The Australian Telescope National Facility (ATNF) provides an extensive catalog of pulsars where the Geminga (PSRJ0633+1746), Monogem (PSR B0656+14), and Vela (PSR J0835-4510) are the most common sources used to describe the rise in the positron fraction and the positron flux [103; 104; 105; 106; 107; 108].
- **Dark Matter:** Many observations such as galaxy rotation curves [109; 110; 111], gravitational lensing [112; 113], Cosmic Microwave Background (CMB) [114; 115], etc., suggest the presence of an additional matter component that accounts for an $\sim 85\%$ of the total mass in the Universe. This mass is called *Dark Matter* because it does not interact with the electromagnetic field, which means it does not emit or absorb electromagnetic radiation and, thus, it is extremely challenging to measure from the point of view of the direct detection. Extensions of the Standard Model (SM) of Particle Physics predict that the Dark Matter could eventually annihilate or decay into SM particles allowing an indirect search with cosmic rays [116; 117]. In particular, the measurement of additional contributions in the antimatter channels (since they are believed to have only secondary components) could provide some hints of the Dark Matter presence in the Galaxy. Many models have been proposed to explain the positron and antiproton excesses by means of Dark Matter [118; 119; 120; 121; 122; 123; 124; 125; 126]. Among them, leptophilic channels of mass ~ 1 TeV are favored to explain the positron excess.

In any case, the search for antimatter with cosmic rays provides valuable information to explore new fundamental physics within the Galaxy.

1.7 Anisotropies

The study of the directionality of the charged cosmic rays is a complementary characterization to the energy spectrum that could help to interpret the observed features (see section 1.2.2 and 1.6). In particular, it could provide additional information to understand the origin and propagation of the cosmic rays.

The charged cosmic rays deflect with the GMF as they propagate through space with a curvature, known as Larmor radius, that depends on the energy E of the particle as

$$r = \frac{p_\perp}{ZeB} \approx \frac{1.08}{Ze}\left(\frac{E}{10^6 GeV}\right)\left(\frac{B}{\mu G}\right)^{-1} \qquad (in\ pc) \tag{1.10}$$

with Ze the charge in electron units (usually protons of Z = 1), and B the magnetic field (typically ranging between 3-6 μG [34]). Depending on the energy of the incoming particles and, therefore, on the Larmor radius, two categories of anisotropies are commonly studied: *Intermediate or small scale anisotropies* and *large scale anisotropies*.

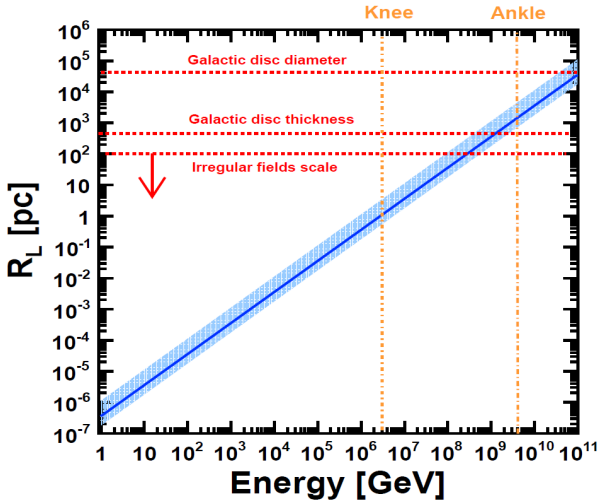

Figure 1.14: Larmor radius r as a function of the energy for protons (Z = 1) in a GMF of B = 3 μG.

Intermediate or small scale anisotropies apply for cosmic rays with $E > 10^9$ GeV where the Larmor radius r (of a few kpc) is much higher than the largest scale of the irregular component of the GMF ($\sim 100 - 300$ pc) (figure 1.14). In this sense, the particle trajectories are not affected by the GMF and local structures (with angular sizes smaller than 60 °) such as hot-spots or point sources can be explored.

Large scale anisotropies apply when the $E < 10^8$ GeV so the Larmor radius r is smaller than the largest scale of the turbulent component of the GMF and the particle trajectories are constantly deflected (figure 1.14). In this energy region, the propagation in the Galaxy is well described in terms of a diffusive mechanism and the cosmic rays are expected to arrive at the Earth almost isotropically. The large scale anisotropies may reveal patterns over the full sky with angular scales greater than 60°. At first order, the anisotropy can be described by a dipole amplitude δ expressed as

$$\delta = \frac{\Phi_{max} - \Phi_{min}}{\Phi_{max} + \Phi_{min}} \tag{1.11}$$

where Φ_{max} and Φ_{min} are the maximum and minimum of the flux and, therefore, δ accounts for the asymmetry between them.

In general, the study of the anisotropies has provided relevant information for different topics in the cosmic rays field:

- **Compton-Getting Effect:** It is an apparent dipole anisotropy due to the relative motion of the Earth with respect to the cosmic rays *local rest-frame*. The magnitude of the anisotropy is expected to be $\delta \approx 5 \times 10^{-4}$, with the maximum in the direction of the Earth's motion around the Sun [127]. The Compton-Getting Effect does not have physical implications, since it is just an effect associated with the kinematics of the Earth, but is commonly used nowadays as a benchmark to test the reliability of the detector and the analysis method in the search for anisotropies. Several experiments have measured this effect, such as: EAS-TOP [128], Tibet [129], Milagro [130], and IceCube [131].
- **Local Environment:** Nagashima, Fujimoto and Jacklyn (NFJ) [132; 133] reported the observation of an excess for $E < 10^4$ GeV in the direction of the heliotail, called *tail-in*, opposite to the motion of the Solar System and a deficit called *loss cone*. The annual variation of the anisotropy showed a modulation with a maximum in December and a minimum, where the anisotropy almost vanishes, in June. The origin of the observation is still unknown but provides information about the local environment that the cosmic rays have to go through.

- **Origin of the high-energy cosmic rays:** Recently, the Pierre Auger Observatory published the results [134] of an anisotropy in the arrival directions of cosmic rays with energies above 8 EeV. The anisotropy was represented by a dipole with an amplitude of 6.5% pointing to the direction in galactic coordinates given by (l, b) = (233º, -13º) which is far from the galactic center (figure 1.15). The magnitude and direction of the anisotropy support the hypothesis of an extragalactic origin for the highest-energy cosmic rays, rather than sources within the galaxy.

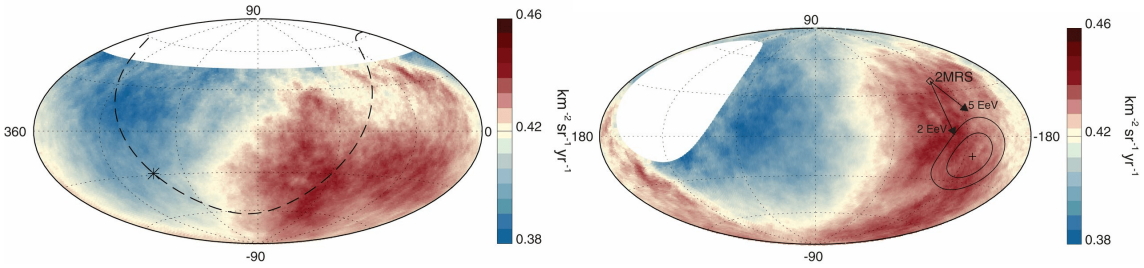

(a) Equatorial Coordinates (b) Galactic Coordinates

Figure 1.15: Skymaps in equatorial (a) and galactic (b) coordinates showing the cosmic ray flux above 8 EeV [134]. For (b) the galactic center is at the origin and the cross indicates the measured dipole direction; the contours denote the 68% and 95% confidence level regions.

In addition, the anisotropy could provide information on other relevant topics within cosmic ray physics:

- **Diffusion:** The diffusion of cosmic rays in the ISM produces density gradients, which cause a dipole anisotropy depending on the diffusion coefficient $D(R)$. The models proposed to describe the diffusion of the cosmic rays predict different rigidity dependences for $D(R)$. Thus, the measurement of the anisotropy as a function of the rigidity may allow to discriminate some of the propagation models.
- **Origin of the knee:** The different hypotheses on the origin of the knee give rise to distinct predictions on the expected anisotropy. In the case of the leakage of cosmic rays out of the Galaxy, an increase of the dipole amplitude at energies around the knee should be observed. On the contrary, if the knee is due to the maximum energy reached by the accelerators, no change of the anisotropy should be expected.
- **Nearby sources:** The current observations (see section 1.6) have shown new features that cannot be described within the standard paradigm of cosmic rays. Some of the explanations require the inclusion of primary sources such as dark matter or astrophysical sources. In particular, the presence of nearby compact sources may induce an anisotropy in the arrival direction of the cosmic rays. Therefore, its measurement could provide relevant information to disentangle the different scenarios proposed.

The measurement of the directionality of the cosmic rays is carried out by comparing the map of events with a reference map in a specific coordinate system, where the latter usually describes the response of the detector to an isotropic flux. Any deviation from the reference might be regarded as a signal. Similarly to the energy spectrum, there are two types of experimental methods to measure the anisotropy: *Indirect Detection* and *Direct Detection*.

1.7.1 Indirect Detection

Traditionally, ground-based detectors have provided results on the anisotropies due to the large collecting areas and long exposure times. For this reasons, this type of experiments are suitable for directionality studies since high statistics are necessary to recover the small signals. Nevertheless,

as a consequence of the small identification capabilities, the particles are classified in a light and a heavy component. The results and techniques presented in this section will cover the anisotropies for the heavy component.

The construction of the reference map requires a precise knowledge of the detector's behavior, something quite challenging for most of the ground-based experiments. Usually, the development of the cascade produced in the interaction of the particles with the atmosphere is difficult to model and the response of the detector is not controlled at the required precision. In most cases, this does not allow to construct a 3D reference map and other techniques have to be used.

For this reason, specific methods based on data have been developed for the construction of the isotropic reference map. Different techniques have been used but, in the end, all of them are equivalent to average the distribution of events out in right ascension within the same band of declination. In the standard analysis for the determination of the anisotropies, the so-called Rayleigh method [135], the distribution of collected events in right ascension is expanded in Fourier series. The amplitude A_1 and phase ϕ_1 of the first harmonic provide the degree of the anisotropy. The A_1 normalized by the mean declination of the collected events only provides the projection of the dipole moment onto the equatorial plane $\delta_\perp$ and, thus, this technique makes most of the ground based-detector not sensitive to the anisotropy on the declination band [3].

Figure 1.16 shows the amplitude A_1 and phase ϕ_1 of the first harmonic, for energies between $10^{11} - 10^{16}$ eV (100 GeV to 10000 TeV), measured by different ground-based experiments since 1973. The different diffusion models predict residual anisotropies with values between $10^{-5} - 10^{-2}$ [31], however, the measured effects could also be explained by the presence of a nearby cosmic rays source [136; 137]. A complete description of the measurements can be found in [138; 139; 140].

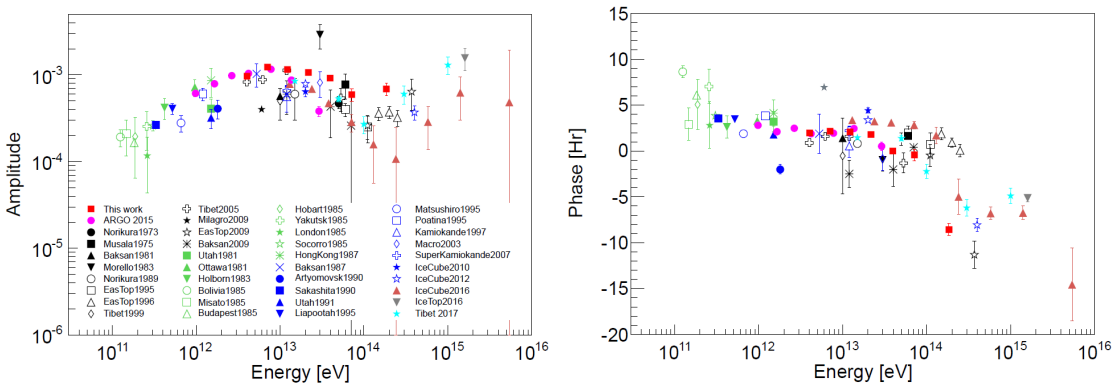

(a) Amplitude (b) Phase

Figure 1.16: Amplitude and Phase of the first harmonic as a function of the energy measured by several experiments [138]. The results show an amplitude between $10^{-4} - 10^{-3}$ with a complex energy dependence. The amplitude increases up to E $\sim 2 \cdot 10^{12}$ eV (2 TeV); then it forms an approximately energy independent plateau between E $\sim 2 \cdot 10^{12} - 2 \cdot 10^{13}$ eV (2-20 TeV); between E $\sim 2 \cdot 10^{13} - 1 \cdot 10^{14}$ eV (20-100 TeV) it decreases; and finally for $E > 10^{14}$ eV 100 TeV the amplitude grows fast.

[3] This limitation is only due to the technique applied since the detector's behavior is not understood at the required precision. For example, Pierre Auger was able to describe the detector's behavior and, thus, to construct a 3D reference map which allowed them to recover the 3D anisotropy

1.7.2 Direct Detection

This method of detection is carried out by space-borne detectors where the different species of cosmic rays can be identified before they interact with the atmosphere. Balloon-born experiments are not suitable for the anisotropy measurements since usually long exposure times are required.

The main advantages of the direct measurement is the particle recognition, the energy measurement, and the almost full sky coverage. In fact, due to their orbit around the Earth, the sky is almost completely covered and a 3-dimensional reconstruction of the dipole amplitude can be performed, contrary to most of the ground-based experiments that can only measure in bands of declination. However, their sizes are limited since they have to be carried to space and, therefore, the acceptances smaller than ground-based experiments. This only allows reaching a lower part of the energy spectrum.

As a consequence of the particle recognition, the positron and electron channels has been investigated during the last years as a tool to discriminate between astrophysical sources or dark matter for the positron excess [141; 142; 143; 144]. More specifically, a local astrophysical source of primary positrons would induce a sizable anisotropy in their arrival directions, in contrast to dark matter, which is assumed to be homogeneously distributed in the halo.

Pulsars represent the leading candidate as primary sources of positrons due to their capability to inject pairs of $e^{\pm}$ in the medium. Contributions from Geminga and Monogem are commonly used to explain the observed excess and predict anisotropies of amplitude $10^{-2} - 10^{-3}$ [145; 146; 147; 148]. Therefore, the measurement of a dipole anisotropy in the positron flux would favor the pulsar origin whereas their absence would favor the more exotic dark matter scenario.

On the other hand, the study of the anisotropy may also help to understand the change in the spectral index for protons and light primary nuclei helium, carbon and oxygen. Typically, results on the all-nuclei anisotropy have been reported by ground-based detectors (figure 1.16). Different models have been proposed to account for such amplitudes, however, transport models are not able to completely explain the measurements [149] and usually the inclusion of local sources is required, such as the SNR associated to Geminga [150; 151]. In this sense, the results reported from space-borne detectors profit from their particle recognition (due to the direct measurement) to provide more constraints on the individual fluxes to the different models, and also allow to extend the measurements to lower energies than ground-based experiments.

No anisotropy has been measured by any space-borne detector, thus only limits to the dipole amplitude have been established. Results on the anisotropy have been provided by PAMELA on the $e^+/e^-, e^+/p$, and p [152; 153]; Fermi-LAT on the $(e^+ + e^-)$ and p [154; 155]; DAMPE on the all-particle component [156]; and CALET on the $(e^+ + e^-)$ [157].

In the case of AMS-02 results on the e^+, e^- and p anisotropy have been reported [158]. In particular, it is the only experiment who has provided absolute values on the e^+ and e^- anisotropy (due to the spectrometer properties) with limits on the dipole amplitude of $\delta_{UL}(e^+) = 2.19\%$ and $\delta_{UL}(e^-) = 0.6\%$ for energies above 16 GeV. For protons the limit quoted is $\delta_{UL}(p) = 1.07\%$ for rigidities above 300 GV. For the light primary nuclei helium, carbon and oxygen no individual anisotropy have been presented. In particular, the investigation on these channels constitutes an additional constraint to the proton one.

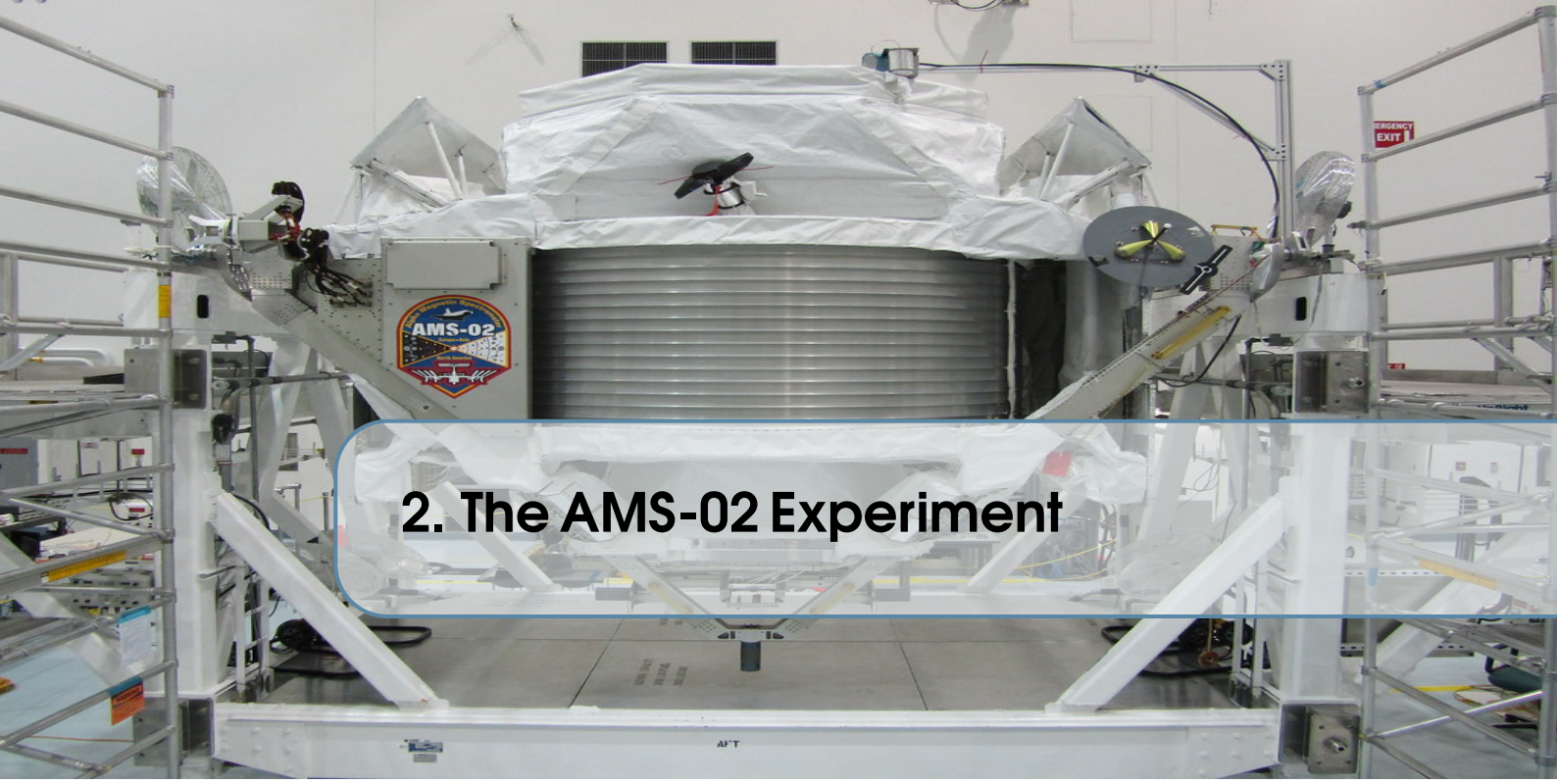

2. The AMS-02 Experiment

"I am nothing but I must be everything."

— Karl Marx

2.1 Introduction

The Alpha Magnetic Spectrometer (AMS-02) is a multipurpose particle physics detector that was installed onboard the International Space Station (ISS) in May 2011 to carry out a long-term mission of fundamental physics research in space. The physics objectives of the experiment include indirect searches of dark matter, the primordial antimatter, and the origin and propagation of the cosmic rays. The AMS-02 experiment is conducted by the AMS collaboration which is composed of 44 institutions from America, Europe, and Asia.

The AMS project was proposed back in 1994 [71] as a large acceptance spectrometer to be installed on a satellite or space station. The innovative design was first tested in a precursor flight, AMS-01, that was flown by the Space Shuttle Discovery in June 1998 during a 10-day mission. The purpose was to validate in a short-term mission the performances and operations of a spectrometer in the space. The AMS-01 mission successfully recorded nearly 80×10^6 cosmic ray events and lead to relevant physics results [159; 160; 161; 162; 163; 164; 165; 166; 167].

After the AMS-01 mission, the design of AMS-02 started. The subdetectors were built in different institutions of the collaboration and finally, assembled together at CERN. Unfortunately, after the accident of the Shuttle Columbia on 1 February 2003, the Space Shuttle program was suspended including the launch that would take AMS-02 to the ISS. Nevertheless, on 15 October 2009, NASA was authorized to add another Space Shuttle flight to transport AMS-02 to the ISS. The launch took place on 16 May 2011 onboard the Space Shuttle Endeavour (figure 2.1a). Three days later, the detector was installed by the crew of the STS-134 mission at the upper Payload Attach Point on the ISS S3 Truss (figure 2.1b). Since then, AMS-02 has been collecting data at a rate of $\sim 16 \times 10^9$ events per year and plans to continue until the end of the ISS (currently scheduled in 2028). Figure 2.1c shows AMS-02 mounted on the ISS.

This chapter will present a general overview of the AMS-02 detector, including a description of each subdetector as well as the data acquisition system and reconstruction procedure.

(a) Space Shuttle Endeavour

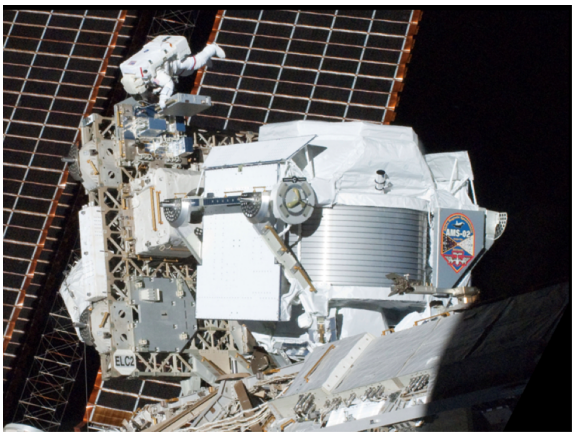

(b) AMS-02 Installation

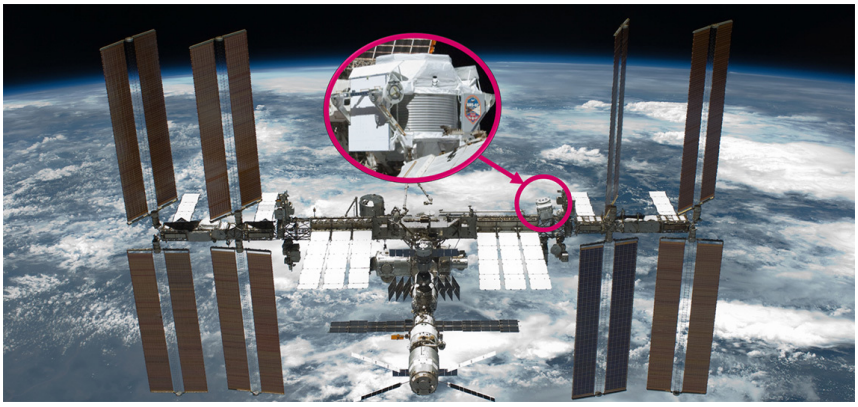

(c) AMS-02 on the ISS

Figure 2.1: (a) Space Shuttle Endeavour (b) Installation of the AMS-02 detector by the STS-134 crew on the ISS (c) AMS-02 mounted on the ISS with a 12 degree angle to the zenith to prevent that the rotating ISS solar arrays may interfere with the AMS field of view.

2.2 The AMS-02 Detector

The AMS-02 detector is a large acceptance ($0.5\ m^2sr$) magnetic spectrometer designed to carry out precise measurements of galactic charged cosmic rays. It is mounted onboard the ISS with 12º inclination with respect to the zenith of the station. The ISS orbits the Earth at an altitude ranging from 370 to 460 km, with an orbital inclination of 51.6º, and with a velocity of 7.6-7.7 km/s, which results in a period of 93 minutes [168].

AMS-02 dimensions, weight, and power consumption were defined to fulfill the conditions required to be launched in the Space Shuttle and installed in the ISS. In particular, it has a weight of 7.5 tons, a size of $3 \times 4 \times 5\ m^3$, and a power budget of 2 kW provided by the ISS.

In order to accomplish the physics objectives, the detector was designed to identify particles with high precision and, in particular, to distinguish matter from antimatter. AMS-02 is composed of a permanent magnet and 6 subdetectors to provide redundant measurements of the velocity $\beta = v/c$, momentum p, and charge Z of the incoming particle. The layout of the detector is shown in figure 2.2.

- **The Permanent Magnet** has a magnetic field of 0.15 T which provides the spectrometer

capabilities.

- **The Silicon Tracker Detector (STD)** is composed of 9 precision silicon tracker layers, L1 to L9, within the magnet bore and above and below the magnet. The trajectory of the particle is bent in the magnet and reconstructed by the STD, allowing to measure the momentum and charge with its sign.
- **The Transition Radiation Detector (TRD)** is located at the top of the AMS and is able to distinguish between protons and positrons.
- **The Time Of Flight (TOF)** consists of two sets of two orthogonal planes located above and below the magnet bore, the upper TOF and the lower TOF, providing a measurement of the particle velocity $\beta = v/c$ and acting as the trigger of the experiment.
- **The Anti-Coincidence Counter (ACC)** is surrounding the tracker within the magnet bore and provides a veto for particles traversing the detector laterally.
- **The Ring Imaging Detector (RICH)** is placed below the lower TOF and provides a precise measurement of the velocity and mass of the particle.
- **The Electromagnetic Calorimeter (ECAL)** is located below the RICH and measures the energy of the electromagnetic particles up to a few TeV.

A detailed description of each of them is presented below.

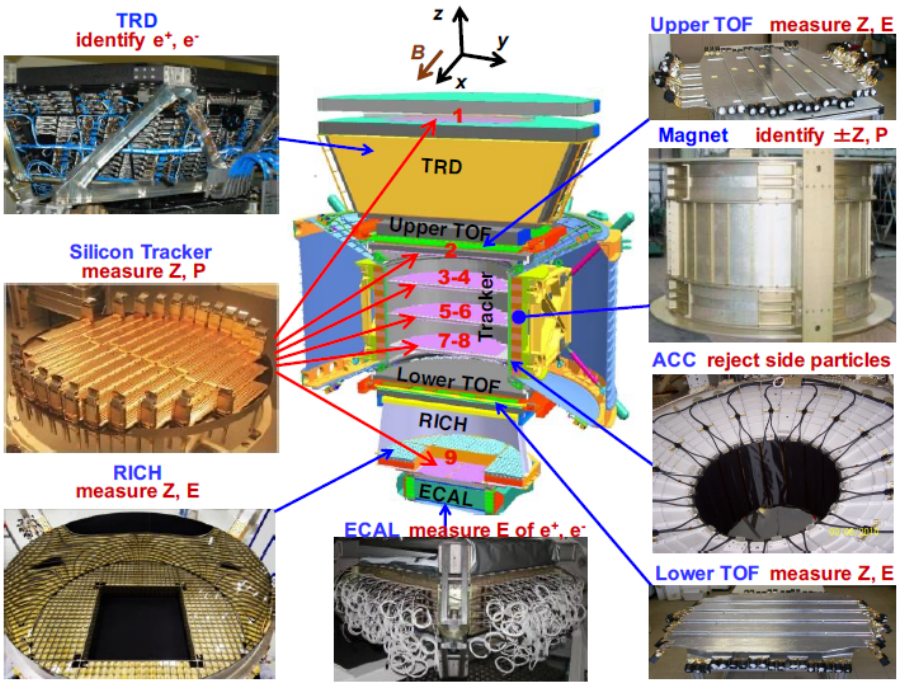

Figure 2.2: Schematic view of the AMS-02 detector where the arrows indicate the different subdetectors.

2.3 Permanent Magnet

The permanent magnet [169; 170; 171; 77], shown in figure 2.12, was previously tested on the AMS-01 flight and is described in detail in [167].

It is located at the central part of AMS-02 and it is assembled in a cylindrical shell structure of 0.8 m height, 1.1 m inner diameter, and 1.29 m outer diameter (figure 2.3a).

The magnet is made of 64 high-grade Nd-Fe-B sectors, each of them composed of 100 blocks

of $5.08 \times 5.08 \times 2.54\ cm^3$. This configuration produces a uniform magnetic field of 1.5 kG (0.15 T) in the X direction at the center of the magnet (figure 2.3b). The AMS local reference system is defined within the magnet, with the Y direction corresponding to the bending plane.

The dipole moment and the fringe field outside the magnet are negligible in order to eliminate the effect of a torque on the ISS (due to its coupling with the Earth magnetic field), which ensures the safe operations of the astronauts in its vicinity.

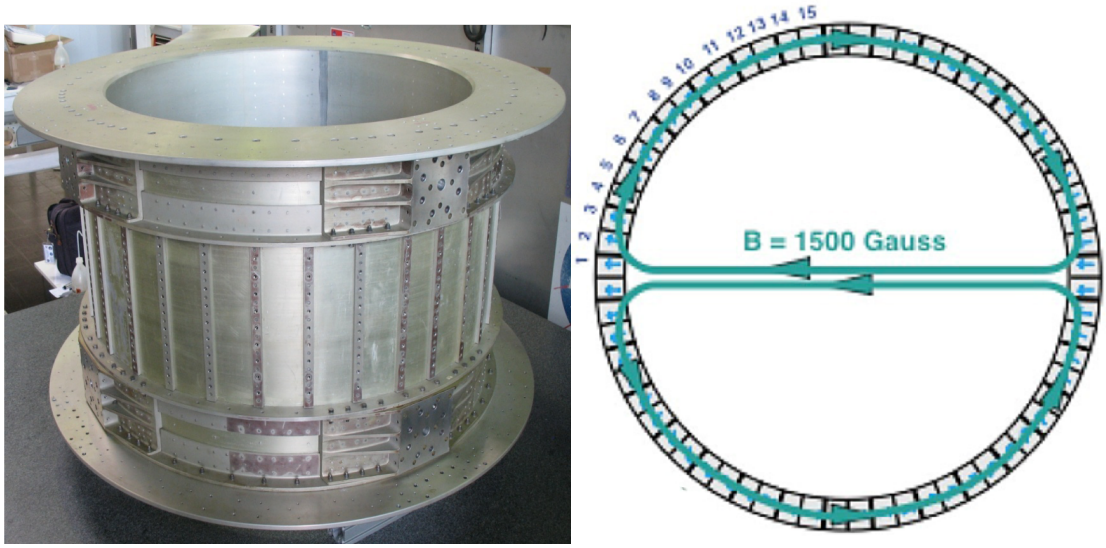

(a) Permanent Magnet (b) Magnetic Field

Figure 2.3: The AMS-02 permanent magnet (a) and its magnetic field (b), showing the field direction of the 64 permanent magnet sectors resulting in negligible dipole moment and field leakage outside the magnet.

2.4 Silicon Tracker Detector (STD)

The Silicon Tracker Detector (STD) has nine layers L1-L9 arranged in 6 planes along the Z-axis. The first (L1) is at the top of the detector, the second (L2) just above the magnet, the central ones are six (L3 to L8) within the bore of the magnet, and the last (L9) just above the ECAL (figure 2.4). Three of the planes are equipped with layers on both sides (L3-L8), as shown in figure 2.4, and are held stable by a special honeycomb carbon fiber structure that matches the shape of the magnet. The STD has a total of 2264 double-sided microstrip silicon sensors that are assembled in 192 readout units called *ladders*, with $\sim$ 200,000 readout channels. The total lever arm of the tracker from L1 to L9 is 3.0 m [169].

The tracker together with the magnet accurately determines the particle trajectory by multiple measurements of the coordinates with a resolution in each layer better than 10 μm in the bending direction (Y) and 30 μm in the non-bending direction (X) [172]. The bending of the trajectories by the magnet allows to determine the rigidity of the incoming particle, R. In addition, the energy losses in the tracker provide the absolute value of the charge yielding into the measurement of the momentum, defined as $p = R\,Z$.

The alignment of the different layers should not compromise the excellent spacial resolution, however, small shifts in their position can induce an intrinsic bias in the rigidity measurement which becomes important at high rigidities.

The external layers (L1 and L9) are dynamically aligned every 2 min using the extrapolation

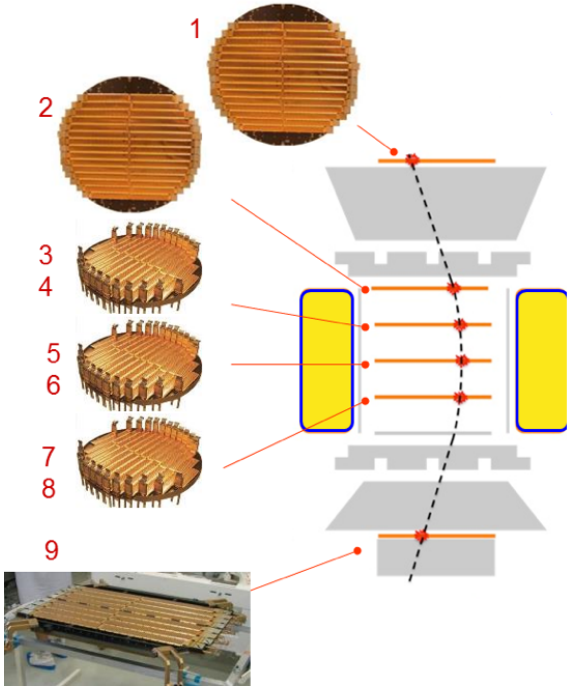

Figure 2.4: The 9 layers of the silicon tracker detector and their location within the detector. Three of the planes are equipped with layers on both sides (L3-L8) whereas the rest are equipped with just one layer (L1,L2 and L9).

of the inner tracker tracks with a precision better than 5 μm for both layers. After the dynamic alignment of the external layers, the precision of the rigidity bias is dominated by the inner tracker layers. Overall, the accuracy of the rigidity scale bias is within 0.034 TV^{-1} or 3% at 1 TV, which corresponds to displacements of the layers L2-L8 of less than 0.2 μm [173].

The measurement of the particle trajectory in the silicon tracker detector is performed by using a track-finding algorithm which first identifies the different track segments in the inner tracker and out of them reconstructs one track as the result of using a χ^2-like track quality estimator. Then, the track is extrapolated to the outer layers and if it finds a segment the track is extended to include these hits [174]. This algorithm is particularly important for heavy nuclei events, in which additional hits or track segments are often present due to delta-ray generation and nuclei interactions with the tracker materials [77].

As a consequence of the track-finding algorithm 4 different tracker patterns can be found:

- **Inner:** No hits in the external layers. It has an aperture angle of 40 º with respect to the AMS zenith direction (figure 2.5a).
- **L1+Inner:** Hit on layer 1 and no-hit on layer 9. It has an aperture angle of 35 º with respect to the AMS zenith direction (figure 2.5b).
- **Inner+L9:** Hit on layer 9 and no-hit on layer 1. It has an aperture angle of 35 º with respect to the AMS zenith direction (figure 2.5c).
- **L1+Inner+L9 (Full Span):** Hits on layer 1 and layer 9. It has an aperture angle of 25 º with respect to the AMS zenith direction (figure 2.5d).

The measurement of the rigidity is determined by using a track-fitting algorithm of the trajectory in the AMS-02 magnet which accounts for the multiple scattering of charged particles and the energy losses in the detector [175].

The rigidity resolution $\Delta R/R$ can be estimated from the Monte Carlo simulation and reaches the 100% in the so-called Maximum Detectable Rigidity (MDR), which is mainly associated to the

different tracker patterns.

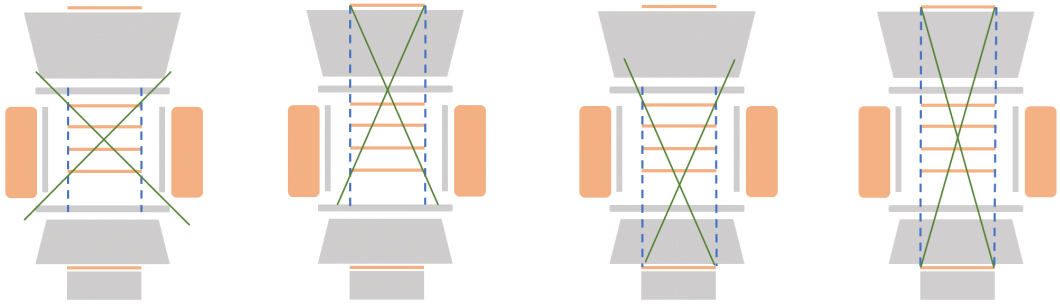

(a) Inner (b) L1+Inner (c) Inner+L9 (d) L1+Inner+L9

Figure 2.5: The four tracker patterns of the AMS-02: (a) Inner, (b) L1+Inner, (c) Inner+L9 and (d) L1+Inner+L9 (Full Span).

The nine tracker layers are able to provide independent precise measurements of the charge Z of cosmic rays since the energy deposition in the silicon is proportional to the square of the charge of the particle according to the Bethe formula, $dE/dx \propto Z^2$ [176].

The resolution $\Delta Z/Z$ of the inner tracker (L2-L8) charge measurement, shown in figure 2.6, allows identify nuclei up to nickel (Z = 28).

Furthermore, the measurement of the trajectory inside the magnet allows to determine the direction of the curvature and therefore the sign of the charge. All this information provides the precise tools to distinguish matter from antimatter.

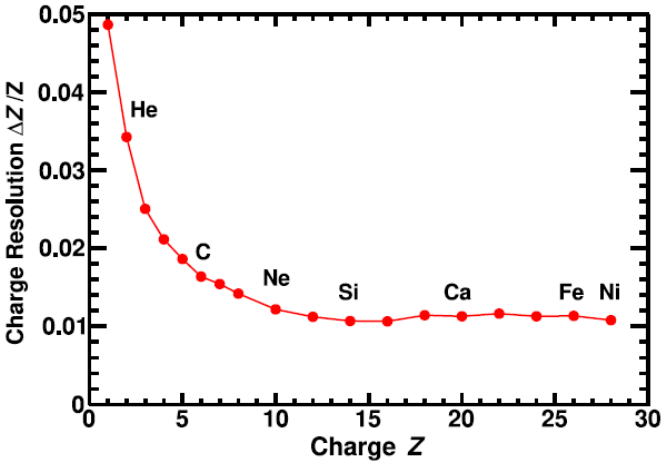

Figure 2.6: Inner tracker (layers L2–L8 combined) charge resolution $\Delta Z/Z$ [77].

2.5 Transition Radiation Detector (TRD)

The Transition Radiation Detector (TRD) [77; 177; 178; 179] is located at the top of AMS, between the L1 and the upper TOF. It consists of 328 modules mounted in 20 layers. Each module is made of 16 tubes with 6 mm diameter and a maximum of 2 m length. As shown in figure 2.7a, each layer is interlaced with a 20 mm thick fiber fleece radiator, LRP375BK, with a density of 0.06

g/cm^3. The layers are supported by an octagonal carbon fiber structure with a very low coefficient of thermal expansion (figure 2.7b) to ensure the minimum relative movement of the TRD elements with the variation of the ambient temperature. There are 12 layers located along the Y-axis, in the middle of the TRD, and the rest along the X-axis, with 4 layers at the top and 4 at the bottom. The tubes are filled with a 90:10 $Xe : CO_2$ gas mixture. The Xenon captures the transition radiation X-rays generated in the radiator whereas the CO_2 ensures a stable operation of the tubes. The signal produced by the ionization is measured by an anode wire in each tube (figure 2.7c).

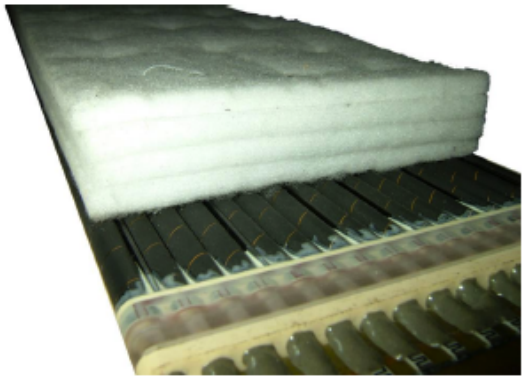

(a) TRD Module

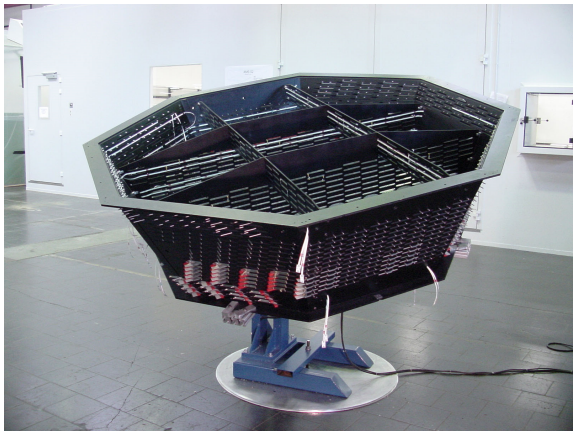

(b) TRD Support Structure

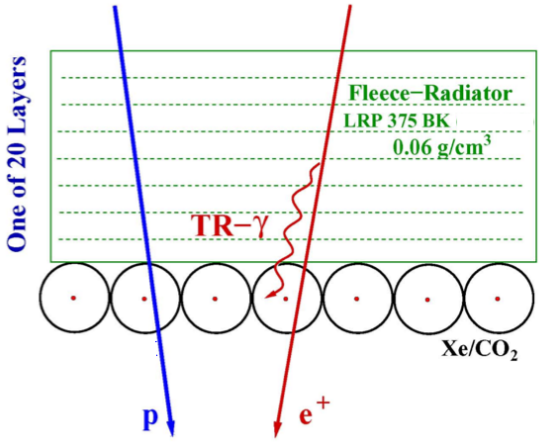

(c) Detection Scheme

Figure 2.7: (a) TRD module prototype with the fiber fleece radiator on top of the layer. (b) The Transition Radiation Detector support structure. (c) Schematic of the detection of ionization losses from charged particles, where protons (blue arrow) are compared to positrons (red arrow) and transition radiation photons (red curved arrow, TR-γ) are emitted when the positrons cross the radiator.

The gas in the tubes is supplied from two tanks of 49 kg of Xe and 5 kg of CO_2, which ensures a livetime of more than 30 years in the space. The measured leak rate is dominated by the CO_2 and amounts to 0.47 g/day on average.

The main purpose of the TRD is to identify electrons and positrons from the proton background very efficiently. The identification principle is based on the electromagnetic transition radiation (TR) emitted when a charged particle traverses the boundary between two different materials. Then, this radiation is efficiently absorbed by the Xe gas in the tubes. Finally, the total energy loss is

proportional to the Lorentz Factor $\gamma = E/m$, which allows to distinguish particles with different masses, in particular, electrons and positrons from protons [180; 181; 182]. Figure 2.8a shows the differences in the energy deposition per tube for electrons and positrons, where due to the high Lorentz factor the electrons will emit TR.

In order to separate between $e^{\pm}$ and protons, signals from the 20 layers are combined in a statistical estimator, TRD_{Lkh}, based on the ratio of probabilities of the $e^{\pm}$ hypothesis and proton hypothesis [183]. Figure 2.8b shows the TRD_{Lkh} distribution from 10-100 GeV together with the Monte Carlo (MC) simulation [184], which reproduces the data over 6 orders of magnitude. The electrons have their maximum at $TRD_{Lkh} = 0.35$ whereas the protons peak at $TRD_{Lkh} = 1$, allowing to reject protons very efficiently. In particular, a cut in the TRD estimator of 0.6 would imply a 90% of efficiency in the electron signal and a proton rejection above 10^3 up to 200 GeV (figure 2.8c). The proton rejection can be increased for the high energy part by tightening the cut in the TRD estimator, so reducing the electron efficiency (figure 2.8c).

In addition, the TRD provides an independent tracking capability due to the position of the layers along the X and Y axis, and the determination of the charge value of the nuclei by measuring their rate of energy loss (dE/dx).

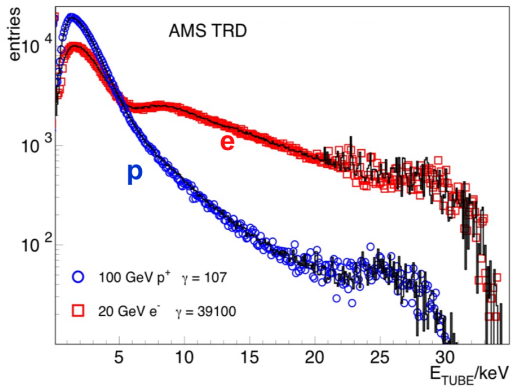

(a) Energy Deposition

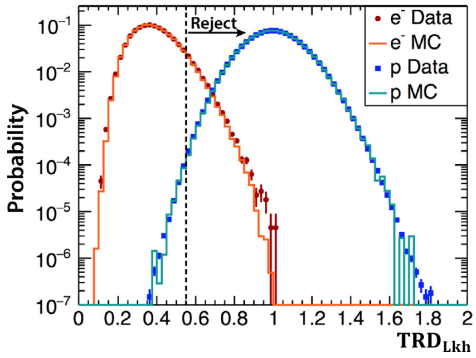

(b) TRD Estimator

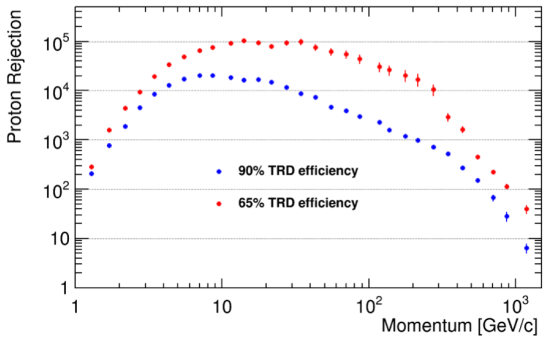

(c) Proton Rejection

Figure 2.8: (a) The energy deposition of protons (blue points) and electrons (red points), where a significant difference in the shape of the proton and electron spectra is used in the likelihood function to separate these two species of cosmic rays [185]. (b) The TRD_{Lkh} distributions for protons (blue) and electrons (red) in the energy range 10–100 GeV together with the Monte Carlo simulation, which describes the data over six orders of magnitude. The vertical dashed line shows the position of the cut corresponding to 90% efficiency of the electron signal. By tightening this cut (reducing the signal efficiency) a higher purity on the electron signal can be achieved [77]. (c) The proton rejection corresponding to a 65% and 90% efficiency in the TRD estimator signal [77].

2.6 Time Of Flight (TOF)

The Time Of Flight (TOF) [186; 187; 188] consists of four layers of scintillation counters arranged in two planes, one on top of the magnet bore (upper TOF) and the other one below it (lower TOF). The layers contain 8 or 10 scintillating paddles 1 cm thick and variable lengths (117 to 134 cm), oriented in the X and Y directions alternatively, with a rectangular geometry for the inner paddles ($\sim$ 12 cm wide) and a trapezoidal shape for the external ones (width 18 to 26 cm) to maximize the geometrical acceptance. Both ends of each paddle are equipped with 2 or 3 PhotoMultiplier Tubes (PMTs) to collect the light emitted by the scintillator. The PMTs are connected to the scintillators by light guides of plexiglass. In total, there are 144 PMTs that collect the light from 34 paddles distributed in the upper and lower TOF. Figure 2.9 shows the upper and lower TOF together with a scheme of one of the paddles.

Figure 2.9: Upper and lower TOF together with a scheme of one of the paddles.

The TOF provides the trigger for charged particles when a coincidence of signals from all four planes is collected, more details about the trigger logic can be found in section 2.10. In addition, the velocity of the particle $\beta = \Delta s / c\Delta t$ can be determined by measuring the time of flight Δt between the upper and lower TOF and the trajectory of the particle Δs. The velocity resolution $\Delta\beta/\beta$ has been measured to be 4% for Z = 1 and decreasing to 1.2% for Z $\geq$ 6, corresponding into a time resolution of 48 ps (figure 2.10a). The precise measurement of the velocity allows to differentiate downward-going particles from upward-going at the 10^{-9} level (figure 2.10b).

The TOF is also able to determine the charge by measuring the energy deposited $dE/dx \propto Z^2$ by a charged particle. Due to the different dynamic ranges, the signal of the PMTs from the anodes and dynodes are used in each case: anodes for $1 \leq Z \leq 3$, anodes and dynodes for $4 \leq Z \leq 8$ and dynodes for $8 \leq Z \leq 30$ (figure 2.11).

Finally, the anode signals are compared to three different thresholds, which are used in the

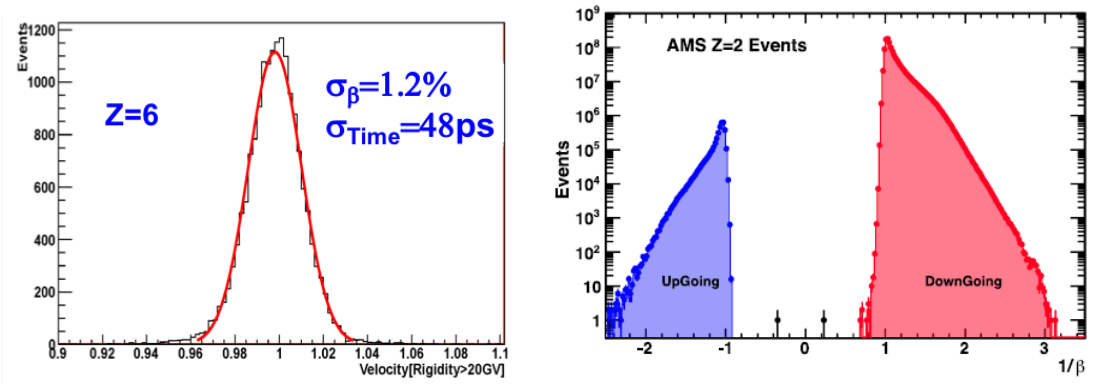

(a) TOF Velocity (b) TOF Inversed Velocity

Figure 2.10: (a) The measured TOF velocity distribution for Z = 6 (C) with a $\sigma = 1.2\%$ from a gaussian fit. This results into a time resolution of 48 ps [189]. (b) The TOF inverse of the velocity distribution $(1/\beta)$ for Z = 2 (He), showing a confusion probability of about 10^{-9} from downward-going and upward-going particles [77].

level-1 trigger (see section 2.10):

- **Low Threshold:** It is used for time measurements and corresponds to $\sim 20\%$ of the Minimum Ionizing Particle (MIP) signal.
- **High Threshold:** It is used for the charged particle trigger ($Z \geq 1$) and corresponds to $\sim 60\%$ of the MIP signal.
- **Super-High Threshold:** It is used for the ions triggers ($Z \geq 2$) and corresponds to $\sim 400\%$ of the MIP signal.

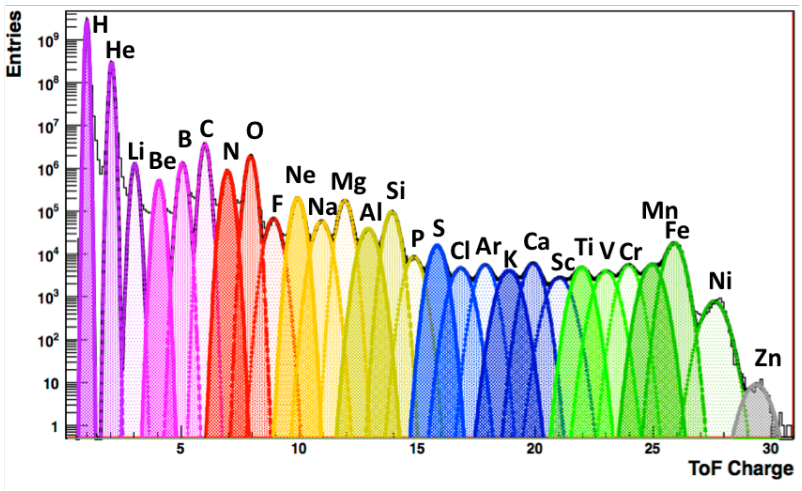

Figure 2.11: The charge distribution in the TOF from Z = 1 (protons) to Z = 30 (zinc) [189].

2.7 Anti-Coincidence Counter (ACC)

The Anti-Coincidence (or veto) Counter (ACC) [190; 191; 192] surrounds the inner tracker inside the magnet bore and is made of 16 scintillator panels of $826 \times 826 \times 8$ mm, arranged in a cylindrical structure of 1.1 m (figure 2.12a). The light of the scintillation panels is absorbed by wavelength shifter fibers of 1 mm diameter and then guided to 16 PMTs (8 at the top and 8 at the bottom) (figure 2.12b). The veto inefficiency has been measured to be less than 10^{-5}.

The principal purpose of the ACC is to detect particles entering the detector from the side or events produced as a result of interactions with the detector material. It is also used to reduce the trigger rate during periods of high flux, such as the SAA. As a consequence, it acts as a fast veto trigger and is used in the trigger logic (see section 2.10).

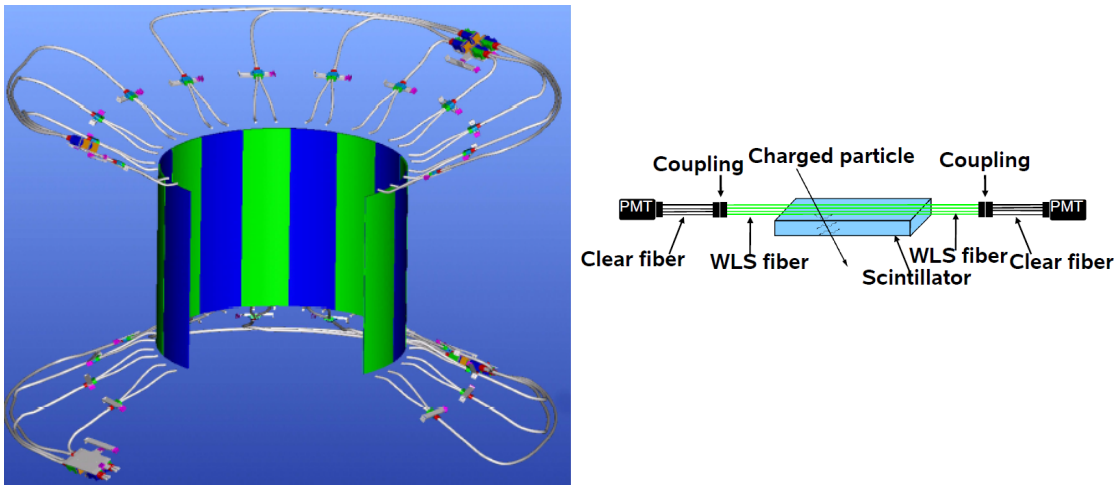

(a) ACC Counters (b) ACC System

Figure 2.12: (a) View of the ACC counters (blue and green colored panels) together with the collection system [190]. (b) Scheme of the ACC system.

2.8 Ring Imaging Cherenkov (RICH)

The Ring Imaging Cherenkov (RICH) [193; 194] is located between the lower TOF and the ECAL. It consists of three main components, a radiator, an expansion volume, and a photo-detection plane. The radiator is composed of two materials, one in the central part made of 16 sodium fluoride (NaF) tiles of $85 \times 85 \times 3$ mm^3 with a refractive index n = 1.33, and the other one surrounding the NaF and made of 92 tiles of silica aerogel each of $113 \times 113 \times 25$ mm^3 and with a refractive index of 1.05. The expansion volume has a length of 470 mm and is surrounded by a conical reflector. Finally, the photo-detection plane is composed of a matrix of 680 sixteen-pixel PMTs placed in 4 rectangular and 4 triangular grids arranged in an octagonal shape. The photo-detection plane has an empty area of 64×64 cm^2 in the center corresponding to the ECAL size and is designed to allow the particles to hit the ECAL with no interferences. Figure 2.13 shows the three parts of the RICH.

The main purpose of the RICH is to determine the velocity and the charge by measuring the Cherenkov radiation of the passing particles. In general, the Cherenkov radiation is emitted when a charged particle traverses a dielectric medium of refractive index n and with a velocity β higher than the phase velocity of light in that medium, known as Cherenkov threshold $\beta_{th} > 1/n$ [195]. The radiation is emitted in a conical shape with an aperture angle θ_c given by

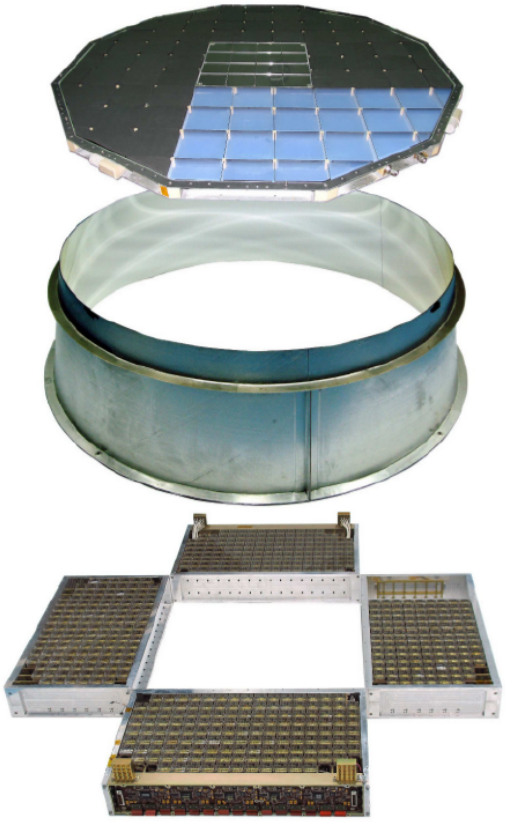

Figure 2.13: Main components of the RICH: radiator (top), expansion volume with conical reflector (center) and photo-detection plane (bottom).

$$cos(\theta_c) = \frac{1}{n\beta} \tag{2.1}$$

In the particular case of the RICH, the cone of Cherenkov radiation is produced in one of the two radiators (NaF and aerogel), where the NaF is able to detect particles with $\beta > 0.75$ and the aerogel with $\beta > 0.953$. The combination of both materials allows to optimize the detection efficiency since the NaF produces radiation with higher θ_c allowing to detect particles falling into the ECAL region. The photons emitted in the radiator are detected by the PMTs in the photo-detection plane and the Cherenkov cone is reconstructed. The efficiency of the process is increased by using the reflector in the expansion volume that reflects photons falling outside of the photo-detection plane (figure 2.14a).

Finally, the velocity of the particle β is determined by measuring the angle of the Cherenkov cone θ_c. The precise knowledge of the refractive indices of the radiators [196] allows to achieve a velocity resolution of $\sigma_\beta \sim 0.8 \times 10^{-3}$ for Z = 2 that improves to $\sigma_\beta \sim 0.5 \times 10^{-3}$ for higher Z [197] (figure 2.14b).

The accurate measurement of the velocity also allows to obtain the mass of the particle with

$$m = R\,Z\frac{\sqrt{1-\beta^2}}{\beta} \tag{2.2}$$

and therefore separate light cosmic ray isotopes.

In addition, the charge of the particle can be measured by counting the amount of photons, N, given by the Frank-Tamm formula $N \propto Z^2 sin^2(\theta_c)$ [198].

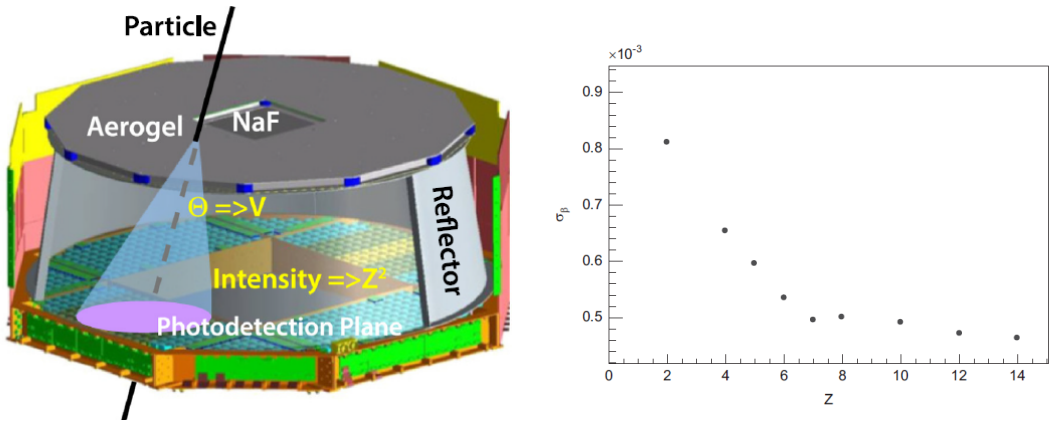

(a) RICH Detection System (b) RICH Velocity Resolution

Figure 2.14: (a) Scheme of the RICH detection system [185].(b) Velocity resolution as a function of the charge Z [197].

2.9 Electromagnetic Calorimeter (ECAL)

The Electromagnetic Calorimeter (ECAL) [199; 200] is located at the bottom of AMS. It has an active area of 648×648 mm^2, a thickness of 166.5 mm, and a total weight of 648 kg including the mechanical structure and the readout cables (figure 2.15a). The calorimeter is composed of 9 modules called *superlayers* of 18.5 mm thickness. Each of them is made of 11 grooved lead foils of 1 mm thick interleaved with 10 layers of scintillating fibers of 1 mm diameter. The fibers run only in one direction, so the 9 superlayers are stacked with fibers alternatively parallel to the X direction (5 superlayers) and the Y direction (4 superlayers), providing a 3D image of the electromagnetic showers (figure 2.15b).

Each superlayer is readout by 36 four-anode PMTs placed alternatively at the two opposite ends in order to avoid dead areas. In total, the ECAL is read out by 324 PMTs that is 1296 anodes. Each anode covers an area of 9×9 mm^2 made of 35 fibers, the so-called *cell*. Figure 2.15c shows one of the superlayers with the footprint of the PMTs and one of the cells superimposed. The 1296 cells are segmented into 18 layers longitudinally (2 per superlayer), with 72 transverse cells in each layer, providing a fine granularity sampling.

The main purpose of the ECAL is to provide an accurate measurement of the energy deposited by electromagnetic particles. Charged particles entering the ECAL develop showers that are better contained for electromagnetic particles (electrons and positrons) due to the high number electromagnetic interaction lengths $\sim 17X_0$. On the contrary, the ECAL design [201; 202] ensures a much smaller number of nuclear interaction lengths, $\sim 0.7\lambda$, such that, although, the electromagnetic showers are well contained up to a few TeV for $e^{\pm}$, the energy leakages for protons are partially contained [203].

The energy of the incoming particle is determined by applying corrections that consider the rear and lateral energy leakages. The corrections ensure the energy linearity to be better than 1% up to 300 GeV. The calorimeter energy resolution $\sigma(E)/E$ was measured during the test beam[204] and is well parametrized by

$$\frac{\sigma(E)}{E} = \sqrt{\frac{(0.104)^2}{E} + (0.014)^2} \tag{2.3}$$

as shown in figure 2.16a.

The ECAL also provides information to separate protons from $e^{\pm}$ very efficiently. In particular, the shape of the shower allows to build an ECAL estimator, $ECAL_{BDT}$, using a multivariate method

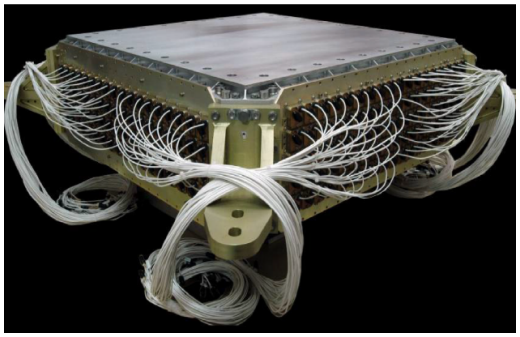

(a) ECAL Structure

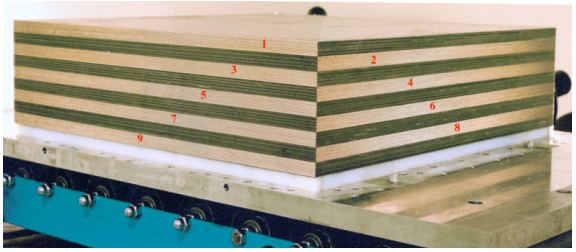

(b) ECAL Distribution of Superlayers

(c) Superlayers Structure

Figure 2.15: (a) The ECAL structure. (b) Distribution of the 9 superlayers, with the fibers stacked in alternating directions. (c) One of the 9 superlayers with the footprint of the PMT and a single cell superimposed.

based on a Boosted Decision Tree (BDT). In addition, the ratio of the energy measured by the ECAL over the momentum determined by the tracker E/p provides discrimination between protons and leptons. This is due to the fact that proton showers are partially contained in the calorimeter, thus the E/p ratio is smaller than 1, whereas for $e^{\pm}$ is almost fully contained and the E/p is close to 1.

The proton rejection using the ECAL estimator and applying a cut in the $E/p > 0.7$ is shown in figure 2.16b. As seen, the proton rejection can be further increased with a tighter cut in the estimator with the corresponding reduction in the selection efficiency.

2.10 Trigger Logic and Data Acquisition System

2.10.1 Trigger Logic

The main purpose of the trigger system of AMS-02 [205; 206] is to record events crossing the detector's fiducial volume and reject the rest of them. The decision has to be fast as to minimize the detector dead-time, which is defined as the time in which the detector is in *busy* state and does not collect events. For this reason, the trigger logic is composed of two stages: the Fast Trigger (FT) and the level-1 trigger.

The FT provides an extremely fast response using the combined information from the TOF and the ECAL. In particular, the FT is activated if one of the following signals is produced:

- **FTC**: The coincidence within 240 ns of signals in any three of the four TOF planes each with a pulse height greater than 0.5 times that deposited by a Z = 1 (MIP). It is used for all cosmic rays.
- **FTE**: Energy deposition in the ECAL consistent with an electromagnetic particle of energy greater than 1 GeV. It is used for electrons, positrons and photons.
- **FTZ**: the coincidence within 640 ns of signals from four TOF planes each with a pulse height greater than 3.5 times a MIP. It is used for slow particles.

Once the FT signal is produced the evaluation of the level-1 trigger starts. In this stage, the

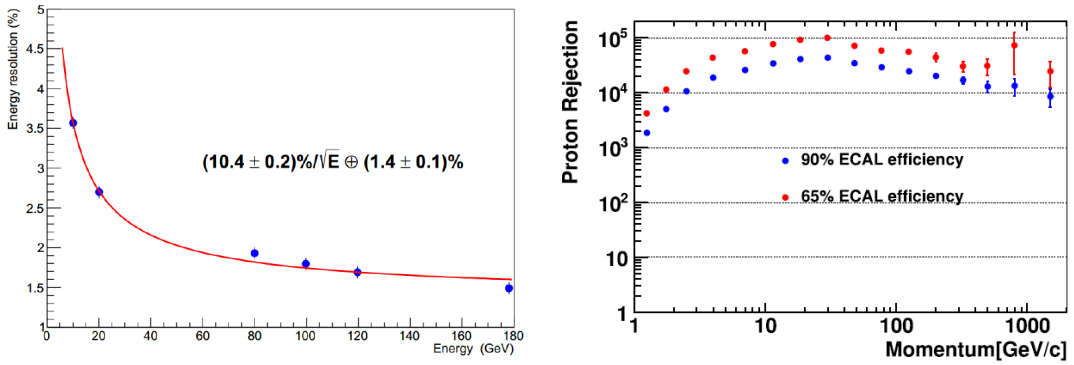

(a) ECAL Energy Resolution (b) ECAL Proton Rejection

Figure 2.16: (a) ECAL energy resolution measured using e^- test beams for perpendicularly incident particles [204]. (b) Comparison of the measured proton rejection for 90% (blue data points) and 65% (red data points) $e^{\pm}$ selection efficiencies. A tighter cut in the ECAL estimator further reduces the proton background by a factor of ~ 3 [77]. This is independent of the rejection power of the TRD shown in 2.8c.

information from the TOF, ECAL, and ACC is used to produced seven sub-triggers:

- **Single Charge (Z = 1):** 4/4 TOF planes passing the HT and no ACC hits.
- **Normal Ions (Z $\geq$ 2):** 4/4 TOF planes passing the SHT and less than 5 ACC hits.
- **Slow Ions:** 4/4 TOF planes passing the SHT in an extended time window.
- **Electrons:** 4/4 TOF planes passing the HT and energy deposited in the ECAL above a threshold in both projections. Once the ECAL trigger is fired the ACC is disabled.
- **Photons:** Energy deposited in the ECAL above a threshold in both projections and a shower angle in the geometric acceptance.
- **Unbiased Charged:** 3/4 TOF planes passing the HT. Due to the large number of signals, the events are prescaled with a factor of 100.
- **Unbiased ECAL:** Energy deposited in the ECAL above a threshold. Events are prescaled by a factor of 1000 in this case.

2.10.2 Data Acquisition System

Each subdetector in AMS-02 is equipped with dedicated Front-End (FE) electronics with a maximum readout time of 90 μs. The Data Acquisition System (DAQ) [207; 208] has been designed to collect and process the signal coming from 300k FE channels. The architecture is based on a tree-like structure with approximately 300 computational nodes, as shown in figure 2.17. Out of the 300 nodes, 264 are dedicated to collect the signal from the FE electronics of each subdetector and perform a first reduction of the data. They are named *xDR* (where *DR* stands for Data Reduction and *x* for the specific subdetector: E for ECAL, R for RICH, T for Tracker, S for TOF and ACC and U for TRD). After that, the signals from the *xDRs* are collected by 14 Low Level DAQ computers (JINF) with double redundancy. In parallel, the trigger signals from the TOF and ACC are collected in 8 SDR nodes and sent to the JLV1 nodes, double redundant, where the Level-1 trigger is produced. Finally, High Level DAQ computers (JINJ), 4 times redundant, collect all the signals from the JINF, the SDR, and the JLV1 and pass the data to the main computer of AMS (JMDC), 4 times redundant as well. The JMDC receives all the information from the event and decides if it is of interest or not [209], this constitutes an additional software trigger level.

The DAQ interconnection is based on a serial wired link protocol (AMSWire), designed with very low latency, low power consumption, and a transfer rate of 100 Mbits/s. In order to minimize

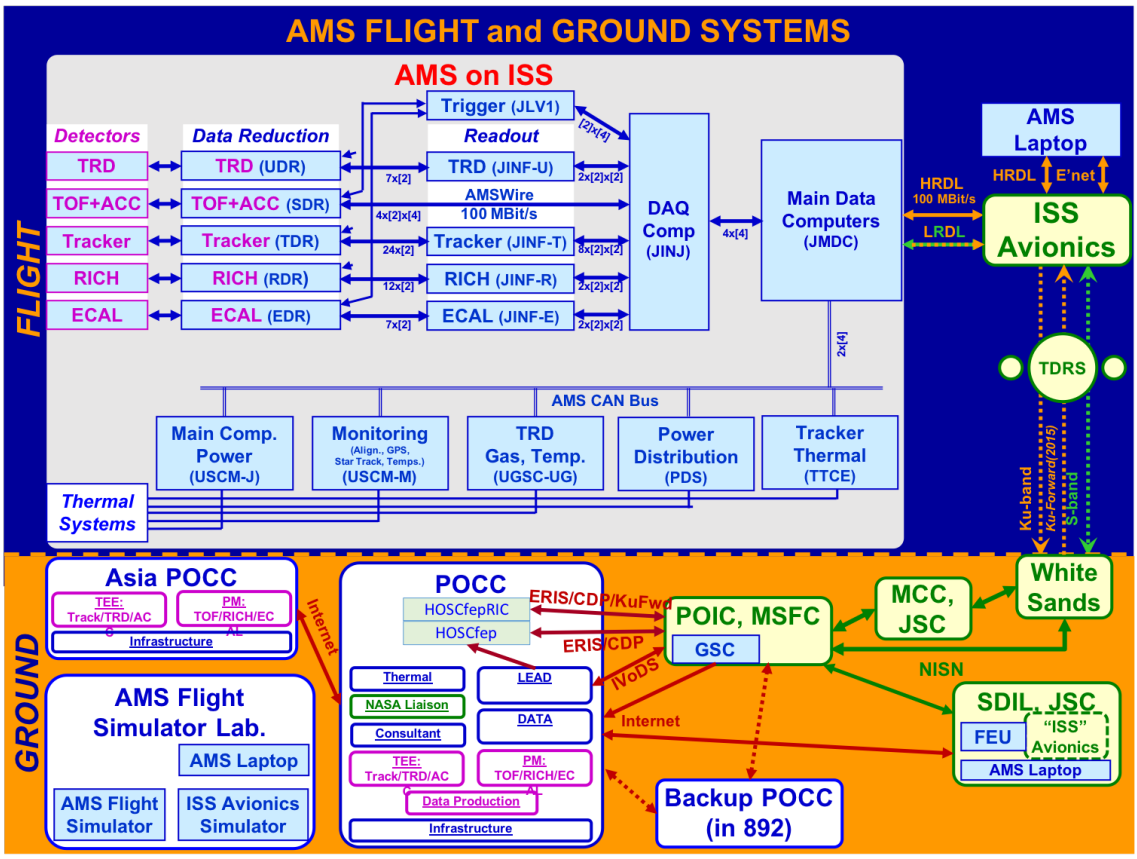

Figure 2.17: Scheme of the DAQ system of AMS-02. The process starts in the Data Reduction Boards for each subdetector, the signals from there are transmitted to the JINF Low Level DAQ computers and collected in the JINJ High Level DAQ computer. The main computer (JMDC), collects all the information from the event and sends it to the ground [185].

the dead-time, all the information related to the event is stored in internal buffers in each of the chains of the DAQ. In particular, the JMDCs have a larger buffer (JBUX) of $\sim$ 1 day, which allows to store data during periods in which the transmission between the ISS and the ground is interrupted.

The DAQ is organized in 23 minutes *runs*, which turns into 4 runs per ISS orbit. Every 2 runs, a full calibration of the subdetectors is performed at the Earth equatorial latitudes.

The transmission from the ISS to the ground is accomplished by means of the NASA Tracking and Data Relay Satellites (TDRS), which transmit the data into the satellite reception dishes at NASA's White Sands Test Facility in New Mexico. The data are sent from there to NASA's Payload Operations Integration Center (POIC) at the Marshall Space Flight Center (MSFC) in Alabama, where the AMS Ground Support Computers are placed. Finally, all the data is sent to the AMS Payload Operations Control Center (POCC) at CERN and the Taiwan control center. The status of the payload and the data-taking is monitored in 8 hours shifts in both centers.

2.10.3 Livetime

The different steps explained before introduce a dead-time period in which the detector does not collect new data. In particular, the process of the level-1 trigger and the reduction and transmission of data takes $\sim$ 220 μs. The status of the DAQ is evaluated in samples of 20 ns, and so the livetime is defined for each second as the ratio of samples where the detector was not in *busy* state with respect to the total number of samples. Therefore, the livetime represents the efficiency of the DAQ

or the fraction of time in which the detector collects data.

As mentioned in section 1.4.2, cosmic ray particles can only penetrate the Earth's magnetic field above the geomagnetic rigidity cutoff and, thus, the lowest energies are only accessible at high geomagnetic latitudes. The spectral shape of the cosmic ray fluxes populates more abundantly the low energy part, which increases the trigger rate at those regions due to the high number of incoming particles crossing the detector, as seen in figure 2.18a. As a consequence of the high trigger rate, the dead time of the detector electronics increases and the livetime is reduced (figure 2.18b).

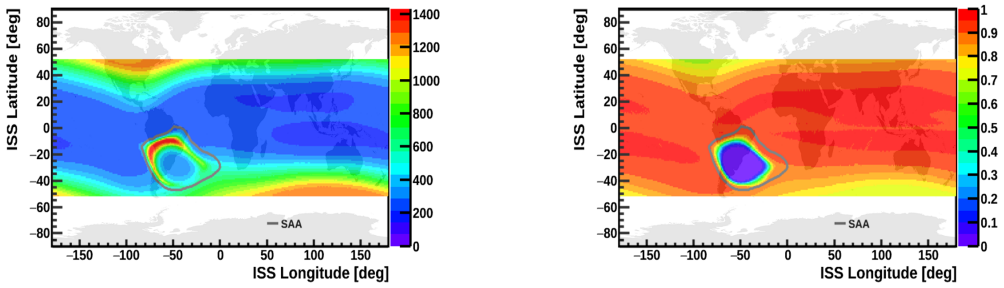

(a) Trigger Rate [Hz] (b) Livetime [s]

Figure 2.18: Mean trigger rate (a) and livetime (b) as a function of the ISS geographical position. Regions close to high geomagnetic latitudes have a higher trigger rate which saturates the DAQ and reduces the livetime.

2.11 Data Taking

The data taking of the AMS-02 detector is affected by different factors that can influence the quality of the data. For this reason, a set of criteria is established in order to ensure that the period of time used for the analysis is optimal and the rest discarded.

Firstly, general conditions regarding the data taking are taken into account. This excludes the initial commissioning, and periods of time within detector operations (calibrations, TRD gas refills) and ISS operations (solar arrays or the robotic-arm within AMS field of view).

Further conditions concerning ISS orbit as well as AMS-02 DAQ parameters are applied on a second by second basis. For this purpose, all the ISS orbit and DAQ parameters are stored in a *Real Time Information* (RTI) database. Only seconds out of the SAA are included as well as those with a livetime greater than 0.5, to avoid seconds when the detector is saturated [1].

Specifically, the measurement of the directionality requires a precise understanding of the detector's behavior and thus additional cuts are applied to further improve the quality of the data. This includes the exclusion of seconds with angles (α) between the AMS pointing direction and the ISS zenith too large $10^{\circ} < \alpha < 14^{\circ}$. This removes periods of time with non-horizontal configurations such as when the station is reoriented from its nominal flight direction (due to docking/undocking of the Soyuz or to Extra-Vehicular Activities (EVAs) of the astronauts). Finally, it is required to have a normal occupancy in the TRD to remove seconds that saturate this subdetector, as shown in figure 2.19.

The time stability of the AMS DAQ system is shown in figure 2.20 for 8.5 years of data taking, which corresponds to the period of time used in this work. The total time in orbit is shown in light gray, whereas the red stands for the DAQ acquiring time, which supposes a $\sim$ 99% of the total

[1] This condition removes short-periods of time at high geomagnetic latitudes with an anomalous solar activity.

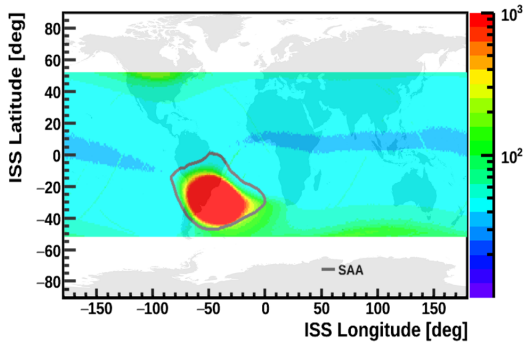

Figure 2.19: TRD occupancy as a function of the ISS geographical position. Regions close to high geomagnetic latitudes and within the SAA have high occupancy in the TRD due to the high rate of incoming particles.

time. Finally, the cyan color presents the fraction of seconds used for the analysis including the conditions explained before and the livetime of the detector, which represents $\sim 83\%$ of the entire time in orbit [2]. The corresponding total exposure time is 1.83×10^8 s.

In general, the AMS DAQ system remains quite stable for the whole period of time with some exceptions. The initial gap observed in figure 2.20 corresponds to the commissioning period, from the 19th of May to the 5th of June 2011. The gap from the beginning of October to the end of November 2014 is due to detector operations to tests the tracker thermal control system. The last intermittent and small gaps from August 2018 to November 2019 are caused by non-nominal configurations of the tracker due to problems with the thermal control system, which was fixed with the installation of the Upgraded Tracker Thermal Pump System (UTTPS) during 4 EVAs from November 2019 to January 2020.

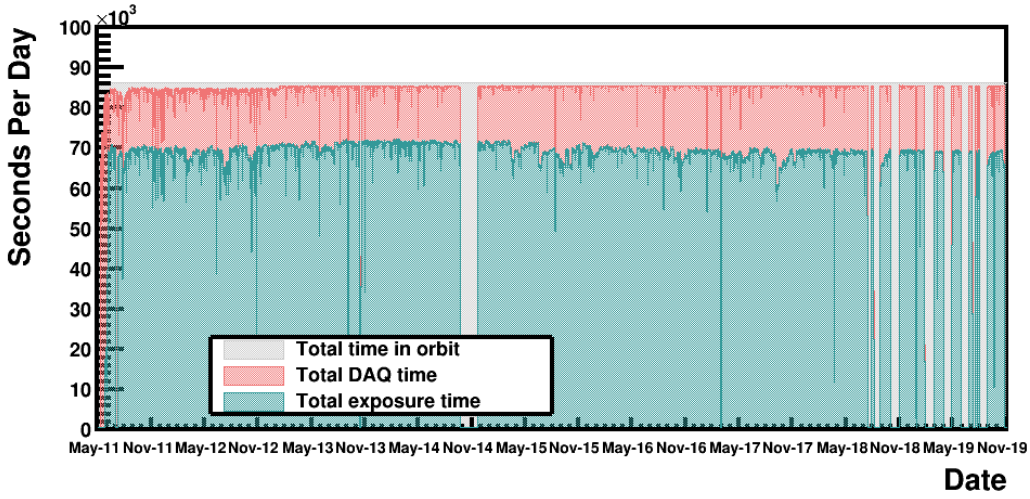

Figure 2.20: Time stability of the data taking in seconds per day. The light gray, red and cyan colors correspond to the time AMS was in orbit, the DAQ was collecting data, and the time used for the analysis (exposure time), respectively.

[2] This reduction also accounts for the time spent in the SAA, which amounts to 7% of the total time in orbit.

2.12 Data Processing and Event Reconstruction

The events collected by the DAQ of AMS-02 containing the raw information coming from the different subdetectors are grouped into periods of time, named as *run*, of ~ 23 minutes (1/4 of an ISS orbit), with an average number of 7×10^5 events. However, the physical analysis cannot be performed directly from the raw data and a reconstruction software has to be used to convert the detector readouts into events with physical information.

For this purpose, a dedicated AMS Offline Sofware was developed to fulfill two main objectives: data reconstruction and simulation of the detector response [210; 211]. The data reconstruction converts the information stored in the raw events into the relevant physical quantities, which will be used for further physics analysis. The simulation provides the evaluation of the detector performance using simulated events and includes for the individual cosmic ray species a precise AMS geometry, and all the relevant physics processes.

The AMS reconstructed data format is based on CERN ROOT package [212] and each reconstructed event is represented by a ROOT tree object that contains high level information needed for the physical analysis.

2.13 AMS-02 Monte Carlo Simulation

The AMS Offline Sofware (see section 2.12) is also used for the simulation of Monte Carlo (MC) events with the same reconstruction procedure used for the data. In particular, the simulation is based on the GEANT4 package [213; 214] and contains a detailed description of the detector (geometry and material composition) and the physical processes that take place inside the detector when a particle goes through (elastic and inelastic interactions). The information of the simulated events is stored in a ROOT tree object in a similar manner as in data.

The simulated particles are generated isotropically from the upper plane of a $3.9 \times 3.9 \times 3.9\ m^3$ cube surrounding the AMS detector (figure 2.21) with a generated momentum p or rigidity R. The spectral shape of the generated events is proportional to the inverse of the momentum (p^{-1}) or to the rigidity (R^{-1}), and so the number of events is N is distributed uniformly as a function of the rigidity according to

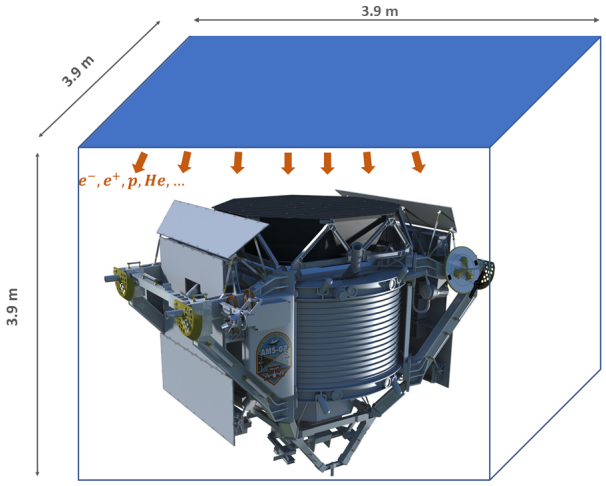

Figure 2.21: Scheme of the MC event generation in the AMS-02 simulation. The events are generated isotropically from the upper plane of a $3.9 \times 3.9 \times 3.9\ m^3$ cube surrounding the detector.

$$\frac{dN}{dR} = k\,R^{-1} \Rightarrow N(R, R+\Delta R) = k \int_R^{R+\Delta R} R^{-1}\,dR = k\,\Delta ln(R) \tag{2.4}$$

where k is a constant value.

The reason to produce events with a harder distribution is to provide enough statistics at high rigidities without overproducing an unmanageable size of low rigidity events. However, the generated spectrum does not follow the natural CR spectrum and it is customarily reweighted in order to reproduce the migrations of the different cosmic ray species.

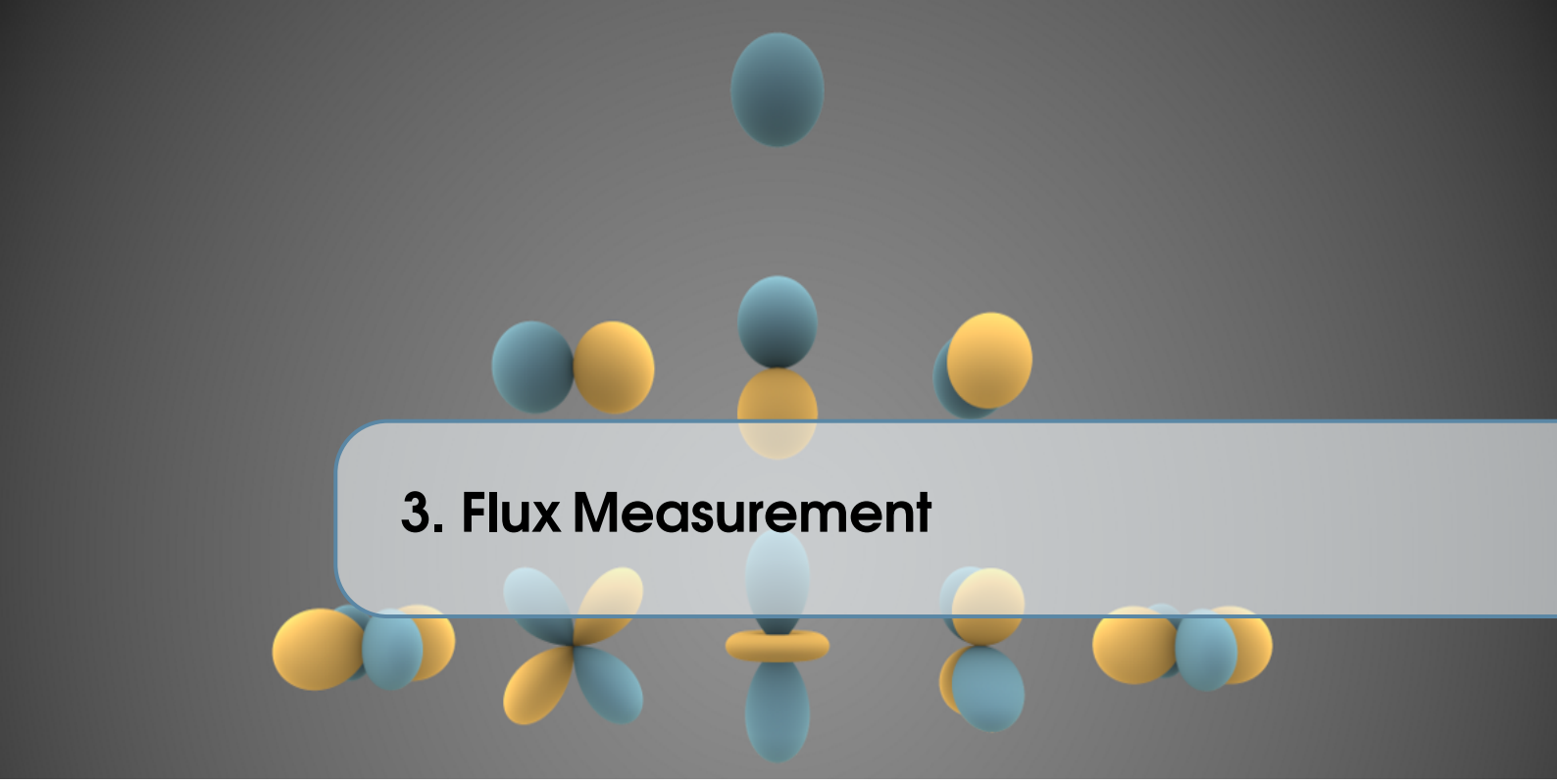

3. Flux Measurement

"The scientist does not study nature because it is useful; he studies it because he delights in it, and he delights in it because it is beautiful."

— Jules Henri Poincaré

This chapter will present the framework needed to measure the flux as a function of the energy and direction of the incoming particles. The first part will explain the general formalism for the calculation of the fluxes whereas the last part will cover the set of tools developed to measure the directionality of the cosmic ray fluxes. This includes the definition of different coordinate systems, the expansion of the flux in spherical harmonics, the construction of the isotropic reference maps and, finally, the statistical tools to establish upper limits.

3.1 Flux Definition

In the most general case, the flux Φ can be defined as the number of particles N traversing a detector per unit of energy E, time t, and solid angle Ω_g and Ω_d (the subindex g stands for the generic coordinate system used in the analysis whereas the d for the local frame of the detector) [215; 216]

$$\Phi(E,t,\hat{r}_g,\hat{r}_d) = \frac{dN(E,t,\hat{r}_g,\hat{r}_d)}{\xi(E,t,\hat{r}_g,\hat{r}_d)\, dE\, dt\, d\Omega_g\, d\Omega_d} \tag{3.1}$$

where $d\Omega_d = \hat{r}_d \cdot d\vec{S}$ stands for the differential area of the detector, with $\hat{r}_d = (\theta_d, \phi_d)$, in a differential solid angle $d\Omega_g$ around the direction of observation $\hat{r}_g = (\theta_g, \phi_g)$ of the incoming particle, and $\xi(E,t,\hat{r}_g,\hat{r}_d)$ represents a factor that includes both the instrumental and the environmental effects. The last term can be factorized as

$$\xi(E,t,\hat{r}_g,\hat{r}_d) = L(t)\, \beta(E,t,\hat{r}_d)\, \varepsilon_{cutoff}(E,t,\hat{r}_g) \tag{3.2}$$

and the different factors correspond to:

- $L(t)$ is the livetime of the detector, defined as the fraction of time in which the instrument is able to collect data (see section 2.10.3).
- $\beta(E,t,\hat{r}_d)$ represents the detector response in local coordinates $\hat{r}_d = (\theta_d, \phi_d)$.
- $\varepsilon_{cutoff}(E,t,\hat{r}_g)$ describes the effects associated to the geomagnetic cutoff (see section 1.4.2).

3.2 Energy Dependences of the Fluxes

The determination of the energy dependences of the flux, assuming that it is isotropic and time-independent $\Phi(E)$, can be carried out directly from equation 3.1. This expression can be simplified considering that the detector response does not depend on time $\beta(E,t,\hat{r}_d) \approx \beta(E,\hat{r}_d)$ and that all the time-dependent effects are grouped in the so-called *exposure time* of the detector

$$T_{exp}(E,\hat{r}_g) = \int dt\, L(t)\, \varepsilon_{cutoff}(E,t,\hat{r}_g) \tag{3.3}$$

which can be reduced into $T_{exp}(E,\hat{r}_g) \approx T_{exp}(E)$ assuming that any dependence on the incoming directions of the particles can be neglected for the exposure time. This is true when the $\varepsilon_{cutoff}(E,t,\hat{r}_g)$ corresponds to the maximum rigidity cutoff within the field of view of the detector (see section 1.4.2).

Then, the number of events from equation 3.1 is expressed as

$$dN(E,t,\hat{r}_g,\hat{r}_d) \approx dN(E,\hat{r}_g,\hat{r}_d) = \Phi(E)\, T_{exp}(E)\, \beta(E,\hat{r}_d)\, d\Omega_g\, d\Omega_d\, dE \tag{3.4}$$

Defining the *effective acceptance* as

$$A_{eff}(E) = \int d\Omega_g \int d\Omega_d\, \beta(E,\hat{r}_d) \tag{3.5}$$

the number of events for an isotropic flux can be written as

$$dN(E) = \Phi(E)\, T_{exp}(E)\, A_{eff}(E)\, dE \tag{3.6}$$

Experimentally, the flux $\Phi(E)$ is determined in energy ranges called bins. Therefore, for the jth energy bin $(E_j, E_j + \Delta E_j)$, the isotropic flux (in units of $GeV^{-1}m^{-2}sr^{-1}s^{-1}$) is given by

$$\Phi_j = \frac{N_j}{(A_{eff})_j\, (T_{exp})_j\, \Delta E_j} \tag{3.7}$$

where the different terms correspond to:

- N_j is the number of particles collected by the detector.
- $(A_{eff})_j$ represents the effective acceptance of the detector.
- $(T_{exp})_j$ is the total time the detector is able to collect data (including the livetime and the geomagnetic cutoff).

3.2.1 Exposure Time

The AMS-02 exposure time depends with the rigidity [1] according to the geomagnetic cutoff (see section 1.4.2) and this section will cover the scheme followed for its computation.

The exposure time defined in equation 3.3 can be simplified assuming that $\varepsilon_{cutoff}(R,t,\hat{r}_g) \approx \varepsilon_{cutoff}(R,t)$, as mentioned in the previous section. Then, the exposure time $T_{exp}(R)$ for each rigidity interval $[R^j_{min}, R^j_{max}]$ is written as

$$T^j_{exp} = \sum_t L(t)\theta(R^j_{min} - R^{max}_c(t)) \tag{3.8}$$

where j stands for the different rigidity intervals, $L(t)$ is the livetime, $R^{max}_c(t)$ the maximum rigidity cutoff within the field of view, and $\theta(R^j_{min} - R^{max}_c(t))$ is the Heaviside step function. For each second

[1] The natural way to evaluate the exposure time is as a function of the rigidity since the geomagnetic cutoff is represented in terms of the rigidity cutoff. In the case of positrons and electrons, the dependence of the exposure time is very similar since $E \sim R$.

the orbital position of the ISS is considered and the corresponding livetime $L(t)$ and maximum rigidity cutoff within the field of view $R_c^{max}(t)$ evaluated. Only the rigidity intervals above $R_c^{max}(t)$ contribute to the exposure time. As a consequence, the rigidity intervals are not equally exposed.

Figure 3.1 shows the rigidity dependence of the exposure time for 8.5 years of data taking with AMS-02. Above $\sim$ 30 GV the value becomes constant due to the fact that all the rigidity ranges are above the maximum rigidity cutoff along the orbit and, therefore, are exposed the same amount of time. The maximum exposure time in orbit corresponds to 1.83×10^8 s. Below 30 GV, the rigidities are not equally exposed and the exposure time decreases.

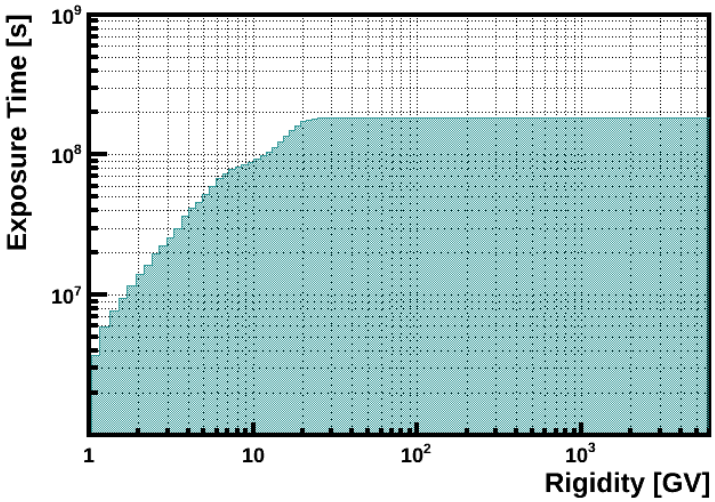

Figure 3.1: AMS-02 exposure time as a function of the rigidity in seconds corresponding to 8.5 years of data taking. Above $\sim$ 30 GV the exposure time reaches the maximum value which amounts to $1.83 \times 10^8 s$, below 30 GV it decreases according to the maximum rigidity cutoff along the orbit for a field of view of 25º.

3.3 Directional Dependences of the Fluxes

The determination of the directionality of the fluxes requires a specific framework to evaluate the possible anisotropies. In this section, the set of tools necessary for its computation will be presented.

3.3.1 Coordinate Systems of Analysis

The measurement of the anisotropy requires to define a coordinate system where the physical signal is intrinsic and so the amplitude of the effect is enhanced. In addition, the definition of a reference system where the signal is totally or partially diluted allows to determine possible spurious effects coming from the detector or other undesired Earth-bound effects. In this context, two types of systems will be used:

- **Non-Physical Systems** are usually bounded to the Earth where no physical signal is expected and both instrumental and environmental effects can be understood. Since most of these effects are associated with the position of the spacecraft along the orbit, for this work, these reference frames will be mainly used to describe geographical or geomagnetic positions.
- **Physical Systems** are used to determine the intrinsic properties and the physical processes of the cosmic rays. In this case, the arrival directions are used to describe a possible anisotropy.

In this section, only the reference systems used for the analysis will be described, more information in other reference systems can be found in [217; 218; 219; 220].

Non-Physical Systems

The geographic coordinate system, also known as Greenwich True of Date (GTOD), is a rotating, right-handed reference frame fixed into the center of the Earth. The orientation is specified by 3 fundamental axes, the positive X-axis pointing towards the prime meridian (Greenwich), the Z-axis is directed along with the Earth's true of date rotational axis and is positive to the north, and the Y-axis completes the right-handed system. The XY plane corresponds to the Earth's True of Date Equatorial plane. The term True of Date refers to the small-time variations (precession and nutation) of the rotational axis (Z-axis) due to the gravitational interaction of the Earth with the Sun and the Moon. In addition, any direction can be represented by two angles: the geographical latitude $\lambda \in [-90^{\circ}, +90^{\circ}]$ and longitude $\phi \in [0^{\circ}, 360^{\circ}]$ (figure 3.2a).

The geomagnetic coordinate system can also be defined by tilting the Z-axis 11° to align it with the dipole axis of the magnetic field (figure 3.2b).

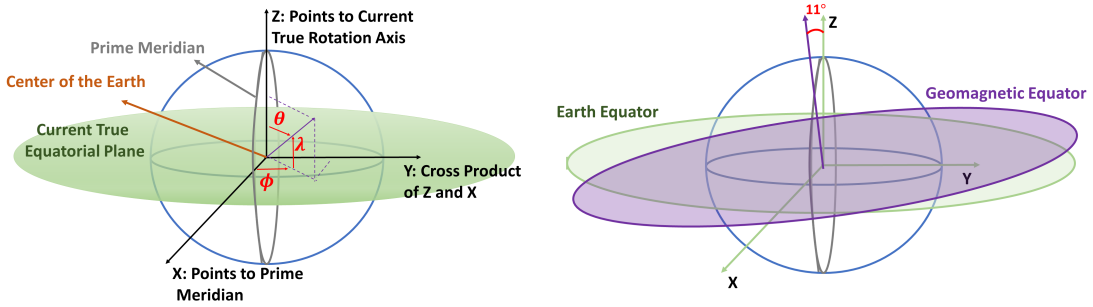

(a) (b)

Figure 3.2: (a) Geographic coordinate system where the X direction points towards the prime meridian, the Z direction towards the Earth's true of date rotational axis, and the Y direction completes the right-handed system. (b) Relation between geomagnetic and geographic coordinates, where the Z direction is tilted 11° and the XY plane is parallel to the geomagnetic equator.

These two reference systems are suitable to characterize the variation of the instrumental effects along the orbit since the physical signals will be diluted due to the Earth's rotation. For this reason, these systems are adequate to interpret the effects that the detector introduces in the measurement of the anisotropies.

Hereinafter, the term *ISS geographical position* and *ISS geomagnetic position* will be used when the position of the spacecraft is projected onto either geographic or geomagnetic coordinates whereas the term *GTOD* will represent the arrival directions of the particles in geographic coordinates.

Physical Systems

The galactic coordinate system is a reference frame that defines a sphere enclosing the Galaxy, with the Sun at its center. The galactic plane is tilted 62.6° with respect to the ecliptic plane (defined as the imaginary plane containing the Earth's orbit around the Sun).

Any direction is represented by 3 fundamental axes, one of them perpendicular to the galactic plane (Z-axis) and the two remaining residing in it: the X-axis pointing to the galactic center (region with the highest density of sources), and the Y-axis completes the right-handed coordinate system (points the Sun's motion around the galactic center) (figure 3.3a). In addition, any direction can be described by the galactic latitude $b \in [-90^{\circ}, +90^{\circ}]$ and longitude $l \in [0^{\circ}, 360^{\circ}]$ (figure 3.3b).

This coordinate system is suitable for astronomical and astrophysical studies and, thus, to measure the directionality of the galactic cosmic rays.

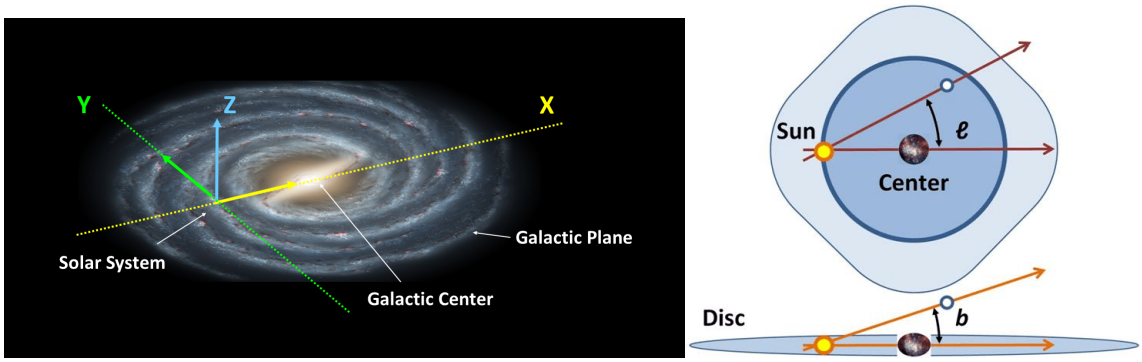

(a) (b)

Figure 3.3: Galactic coordinate system where any direction can be represented by 3 fundamental axes: the Z direction is perpendicular to the galactic plane, the X direction points towards the galactic center and the Y direction completes the right-handed system (a) or by the galactic longitude and latitude (l,b) (b).

3.3.2 Multipolar Expansion of the Cosmic Rays Fluxes

The measurement of the directionality of the fluxes requires a clear definition in order to account for the directional fluctuations. Thus, the differential flux of cosmic rays given in equation 3.1, assuming in this case that we are just interested in the directional dependences, can be expressed as follows

$$\Phi(E,t,\hat{r}_g,\hat{r}_d) \approx \Phi(\theta_g,\phi_g) = \Phi_0 + \Delta\Phi(\theta_g,\phi_g) = \Phi_0(1+\Delta(\phi_g,\theta_g)) \tag{3.9}$$

where Φ_0 stands for the isotropic flux and $\Delta(\theta_g,\phi_g) = \Delta\Phi(\theta_g,\phi_g)/\Phi_0$ for the directional fluctuations, assumed to be small ($\Delta \ll 1$).

As the spherical harmonics are defined to be a complete set of orthonormal functions in a spherical surface, they can be used to describe spherical distributions. They are defined in its complex form in colatitude $\theta \in [0,\pi]$ and longitude $\phi \in [0,2\pi]$ [221; 222] and constitute a basis of the Hilbert space. For any physical measurement it is more convenient to use the real form, which is defined in terms of the complex spherical harmonics [223]. Therefore, any function $f(\theta,\phi)$ on a unit sphere can be expanded as a linear combination of real spherical harmonics as

$$f(\theta,\phi) = \sum_{\ell=0}\sum_{m=-\ell}^{m=+\ell} c_{\ell m}Y_{\ell m}(\theta,\phi) = c_{00}Y_{00} + \sum_{\ell=1}\sum_{m=-\ell}^{m=+\ell} c_{\ell m}Y_{\ell m}(\theta,\phi) =$$

$$= c_{00}Y_{00}\left(1+\sum_{\ell=1}\sum_{m=-\ell}^{m=+\ell}\frac{c_{\ell m}}{c_{00}Y_{00}}Y_{\ell m}(\theta,\phi)\right) \quad .$$

Then, the flux can be written in terms of these functions

$$\Phi(\theta_g,\phi_g) = \Phi_0\left(1+\sum_{\ell=1}\sum_{m=-\ell}^{m=+\ell} a_{\ell m}Y_{\ell m}(\theta_g,\phi_g)\right) \tag{3.10}$$

where $\Phi_0 = c_{00}Y_{00}$ corresponds to the isotropic component and $a_{\ell m} = \frac{c_{\ell m}}{\Phi_0}$ are the coefficients of the expansion, which determine the degree of the anisotropy.

In the case of the dipole components ($\ell = 1$), the flux can be written as

$$\Phi(\theta_g,\phi_g) = \Phi_0(1 + a_{1-1}Y_{1-1} + a_{10}Y_{10} + a_{11}Y_{11}) \tag{3.11}$$

where the three real spherical harmonics (figure 3.4) are

$$\begin{aligned} Y_{1-1} &= \sqrt{\frac{3}{4\pi}} sin(\theta) sin(\phi) \\ Y_{10} &= \sqrt{\frac{3}{4\pi}} cos(\theta) \\ Y_{11} &= \sqrt{\frac{3}{4\pi}} sin(\theta) cos(\phi) \end{aligned} \tag{3.12}$$

which can be defined by three orthogonal axes in spherical coordinates

$$x = rsin(\theta)cos(\phi) \qquad y = rsin(\theta)sin(\phi) \qquad z = rcos(\theta) \quad . \tag{3.13}$$

Thus, the flux can be expressed as

$$\Phi(\theta_g, \phi_g) \approx \Phi_0 \left(1 + a_{1-1}\sqrt{\frac{3}{4\pi}}\frac{y}{r} + a_{10}\sqrt{\frac{3}{4\pi}}\frac{z}{r} + a_{11}\sqrt{\frac{3}{4\pi}}\frac{x}{r}\right) \tag{3.14}$$

and the dipole components can be defined as the projection of the dipole amplitude onto each axis. The three directions will be denoted as East-West (EW), North-South (NS) and Forward-Backward (FB) so that

$$\begin{aligned} \rho_{EW} &= \sqrt{\frac{3}{4\pi}} a_{1-1} \\ \rho_{NS} &= \sqrt{\frac{3}{4\pi}} a_{10} \\ \rho_{FB} &= \sqrt{\frac{3}{4\pi}} a_{11} \quad . \end{aligned} \tag{3.15}$$

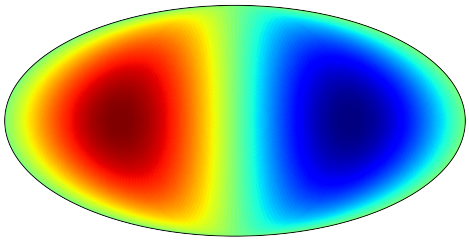

(a) Y_{1-1}

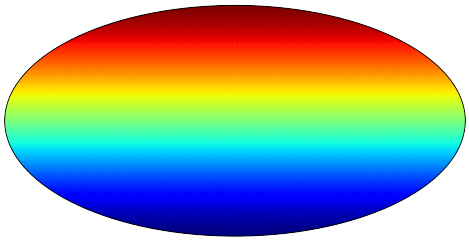

(b) Y_{10}

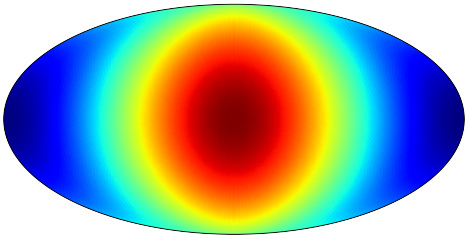

(c) Y_{11}

Figure 3.4: Representation of the real spherical harmonics for $\ell = 1$: (a) Y_{1-1}, (b) Y_{10} and (c) Y_{11}.

Finally, this allows to define the dipole amplitude as the modulus of the dipole vector

$$\delta = \left(\frac{\Delta\Phi(\theta_g,\phi_g)}{\Phi_0}\right) = \sqrt{\rho_{EW}^2+\rho_{NS}^2+\rho_{FB}^2} \tag{3.16}$$

which quantifies the magnitude of the dipole anisotropy.

The determination of the dipole components is sufficient to describe large scale anisotropies, however, for this work the quadrupole components will be also used since they are more sensitive to possible systematic effects. They are defined as

$$\rho_{2m} = \sqrt{\frac{3}{4\pi}}a_{2m} \tag{3.17}$$

Experimentally, the determination of the multipole components is performed with a finite sample of events, N, where the estimated coefficients of the expansion $a_{\ell m}$ are assumed to be Gaussian distributed random variables and, in particular, in the limit $a_{\ell m} \to 0$ the standard deviation is [224]

$$\sigma(a_{\ell m}) = \sqrt{\frac{4\pi}{N}} \tag{3.18}$$

In addition, the coefficients of the expansion can be determined for each reference system and transformed between them by means of effective coordinate transformations. In our case, this allows to understand which components in the non-physical system transform to the physical one and, thus, to interpret the impact of the instrumental effects into the measurement of the dipole anisotropy. The transformation of the multipole components of a signal can be quantified by means of a Toy Monte Carlo simulation of an ideal AMS-like detector. More details on how the multipole components of the reference systems used in this analysis are transformed can be found in appendix A.

3.3.3 Reference Map for Anisotropies

The determination of the directionality of the fluxes mainly relies on the construction of an isotropic skymap (reference map) which is compared with the skymap of measured events. The observation of any deviation of this map from the reference will be interpreted as a signal. Depending on the reference map used two types of anisotropies are defined:

- **Absolute anisotropies:** the reference map describes the directional response of the detector to an isotropic flux. This requires a precise understanding of the detector, especially at different geographical positions, where the detector's behavior may change due to the variation of the particles rate along the orbit.
- **Relative Anisotropies:** the reference map is constructed with a data sample which is assumed to be isotropic for the analysis.

The construction of both reference maps is described below.

Absolute Anisotropies

The general expression for the construction of the reference maps can be derived from equation 3.1 assuming that the flux only depends on the energy and direction of observation $\Phi(E,\hat{r}_g)$. Then, the differential number of events is expressed as

$$\frac{dN(E,\hat{r}_g)}{dE\,d\Omega_g} = \Phi(E,\hat{r}_g)\int dt \int d\Omega_d\,\beta(E,t,\hat{r}_d)\,L(t)\,\varepsilon_{cutoff}(E,t,\hat{r}_g) \tag{3.19}$$

which can be grouped in the following terms

$$\frac{dN(E,\hat{r}_g)}{dE\, d\Omega_g} = \Phi(E,\hat{r}_g)\, F(E,\hat{r}_g) \tag{3.20}$$

where

$$\begin{aligned} F(E,\hat{r}_g) &= \int dt \int d\Omega_d\, \beta(E,t,\hat{r}_d)\, L(t)\, \varepsilon_{cutoff}(E,t) \\ &= \int dt \int d\Omega_d\ A(E,\hat{r}_d)\, \varepsilon(t)\, L(t)\, \varepsilon_{cutoff}(E,t) \end{aligned} \tag{3.21}$$

and in this case, the response of the detector $\beta(E,t,\hat{r}_d) = A(E,\hat{r}_d)\varepsilon(t)$ has been factorized into the differential acceptance $A(E,\hat{r}_d)$ and the time variation of the detection efficiencies $\varepsilon(t)$ [2].

The number of events collected by a detector can be discretized in small intervals of time Δt^i, energy ΔE^j and directions in both coordinate system of analysis and local frame of the detector $\Delta\Omega_g^s, \Delta\Omega_d^r$. In this sense, the number of events per pixel [3] of the sky s and energy interval j is expressed as

$$n_{j,s} \equiv \left(\frac{\Delta N}{\Delta E \Delta\Omega_g}\right)_{j,s} = \Phi_{j,s} \sum_i \sum_r A_j^r\, \varepsilon^i\, L^i\, (\varepsilon_{cutoff})_j^i \tag{3.22}$$

In the particular case of the AMS-02 detector, the time variation of the efficiencies $\varepsilon(t)$ intrinsically depends on environmental effects along the orbit. Indeed, due to the geomagnetic cutoff (see section 1.4.2) the rate of cosmic rays will be higher in certain positions of the ISS ($\hat{r}_{ISS}$). Also, $\varepsilon_{cutoff}(E,t)$, depends on the energy of the particle and so these effects will have an impact that has to be included. In addition, the fact that $\varepsilon(t)$ intrinsically depends in $\hat{r}_{ISS}$ makes it depend on the reference system of analysis $\hat{r}_g$ by means of a coordinate transformation. All these dependences can be included as $\varepsilon(t) = \varepsilon(t(\hat{r}_{ISS},E)) = \varepsilon(t(\hat{r}_g,E))$, which can be also expressed using the previous notation as

$$n_{j,s} \equiv \left(\frac{\Delta N}{\Delta E \Delta\Omega_g}\right)_{j,s} = \Phi_{j,s} \sum_i \sum_r A_j^r\, \varepsilon_{(j,s)}^i\, L^i (\varepsilon_{cutoff})_j^i = \Phi_{j,s}\, F_{j,s} \tag{3.23}$$

where $\Phi_{j,s}$ and $F_{j,s}$ are the incoming flux and the *exposure map* for each pixel of the sky s and energy interval j. In this sense, all the detector effects are included into the exposure map which represents the skymap observed by the instrument and serves as the null hypothesis (isotropic skymap) for the directional studies.

Different approaches have been used in the literature to construct $F_{j,s}$, some of them have exploited the MC simulations to understand the response of the detector whereas others have used other techniques based on data samples [225; 226; 227]. In the case of AMS-02 none of them applies, since the precision required for the anisotropy searches would be limited by the computation of the MC acceptances and the techniques based on data samples were created for ground-based detectors and cannot be applied to AMS due to its limited field of view. In this sense, for AMS-02 a different method has to be applied and, in particular, the method developed in [228] will be used in this work.

The field of view of AMS-02 is divided into small pixels r in the local reference frame such that the number of events from equation 3.23 is expressed as

$$n_{j,s}^r \equiv \left(\frac{\Delta N}{\Delta E \Delta\Omega_g}\right)_{j,s}^r = \Phi_{j,s} \sum_i A_j^r\, L^i\, (\varepsilon_{cutoff})_j^i\, \varepsilon_{(j,s)}^i = \Phi_{j,s}\, F_{j,s}^r \tag{3.24}$$

[2] It has been assumed that $\varepsilon_{cutoff}(E,t,\hat{r}_g) \approx \varepsilon_{cutoff}(E,t)$, more details can be found in section 1.4.2.

[3] The HEALPix scheme is used to divide the incoming directions in small intervals s of $\hat{r}_g = (\theta_g, \phi_g)$ called pixels.

This means each pixel r has an associated exposure map which is defined as

$$F^r_{j,s} = A^r_j \, T^r_{j,s} \, \varepsilon_{j,s} \tag{3.25}$$

where each factor represents the following:

- The A^r_j represents the acceptance for the pixel r.
- The $T^r_{j,s}$ constitute the exposure time maps and describes the amount of time that a certain direction in the skymap s is observed by a given pixel r in which the acceptance is divided. Their computation is explained below.
- The $\varepsilon_{j,s}$ describe the efficiency correction maps, which represents the integrated projection of the geographical dependence of the efficiencies to the coordinate system of analysis. Their computation is explained below.

Construction of the exposure time maps

The exposure time maps, $T^r_{j,s}$, represent the amount of time that a certain direction in the skymap (θ^s_g, ϕ^s_g) is observed by a given pixel (θ^r_d, ϕ^r_d) in which the acceptance is divided, as defined in equation 3.25.

In general, the maps are constructed as follows:

1. For each acceptance pixel r and rigidity interval j individual maps with latitude-longitude ((θ_g, ϕ_g) in the coordinate system of analysis) are created.
2. For each second of the analysis: a coordinate transformation from local coordinates (θ^r_d, ϕ^r_d) of each acceptance pixel r to the generic coordinate system of the analysis (θ^s_g, ϕ^s_g) is made; the orbital position of the ISS is considered and the corresponding livetime $L(t)$ and maximum rigidity cutoff $R^{maxc}_c(t)$ within the field of view evaluated; and the directions in the map (θ^s_g, ϕ^s_g) with rigidities above $R^{max}_c(t)$ are filled with $L(t)$.
3. The same strategy is followed for each acceptance pixel r.

For this work, the acceptance is divided into pixels of equal area by using the HEALPix scheme [229]. The size of the pixels is represented with a size parameter that, for our case, is chosen to be $N_{side} = 32$ and corresponds to 12288 pixels of $\sim 3\ deg^2$. Depending on the angular aperture of the analysis, the number of pixels covering the field of view will be different. In the case of Full Span tracker pattern the opening angle about the AMS Z axis is 25º which corresponds to 544 pixels out of a total of 12288. For L1+Inner the angle is 35º, and the number of pixels 1114 [4].

As an illustration of the process, figure 3.5 shows the exposure time map above the maximum rigidity cutoff for a selected pixel of the acceptance in galactic coordinates, $r = 0$ (corresponds to vertical position). The map follows the astronomical convention, where the East (longitude +90º) is displayed on the left and the West (longitude -90º) on the right. The almost full sky coverage of the exposure time map is observed in figure 3.5.

The information of the event and exposure time maps for each pixel r is included in a binned-likelihood fit allowing to obtain the multipole coefficients $a_{\ell m}$ [5] (see section 3.3.4). Therefore, this method provides independent measurements of the anisotropy for each pixel of the acceptance r. Furthermore, the information from all pixels r can be introduced in the binned-likehood establishing a unique measurement of the anisotropy. Following this procedure the determination of the absolute acceptance is not necessary since it only acts as a normalization factor in the binned-likelihood fit.

Likewise, figures 3.6 and 3.7 show the exposure time maps above the maximum rigidity cutoff for the Full Span and the L1+Inner tracker patterns. Maps in geographical coordinates in both ISS positions (left) and arrival directions of the particles (right) are displayed in the upper part. For ISS geographical positions a larger exposure time is observed at high latitudes due to the ISS orbit [6]. The map in geographical coordinates for the arrival directions shows the same features taking

[4] For display purposes the Mollweide projection is used.

[5] Event maps are built following the same strategy as the exposure time maps.

[6] The low exposure line in the equator corresponds to the calibration of the subdetectors every 2 runs.

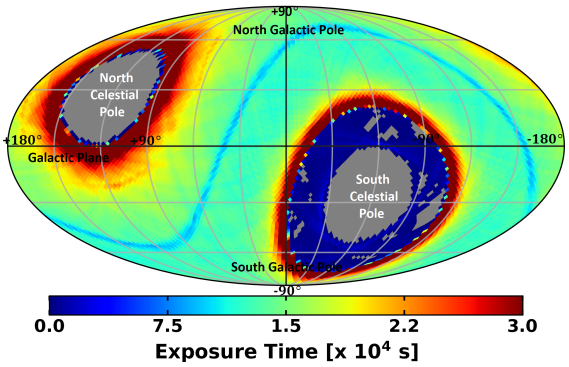

Figure 3.5: Exposure time map above the maximum rigidity cutoff for a selected pixel of the acceptance $r = 0$ (corresponds to vertical positions) in galactic coordinates.

into account the AMS field of view and the tilt of 12º of the detector with respect to the ISS zenith. In particular, regions in the Northern and Southern Hemispheres that were not covered by the ISS position are now exposed. The Hemispheres are not equally exposed due to the tilt of 12º of the detector, which creates a North-South asymmetry. It is also observed that both Hemispheres are more exposed in the L1+Inner map 3.7b with respect to the Full Span map, figure 3.6b. This is due to the fact that the L1+Inner tracker pattern has a wider opening angle and is able to reach higher latitudes than the Full Span tracker pattern. The features observed in the exposure time map in galactic coordinates can be understood from the figures 3.6b and 3.7b. In particular, the North Celestial Pole is more exposed than the South one due to the ISS orbit and orientation of AMS-02 detector. In this case, both Celestial Poles are more exposed in L1+Inner due to the wider opening angle.

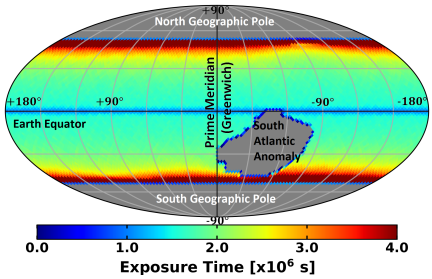

(a) ISS Geographic Positions

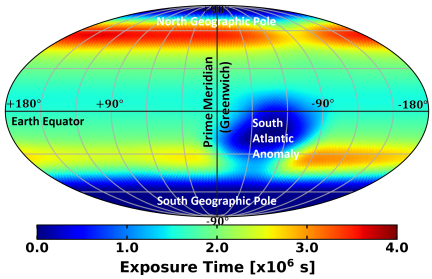

(b) Geographic Arrival Directions

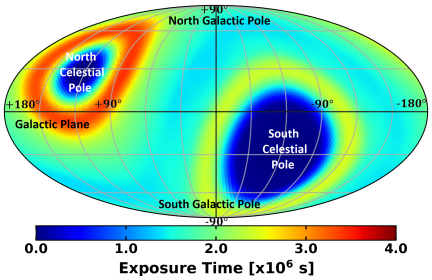

(c) Galactic Coordinates

Figure 3.6: Exposure time maps above the maximum rigidity cutoff for the Full Span tracker pattern in: (a) ISS geographical position coordinate system, (b) arrival directions geographic coordinate system and (c) galactic coordinate system.

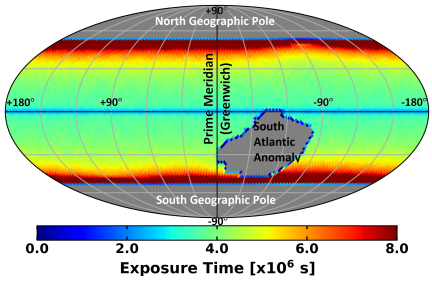

(a) ISS Geographic Positions

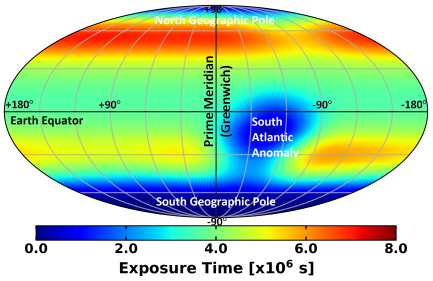

(b) Geographic Arrival Directions

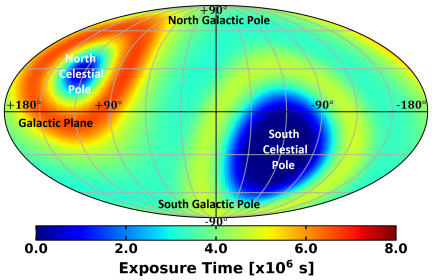

(c) Galactic Coordinates

Figure 3.7: Exposure time maps above the maximum rigidity cutoff for the L1+Inner tracker pattern in: (a) ISS geographical position coordinate system, (b) arrival directions geographic coordinate system and (c) galactic coordinate system.

Construction of the efficiency correction maps

The skymap efficiency distribution, $\varepsilon(\theta,\phi)$, for each efficiency involved in the analysis can be obtained as

$$\varepsilon(\theta,\phi) = \frac{N_{ok}(\theta,\phi)}{N_{ok}(\theta,\phi)+N_{ko}(\theta,\phi)} = \frac{1}{1+\eta(\theta,\phi)} \tag{3.26}$$

where the $N_{ok}(\theta,\phi)$ and $N_{ko}(\theta,\phi)$ are the skymap distribution of accepted and rejected events, and $\eta(\theta,\phi) = N_{ko}(\theta,\phi)/N_{ok}(\theta,\phi)$.

The last expression motivates the expansion of the $\eta(\theta,\phi)$ in terms of spherical harmonics in the coordinate system of analysis as

$$\eta(\theta,\phi) \sim \eta_0 \left(1 + \sum_{\ell=1} \sum_{m=-\ell}^{m=+\ell} \eta_{\ell m}\, Y_{\ell m}(\theta,\phi)\right) \tag{3.27}$$

since now the coefficients of the expansion $\eta_{\ell m}$ can be computed from the relative analysis of anisotropies (described in sections 3.3.3 and 3.3.4) of the N_{ko} and N_{ok} samples for each energy range. The $\eta_0 \sim N_{ko}/N_{ok}$ factor accounts for the average ratio of the samples in a certain energy range $\Delta E = [E_{min}, E_{max}]$.

Then, the exposure time map can be corrected using equation 3.26 to create the isotropic reference. The inclusion of the efficiency correction maps, due to the orthonormality of the spherical harmonics, modifies the $a_{\ell m}$ such that

$$a_{\ell m}^{corr} \sim a_{\ell m} + \Delta_{\ell m} \tag{3.28}$$

with $\Delta_{\ell m} = \frac{\eta_0}{1+\eta_0}\eta_{\ell m}$ the correction applied to each coefficient.

The same procedure is applied for each efficiency of the analysis and the total correction can be estimated, under the assumption of uncorrelated efficiencies, as the sum of the individual ones

$$\Delta_{\ell m} = \sum_{i}^{N_{effs}} \Delta^{i}_{\ell m} \tag{3.29}$$

Relative Anisotropies

In the analysis of relative anisotropies, the flux ratio is expanded in spherical harmonics as

$$\frac{\Phi(\theta,\phi)}{\Phi_{ref}(\theta,\phi)} = \Phi_0 \left(1 + \sum_{\ell=1} \sum_{m=-\ell}^{m=+\ell} a_{\ell m}\, Y_{\ell m}(\theta,\phi)\right) \tag{3.30}$$

where now $\Phi_0 = (\Phi/\Phi_{ref})_0$ stands for the isotropic flux ratio and the coefficients of the expansion, $a_{\ell m}$, represent the directional fluctuations, thus, the degree of the relative anisotropy.

According to equations 3.24 and 3.25, the ratio of events for each pixel of acceptance r, pixel of the sky s and energy interval j can be written as

$$\left(\frac{n}{n_{ref}}\right)^{r}_{j,s} \propto \left(\frac{\Phi}{\Phi_{ref}}\right)_{j,s} \left(\frac{T}{T_{ref}}\right)^{r}_{j,s} \left(\frac{\varepsilon}{\varepsilon_{ref}}\right)_{j,s} \tag{3.31}$$

which allows to express the distribution of the numerator events as

$$n^{r}_{j,s} \propto \left(\frac{\Phi}{\Phi_{ref}}\right)_{j,s} \mathcal{R}^{r}_{j,s} \tag{3.32}$$

where

$$\mathcal{R}^{r}_{j,s} = \left(\frac{T}{T_{ref}}\right)^{r}_{j,s} \left(\frac{\varepsilon}{\varepsilon_{ref}}\right)_{j,s} (n_{ref})^{r}_{j,s} \tag{3.33}$$

is the reference map for the relative anisotropy.

The reference map can be simplified if the numerator and denominator have the same exposure time and efficiency maps. In this case, the reference is simply

$$\mathcal{R}^{r}_{j,s} = (n_{ref})^{r}_{j,s} \tag{3.34}$$

In addition, if the acceptance is the same for the numerator and denominator, the reference map can be combined for each acceptance pixel r

$$\mathcal{R}_{j,s} = \sum_{r} \mathcal{R}^{r}_{j,s} \tag{3.35}$$

and, thus, the reference map is the distribution of events in the sky for each energy interval j.

3.3.4 Likelihood Fit

The determination of the multipole components defining the large scale anisotropy can be estimated with the use of a maximum likelihood fit. This section will present the prescriptions used for the absolute and relative anisotropies.

Absolute Anisotropies

The number of events in the skymap follows a multinomial probability distribution

$$f_j^r \equiv f_j^r(n_1,...,n_{N_s};N_j^r,\mu_1,...,\mu_{N_s}) = \frac{N_j^r!}{\prod_{s=1}^{N_s} n_{j,s}^r!}\prod_{s=1}^{N_s}(\mu_{j,s}^r)^{n_{j,s}^r} \tag{3.36}$$

where $n_{j,s}^r$ correspond to the number of events per acceptance pixel r, energy interval j and sky pixel s, $N_j^r = \sum_s^{N_s} n_{j,s}^r$ stands for the sum over all sky pixels, N_s, of the number of events, and $\mu_{j,s}^r$ is the expected number of events, which can be expressed as

$$\begin{aligned}\mu_{j,s}^r &= \frac{1}{\mathcal{N}_j^r}\Phi_{j,s}\,A_j^r\,T_{j,s}^r\,\varepsilon_{j,s} = \frac{1}{\mathcal{N}_j^r}\Phi_{0,j}\left(1+\sum_{\ell=1}\sum_{m=-\ell}^{m=+\ell} a_{\ell m}Y_{\ell m}^s\right)A_j^r\,T_{j,s}^r\,\varepsilon_{j,s} \propto \\ &\propto \frac{1}{\mathcal{N}_j^r}\left(1+\sum_{\ell=1}\sum_{m=-\ell}^{m=+\ell} a_{\ell m}Y_{\ell m}^s\right)T_{j,s}^r\,\varepsilon_{j,s}\end{aligned} \tag{3.37}$$

where the flux $\Phi_{j,s}$ has been expanded in terms of spherical hamonics using the equation 3.10, $\mathcal{N}_j^r$ is a normalization factor introduced to ensure that the discrete probability function is normalized to the total number of events $\sum_s^{N_s}\mu_{j,s}^r = N_j^r$ and $\Phi_{0,j}\,A_j^r$ are constant factors.

The probability function taking into account all the acceptance pixels r and energy intervals j is $f = \prod_{r,j} f_j^r$, which motivates the use of a binned-likelihood statistical method. The likelihood can be expressed as $\mathcal{L} = \prod_{r,j}\mathcal{L}_j^r$ and the corresponding log-likehood is

$$\begin{aligned}log\mathcal{L} &= \sum_{r,j} log\mathcal{L}_j^r = \sum_{r,j}\sum_s n_{j,s}^r\,log\,\mu_{j,s}^r = \\ &= \sum_{r,j,s} n_{j,s}^r\,log\left[\frac{(1+\sum_{\ell=1}\sum_{m=-\ell}^{m=+\ell}a_{\ell m}Y_{\ell m}^s)T_{j,s}^r\,\varepsilon_{j,s}}{\mathcal{N}_j^r}\right]\end{aligned} \tag{3.38}$$

where

$$\mathcal{N}_j^r = \sum_s\left(1+\sum_{m=-\ell}^{m=+\ell}a_{\ell m}Y_{\ell m}^s\right)T_{j,s}^r\,\varepsilon_{j,s} \tag{3.39}$$

and the coefficients of the expansion $a_{\ell m}$ are obtained by maximizing the log-likelihood function.

In addition, the presence of an isotropic background can be statistically accounted in the probability distribution function in terms of the purity of the sample $p = N_{sig}/(N_{sig}+N_{bkg})$ as a multiplicative factor

$$\mu_{j,s}^r = \frac{1}{\mathcal{N}_j^r}\left(1+p_{j,s}^r\sum_{\ell=1}\sum_{m=-\ell}^{m=+\ell}a_{\ell m}Y_{\ell m}^s\right)T_{j,s}^r\,\varepsilon_{j,s} \tag{3.40}$$

In this case, the log-likelihood function is expressed as

$$log\mathcal{L} = \sum_{r,j,s} n_{j,s}^r\,log\left[\frac{(1+p_{j,s}^r\,\sum_{\ell=1}\sum_{m=-\ell}^{m=+\ell}a_{\ell m}Y_{\ell m}^s)T_{j,s}^r\,\varepsilon_{j,s}}{\mathcal{N}_j^r}\right] \tag{3.41}$$

with

$$\mathcal{N}_j^r = \sum_s \left(1 + p_{j,s}^r \sum_{\ell=1} \sum_{m=-\ell}^{m=+\ell} a_{\ell m} Y_{\ell m}^s\right) T_{j,s}^r \, \varepsilon_{j,s}^r \tag{3.42}$$

As observed in equation 3.41, the overall effect of the presence of the background will bias the $a_{\ell m}$ estimator and reduce its sensitivity. It can be quantified with the following expressions

$$a_{\ell m} \approx \frac{\bar{a}_{\ell m}}{\langle p \rangle} \qquad \sigma(a_{\ell m}) \approx \frac{\sigma(\bar{a}_{\ell m})}{\sqrt{\langle p^2 \rangle}} \tag{3.43}$$

where the $a_{\ell m}$ are the multipole components including the purity, $\bar{a}_{\ell m}$ the results under the assumption of no background in the sample, and $\langle p \rangle, \langle p^2 \rangle$ the first and second moments of the purity distributions. They are written as

$$\langle p \rangle = \frac{\sum_{r,j,s} n_{j,s}^r \, p_{j,s}^r}{\sum_{r,j,s} n_{j,s}^r} \qquad \langle p^2 \rangle = \frac{\sum_{r,j,s} n_{j,s}^r \, (p_{j,s}^r)^2}{\sum_{r,j,s} n_{j,s}^r} \tag{3.44}$$

The ratio of errors determines the reduction of the sensitivity in the analysis and is quantified by means of the *dilution factor*, which is expressed as

$$\frac{\sigma(a_{\ell m})}{\sigma(\bar{a}_{\ell m})} \approx \sqrt{\langle p^2 \rangle} \tag{3.45}$$

Relative Anisotropies

Contrary to the absolute anisotropy where the reference of the probability distribution function was the exposure time map, in the case of the relative anisotropy the reference map is built with the event map of the denominator. Due to the limited statistics in some pixels, special care has to be taken in the definition of the likelihood estimator. In this work, the Li-Ma log-likelihood [230] is used, which can be expressed as

$$log\mathcal{L} = \sum_{r,j,s} \left[n_{j,s}^r \, log \, \alpha_{j,s}^r - \left(n_{j,s}^r + (n_{ref})_{j,s}^r\right) log(1 + \alpha_{j,s}^r) \right] \tag{3.46}$$

where $n_{j,s}^r$ and $(n_{ref})_{j,s}^r$ are the measured number of events for the numerator and denominator, respectively, and

$$\alpha_{j,s}^r = \frac{1}{\mathcal{N}_j^r} \frac{N_j^r}{(N_{ref})_j^r} \left(1 + \sum_{\ell=1} \sum_{m=-\ell}^{m=+\ell} a_{\ell m} Y_{\ell m}^s\right) \tag{3.47}$$

with

$$N_j^r = \sum_s n_{j,s}^r \qquad ; \qquad (N_{ref})_j^r = \sum_s (n_{ref})_{j,s}^r \tag{3.48}$$

The term $\mathcal{N}_j^r$ is the normalization factor which ensures that the total number of events is preserved and can be written as

$$\mathcal{N}_j^r = 1 + \frac{1}{(N_{ref})_j^r} \sum_{\ell=1} \sum_{m=-\ell}^{m=+\ell} a_{\ell m} \sum_s (n_{ref})_{j,s}^r \, Y_{\ell m}^s \tag{3.49}$$

The maximization of the log-likelihood function provides the coefficients of the expansion for the relative analysis of anisotropies.

3.3.5 Computation of Upper Limits

In the previous sections, a set of tools was presented to obtain the multipole components $a_{\ell m}$ coming from the expansion of the cosmic ray fluxes into spherical harmonics. From those values the measured dipole anisotropy can be expressed as

$$\delta_M = \sqrt{\frac{3}{4\pi}(a_{1-1}^2 + a_{10}^2 + a_{11}^2)} \tag{3.50}$$

Since δ_M is defined as a positive quantity, its evaluation over a finite sample N provides a value larger than zero. In particular, the probability distribution function for an isotropic sample, $p(\delta_M|\delta_T = 0)$, has a non-zero expected value $E[\delta_M] \sim 2.76/\sqrt{N}$, as shown in figure 3.8. Furthermore, if the measured value is consistent with isotropy limits on the dipole amplitude can be established. Two methods can be used for this purpose: the *Frequentist* and the *Bayesian*.

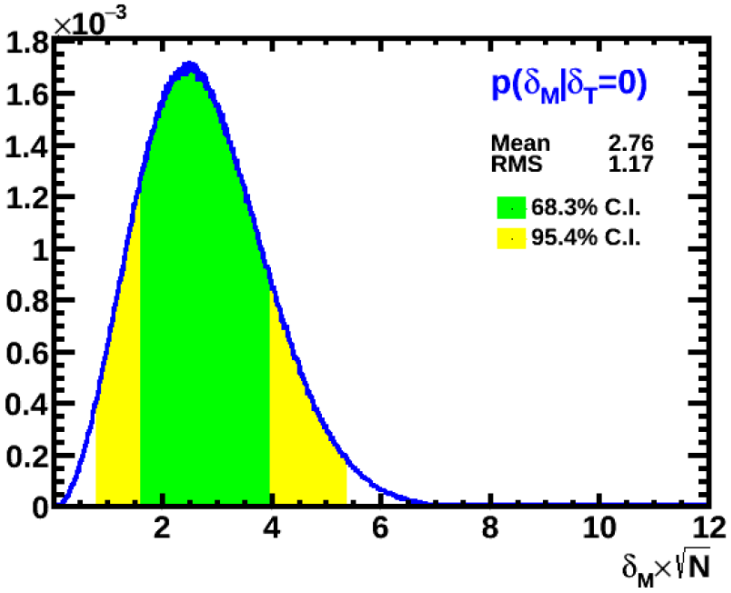

Figure 3.8: Probability distribution function for $\delta_T = 0$ ($p(\delta_M|\delta_T = 0)$). The δ_M is scaled to the size of the sample $\sqrt{N}$ and the two-sided intervals for the 68.3% and 95.4% probability are displayed.

In the frequentist prescriptions, where the classical procedure is due to Neyman [231], the upper limit corresponds to the δ_T which assures that the probability of measuring a dipole amplitude below δ_M is 1-α (where α is the confidence interval)

$$\int_0^{\delta_M} p(\delta_M|\delta_T)d\delta_M = 1 - \alpha \tag{3.51}$$

However, this treatment fails to set upper limits for very small signals. To avoid this, Feldman and Cousin [232] proposed a modification by introducing an *ordering rule* to establish limits when the signals are small. In this case, for large values of δ_M provides a two-sided confidence interval and not a direct upper limit.

In the Bayesian prescription, the upper limit corresponds to the value $\delta_T^{U.L.}$ which ensures that the probability of δ_T being below $\delta_T^{U.L.}$ is α

$$\int_0^{\delta_T^{U.L.}} p(\delta_T|\delta_M)d\delta_T = \alpha \tag{3.52}$$

This treatment requires an assumption on the δ_T, called prior $\pi(\delta_T)$, such that

$$p(\delta_T|\delta_M) \propto \pi(\delta_T)p(\delta_M|\delta_T) \tag{3.53}$$

where $\pi(\delta_T)$ is assumed to be constant [233]. The definition of the prior allows to set upper limits on δ_T for any δ_M.

As an illustration for the computation of the upper limits figure 3.9a shows the probability distribution function $p(\delta_M|\delta_T)$ for different values of δ_T and δ_M. The δ_T is distributed according to $\pi(\delta_T) \sim const$ and both, δ_T and δ_M, are scaled to the sample size $\sqrt{N}$. On the one hand, the projection on the horizontal axis for a value of δ_T provides the distribution $p(\delta_M|\delta_T)$ from which the Neyman prescription can be applied. On the other hand, the projection on the vertical axis for a measured value of δ_M provides the distribution $p(\delta_T|\delta_M)$ from which the Bayesian prescription can be applied.

Figures 3.9b and 3.9c show an example for a measured delta $\delta_M \times \sqrt{N} = 4$ in the Neyman and Bayesian presciptions respectively. The value of the limit at the 95% C.L. for Neyman is $\delta_T^{U.L.} \times \sqrt{N} \sim 6.25$, which agrees $\delta_T^{U.L.} \times \sqrt{N} \sim 6.18$ with the 95% C.I. value in the Bayesian method.

Finally, the comparison of the three presciptions for any value of δ_M is shown in figure 3.10. In the Neyman approach the upper limits are understimated for $\delta_M \times \sqrt{N} < 3$, whereas Feldman and Cousin provide a good determination of the limits for small $\delta_M \times \sqrt{N}$, but set a two-sided interval for $\delta_M \times \sqrt{N} > 5$. The Bayesian method provides a more convenient description of the upper limits for the whole range of $\delta_M \times \sqrt{N}$. For this reason, the Bayesian approach will be used for this work.

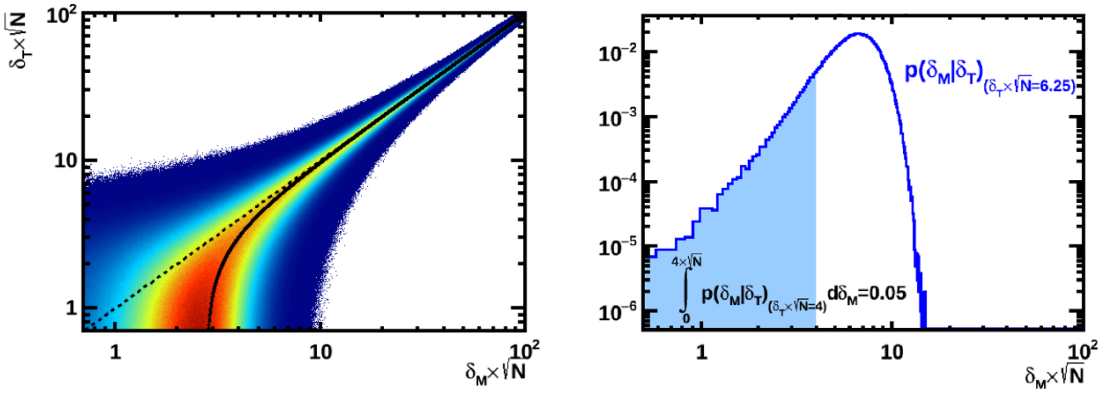

(a) (b) Frequentist (Neyman)

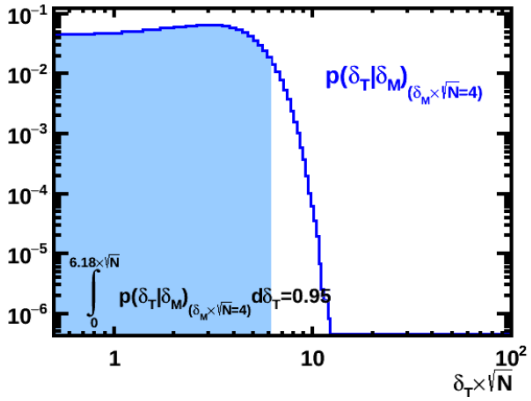

(c) Bayesian

Figure 3.9: (a) Probability distribution function $p(\delta_M|\delta_T)$ for different values of δ_T. The solid black line shows the expected value on δ_M according to $p(\delta_M|\delta_T)$ for each δ_T. (b) Probability distribution function $p(\delta_M|\delta_T)$ for $\delta_M \times \sqrt{N} = 4$ showing the upper limit computation in the Neyman presciption. (c) Posterior probability $p(\delta_T|\delta_M)$ for $\delta_M \times \sqrt{N} = 4$ showing the upper limit computation in the Bayesian presciption. The δ_M and δ_T are scaled to the size of the sample $\sqrt{N}$.[228]

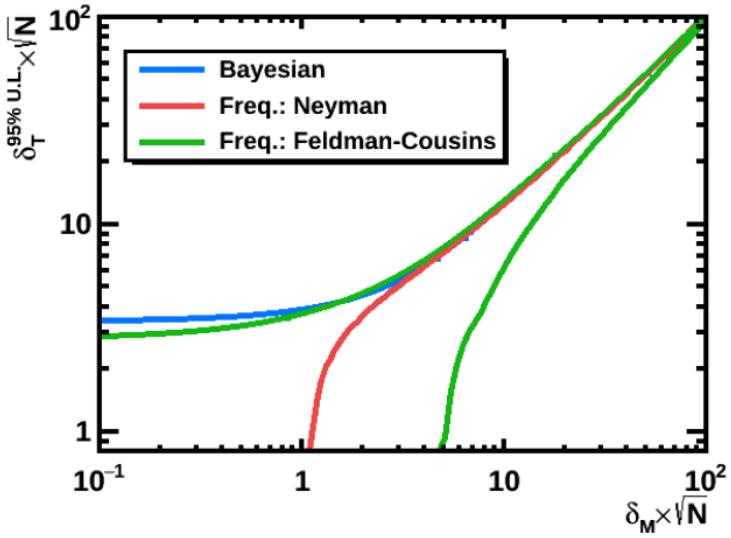

Figure 3.10: Comparison of the upper limits on δ_T for any value of δ_M in the Neyman, Feldman and Cousin and Bayesian prescriptions. The δ_M and δ_T are scaled to the size of the sample $\sqrt{N}$.[228]

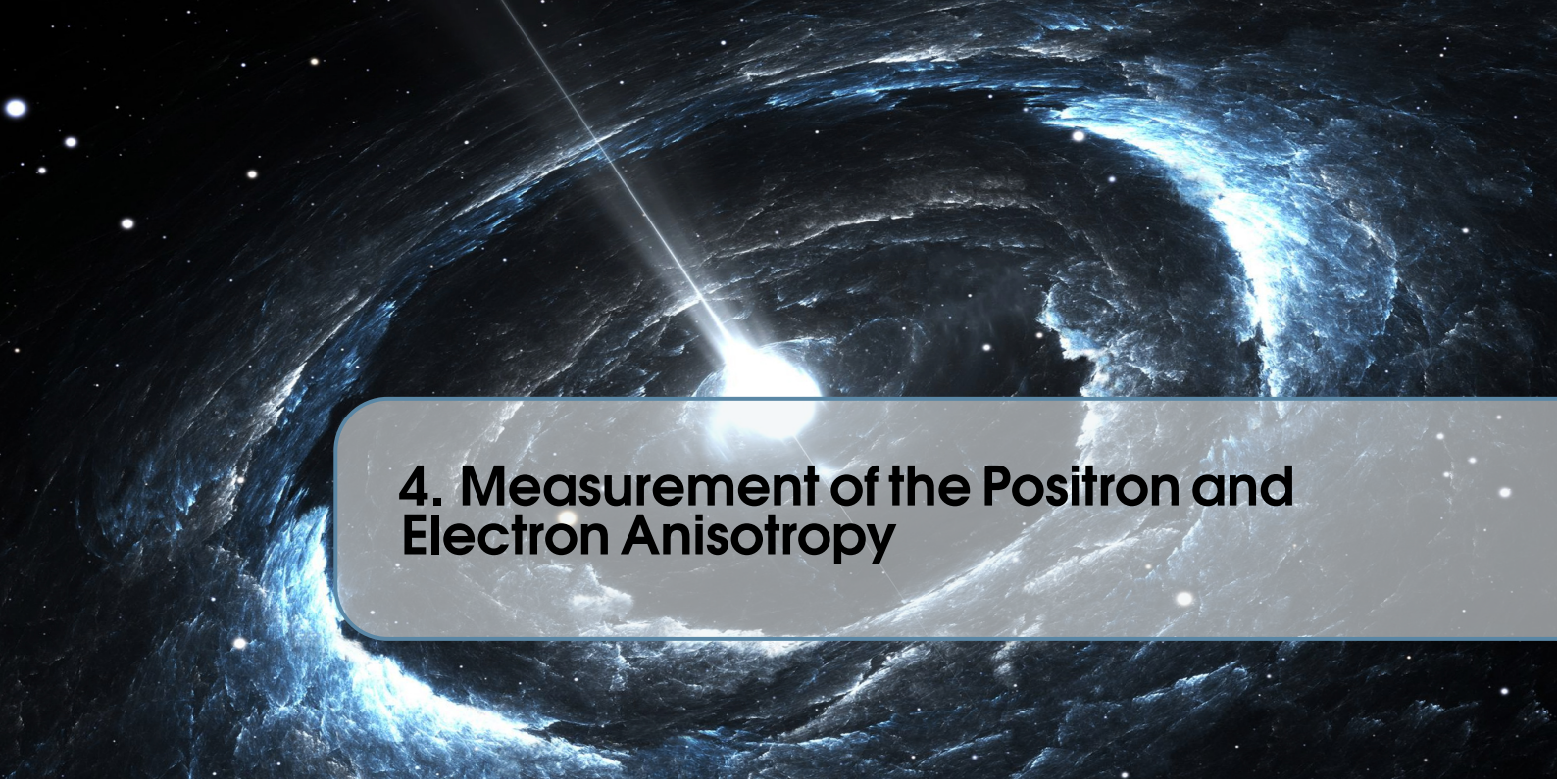

4. Measurement of the Positron and Electron Anisotropy

"Measure what is measurable, and make measurable what is not so."

— Galileo Galilei

Recent observations on the electron and positron fluxes challenge the standard paradigm of cosmic rays (see sections 1.6.2 and 1.7). On the one hand, the excess at high energies in the positrons cannot be described by a pure secondary production according to the traditional models and, typically, the inclusion of primary sources is necessary, such as pulsars or dark matter. On the other hand, the electrons also show an excess at high energies whose origin is different from the positron one. Many models have been proposed to explain the spectral features and, in particular, some of them predict that pulsars would imprint a dipole anisotropy up to 1% at $\sim$ 10 GeV in the positrons. Therefore, the determination of the directionality of electrons and positrons provides a complementary characterization to the fluxes that may help to understand the observed features.

Previous results on the electron and positron anisotropy with AMS-02 were reported in [158] where the analysis was performed with a cut-based selection and both were consistent with isotropy. Since no deviations from isotropy were found, limits to the dipole amplitude were established. This first results showed the capabilities of AMS-02 to measure the dipole anisotropy and, in particular, the connection between the level of sensitivity on the positron sample to the source term with the pulsar model predictions.

In this context, this chapter will present the optimization of the analysis that will improve the sensitivity towards reaching the pulsar predictions. For this purpose, two factors are crucial: the extension of the sample to include all the available data and the optimization of the analysis to maximize the statistics.

The first sections of this chapter will explain the standard method of analysis for an extended sample, which can be summarized as: standard cut-based selection, evaluation of the background, determination of the instrumental effects, and results on the dipole components. The results obtained in this analysis have been included in two recent AMS publications in Physical Review Letters [88; 89].

The last sections will describe the optimized analysis method using a *template fit*. This includes the selection of positrons and electrons, the techniques developed to include this procedure in the anisotropy analysis and, finally, the optimized results on the dipole anisotropy.

4.1 Positron and Electron Selection

This section will describe the specific criteria corresponding to the analysis published in [88] and [89]. The selection of positrons and electrons is applied to the data collected in the first 6.5 years of data taking with AMS-02, which represents the period of time from May 2011 to November 2017 and amounts to 1.49×10^8 s of exposure time.

1. **Reconstruction, Selection and Quality Criteria**
   The main purpose of this step in the selection is to provide a clean sample of unitary charged particles from which the positrons and electrons will be identified. Preselected events fulfill the following:
   - **Inner Tracker**
     Reconstruction:
     – Reconstructed track exists in the inner tracker with at least 4 hits between L2-L8. One of them in the L2, and the rest in either L3-L4, L5-L6 and L7-L8.
     Selection:
     – Charge measurement consistent with $|Z=1|$ $\left(0.7 < Q_{Inn} < 1.5\right)$.
     Quality Criteria:
     – Quality criteria on the inner track reconstruction in both bending (Y) and non-bending (X) planes $\left(\chi^2_{Inn}(X,Y)/d.o.f < 10\right)$.
     – Good spatial matching between between the inner tracker track extrapolation and the ECAL shower in both bending (Y) and non-bending (X) planes $\left(\Delta(X,Y) < 3\right)$ cm.
     – Single track reconstruction.
   - **TRD Reconstruction**
     – Reconstructed track exists in the TRD with an associated TRD_{Lkh} estimator.
   - **ECAL Reconstruction**
     – Reconstructed shower in the ECAL with an associated $ECAL_{BDT}$ estimator.
   - **TOF Reconstruction**
     – Reconstructed track exists in the TOF with 4 TOF hits between the planes.
     – Relativistic downward-going particles ($\beta > 0.7$).
     – Charge measurement in the lower TOF consistent with with $|Z=1|$ $\left(0.5 < Q_{LTOF} < 1.5\right)$.
   - **Fiducial Volume**
     – Inner tracker track extrapolation inside the TRD and ECAL
2. **Identification**
   The identification of positrons and electrons is achieved by means of a cut-based selection on the TRD and ECAL estimators as well as a good energy-momentum matching:
   - **TRD:** TRD Likelihood estimator < 0.6
   - **ECAL:** ECAL BDT estimator > 0
   - **ECAL-Tracker:** Good energy momentum matching $0.65 < E/|p| < 5$
   - **Tracker:** The curvature in the inner tracker determines the sign of the charge which will be used to separate electrons and positrons.

In addition, the reconstructed rigidity of all events is required to be above 1.2 the maximum geomagnetic rigidity cutoff within the field of view in absolute value for either positive or negative particles in order to avoid secondary particles trapped in the geomagnetic field.

The measurement of the anisotropy is performed in 5 cumulative energy ranges, with a minimum energy $E_{min} = 16, 25, 40, 65, 100$ GeV, and a maximum energy $E_{max} = 350$ GeV. The number of selected positrons and electrons in the different energy ranges is presented in table 4.1.

$E_{min}(GeV)$	$N_{e^+}^{meas}(\times 10^3)$	$N_{e^-}^{meas}(\times 10^3)$
16	98.90	1304.25
25	50.04	572.98
40	20.46	190.95
65	7.92	59.61
100	3.32	20.63

Table 4.1: Number of measured positron and electron events in the 5 cumulative energy ranges for 6.5 years of data taking.

4.2 Background Estimation

In general, two types of background appear in the electron and positron samples: residual protons and charge confused leptons (electrons or positrons whose sign has been wrongly reconstructed). On the one hand, the cut-based selection applied for this analysis has been shown to provide a sample of positrons and electrons with a proton background below the percent level in the different energy ranges [228] and, therefore, its contribution is negligible. On the other hand, charge confused electrons are mainly present in the positrons (for electrons the effect is negligible due to the low abundance of positrons). Consequently, the electrons are considered to be pure and the main source of background in the positrons arises from the charge confused electrons.

The procedure to estimate and include the presence of the background in the analysis is explained below.

4.2.1 Charge Confusion

Charge confused electrons are events reconstructed with positive rigidity sign mainly due to two sources: *spillover* and *interactions*.

Spillover events are related to the finite tracker resolution and become dominant at high energies, where the tracker resolution worsens and some trajectories are reconstructed with the opposite sign. This effect cannot be avoided since the tracker resolution is intrinsic to the magnet and to the STD capabilities.

In the low energy part, the biggest contribution comes from interactions in the detector material, where secondary particles can produce spurious signals that induce a wrong reconstruction of the trajectory and, thus, of the particle sign.

The charge confusion is defined as the fraction of events that are reconstructed with the wrong sign and can be expressed as

$$CC = \frac{N(R_{rec} \times R_{gen} < 0)}{N_{tot}} \tag{4.1}$$

which can be estimated on Monte Carlo simulated electrons, as shown in figure 4.1a.

The estimation of the charge confusion allows to compute the number of background electrons, $N_{e^-}^{bkg}$, on the positron sample using the expression

$$N_{e^-}^{bkg} = \frac{CC}{1-CC} N_{e^-}^{meas} \tag{4.2}$$

where $N_{e^-}^{meas}$ stands for the measured number of electrons on the data sample. In addition, charge confused electrons for a certain energy interval are associated with the same energy interval in the positron sample.

The comparison between the measured number of positrons, $N_{e^+}^{meas}$, the charge confused electrons, $N_{e^-}^{bkg}$, and the corrected number of positrons after the subtraction of the background, $N_{e^+}^{corr}$, is shown in figure 4.1b.

As discussed in section 3.3.4, the analysis of anisotropies takes into account the presence of the background in terms of the purity of the sample, defined for the charge confusion as $p_{CC} = N_{e^+}^{corr}/N_{e^+}^{meas}$. The positron purity is shown in figure 4.1c where as can be seen at high energies $\sim 10\%$ of the positron events are charged confused electrons.

Finally, the numerical values for the measured and corrected number of positron events in the different energy ranges can be found in table 4.2. In addition, the dilution factor from equation 3.45 is presented to quantify the reduction of the sensitivity due to the presence of the background in the sample.

$E_{min}(GeV)$	$N_{e^+}^{meas}(\times 10^3)$	$N_{e^+}^{corr}(\times 10^3)$	Dilution
16	98.90	95.46 ± 0.32	1.02
25	50.04	48.65 ± 0.23	1.02
40	20.46	20.08 ± 0.14	1.02
65	7.92	7.87 ± 0.09	1.03
100	3.32	3.37 ± 0.06	1.04

Table 4.2: Number of measured and corrected positron events in the 5 cumulative energy ranges for 6.5 years of data taking.

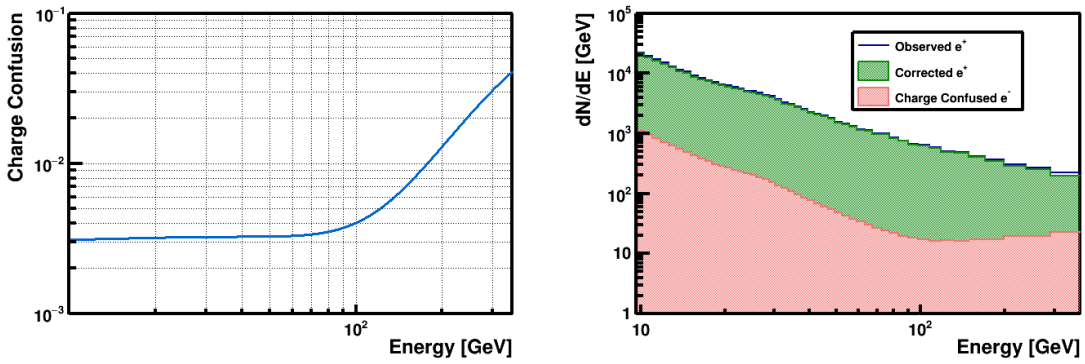

(a) (b)

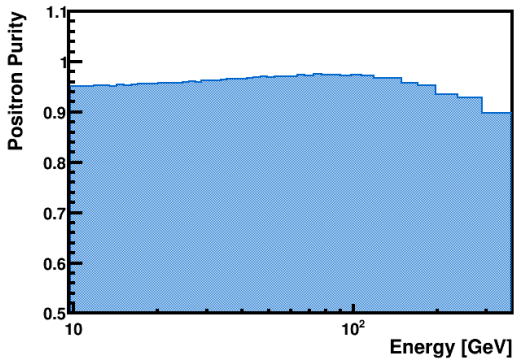

(c)

Figure 4.1: (a) Charge confusion probability determined from MC simulated electrons with respect to the generated energy. (b) Number of measured and corrected positrons (blue and green respectively), and charge confused electrons (red). (c) Positron purity as a function of the energy.

4.3 Positron and Electron Efficiencies

The selection criteria described in section 4.1 have associated efficiencies whose geographical dependences may induce spurious signals in the anisotropy analysis and need to be studied in detail. The efficiency of each selection cut is defined as

$$\varepsilon = \frac{N_{ok}}{N_{tot}} = \frac{N_{ok}}{N_{ok} + N_{ko}} \tag{4.3}$$

where N_{ok} and N_{ko} represent the number of accepted and rejected events, and N_{tot} the initial sample of signal events. In particular, the N_{ko} and N_{ok} distributions in the skymap will be used to parametrize the efficiencies in terms of spherical harmonics, as described in section 3.3.3.

The study of the efficiencies is performed sequentially on data where the sample of events passing one cut determines the initial sample of the following efficiency. This procedure allows to minimize correlations between the different subdetectors and factorize them in terms of the individual ones.

Taking advantage of the identical response of the detector to opposite signs, the efficiencies are evaluated on electrons and applied to positrons. This has two main advantages: the proton background in the electron sample is highly suppressed and the available statistics is higher than in positrons, allowing to obtain a more precise determination of the efficiencies.

Special care has to be taken to remove the dominating proton background at all stages of the efficiency computations, so that the evaluations of their dependences corresponds to that of the electron sample. Finally, the computation of the efficiencies is performed as a function of the energy and within the corresponding fiducial volume.

4.3.1 Electron Efficiencies

The computation of the electron efficiencies is presented as follows: inner tracker efficiencies, TRD and ECAL reconstruction efficiencies, identification efficiencies, and trigger efficiency.

Inner Tracker Efficiencies

The initial sample corresponds to relativistic downward-going particles ($\beta > 0.7$) within the fiducial volume with unitary TOF charge ($|Q_{TOF}| = 1$) and physics trigger [1]. The electron identification is performed by means of a tight cut on the $ECAL_{BDT}$ estimator ($ECAL_{BDT} > 0.95$).

The efficiencies are then computed sequentially requiring the following conditions:

- **Tracker reconstruction efficiency:** Reconstructed track exists in the inner tracker with at least 4 hits between L2-L8.
  Once the rigidity is available its sign allows to distinguish electrons and the extrapolation of the inner track to the ECAL and TRD provides the fiducial volume for the rest of the efficiencies.
- **Tracker selection efficiency:** Unitary inner charge $|Q_{Inn}| \sim 1$.
- **Tracker quality criteria efficiencies:** Three different efficiencies are evaluated:
  1. *Track good χ^2:* Inner tracker good χ^2 in both bending (Y) and non-bending (X) planes.
  2. *Track-ECAL (X,Y) match:* Good spatial matching between the inner tracker track extrapolation and the ECAL shower in X and Y directions.
  3. *Single track reconstruction*

TRD and ECAL Reconstruction Efficiencies

After the evaluation of the inner tracker efficiencies the TRD and ECAL reconstruction efficiencies can be computed. The electron identification for the TRD reconstruction efficiency is identical as in the previous step ($ECAL_{BDT} > 0.95$). For the ECAL reconstruction efficiency, the electron identification requires a tight cut in the TRD_{Lkh} estimator ($TRD_{Lkh} < 0.3$).

[1] At this stage the fiducial volume is determined with the extrapolation of the TOF track into the TRD and ECAL.

The evaluation of the TRD and ECAL reconstruction efficiencies is achieved by requiring the following conditions:

- **TRD reconstruction efficiency:** TRD track with an associated TRD_{Lkh} estimator.
- **ECAL reconstruction efficiency:** Shower in the ECAL with an associated $ECAL_{BDT}$ estimator.

Identification Efficiencies

Identification efficiencies are determined after evaluating the previous ones. In particular, the electron separation from the background for the TRD identification efficiency is performed with a tight cut on the ECAL estimator ($ECAL_{BDT} > 0.95$) whereas the ECAL identification efficiency makes use of a tight cut in the TRD estimator ($TRD_{Lkh} < 0.3$) (as in the TRD and ECAL reconstruction efficiencies).

Finally, the good energy-momentum matching, $E/|p|$, efficiency is calculated as a last cut, due to the correlation between the energy in the ECAL and the $ECAL_{BDT}$. The initial sample corresponds to the electron events passing the standard cuts of the TRD and ECAL estimators.

The identification efficiencies are evaluated by requiring the cuts from the selection:

- **$\mathbf{TRD_{Lkh}}$ efficiency:** TRD_{Lkh} estimator < 0.6
- **$\mathbf{ECAL_{BDT}}$ efficiency:** $ECAL_{BDT}$ estimator > 0
- **$\mathbf{E/|p|}$ efficiency:** Good energy momentum matching $0.65 < E/|p| < 5$

Trigger Efficiency

The trigger efficiency on the selected sample is evaluated directly from data by constructing a sample that consists of events satisfying all selection cuts with any physics trigger N_{phys} or with a looser condition in the physics trigger N_{unb} (called trigger unbiased) which requires that 3/4 TOF planes are fired instead of 4/4. In order to reduce the data size in the acquisition system, the unbiased events are prescaled by a factor of 1/100. Consequently, the trigger efficiency is expressed as

$$\varepsilon_{trig} = \frac{N_{phys}}{N_{phys} + 100\, N_{unb}} \tag{4.4}$$

where the factor 100 accounts for the prescaled unbiased events.

4.4 Positron Fraction Computation

The selection presented in section 4.1 has been especially designed for anisotropies in the energy range of the analysis. The determination of the positron fraction for jth energy bin $(\Delta R_j, R_j + \Delta R_j)$ is defined as

$$PF_j = \frac{(\Phi_{e^+})_j}{(\Phi_{e^+})_j + (\Phi_{e^-})_j} \tag{4.5}$$

which reduces to the ratio of the number of events, since the detector response is identical for opposite signs.

Results are presented in figure 4.2a together with the comparison with the latest AMS-02 publication. As can be seen, the results are fully compatible in the energy range of this work, which is further confirmed by the ratio in figure 4.2b.

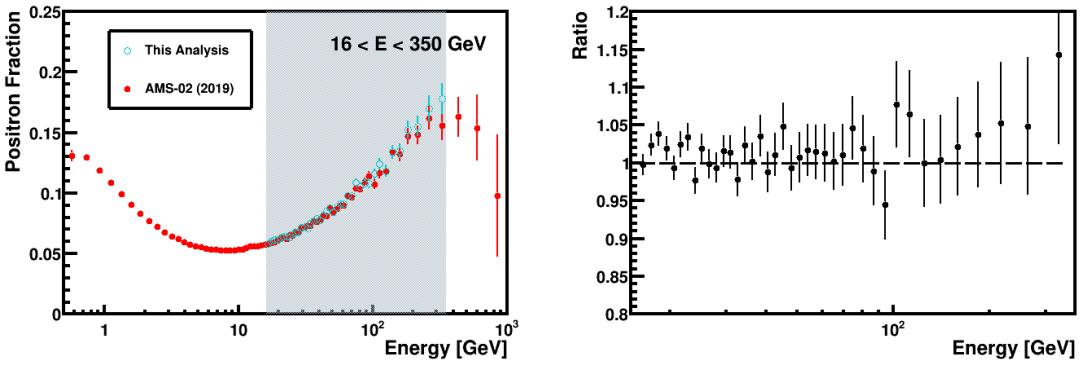

(a) (b)

Figure 4.2: (a) Comparison of the positron fraction obtained with this analysis for 6.5 years of data taking with the AMS-02 latest publication [88]. (b) Ratio between this analysis and the AMS-02 publication.

4.5 Parametrization of the Electron Efficiencies for Anisotropies

The computation of the isotropic reference for the anisotropy searches requires a precise understanding of the efficiency dependences, since if not properly accounted they may arise as spurious effects.

The origin of the detector effects can be first understood in a coordinate system where no physical signal is expected. In this work, ISS geographical position coordinates will be used. This reference system allows to interpret the variation of the efficiencies along the ISS orbit where some inefficiencies are likely to appear due to the particles rate changes associated to the geomagnetic cutoff. Furthermore, the ISS geographical position coordinates provides direct information on the effect of the efficiency dependences on the anisotropy measurement in the physical system by means of the effective coordinate transformation (see appendix A).

The aim of this section is to present the set of tools developed to understand the efficiency dependences and quantify their effect in the analysis of anisotropies.

One-Dimensional Study in Geomagnetic Colatitude

The study of the one-dimensional efficiency distributions as a function of the geomagnetic colatitude provides valuable information about the behavior of the different subdetectors along the ISS orbit and serves as a first estimation to quantify the impact of the efficiency corrections in the multipolar analysis.

As an illustration, the figure 4.3 shows the relative variation of the TRD reconstruction efficiency (the most relevant in the anisotropy analysis) as a function of the cosine of the geomagnetic latitude for two energy ranges, E_{min} = 16 GeV and E_{min} = 65 GeV, where $cos(\theta_M) = -1$ corresponds to the northern geomagnetic pole and the $cos(\theta_M) = +1$ to the southern. The distribution shows a drop of $\sim 2\%$ in the regions close to the poles with respect to the equator. This effect is due to the high rate of particles in the poles that produces a reduction of the TRD reconstruction efficiency.

The variation of the efficiencies can be parametrized in terms of a second order polynomial function

$$f(cos\theta_M) = p_0 + p_1 \times cos\theta_M + p_2 \times cos^2\theta_M \tag{4.6}$$

where p_1 quantifies the North-South asymmetry and p_2 describes the symmetric drop at high latitudes. These parameters are related with the a_{10} and a_{20} components of the spherical harmonic expansion as

$$a_{10} = \sqrt{\frac{4\pi}{3}}\, p_1, \qquad a_{20} = \frac{1}{3}\sqrt{\frac{16\pi}{5}} p_2 = \sqrt{\frac{16\pi}{5}}(1-p_0) \tag{4.7}$$

Therefore, the fit parameters quantify the amplitude of the efficiency corrections, in particular in the NS and $2+0$ components, in positional coordinates, which in turn constitute the most relevant contributions to the corrections in the analysis in galactic coordinates.

In addition, the one dimensional approach provides a first estimation of the energy dependence of the efficiency corrections by comparing the relative variation for different energy ranges, as can be seen in figure 4.3.

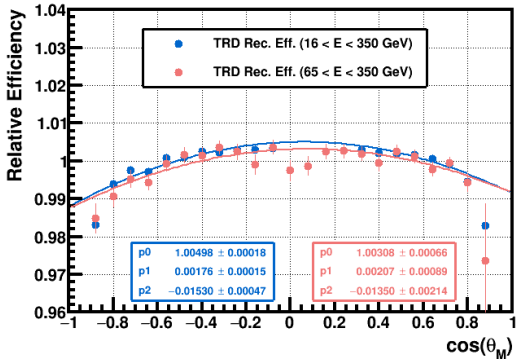

Figure 4.3: Relative variation of the TRD reconstruction efficiency as a function of the geomagnetic colatitude for the energy ranges $16 < E < 350$ GeV and $65 < E < 350$ GeV. The distributions are fitted to a quadratic function to quantify the North-South direction.

Spherical Harmonic Study in ISS Geographical Position Coordinates

The spherical harmonic parametrization of the skymap efficiency distributions provides the multipole components $\eta_{\ell m}$ that will be used to correct the exposure time map. The coefficients of the expansion, $\eta_{\ell m}$, are computed from the relative anisotropies (see section 3.3.3) of the samples of rejected, N_{ko}, and accepted, N_{ok}, events for each energy range.

The efficiency corrections for the multipole components of the analysis are expressed according to equation 3.29 as

$$\Delta^i_{\ell m} = \frac{\eta^i_0}{1+\eta^i_0}\,\eta^i_{\ell m} \tag{4.8}$$

where the subindex i stands for the different efficiencies, and $\eta^i_0 = N^i_{ko}/N^i_{ok}$ accounts for the average ratio of the samples in a certain energy range $[E_{min}, E_{max}]$. The total efficiency correction, assuming no correlations, is the sum of the individual corrections $\Delta_{\ell m} = \sum_i^{N_{effs}} \Delta^i_{\ell m}$.

Therefore, the uncertainty of the total efficiency correction is affected by the errors of the individual ones. In order to reduce the overall error two strategies have been followed:

- The energy dependence of each efficiency correction is described with a parametrization. This allows to avoid the inclusion of the efficiency corrections for each energy range, in particular, at high energies where the statistics is low and the associated errors larger.
- The efficiency corrections consistent with statistical fluctuations are excluded and, thereby, their contribution to the total error.

The energy dependence of the corrections is described with a first and second order polynomial parametrization as a function of the logarithm of the energy for the dipole ($\ell = 1$) and quadrupole

($\ell = 2$) components respectively. The use of a higher order function for the ($\ell = 2$) allows the parametrization to be more sensitive to energy variations and high amplitudes.

As an example, figures 4.4a and 4.4b show the TRD reconstruction efficiency corrections for the Δ_{NS} and Δ_{2+0} components in ISS geographical position coordinates and their corresponding parametrizations. The same procedure is applied to the individual efficiencies described in section 4.3.1.

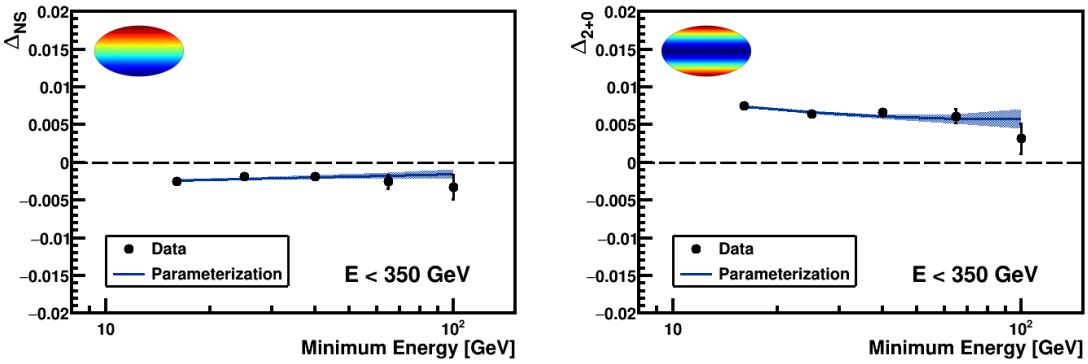

(a) (b)

Figure 4.4: TRD reconstruction efficiency corrections for the Δ_{NS} (a) and Δ_{2+0} (b) components. The data points are obtained from the relative analysis of the N_{ko} and N_{ok} samples. The corrections are fitted to a linear and quadratic parametrization for the $\ell = 1$ and $\ell = 2$ respectively.

For this work, the same method used in [228] to decide the significant efficiencies is followed, which can be summarized as:

1. The distribution of pulls, computed as $\Delta^i_{\ell m}/\sigma(\Delta^i_{\ell m})$ for each energy range, is obtained (figure 4.5). The corrections compatible with statistical fluctuations will be grouped in a central core consistent with a normal distribution, whereas the tails represent the significant corrections.
2. The cut value to determine the significant efficiencies is obtained using the pulls distribution. A fit to a Gaussian is performed for the interval $[-x, +x]$, and a scan in the mean and sigma of the fit allows to choose the optimal value (threshold) such that the Gaussian is around 0 and has a width 1, as shown in figures 4.6a and 4.6b.
3. The efficiencies that are significant in the lowest energy range are also included in the higher energies. The correction is introduced using the aforementioned parametrization.

Figure 4.7 shows the dipole and quadrupole components for each efficiency (top panel) as well as the total efficiency correction (bottom panel) for the energy range $16 < E < 350$ GeV. The total efficiency correction is computed as the sum of the individual corrections, where only those tagged as significant following the previous method are included. The biggest contribution comes from the TRD reconstruction efficiency and, it mainly affects the North-South direction, represented by the Δ_{NS} and Δ_{2+0}. This is explained by the high rate of particles that saturate the TRD at high geomagnetic latitudes, as was observed in the one-dimensional study of the efficiencies. The amplitude of the Δ_{2-1} also contributes due to the asymmetry of the geomagnetic poles in ISS geographical position coordinates. Overall, the corrections are at the percent and permil level for the quadrupole and dipole components respectively.

Figures 4.8a and 4.8b show the skymap of the spherical harmonic parametrization of the TRD reconstruction efficiency as well as the total one up to $\ell = 2$ for $16 < E < 350$ GeV, where only significant corrections have been included. The North-South asymmetry is clearly observed in both figures. The dependences of the total efficiency defines the corrections to the exposure time map which constitutes the reference map for the anisotropies analysis in ISS geographical positions.

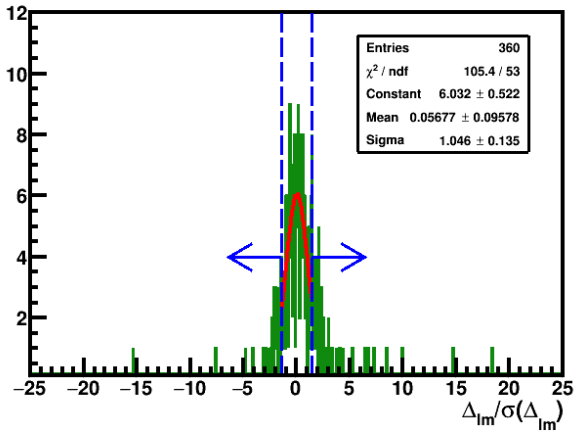

Figure 4.5: Distribution of efficiency correction pulls for each efficiency (9), energy range (5), dipole and quadrupole components (8). Efficiency corrections whose pull is below the threshold are consistent with statistical fluctuations and described by a normal distribution. Those corrections above the threshold are significant and include it in the analysis (indicated by an arrow).

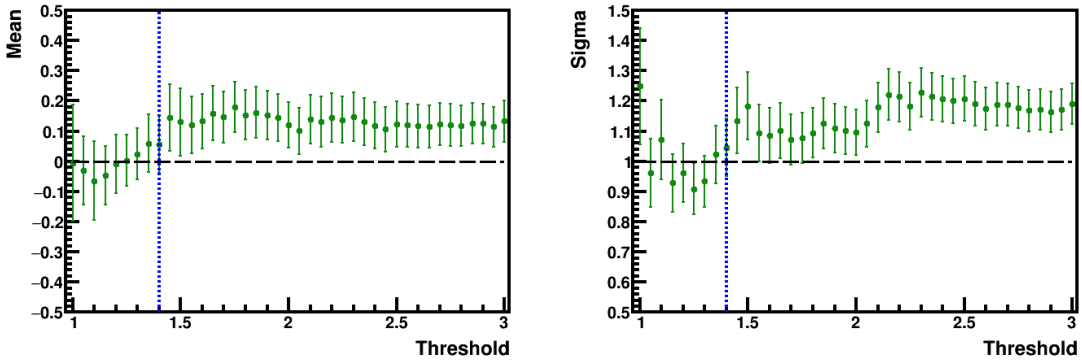

(a) Mean (b) Sigma

Figure 4.6: Scan in the mean (a) and sigma (b) parameters of the fit to a Gaussian function of the pulls distribution in figure 4.5 as a function of the threshold value. The optimum value of a threshold, which corresponds to mean ~ 0 and sigma ~ 1, ensures that the efficiency corrections with pull below that value are well described by a Gaussian distribution and, therefore, consistent with statistical fluctuations.

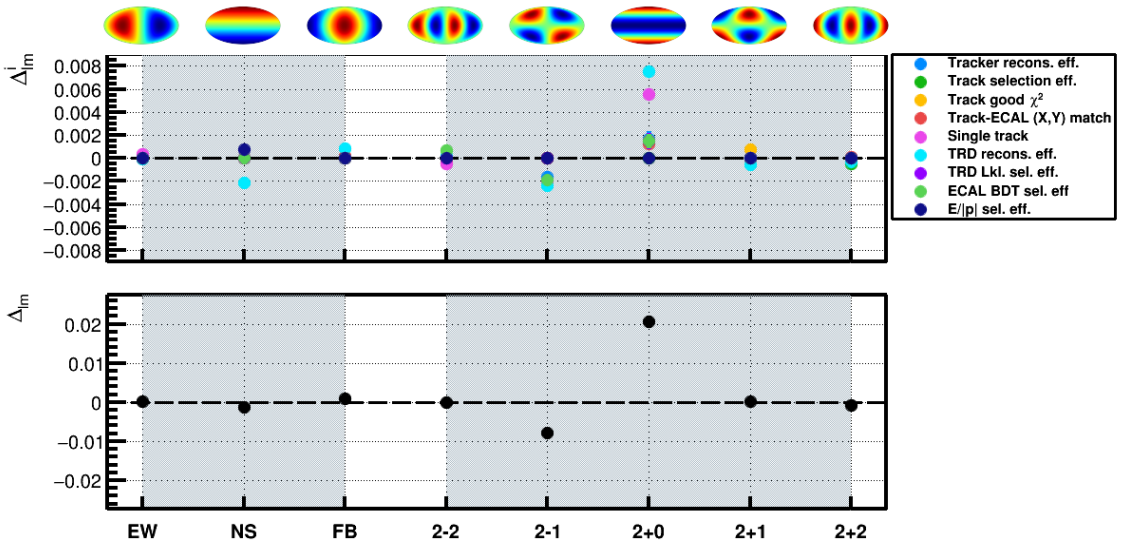

Figure 4.7: Individual (top) and total (bottom) efficiency corrections for the dipole ($\ell = 1$) and quadrupole ($\ell = 2$) components for $16 < E < 350$ GeV in ISS geographical position coordinates. The main direction affected is the North-South with the biggest contribution coming from the TRD reconstruction efficiency.

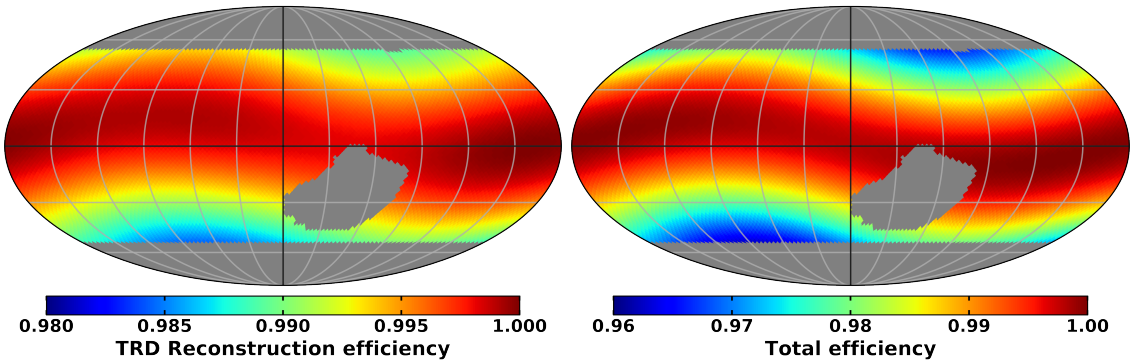

(a) TRD Reconstruction Efficiency

(b) Total Efficiency

Figure 4.8: ISS geographical position skymap of the spherical harmonic parametrization of the TRD reconstruction efficiency (a) as well as the total one (b) up to $\ell = 2$ for $16 < E < 350$ GeV, where only significant corrections have been included.

Spherical Harmonic Study in Galactic Coordinates

The study of the efficiency corrections in ISS geographical position coordinates allows to understand the effect of the efficiency dependences in the physical system, since most of the effects can be understood from a coordinate transformation of the Δ^i_{NS} and Δ^i_{2+0} (see figure A.1c).

Similarly to the previous section, the multipole components for each efficiency are obtained from the relative analysis of anisotropies with the N_{ko} and N_{ok} samples in galactic coordinates. The components are computed for each cumulative energy range and the same procedure presented before to parametrize the energy dependence and determine which efficiencies are significant is followed.

The dipole and quadrupole components for each efficiency correction (top panel) and for the total efficiency correction (bottom panel) for $16 < E < 350$ GeV are shown in figure 4.9. Results

are qualitatively understood with the transformation from geographic to galactic coordinates. In particular, the North-South asymmetry observed in ISS geographical position coordinates is projected onto all directions in galactic coordinates and most of the components are now significant, with, again, a dominant contribution from the TRD reconstruction efficiency. Due to the spread in the different components, the amplitude of the corrections is lower.

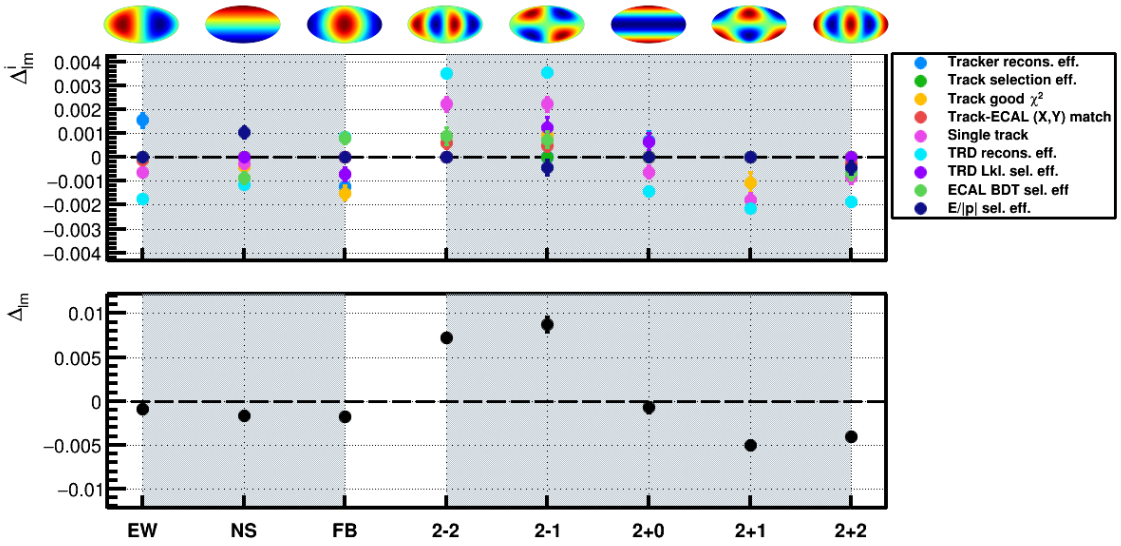

Figure 4.9: Individual (top) and total (bottom) efficiency corrections for the dipole ($\ell = 1$) and quadrupole ($\ell = 2$) components for $16 < E < 350$ GeV in galactic coordinates. Most of the components are now significant due to the projection of the Δ^i_{NS} and Δ^i_{2+0} from ISS geographical position coordinates into galactic coordinates. The main contribution comes from the TRD reconstruction efficiency.

The skymaps of the spherical harmonic parametrization of the TRD reconstruction efficiency as well as the total one up to $\ell = 2$ for $16 < E < 350$ GeV in galactic coordinates are shown in figures 4.10a and 4.10b. For the total efficiency, only significant corrections have been included. The skymap of the total efficiency defines the corrections to the exposure time map which constitutes the reference map for the anisotropy analysis in galactic coordinates.

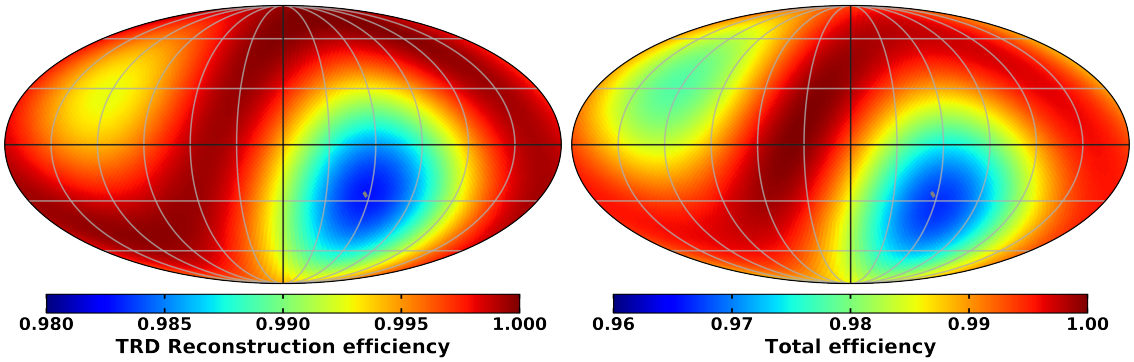

(a) (b)

Figure 4.10: Skymap of the spherical harmonic parametrization of the TRD reconstruction efficiency (a) as well as the total one (b) up to $\ell = 2$ for $16 < E < 350$ GeV in galactic coordinates, where only significant corrections have been included.

4.6 Results on the Electron and Positron Anisotropy

The measurement of the electron and positron anisotropy is performed by correcting the exposure time map with the efficiency map. The efficiency map has been evaluated on the electron sample due to its larger size and background free condition. Since the detector response is independent of the charge sign the same corrections on the positron sample will be directly applied. The electrons will not only serve to search for possible source contribution but also constitute a test of the systematic uncertainties for the positron sample.

A detailed description of the analysis will be presented for the electron sample and, then, the final results for positrons applying the corrections evaluated on electrons.

4.6.1 Electrons

ISS Geographical Position Coordinates

As mentioned in 4.5 the analysis of anisotropies can be first understood in ISS geographical positions by means of the one-dimensional approach. This study provides a first look at the impact of the efficiency corrections into the North-South direction, which is the one that projects onto galactic coordinates and, therefore, the most relevant for this analysis.

Figure 4.11a shows the relative variation of the raw rate together with the total efficiency as a function of the cosine of the geomagnetic colatitude for $16 < E < 350$ GeV. The raw rate presents a drop of $\sim 5\%$ at high latitudes with a similar trend for the total efficiency dependences. However, the drop in the efficiencies is not sufficient to completely explain the decrease in the rate and a residual drop of $\sim 2\%$ is still present, as can be seen in the fits to a quadratic function.

This result is better observed in figure 4.11b where the rate corrected by the efficiency dependences is presented. This effect might come from an underestimation of the efficiency determination due to a residual correlation between subdetectors. The observed deviation will be incorporated as an additional source of systematic in the anisotropy analysis.

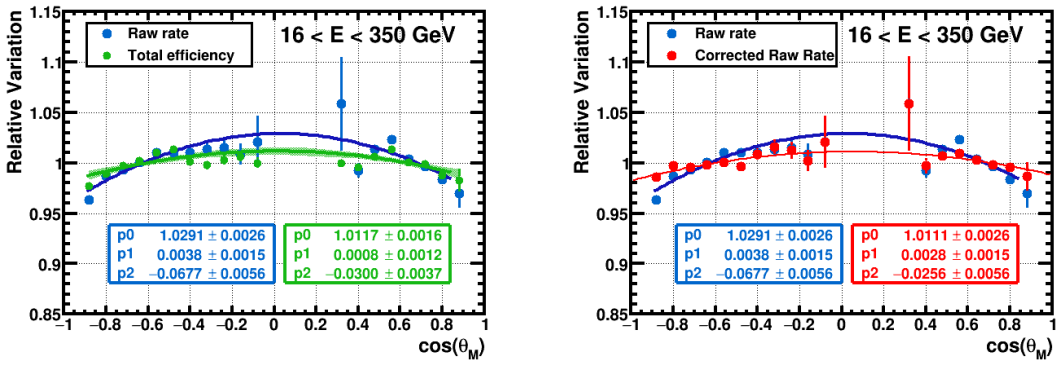

(a) (b)

Figure 4.11: Relative variation of the electron raw rate (blue) together with total efficiency (green) as a function of the geomagnetic colatitude (a) and corrected raw rate (b) for the energy range $16 < E < 350$ GeV. A drop at high latitudes is observed in the raw rate and the total efficiency, but it is not sufficient to completely correct the rate.

For the spherical harmonic analysis, the corrections to the exposure time map by means of the total efficiency map determined in 4.5 allows to compute the isotropic reference map and, thus, the skymap of the expected number of events.

The determination of the multipole components is carried out by using the binned-likelihood fit from equation 3.38 for the different energy ranges. In order to see the impact of the efficiency corrections in the components the corrected and uncorrected exposure time maps are used as a

reference. The results for the ρ_{NS} and ρ_{2+0} components (the ones that mainly project into galactic coordinates) are shown in figure 4.12 in ISS geographical position coordinates. The top panel presents the components for the different energy ranges and the bottom panel the deviations with respect to isotropy in terms of standard deviations for each of the points.

Significant deviations from isotropy are observed for the uncorrected results, especially in the quadrupole component. The parametrization of the efficiency corrections reduces the deviations but it is not enough to completely cancel the ρ_{2+0}, especially at low energies. These observations agree with the results from the one-dimensional analysis where the corrected raw rate had a residual drop at high latitudes (figure 4.11b).

The residual deviation will be included as an *effective missing correction* in the anisotropy analysis. This assumption is well justified since no physical signal is expected in ISS geographical positions and, therefore, the deviations are expected to come from instrumental effects. The missing correction is taken to be half of the remaining value of the deviation and the uncertainty is propagated into the systematic errors. After applying this corrections the ρ_{NS} and ρ_{2+0} in figure 4.12 are consistent with isotropy within the uncertainties in ISS geographical positions.

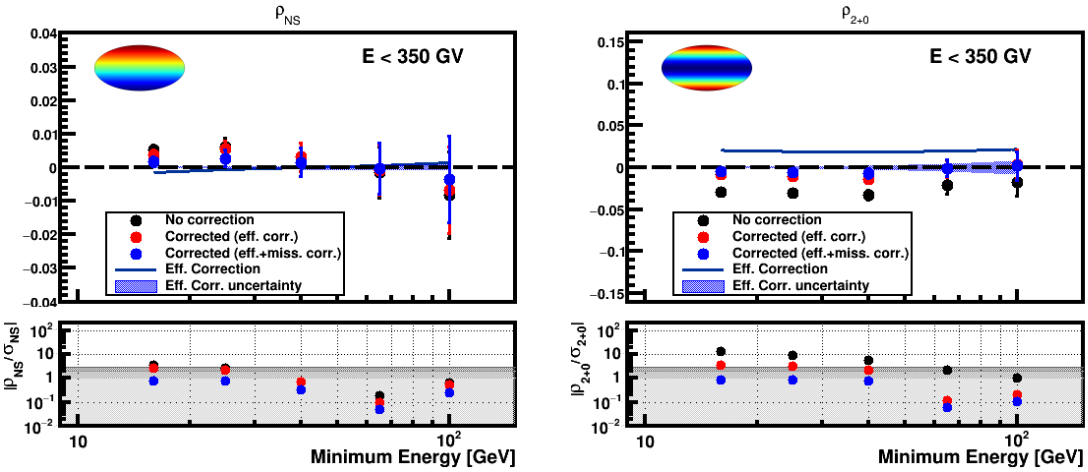

(a) (b)

Figure 4.12: Electron multipole components corresponding to the North-South direction, ρ_{NS} (a) and ρ_{2+0} (b), in ISS geographical position coordinates where no corrections (black dots), efficiency corrections (red dots) and efficiency plus missing corrections (blue dots) are included. The error bars in the dots stand for the statistical uncertainties. Efficiency corrections are shown as a blue line with its uncertainty displayed as a blue band. Finally, in the bottom panel the absolute deviations from isotropy are evaluated in terms of the standard deviations.

An independent validation of the description of the data is obtained with a non-parametric analysis. The goodness of the description ensures that there are no significant deviations in the map of measured events. The estimator is constructed in each pixel i of the skymap as

$$S_i = \frac{N_i - \langle \tilde{N} \rangle_i}{\sqrt{\langle \tilde{N} \rangle_i}} \tag{4.9}$$

where N_i and $\langle \tilde{N} \rangle_i$ represent the measured and expected events according to the isotropic reference respectively.

As an example, figure 4.13 shows the skymap of measured electrons and the isotropic reference for $16 < E < 350$ GeV in ISS geographical position coordinates. The good description of the data is evaluated with the significance map and histogram (figure 4.14). No structures are observed in

figure 4.14a. This is further confirmed by the significance histogram, figure 4.14b, which is well described with a normal distribution.

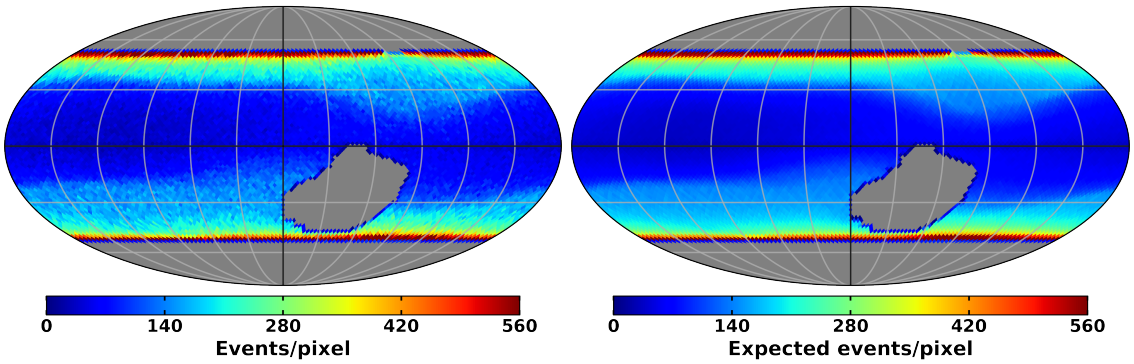

(a) (b)

Figure 4.13: Electron skymap distributions of measured (a) and expected events (b) for the energy range $16 < E < 350$ GeV in ISS geographical position coordinates.

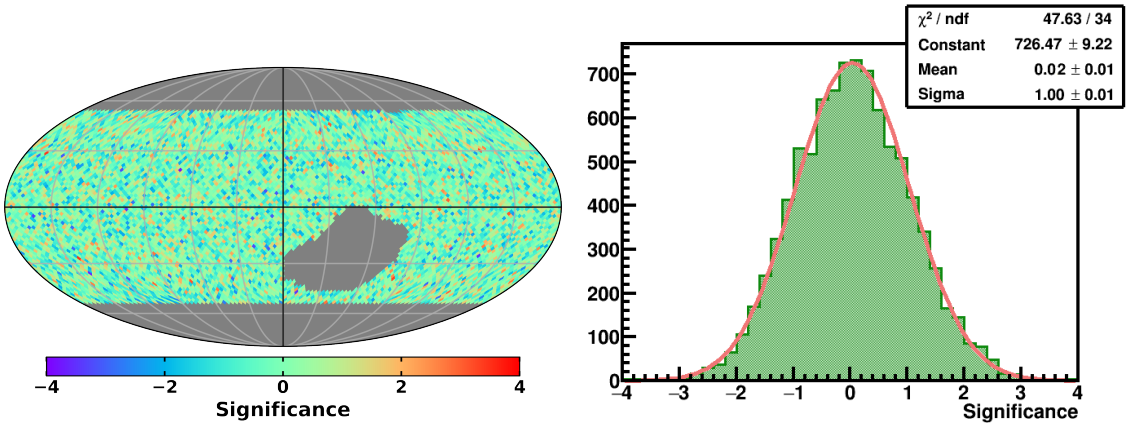

(a) (b)

Figure 4.14: Electron significance skymap (a) and distribution for the energy range $16 < E < 350$ GeV in ISS geographical position coordinates.

Galactic Coordinates

The precise understanding of the ISS geographical position coordinate systems allows to extend the analysis to the physical reference system, where a signal could be measured. The skymap of measured events, as well as the corrected and uncorrected reference, are introduced in the binned-likelihood to retrieve the multipole components in galactic coordinates. The same scheme of corrections followed in the non-physical reference system is applied in the physical system where the efficiency corrections are determined directly in galactic coordinates and the missing corrections are obtained by means of the matrix transformation from ISS geographical position to galactic coordinates.

Figure 4.15 shows the ρ_{EW} and ρ_{2-2} components which are the ones that receive the biggest contribution from the North-South direction in ISS geographical position. The components for the different energy ranges as well as the consistency with respect to isotropy are displayed. The uncorrected results show deviations from isotropy, especially in the quadrupole. After including the corrections both dipole and quadrupole components are consistent with isotropy.

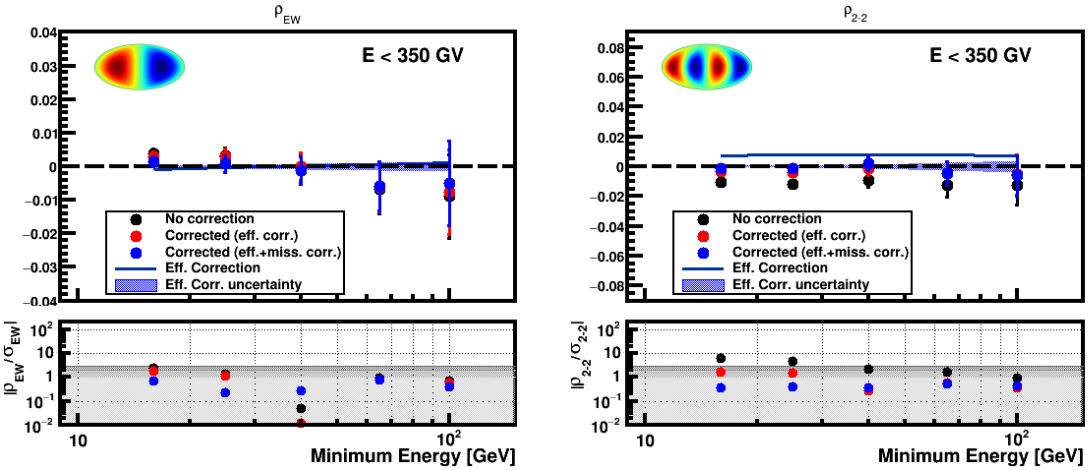

(a) (b)

Figure 4.15: Electron multipole components ρ_{EW} (a) and ρ_{2-2} (b), in galactic coordinates where no corrections (black dots), efficiency corrections (red dots) and efficiency plus missing corrections (blue dots) are included. The error bars in the dots stand for the statistical uncertainties. Efficiency corrections are shown as a blue line with its uncertainty displayed as a blue band. Finally, in the bottom panel the absolute deviations from isotropy are evaluated in terms of standard deviations.

Similarly to the ISS geographical position, the same significance estimator can be used to confirm that there are no significant contributions from higher multipoles and the skymap is consistent with isotropy. Figure 4.16 shows skymap of measured electrons and the isotropic reference for $16 < E < 350$ GeV in galactic coordinates. The significance map and distribution are shown in figure 4.17. No evident structures are found in figure 4.17a, which is further confirmed with the good description by a normal distribution of the significance histogram (figure 4.17b).

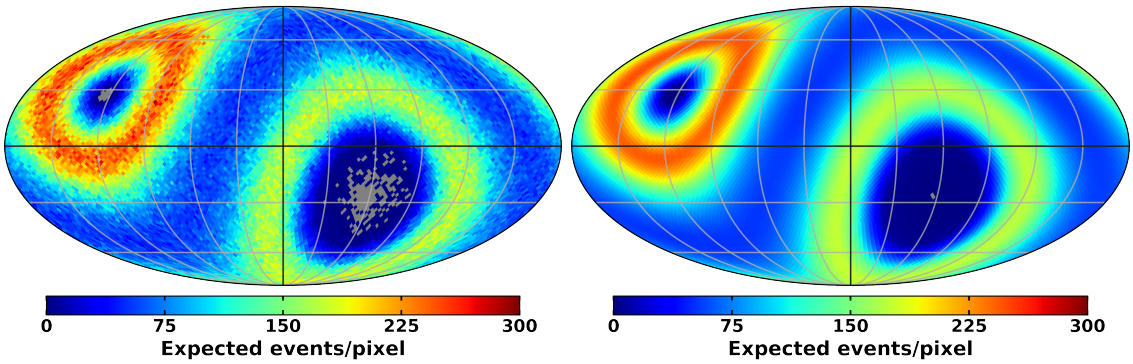

(a) (b)

Figure 4.16: Electron skymap distributions of measured (a) and expected events (b) for the energy range $16 < E < 350$ GeV in galactic coordinates.

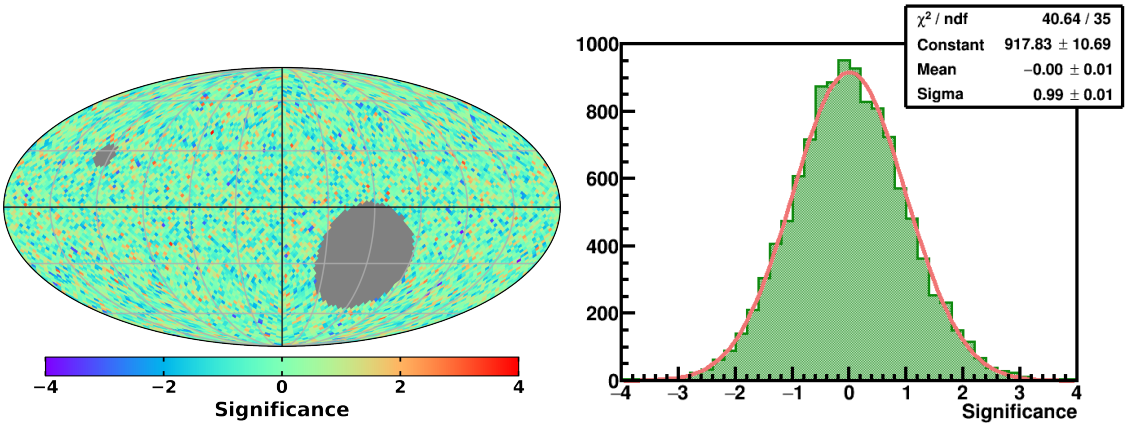

(a) (b)

Figure 4.17: Electron significance skymap (a) and distribution (b) for the energy range $16 < E < 350$ GeV in galactic coordinates.

Results on the Electron Dipole Components in Galactic Coordinates

The measurement of the dipole components and the computation of the dipole amplitude are the relevant quantities for a physical interpretation. Furthermore, since no deviations from isotropy are observed upper limits to the dipole amplitude can be established. This section will present the results on the dipole anisotropy for electrons in galactic coordinates together with a discussion about the statistical and systematic uncertainties on the dipole components.

The statistical uncertainties on the dipole components are associated to the size of the data sample. The systematic uncertainties have different sources:

- **Efficiency Corrections:** The statistical uncertainty of the contributing individual efficiency corrections are propagated. As observed in equation 4.8 two factors are relevant: the η_0 which accounts for the average efficiency and the uncertainty associated to the sample size of the N_{ko} and N_{ok}.
- **Election of Significant Corrections:** It accounts for the effect of the choice of a threshold value in the determination of the significant efficiencies. For this purpose, the threshold value is shifted $\pm$ 0.2 and the difference between both values is taken as a systematic uncertainty.
- **Missing Corrections:** The uncertainty associated to this correction, obtained by means of the matrix transformation from ISS geographical position, is included in the systematic uncertainties.

The sources of the systematic uncertainties do not affect equally each dipole component. For this reason, the *equivalent uncertainty* is defined as

$$\sigma_{eq}^2 = \frac{1}{3}\sum_{k=1}^{3} \sigma_k^2 \tag{4.10}$$

where σ_k is the uncertainty on each dipole component, $k = 1,2,3$ [2].

Figure 4.18a shows the total equivalent systematic uncertainty together with each contribution, where the uncertainty associated with the efficiency and the missing corrections are the dominant ones. In addition, the comparison between the statistical and the systematic uncertainties is shown in figure 4.18b, where it is observed how the statistical uncertainty dominates in the whole energy range.

The three electron dipole components, ρ_{EW}, ρ_{NS} and ρ_{FB} are shown in figure 4.19 as a function

[2] It should be note that the equivalent statistical and total uncertainties will also be computed.

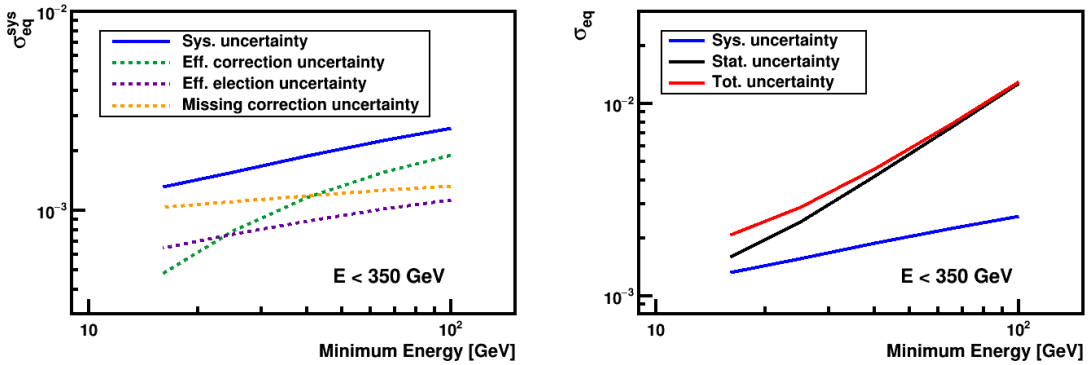

(a) (b)

Figure 4.18: (a) Different contributions to the total equivalent systematic uncertainties (blue solid line): efficiency corrections (green dotted line), efficiency election (purple dotted line), and missing correction (yellow dotted line). (b) Comparison of the statistical, systematic and total equivalent uncertainties on the electron dipole components.

of the minimum energy with the 1 and 2-sigma bands from isotropy, where the statistical and systematic uncertainties are added in quadrature.

The dipole amplitude, figure 4.20a, is computed with the three dipole components and in the lowest energy range, $E_{min} = 16$ GeV, the dipole amplitude is $\delta_M(16GeV) = 0.27\%$.

Results are compatible with isotropy and the 95% C.I. upper limit is established for each energy range (figure 4.20b). For $E_{min} = 16$ GeV the upper limit is $\delta^{95\%}_{UL}(16GeV) = 0.5\%$. The results reported in this section were included in [88].

The numerical results corresponding to the electron dipole anisotropy are presented in the table D.1 from appendix D.2.

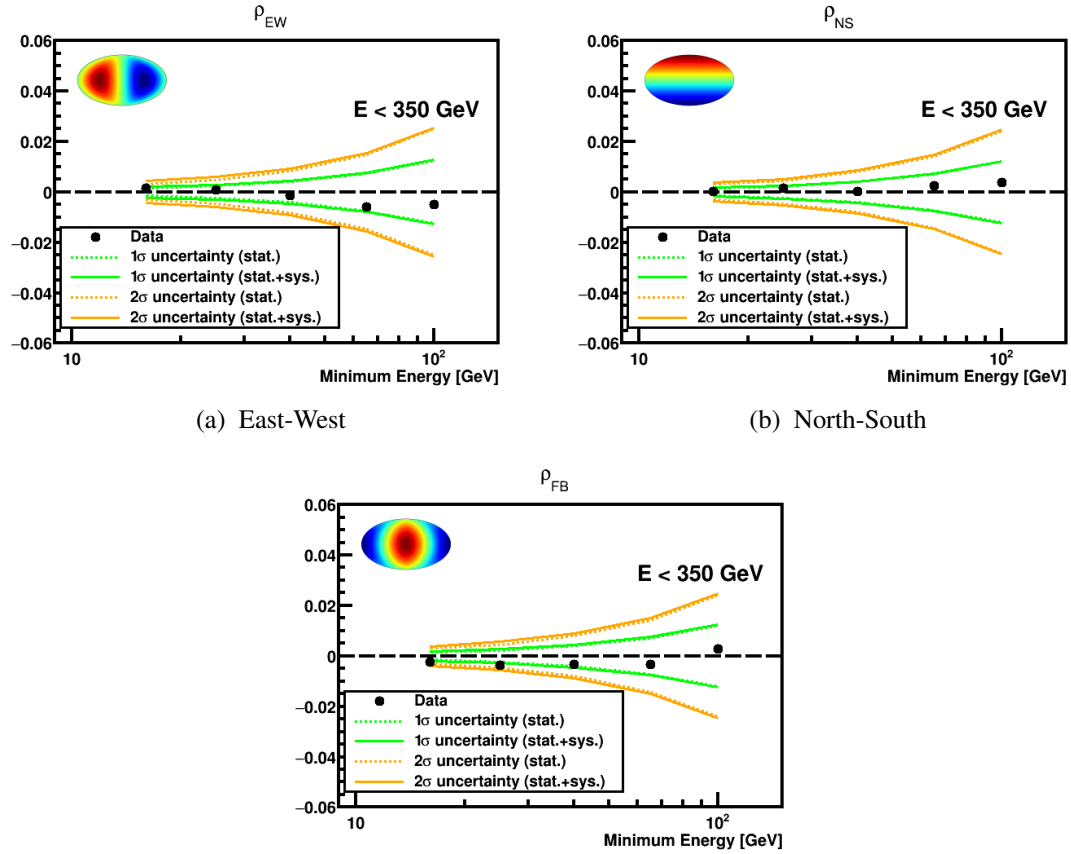

(a) East-West (b) North-South

(c) Forward-Backward

Figure 4.19: Electron dipole components, *EW*, *NS* and *FB* in galactic coordinates where the 1 and 2-sigma deviations from isotropy (green and yellow, respectively) corresponding to the statistical (dotted line) and total (solid line) uncertainties are shown.

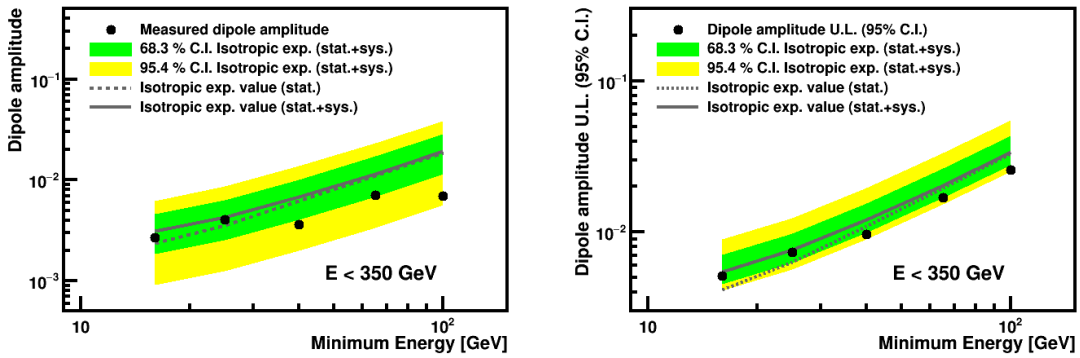

(a) Dipole Amplitude (b) Upper Limit

Figure 4.20: Electron measured dipole amplitude (a) and 95% C.I. upper limit (b) as a function of the minimum energy in galactic coordinates. The 1 and 2-sigma total uncertainty bands are shown in green and yellow respectively. The expected value from isotropy considering the statistical (dotted line) and the statistical + systematic (solid line) uncertainties is also displayed.

4.6.2 Positrons

For positrons, the symmetric response of the detector allows to make use of the electron efficiencies to build the isotropic reference map. Then, the impact of the electron efficiency corrections in the positron sample can be studied by comparing the results from the corrected and uncorrected reference maps. The determination of the multipole components in the positrons follows the same procedure of the electron analysis with the difference that now the sample is not completely pure and the background contamination is included by means of the purity (charge confusion purity) in the binned-likelihood fit, equation 3.41.

Figure 4.21 shows the ρ_{NS} and ρ_{2+0} components in ISS geographical position coordinates where less significant deviations with respect to isotropy are observed due to the limited sample size. Nevertheless, a general improvement is observed in the dipole and, in particular, the quadrupole components when the corrections are applied.

In addition, results for the ρ_{EW} and ρ_{2-2} components in galactic coordinates are shown in figure 4.22. As can be seen, the dipole component is almost unaffected by the efficiency corrections and the quadrupole component suffers a slight change.

In general, positrons in both reference systems are consistent with isotropy within the uncertainties and the electron corrections help to improve the data points when included.

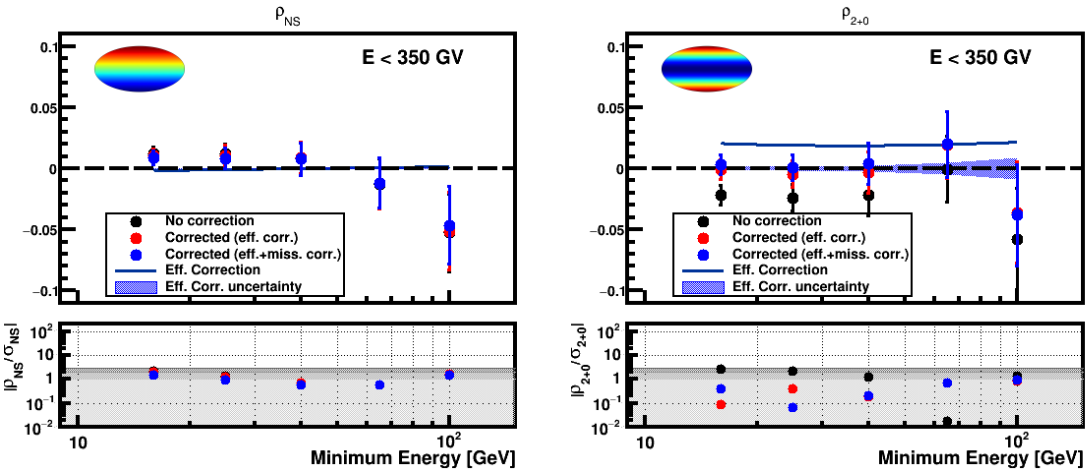

(a) (b)

Figure 4.21: Positron multipole components ρ_{NS} (a) and ρ_{2+0} (b), in ISS geographical position coordinates where no corrections (black dots), efficiency corrections (red dots) and efficiency plus missing corrections (blue dots) are included. The error bars in the dots stand for the statistical uncertainties. Efficiency corrections are shown as a blue line with its uncertainty displayed as a blue band. Finally, in the bottom panel the absolute deviations from isotropy are evaluated in terms of standard deviations.

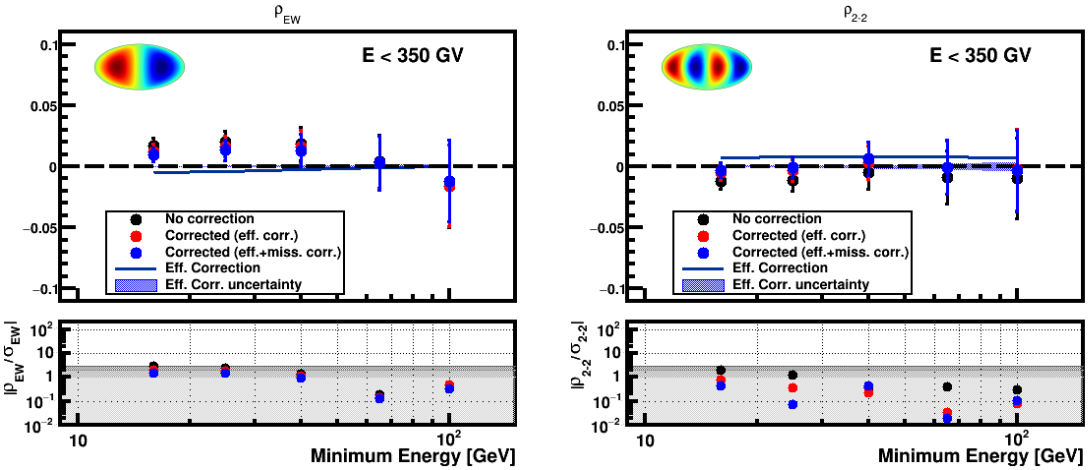

(a) (b)

Figure 4.22: Positron multipole components ρ_{EW} (a) and ρ_{2-2} (b), in galactic coordinates where no corrections (black dots), efficiency corrections (red dots) and efficiency plus missing corrections (blue dots) are included. The error bars in the dots stand for the statistical uncertainties. Efficiency corrections are shown as a blue line with its uncertainty displayed as a blue band. Finally, in the bottom panel the absolute deviations from isotropy are evaluated in terms of standard deviations.

Results on the Positron Dipole Components in Galactic Coordinates

For positrons, the presence of the background reduces the statistical power of the measurement and, therefore increases the statistical uncertainties. Figure 4.23a shows the comparison between the equivalent statistical uncertainty with and without introducing the background, the effect is more evident at high energies where the charge confused electrons become more important. The contribution of the systematic uncertainty on positrons to the total one is less significant than in the case of electrons due to the much smaller sample size. The comparison between the equivalent systematic, statistical, and total uncertainties for the positron dipole components is shown in figure 4.23b.

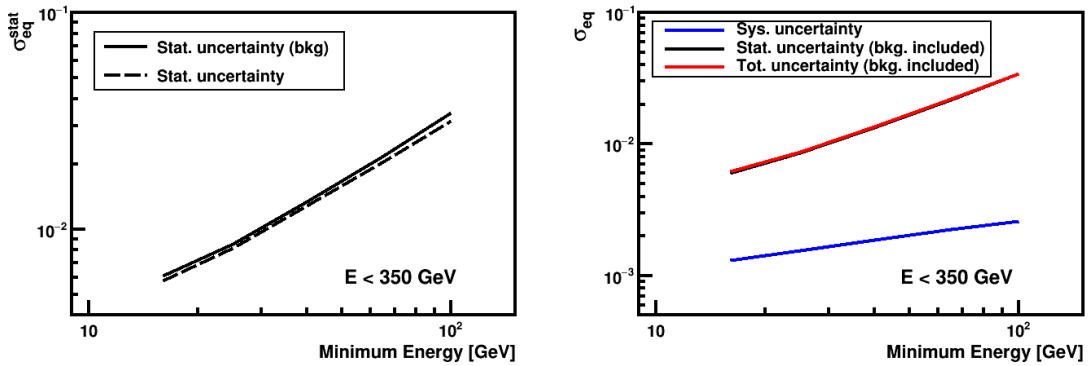

(a) (b)

Figure 4.23: (a) Positron statistical uncertainties assuming that the sample is pure (dashed line) and it has background (solid line). (b) Comparison of the statistical, systematic and total equivalent uncertainties on the positron dipole components.

The three dipole components, ρ_{EW}, ρ_{NS} and ρ_{FB} as a function of the minimum energy are shown in figure 4.24, where no deviations from isotropy within the uncertainties are observed.

The results of the dipole components are used to compute the dipole amplitude at the different energy ranges, figure 4.25a. In the lowest energy range, $E_{min} = 16$ GeV the measured dipole amplitude is $\delta_M(16GeV) = 1.18\%$.

Finally, since the results are consistent with isotropy the 95% C.I. upper limits on the dipole amplitude can be established, figure 4.25b, with a value of $\delta_{UL}^{95\%C.I.}(16GeV) = 1.9\%$. The results reported in this section were included in [89].

The numerical results corresponding to the positron dipole anisotropy are presented in the table D.3 from appendix D.2.

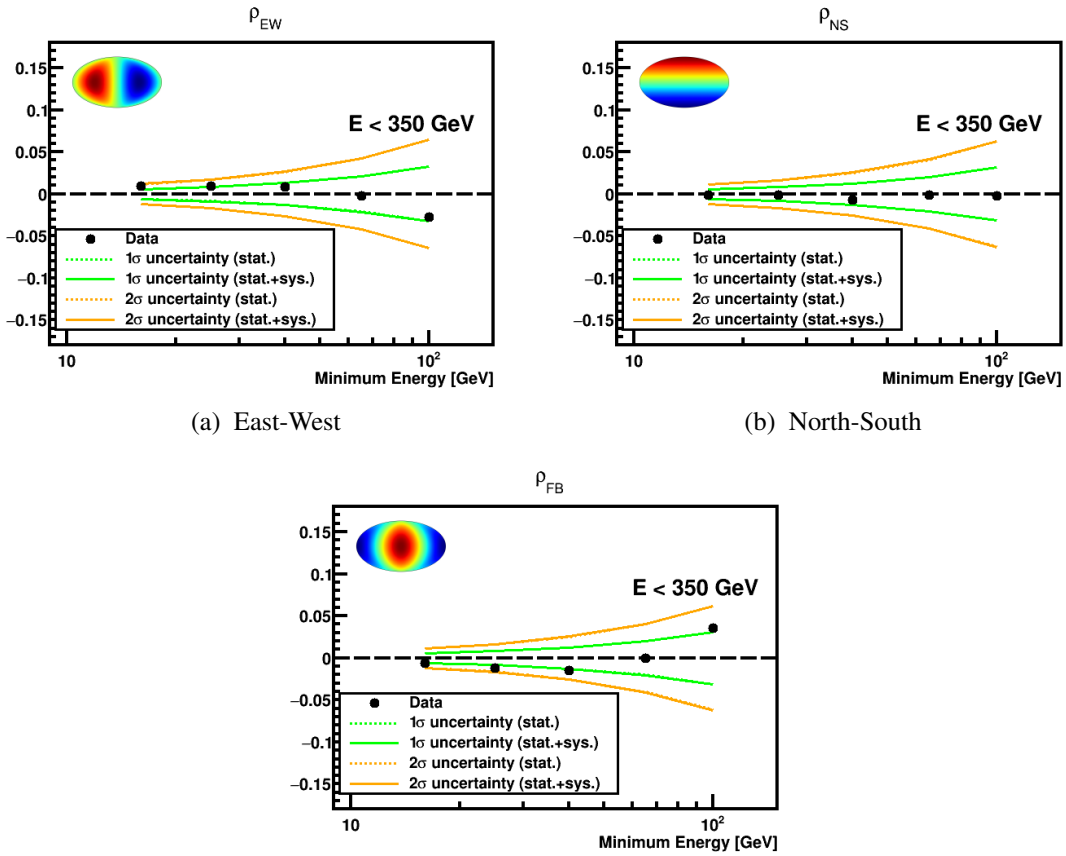

(a) East-West

(b) North-South

(c) Forward-Backward

Figure 4.24: Positron dipole components, EW, NS and FB in galactic coordinates where the 1 and 2-sigma deviations from isotropy (green and yellow, respectively) corresponding to the statistical (dotted line) and total (solid line) uncertainties are shown.

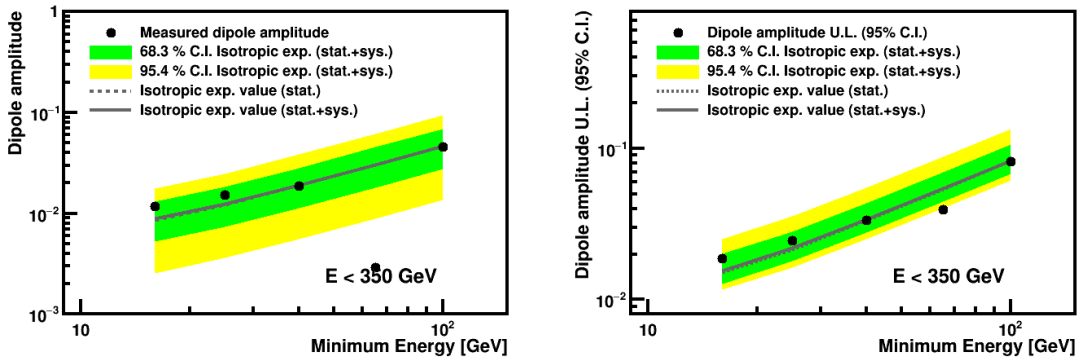

(a) (b)

Figure 4.25: Positron measured dipole amplitude (a) and 95% C.I. upper limit (b) as a function of the minimum energy in galactic coordinates. The 1 and 2-sigma total uncertainty bands are shown in green and yellow respectively. The expected value from isotropy considering the statistical (dotted line) and the statistical + systematic (solid line) uncertainties is also displayed.

4.7 Optimization of the Positron and Electron Anisotropy Analysis

The results presented in the previous section were obtained by means of a cut-based selection where the lepton identification was performed with cuts on the $ECAL_{BDT}$, the good energy-momentum matching, and the TRD_{Lkh} estimator. This selection provides a pure sample of events but limits the available statistics. On the one hand, the cut in the TRD_{Lkh} has a limited efficiency on the positron sample and, on the other hand, the energy range is constrained up to 350 GeV where the TRD_{Lkh} efficiency starts decreasing and the proton background begins to be non-negligible.

The analysis can be optimized by using a template fit method based on the TRD_{Lkh} estimator to separate electrons and positrons from the proton background. This procedure allows to recover the loss of statistics when the TRD_{Lkh} cut is applied and, also, to increase the energy range of the analysis.

In addition, to maximize the statistics in the low energy range some variations in the selection criteria presented in 4.1 are included. In particular, a looser cut in the good energy-momentum matching is applied and the safety factor in the geomagnetic cutoff is removed.

The data sample is increased from 6.5 years to 8.5 years of data taking with AMS-02, which covers the time between May 2011 and November 2019. The exposure time increments from 1.49×10^8 s to 1.82×10^8 s, which amounts to $\sim 22\%$ more of statistics.

Technically, the most relevant modification introduced by this optimization arises from the template fit and its implementation in the directionality studies. This section will cover: dependences of the templates, template fit method, sample of analysis and determination of the anisotropy.

4.7.1 TRD Templates

The TRD templates are obtained directly on data applying a tighter cut on the $ECAL_{BDT}$ for either the signal ($ECAL_{BDT} > 0.95$) or background ($ECAL_{BDT} < -0.95$) contributions. Since the response of the TRD to electrons and positrons is identical, the templates obtained on electrons can be applied to positrons. This definition ensures a high purity for the templates and maximizes the statistics.

The TRD response may depend on the energy, geographical position, and direction of the particle in the AMS field of view. These dependences are specially relevant for the anisotropy studies and this section will cover a detailed descriptions of their variation.

Energy Dependences of the TRD Templates

The energy dependence of the TRD_{Lkh} estimator for two energy bins (one in the low energy part $16.00 < E_1 < 16.92$ and the other one for intermediate energies $80.62 < E_2 < 89.79$) is shown in figure 4.26 for electrons and protons. The results show similar behavior for the electron template whereas a different one for the protons, which can be better quantified with the mean and the RMS of the distributions, as displayed in figures 4.26a and 4.26b.

The study can be extended to other energies by retrieving the mean and RMS value of the distributions in each energy bin. The results are presented in the figure 4.27, where electrons show no variation with respect to the energy and the protons a decreasing trend in the mean value [3].

Hereinafter, in order to maximize the statistics of the electron templates and, since there is no energy dependence, the integrated template from 16 to 100 GeV is used. In the case of protons, since they strongly depend on the energy, individual templates for each energy bin have to be used.

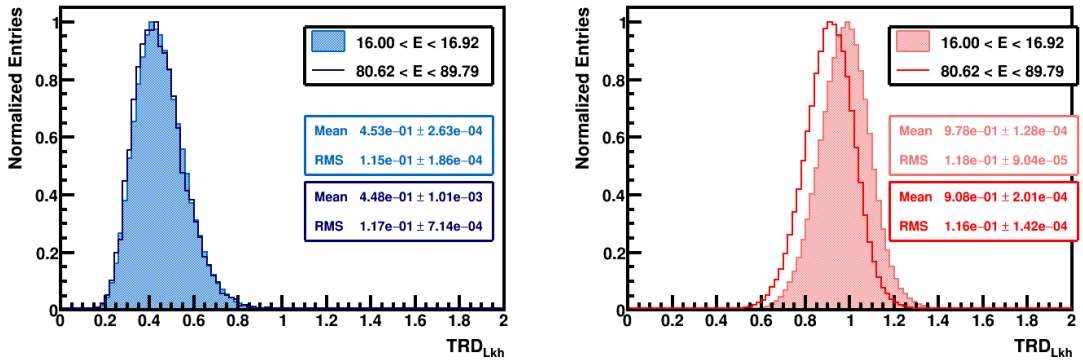

(a) Electron Templates (b) Proton Templates

Figure 4.26: Electron (a) and proton (b) TRD_{Lkh} templates for two different energy bins ($16.00 < E_1 < 16.92$ and $80.62 < E_2 < 89.79$). The TRD templates show a similar behavior for electrons and a variation with the energy for protons.

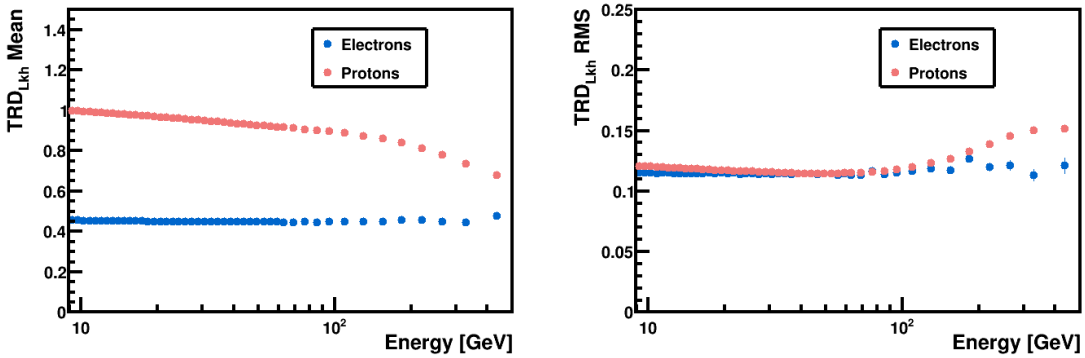

(a) (b)

Figure 4.27: Mean (a) and RMS (b) values of the electrons (blue) and protons (red) TRD_{Lkh} distributions as a function of the energy. For electrons, the mean and RMS values remain almost constant. For protons, a strong dependence with the energy of the mean value is observed.

[3] The shift of the proton TRD template to lower values of energy produces the increase of the proton background at high energies with the cut-based analysis.

Directional Dependences of the TRD Templates

The measurement of the directionality requires to understand additional template dependences in order to ensure the stability of the template response with respect to the variables relevant for the anisotropy studies.

Geomagnetic Colatitude Dependences

In the one-dimensional approach, the raw rate and efficiencies were investigated as a function of the geomagnetic colatitude and this allowed to have a first estimation of the efficiency corrections for the dipole and quadrupole components. Since this kind of study provides valuable information before computing the spherical harmonic analysis, a similar study of the variation of the templates with respect to $cos(\theta_M)$ has been performed.

The electron and proton templates with respect to $cos(\theta_M)$, figures 4.28a and 4.28b respectively, are shown for two different ranges in geomagnetic colatitudes (one bin at high geomagnetic colatitudes, $-0.8 < cos(\theta_M) < -0.7$, and the other in the geomagnetic equator, $0 < cos(\theta_M) < 0.1$). As mentioned above, the integrated templates from $16 < E < 100$ GeV are used for electrons and the individual ones for protons (for this example the energy interval $16 < E < 16.92$ GeV for protons is presented). The results show similar behavior for both species, as can be seen in the mean and RMS values of the distributions.

Similarly, the study can be extended for each geomagnetic colatitude range by retrieving the mean and RMS values from each distribution. Figures 4.29a and 4.29b show the results, where an additional bin at intermediate energies has been included for protons, $80.62 < E < 89.79$ GeV, in order to explore possible correlations between the energy and $cos(\theta_M)$.

In conclusion, the electron and proton templates do not show any visible dependence with the geomagnetic colatitude and, therefore, the same template will be applied when these studies are performed.

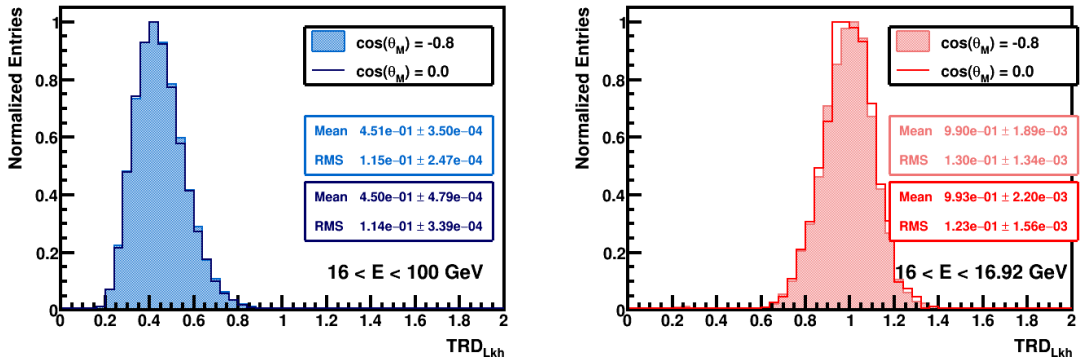

(a) Electron Templates (b) Proton Templates

Figure 4.28: Electron (a) and proton (b) TRD_{Lkh} templates for two different geomagnetic locations ($-0.8 < cos(\theta_M) < -0.7$ and $0 < cos(\theta_M) < 0.1$), where both show a similar behavior.

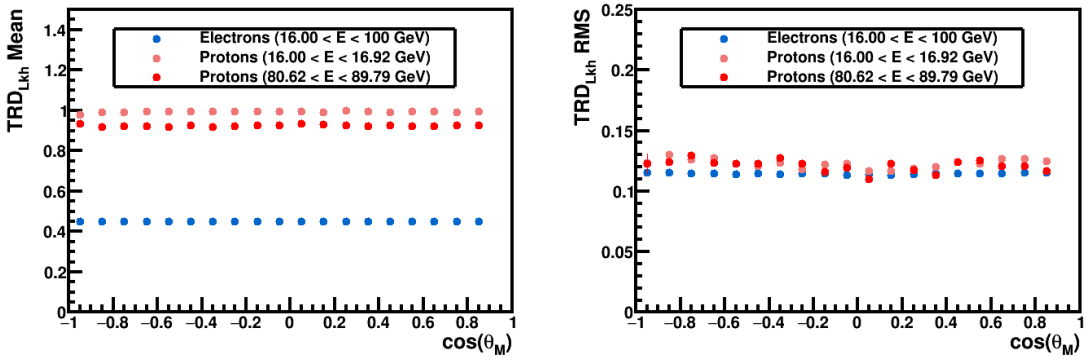

(a) (b)

Figure 4.29: Mean (a) and RMS (b) values of the electrons (blue) and protons (red for $16.00 < E_1 < 16.92$ and darker red for $80.62 < E_2 < 89.79$) TRD_{Lkh} distributions as a function of the cosine of the geomagnetic colatitude. No dependence with respect to $cos(\theta_M)$ is observed, although the energy dependence of protons is clearly seen.

Acceptance Dependences

To asses the possible variations of the TRD response with respect to the local coordinates of the detector (θ_d, ϕ_d), electron and proton templates are constructed for each acceptance pixel. Due to the limited statistics of the templates, the dependences are investigated with a reduced size parameter $N_{side} = 2$ instead of the standard $N_{side} = 32$.

As an example, figure 4.30 shows the HEALPix pixelization for $N_{side} = 2$, where only the 12 first pixels correspond to the AMS-02 field of view of 25º.

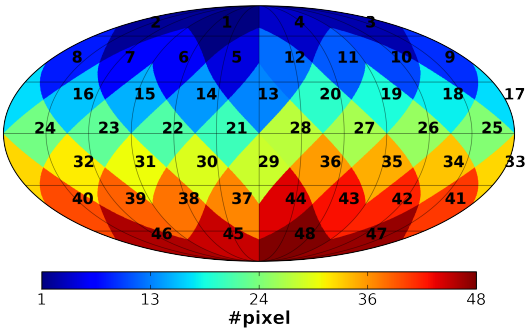

Figure 4.30: HEALPix scheme pixelization for $N_{side} = 2$, where the 12 first pixels correspond to the AMS-02 acceptance within an opening angle of 25º with respect to the AMS-zenith.

The electron and proton templates are shown in figures 4.31a and 4.31b for two different acceptance bins. The first one is closed to nearly vertical trajectories (acceptance bin = 1), and the second one corresponds to the local coordinates $(\theta_g, \phi_g) = (23º, 337º)$ (acceptance bin = 8). Again, since the electron templates did not depend on the energy the integrated distribution from $16 < E < 100$ GeV is used, whereas for protons a template for each energy range has to be used, in the example the energy bin 16.00-16.92 GeV is shown. The results show equivalent distributions for both.

Finally, the mean and RMS values for each acceptance bin are shown in figures 4.32a and 4.32b. No significant differences are observed for the electron and proton templates. The same template for all the acceptance pixels will be used in this work.

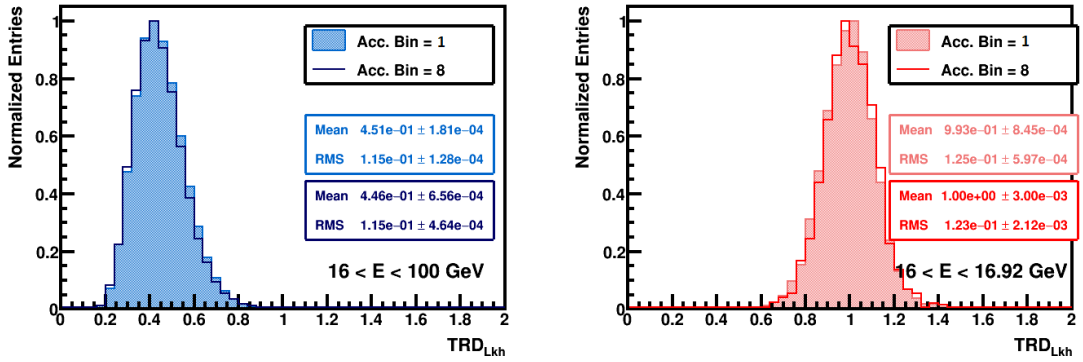

(a) Electron Templates (b) Proton Templates

Figure 4.31: Electron (a) and proton (b) TRD_{Lkh} templates for two different acceptance pixels of the AMS-02 field of view for an $N_{side} = 2$, one close to nearly vertical trajectories (acceptance bin = 1) and the other one corresponds to the local coordinates $(\theta_g, \phi_g) = (23°, 337°)$ (acceptance bin = 8). No significant differences are observed in any of the distributions.

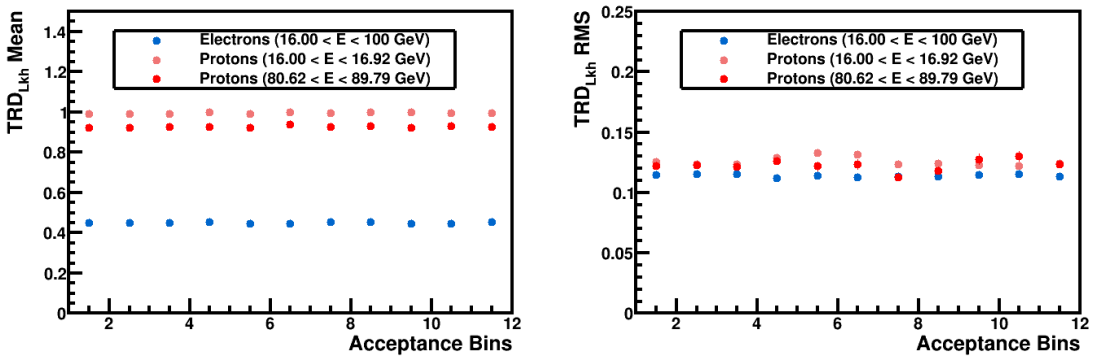

(a) (b)

Figure 4.32: Mean (a) and RMS (b) values of the electrons (blue) and protons (red for $16.00 < E_1 < 16.92$ and darker red for $80.62 < E_2 < 89.79$) TRD_{Lkh} distributions as a function of the acceptance bins of the AMS-02 field view for an $N_{side} = 2$. No dependence with respect to the acceptance bins is observed, although the energy dependence of the protons is clearly seen.

4.7.2 Template Fit Method

The number of electrons and positrons are extracted from the background of protons by means of a *template fit* method performed on the TRD_{Lkh} distribution. The procedure is based on a binned-likelihood where the electron and proton templates are used to retrieve the fraction of signal and background on the data sample.

The strategy to establish the signal and background contributions follows from the studies in the previous section where the template dependences were investigated. On the one hand, the signal templates will be the integrated electron templates from $16 < E < 100$ GeV and, on the other hand, the background templates will be the individual proton templates for each energy range.

An example of the template fit is shown in figure 4.33 for electrons and positrons in the energy range $80.62 < E < 89.79$ GeV. The procedure provides a complete description of the signal and background contributions, especially in the positron sample where a non-negligible contribution of the proton background is clearly observed.

The template fit provides the estimated number of signal events and its associated error. Due to the finite capabilities of the TRD there is an overlap region in the TRD_{Lkh} distribution where the contribution of the background cannot be neglected. As a consequence, the uncertainty on the estimated number of events is larger than the pure Poissonian error and the statistical power of the signal sample is diluted accordingly.

For the anisotropy analysis the signal purity associated to the proton background, p_{pr}, has to be included. It is computed scaling the electron and proton templates with the number of signal and background events obtained with the template fit. Figure 4.34 shows the purity associated to the proton background for positrons and electrons in the energy range $80.62 < E < 89.79$ GeV. As can be seen, positron events with $TRD_{Lkh} > 0.6$ have a non-negligible proton contamination whereas the electrons show a purity of almost 100%.

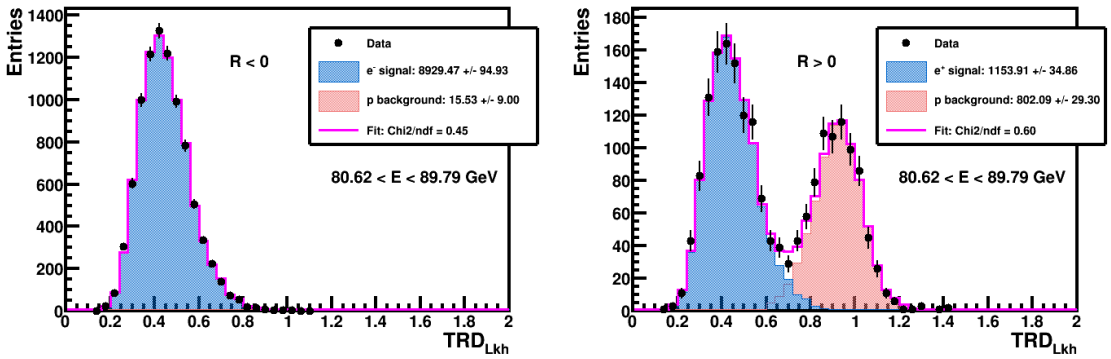

(a) Electron Template Fit (b) Positron Template Fit

Figure 4.33: Template fit for electrons (a) and positrons (b) for the energy range $80.62 < E < 89.79$ GeV. The data sample (black points) is fitted (pink line) with the contribution of a signal (blue line) and a background (red line) templates. As a result, the fraction of signal and background events is obtained.

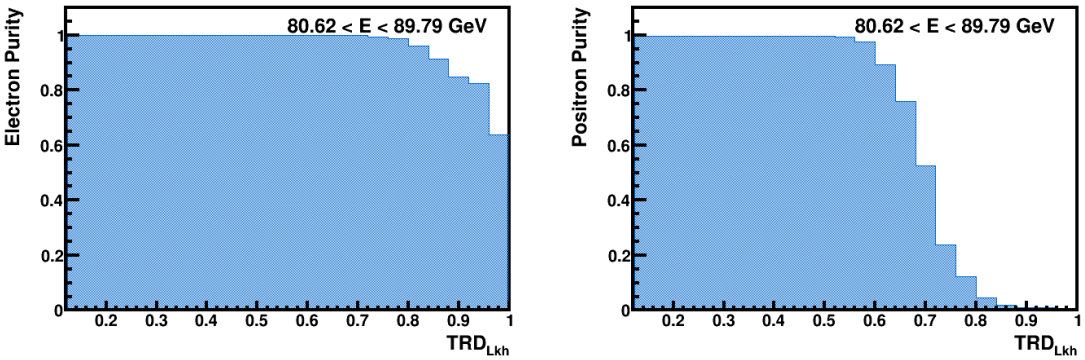

(a) Electron Purity (b) Positron Purity

Figure 4.34: Electron (a) and positron (b) purity associated to the proton background for the TRD_{Lkh} distribution in the energy range $80.62 < E < 89.79$ GeV. As seen can be seen, positron events with $TRD_{Lkh} > 0.6$ have a non-negligible proton contamination whereas the electrons show a purity of almost 100%. Figures are displayed up to values ($TRD_{Lkh} = 1$) where there is a non-negligible contribution of the background.

4.7.3 Sample of Analysis

Technically, the template fit method constitutes the most relevant modification in the lepton selection. For this reason, a detailed study of the template dependences relevant for the anisotropy studies and of the fitting procedure has been presented. In addition, as mentioned in section 4.7, the statistics can be further increased in the low energy part by means of a reduction in the cutoff safety factor and an optimization of the $E/|p|$ cut.

The effect of the cutoff reduction is studied by comparing the rate of events for the optimized safety factor (SF = 1) and the previous one (SF = 1.2). Results are presented in figure 4.35a, where no differences are observed and, therefore, no relevant impact in the measurement is expected. As a consequence of the reduced safety factor, an increase of up to 30% in statistics for energies between $16 < E < 30$ GeV is obtained, as can be seen in the comparison of the electron number of events and their ratio (figure 4.35b).

On the other hand, the tight cut in the good energy-momentum matching, $0.65 < E/|p| < 5$, mainly contributes to reduce the charge confusion background, specially at high energies, but limits the available statistics at low energies. In order to quantify the differences in the charge confusion background with the looser condition, $E/|p| > 0.65$, the positron purity for both cuts is compared (figure 4.36a). Event though the purity is slightly lower with the looser cut, the gain in the effective statistics, figure 4.36b, compensates the modification of the cut.

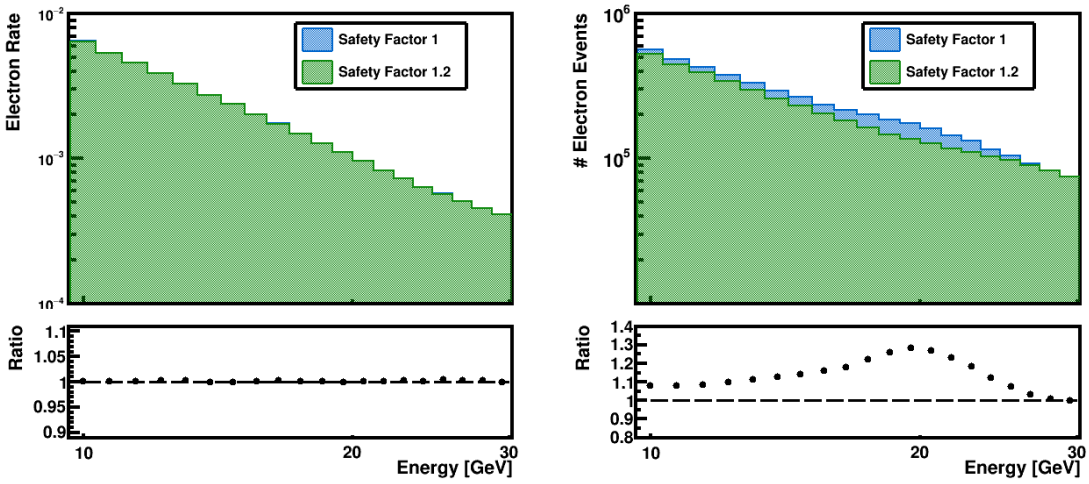

(a) (b)

Figure 4.35: Comparison of the electron rate (a) and number of events (b) for a safety factor 1 and 1.2 (upper panels) together with the ratios (lower panels).

The number of electron and positron events obtained with the optimized analysis and the standard analysis, both with charge confusion background subtracted, are compared in tables 4.3 and 4.4 respectively. The dilution factor is also displayed, equation 3.45, to quantify the reduction of the sensitivity due to the presence of the background in the samples. In any case, the dilution factor is below 10% and becomes more relevant in the highest energy ranges. The total increase in the statistics is included in the tables, which is only partially due to the extended period of observation ($\sim$ 22%). The outcome of the optimization described in 4.7 accounts for most of the statistics increase.

As a crosscheck of the results obtained figure 4.37 shows the positron fraction with the optimized analysis together with the AMS-02 latest publication corresponding to 6.5 years of data taking. The positron fraction is consistent with the published results up to 500 GeV and, therefore, the range of energy of the analysis can be increased. As an illustration, the results obtained in section 4.4 in this

extended energy range are also displayed.

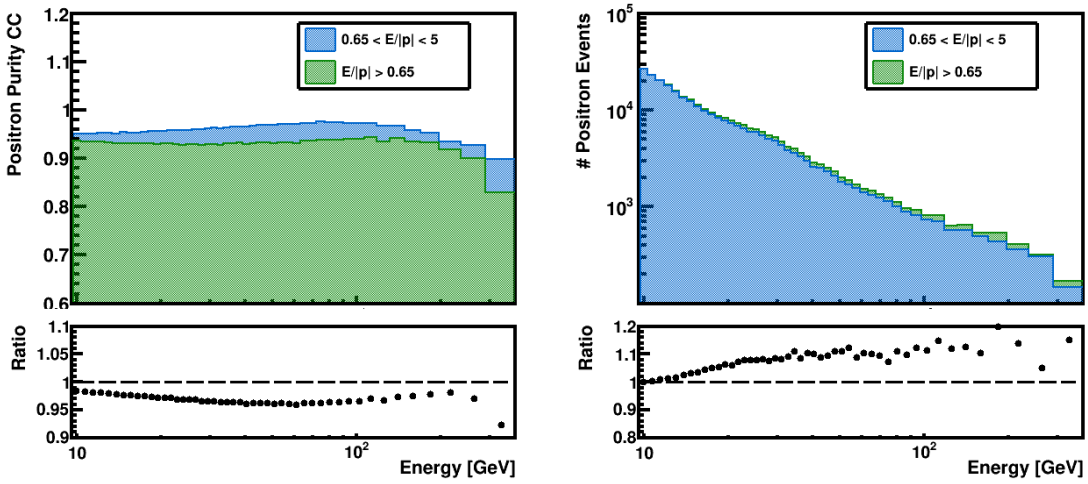

(a) (b)

Figure 4.36: Comparison of the positron purity associated to the charge confusion (a) and corrected number of positrons events (b) for a tight, $0.65 < E/|p| < 5$, and a loose, $E/|p| > 0.65$, cut in the good energy-momentum matching (upper panels) together with their ratios (lower panels).

	Optimized Analysis (8.5 Years)		**Standard Analysis (6.5 Years)**		**Stat. Increase (%)**
E_{min} (GeV)	$(N_{e^-}^{corr})(\times 10^4)$	Dilution	$(N_{e^-}^{corr})(\times 10^4)$	Dilution	
16	228.60 ± 1.52	1.00	131.43 ± 1.15	1.00	1.75
25	90.61 ± 0.96	1.01	57.81 ± 0.76	1.00	1.56
40	30.25 ± 0.56	1.01	19.32 ± 0.44	1.00	1.56
65	9.52 ± 0.31	1.01	6.07 ± 0.25	1.00	1.56
100	3.32 ± 0.19	1.02	2.14 ± 0.15	1.00	1.55

Table 4.3: Comparison of the number of electron events for the optimized and standard analysis with the charge confusion background subtracted in the 5 cumulative energy ranges. The dilution factor is also displayed to quantify the reduction of the sensitivity due to the presence of the background. In addition, the total statistics increase is presented.

	Optimized Analysis (8.5 Years)		**Standard Analysis (6.5 Years)**		**Stat. Increase (%)**
E_{min} (GeV)	$(N_{e^+}^{corr})(\times 10^3)$	Dilution	$(N_{e^+}^{corr})(\times 10^3)$	Dilution	
16	169.62 ± 0.44	1.06	95.46 ± 0.32	1.02	1.78
25	78.40 ± 0.30	1.06	48.65 ± 0.23	1.02	1.61
40	31.74 ± 0.19	1.07	20.08 ± 0.14	1.02	1.58
65	12.27 ± 0.12	1.08	7.87 ± 0.09	1.03	1.56
100	5.11 ± 0.08	1.10	3.37 ± 0.06	1.04	1.52

Table 4.4: Comparison of the number of positron events for the optimized and standard analysis with the charge confusion background subtracted in the 5 cumulative energy ranges. The dilution factor is also displayed to quantify the reduction of the sensitivity due to the presence of the background. In addition, the total statistics increase is presented.

In conclusion, the selection performed with the template fit method provides an efficient separation of the positrons and electrons from the proton background. This has two main implications in the anisotropy analysis: the statistics increases due to the inclusion of the events for $TRD_{Lkh} > 0.6$ and the energy range of analysis can be extended up to $E < 500$ GeV.

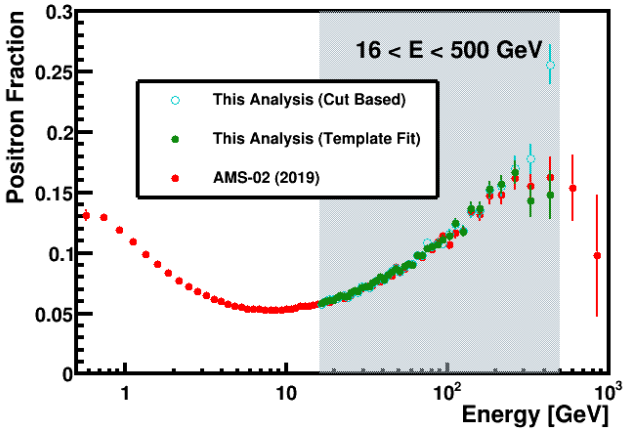

Figure 4.37: Comparison of the positron fraction obtained with the optimized analysis with the cut based selection and the AMS-02 latest publication [88].

4.7.4 Determination of the Anisotropy

The measurement of the directionality with the cut based selection was performed by including the information from the skymap of measured events and the exposure for each bin of acceptance r, energy interval j, and pixel of the sky s into a binned-likelihood, equation 3.41. The maximization of the function provided the coefficients of the expansion and, therefore, the amplitude of the anisotropy.

In the optimized analysis, the skymap of measured events is computed by retrieving the number of signal events from the template fit. As mentioned before, the sensitivity of the analysis is reduced by the presence of the background for each bin in the TRD_{Lkh} distribution. Since the binned-likelihood does not include this contribution a new formalism has to be derived to obtain the coefficients of the expansion. It can be summarized in the following steps:

1. Individual TRD_{Lkh} distributions are obtained for each acceptance pixel r, energy interval j, and pixel of the sky s in the coordinate system of the analysis.
2. The template fit method applied to each TRD_{Lkh} distributions provides the number of signal and background events, and the purity distributions $(p_{pr})^r_{j,s,h}$, which are defined as

$$(p_{pr})^r_{j,s,h} = \frac{(n_{sig})^r_{j,s,h}}{\left((n_{sig})_{j,s,h^r} + (n_{bkg})^r_{j,s,h}\right)} \tag{4.11}$$

3. Each event events is included in the likelihood with its corresponding purity from the template fit $(p_{pr})^r_{j,s,h}$ and charge confusion $(p_{CC})_j$ according to:

$$log\mathcal{L} = \sum_{r,j,s,h} n^r_{j,s,h}\, log\left[\frac{(1 + p^r_{j,s,h}\, \Sigma_{\ell=1} \Sigma^{m=+\ell}_{m=-\ell} a_{\ell m} Y^s_{\ell m}) T^r_{j,s}\, \varepsilon_{j,s}}{\mathcal{N}^r_j}\right] \tag{4.12}$$

where $p^r_{j,s,h} = (p_{CC})_j \, (p_{pr})^r_{j,s,h}$ is the total purity [4]. The normalization factor is written as:

$$\mathcal{N}^r_j = \sum_{s,h} \left(1 + p^r_{j,s,h} \sum_{\ell=1} \sum_{m=-\ell}^{m=+\ell} a_{\ell m} Y^s_{\ell m} \right) T^r_{j,s} \, \varepsilon^r_{j,s} \tag{4.13}$$

4. The maximization of this function provides the coefficients of the expansion into spherical harmonics and, thus, the degree of the anisotropy.

This procedure slightly modifies the binned-likelihood, since each bin h in the TRD_{Lkh} distribution of measured events has an associated purity, and ensures that the contamination is correctly accounted in the analysis. Nevertheless, since the computation of the purity depends on the statistics in each bin (r, j, s), in order to avoid high statistical fluctuations the HEALPix size parameter is decreased to $N_{side} = 2$ (as in section 4.7.1).

4.8 Results of the Optimized Analysis on the Electron and Positron Anisotropy

Following the same steps presented in section 4.6, the impact of the efficiency corrections in the analysis can be first understood using the one-dimensional approach. The computation of the efficiencies and the choice of the significant ones is calculated as in section 4.5, with the difference that now the TRD identification efficiency is not included.

The relative variation of the raw rate and the total efficiency as a function of the geomagnetic colatitude for $16 < E < 500$ GeV is shown in figure 4.38a. The efficiency dependences provides a good description of the drop at high latitudes. This can be better observed in figure 4.38b where the raw and corrected rates are presented.

The impact of the efficiency corrections in the ρ_{NS} and ρ_{2+0} components (the ones that transform into galactic coordinates) in ISS geographical position coordinates is presented in figure 4.39. Significant deviations are observed, especially in the quadrupole component, which are almost fully accounted by the efficiencies.

The results from the one-dimensional approach and the spherical harmonic analysis show a better determination of the efficiency variations in geographical coordinates with respect to the standard analysis [5]. Therefore, in contrast to section 4.6 the inclusion of the missing corrections is not needed.

Finally, figures 4.40 and 4.41 show the ρ_{EW} and ρ_{2-2} in galactic coordinates, which receive the biggest contribution from ISS geographical position coordinates, for electrons and positrons, respectively. In both cases, the dipole and quadrupole components are consistent with isotropy after applying the efficiency corrections.

[4] It should be noted that only the intervals with purities $p^r_{j,s,h} > 0.1$ are included in the likelihood in order to avoid the inclusion of events in the tails arising from the proton distribution.

[5] When compared to the standard analysis the raw rate as a function of the geomagnetic colatitude presents a reduced dependence.

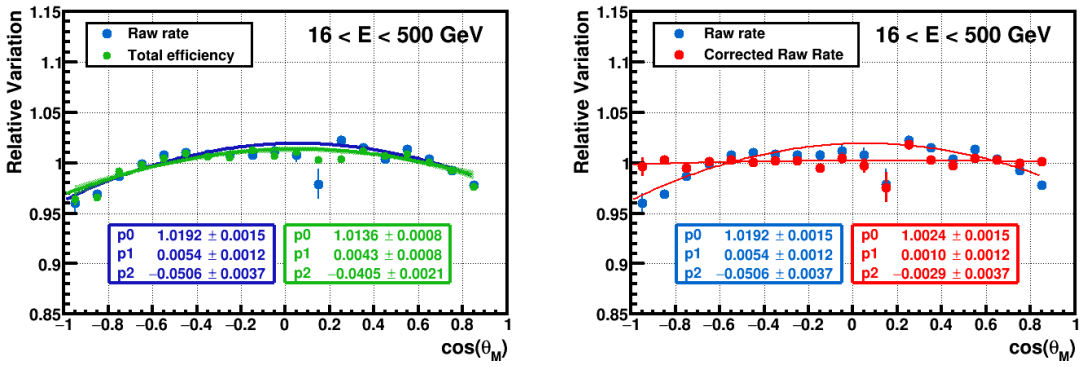

(a) (b)

Figure 4.38: Relative variation of the electron raw rate (blue) together with total efficiency (green) as a function of the geomagnetic colatitude (a) and corrected raw rate (b) for the energy range $16 < E < 500$ GeV. A drop at high latitudes is observed in both distributions which is corrected by the efficiency variation.

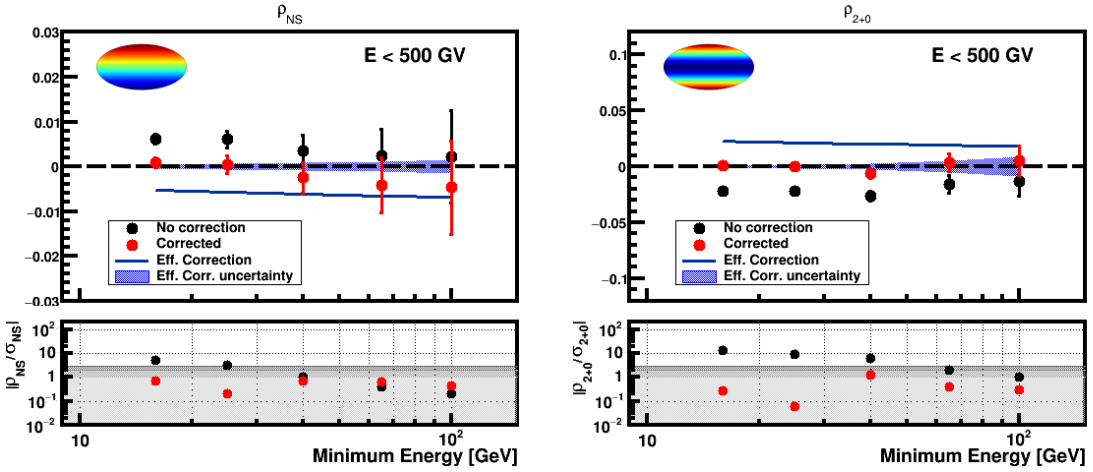

(a) (b)

Figure 4.39: Electron multipole components corresponding to the North-South direction, ρ_{NS} (a) and ρ_{2+0} (b), in ISS geographical position coordinates where no corrections (black dots), and efficiency corrections (red dots) are included. The error bars in the dots stand for the statistical uncertainties. Efficiency corrections are shown as a blue line with its uncertainty displayed as a blue band. Finally, in the bottom panel the deviations from isotropy are evaluated in terms of standard deviations.

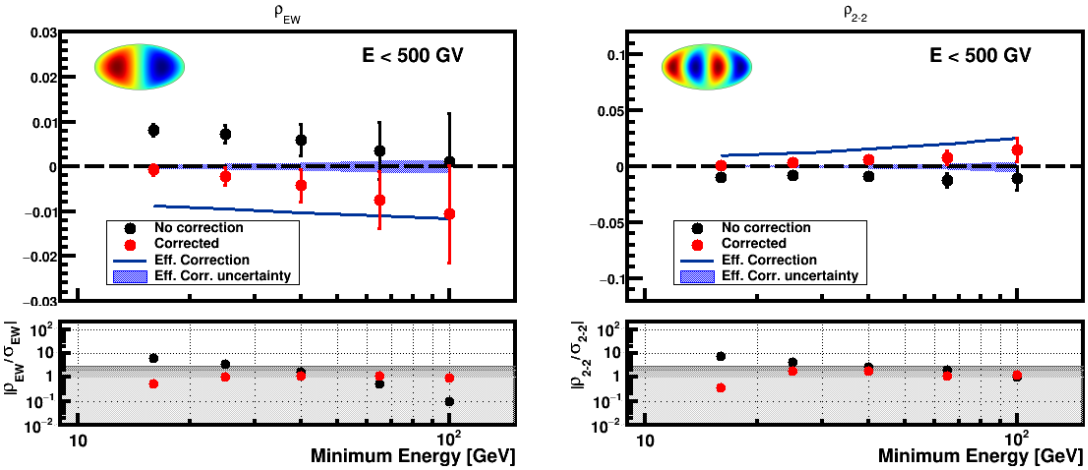

(a) (b)

Figure 4.40: Electron multipole components ρ_{EW} (a) and ρ_{2-2} (b), in galactic coordinates where no corrections (black dots), and efficiency corrections (red dots) are included. The error bars in the dots stand for the statistical uncertainties. Efficiency corrections are shown as a blue line with its uncertainty displayed as a blue band. Finally, in the bottom panel the deviations from isotropy are evaluated in terms of standard deviations.

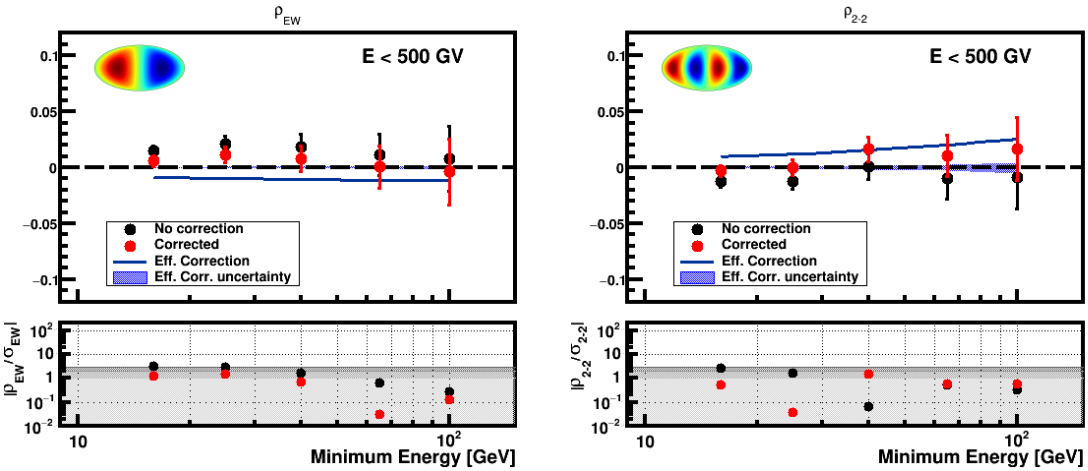

(a) (b)

Figure 4.41: Positron multipole components ρ_{EW} (a) and ρ_{2-2} (b), in galactic coordinates where no corrections (black dots), and efficiency corrections (red dots) are included. The error bars in the dots stand for the statistical uncertainties. Efficiency corrections are shown as a blue line with its uncertainty displayed as a blue band. Finally, in the bottom panel the deviations from isotropy are evaluated in terms of the sigmas.

Results on the Electron and Positron Dipole Components in Galactic Coordinates

The determination of the electron and positron corrected dipole components together with their uncertainties follows the same procedure described for the cut-based analysis (see section 4.6.1). For this reason, only the final results are presented in this section.

The one-dimensional and spherical harmonic studies of the anisotropy in geographical coor-

dinates show that no missing corrections are needed to completely correct the electrons with the template fit. Therefore, the absence of these corrections will reduce the total systematic uncertainty at low energies with respect to the standard analysis.

The total equivalent uncertainty (equation 4.10) together with the systematic and statistical errors for the electrons and positrons are shown in figures 4.42a and 4.42b respectively, where the systematic for the latter is identical since the efficiency corrections applied are the same. Both measurements are dominated by the statistical uncertainties in the entire energy range.

The three dipole components, ρ_{EW}, ρ_{NS} and ρ_{FB} for electrons and positrons are shown in figures 4.43 and 4.44 for the different energy ranges with the 1 and 2 sigma deviations corresponding to the statistical and the statistical plus systematic uncertainties.

The dipole amplitude is computed using the three dipole components as a function of the minimum energy, figures 4.45a and 4.45b. In particular, in the lowest energy range, $E_{min} = 16$ GeV, the electron and positron dipole amplitudes are $\delta_M^{e^-}(16GeV) = 0.21\%$ and $\delta_M^{e^+}(16GeV) = 1.13\%$.

Since the results are consistent with isotropy the 95% C.I. upper limits on the dipole amplitude can be established, figures 4.46a and 4.46b. In the lowest energy range, the upper limits for electrons and positrons are $(\delta_{UL}^{95\%})^{e^-}(16GeV) = 0.37\%$ and $(\delta_{UL}^{95\%})^{e^+}(16GeV) = 1.70\%$.

The numerical results corresponding to the electron and positron dipole anisotropies are presented in the tables D.2 and D.4 from appendix D.2, respectively.

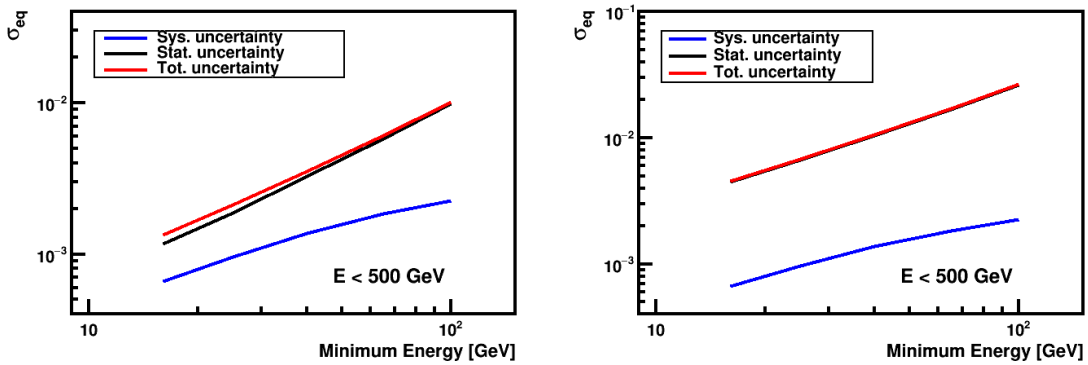

(a) (b)

Figure 4.42: Comparison of the statistical, systematic and total equivalent uncertainties on the electron (a) and positron (b) dipole components. The measurement is dominated by the statistical errors in the entire energy range.

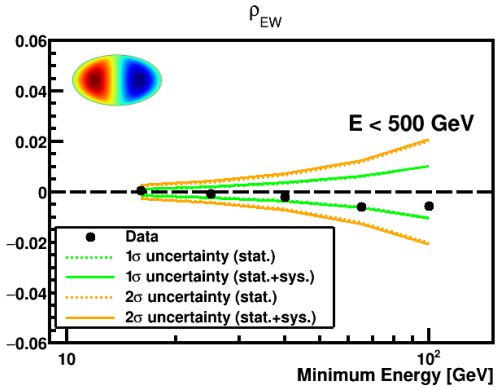

(a) East-West

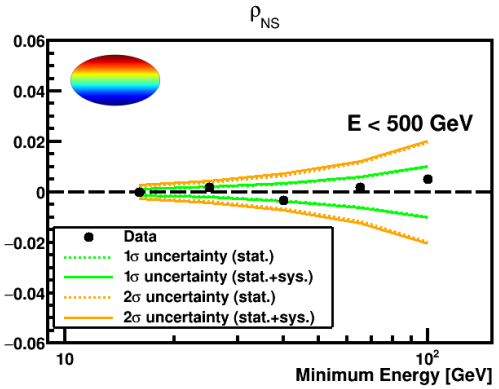

(b) North-South

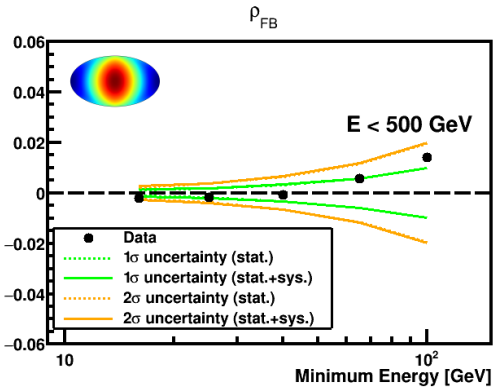

(c) Forward-Backward

Figure 4.43: Electron dipole components, EW, NS and FB in galactic coordinates where the 1 and 2-sigma deviations from isotropy (green and yellow, respectively) corresponding to the statistical (dotted line) and total (solid line) uncertainties are shown.

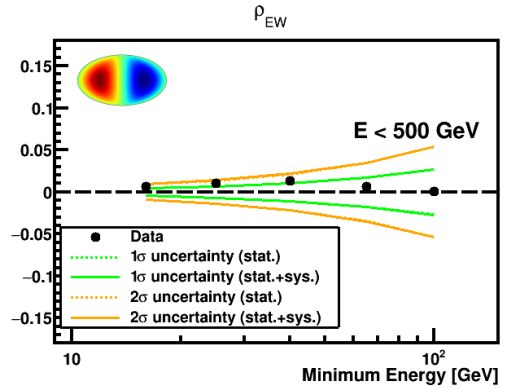

(a) East-West

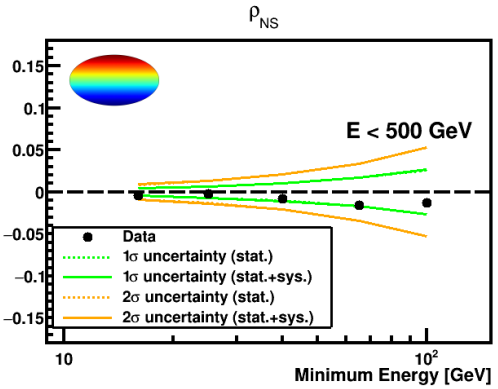

(b) North-South

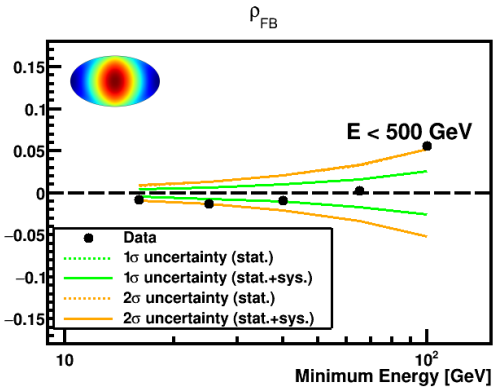

(c) Forward-Backward

Figure 4.44: Positron dipole components, EW, NS and FB in galactic coordinates where the 1 and 2-sigma deviations from isotropy (green and yellow, respectively) corresponding to the statistical (dotted line) and total (solid line) uncertainties are shown.

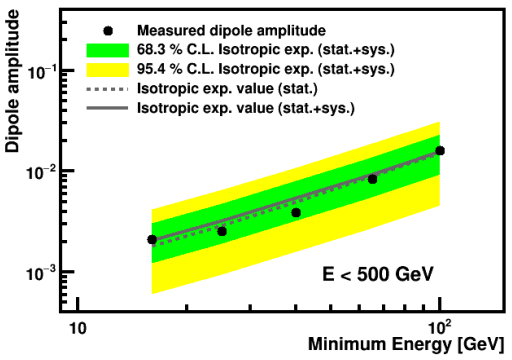

(a)

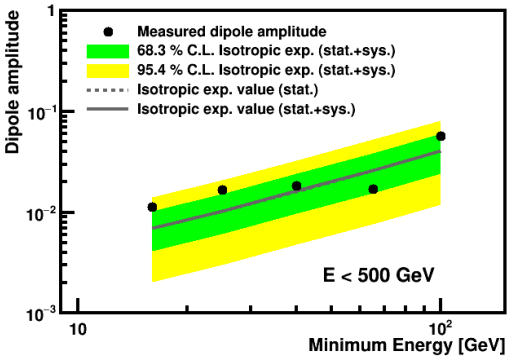

(b)

Figure 4.45: Electron (a) and positron (b) measured dipole amplitude as a function of the minimum energy in galactic coordinates. The 1 and 2-sigma total uncertainty bands are shown in green and yellow respectively. The expected value from isotropy considering the statistical (dotted line) and the statistical + systematic (solid line) uncertainties is also displayed.

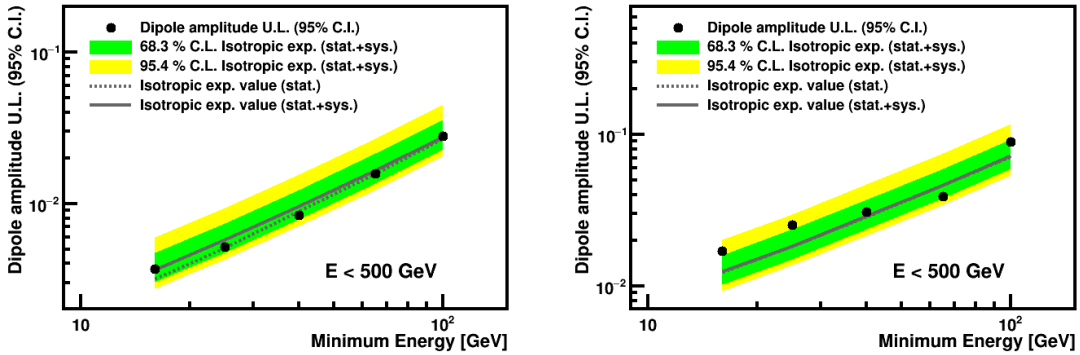

Figure 4.46: Electron (a) and positron (b) 95% C.I. upper limit as a function of the minimum energy in galactic coordinates. The 1 and 2-sigma total uncertainty bands are shown in green and yellow respectively. The expected value from isotropy considering the statistical (dotted line) and the statistical + systematic (solid line) uncertainties is also displayed.

Seasonal Anisotropy Analysis

The results presented on the positron sample have been shown to be compatible with isotropy within the uncertainties after applying the electron efficiency corrections. Nevertheless, a residual deviation slightly higher than 1 sigma is observed for $E_{min} = 16$ GeV. Even though, the measured deviation is not significant, due to the physical implications of the measurement a specific check has been performed.

Since the electron results are consistent with the isotropic expectation value, a time evolution analysis for the relative anisotropy of the positron-to-electron ratio can be carried out. This study allows to investigate if the deviation found in the positrons for $E_{min} = 16$ GeV arises from a certain period of time or any specific pattern is observed.

For this purpose, the skymaps of measured positron and electron events are included in the likelihood fit from equation 3.46 for 8.5 years of data taking. The period of time is divided in seasons ($\sim$ 4 months each one), and each season provides an independent measurement of the anisotropy.

Results for the ρ_{EW}, ρ_{NS} and ρ_{FB} dipole components are shown in figure 4.47 for $E_{min} = 16$ GeV in galactic coordinates. As can be seen, the dipole components for the different time periods are consistent with a common value, which can be further confirmed by means of a fit to a constant value in each component.

In addition, the dipole amplitude scaled by the isotropic expectation is shown in figure 4.48 for $E_{min} = 16$ GeV in galactic coordinates. No special patterns or significant deviations are observed.

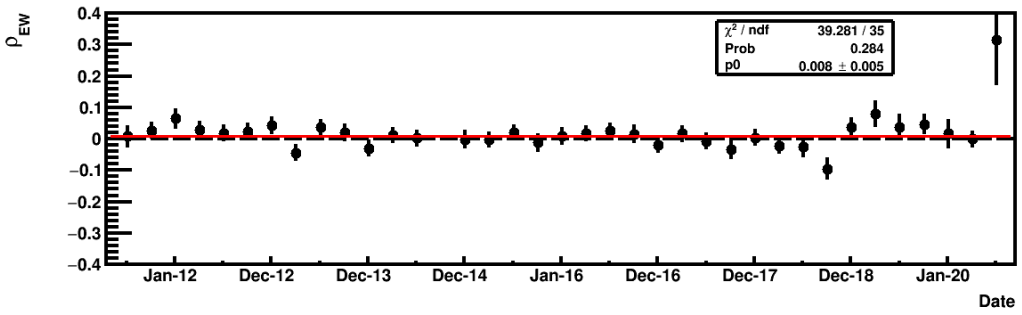

(a) East-West

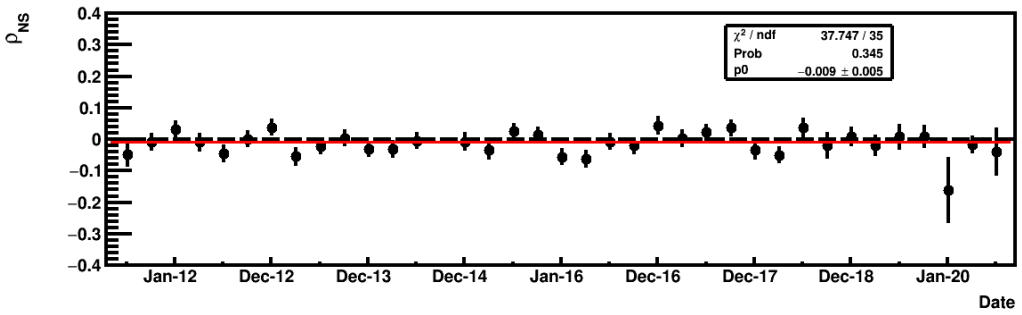

(b) North-South

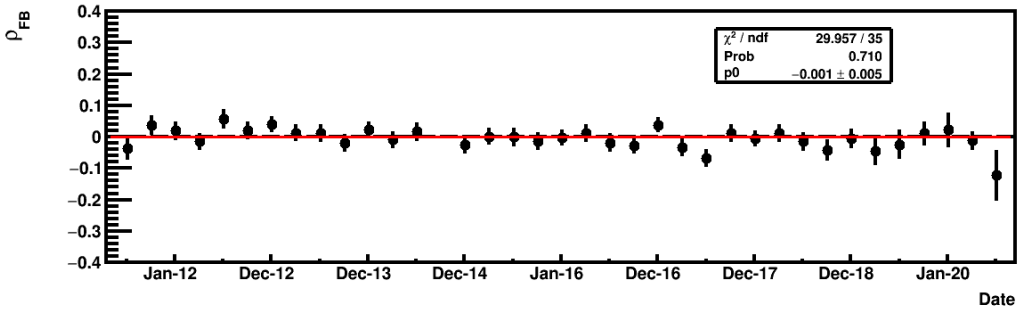

(c) Forward-Backward

Figure 4.47: Dipole components, EW, NS, and FB in galactic coordinates on the positron-to-electron seasonal anisotropy for $E_{min} = 16$ GeV.

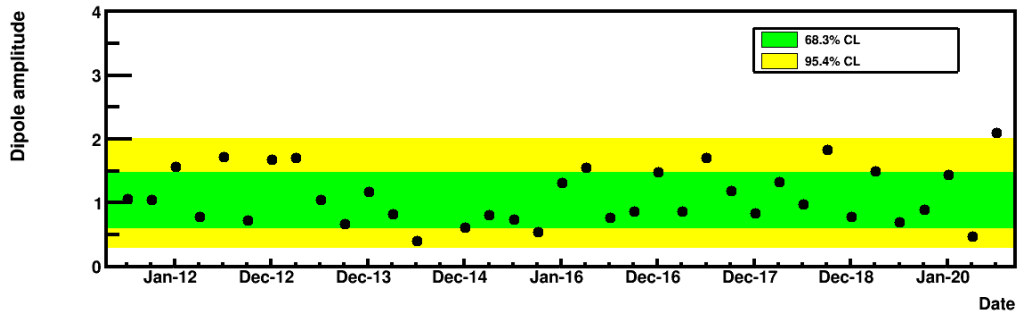

Figure 4.48: Dipole amplitude on the positron-to electron seasonal anisotropy in galactic coordinates $E_{min} = 16$ GeV. The data points are scaled by the expectation value from isotropy.

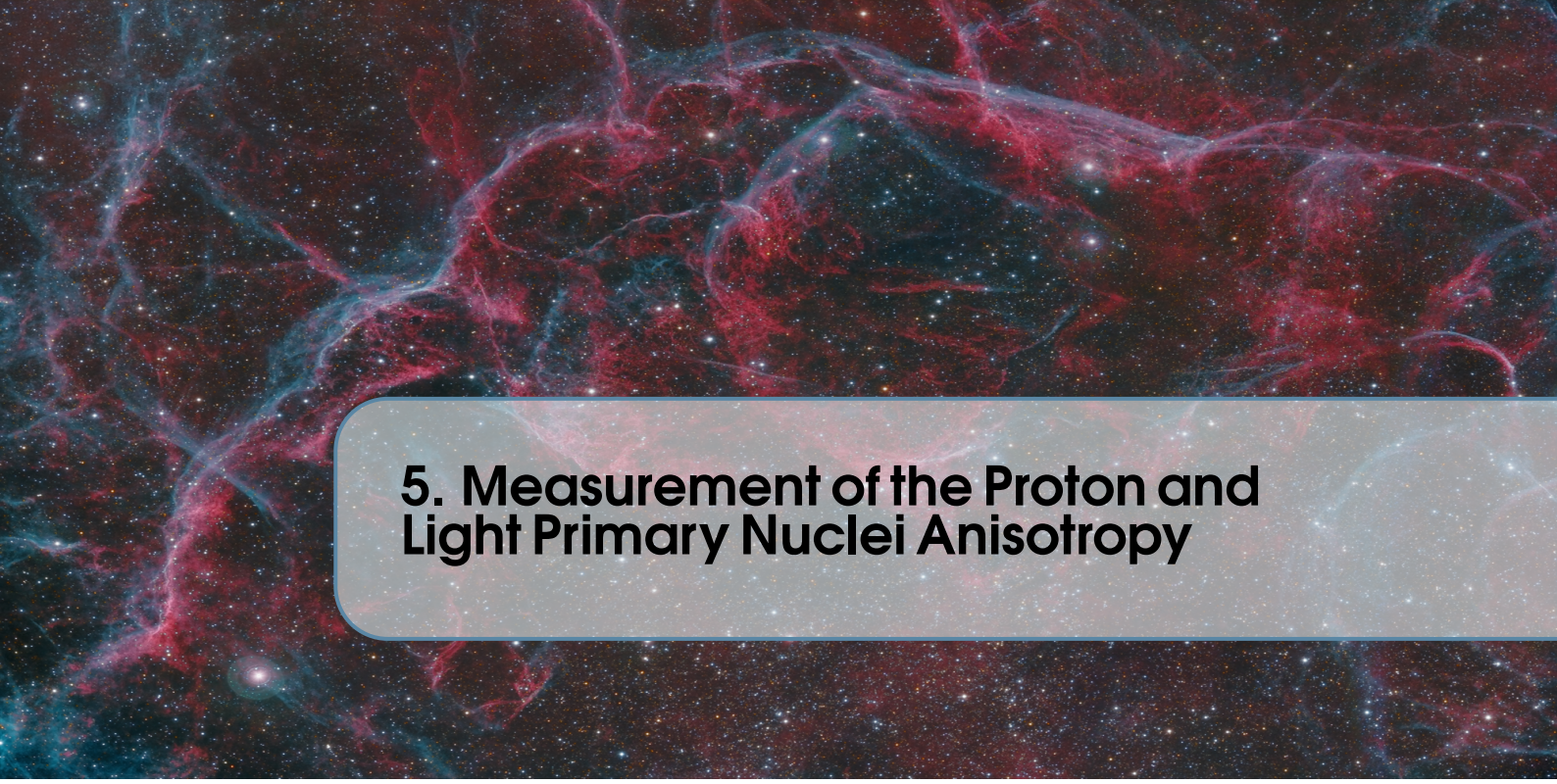

5. Measurement of the Proton and Light Primary Nuclei Anisotropy

"I believe in the cosmos. All of us are linked to the cosmos."

— Mikhail Gorbachev

Recent observations on the proton and light primary nuclei fluxes have shown that they cannot be described by a single power law and the spectral index progressively hardens above $\sim$ 200 GV. Different models have been proposed to explain the deviations, but, typically, they are grouped in two scenarios: non-linear propagation models or nearby sources of high rigidity cosmic rays. In particular, the measurement of a sizable anisotropy in the rigidities where the spectral breaks are observed would favor the nearby sources, since transport models usually predict smaller amplitudes. Therefore, the determination of the directionality of protons and light primary nuclei helium, carbon and oxygen provides a complementary characterization to the fluxes that may help to understand the origin of the observed features.

Proton and helium events constitute the most abundant species of cosmic rays, which requires an extremely precise knowledge of the instrumental effects in order to avoid spurious signals. This makes the measurement especially challenging and provides a benchmark test of the method presented in this work.

Previous results on the proton anisotropy with AMS-02 were reported in [158] for 5 years of data taking. No deviations from isotropy were found and upper limits on the dipole amplitude were established. For light primary nuclei, no prior determination of the anisotropy has been presented before.

This chapter will present the extension of the proton analysis to higher Z together with the proton update with a larger sample size. First, a detailed description of the measurement of the anisotropy for helium, carbon and oxygen will be reported. This includes the selection of a pure sample of events, the evaluation of the instrumental effects and the results on the dipole anisotropy. The last part will cover the update on the proton analysis.

5.1 Light Primary Nuclei Selection

The selection of the light primary nuclei helium, carbon, and oxygen is applied to the data collected in the first 8.5 years of data taking with AMS-02, which corresponds to the period of time from May 2011 to November 2019 and amounts to 1.83×10^8 s of exposure time. Events are required to satisfy the following conditions:

- **TOF**
  - Reconstructed track exists in the TOF with 4 TOF hits between the planes.
  - Relativistic downward-going particles $\beta > 0.4$
  - TOF charge measurement consistent with Z = 2, 6, 8 for helium, carbon and oxygen respectively (see table 5.1).
- **Inner Tracker**

  Reconstruction:
  - Reconstructed track exists in the inner tracker with at least 4 hits between L2-L8. One of them in the L2, and the rest in either L3-L4, L5-L6 and L7-L8.

  Selection:
  - Inner charge measurement consistent with Z = 2, 6, 8 for helium, carbon and oxygen respectively (see table 5.1).

  Quality Criteria:
  - Quality criteria on the inner track reconstruction in both bending (Y) and non-bending (X) planes $\chi^2_{Inn}(X,Y)/d.o.f. < 10$.
- **External Layers**
  - Reconstructed track exists in the L1+Inner (L1-L8) with associated hit in X and Y projections in L1.
  - Quality criteria on the L1+Inner reconstruction in the bending (Y) plane is required $\chi^2_{L1+Inn}(Y)/d.o.f. < 10$.
  - L1 charge measurement consistent with Z = 2, 6, 8 for helium, carbon and oxygen respectively (see table 5.1).

The set of charge selection cuts is summarized in table 5.1.

The cuts associated to the external layer L1 define the L1+Inner tracker pattern sample of analysis. The inclusion of the external layer L9 with the associated cuts (same as in L1) defines the Full Span tracker pattern sample which corresponds to a sub-sample of L1+Inner. Each tracker pattern has different advantages: L1+Inner provides more statistics below its MDR ($\sim$ 1.2 TV [76]) whereas Full Span allows to compute the flux for rigidities above 1.2 TV, since the MDR is higher ($\sim$ 3.5 TV [76]). Therefore, the combination of both allows to exploit the rigidity resolution as well as the maximum available statistics. In addition, the tracker patterns define the fiducial volume of the sample by means of the inner tracker track extrapolation to L1 (L1+Inner sample) or L1-L9 (Full Span sample).

The reconstructed rigidity of all events is required to be above the maximum rigidity cutoff within the field of view in order to avoid secondary particles trapped in the geomagnetic field.

The measurement of the anisotropy is performed in 9 cumulative rigidity ranges, with a minimum rigidity of R_{min} = 18, 30, 45, 80, 150, 200, 300, 500, and 1000 GV. The number of selected helium, carbon, and oxygen events for the different rigidity ranges and tracker patterns are presented in tables 5.2 and 5.3. As can be seen, the L1+Inner tracker pattern has about 4 times more statistics than the Full Span sample.

The L1+Inner tracker pattern sample will be used for the anisotropy studies for two reasons: on the one hand, the analysis is dominated by statistics, as we will see in section 5.6 and, on the other hand, the analysis is performed in cumulative rigidity ranges, so that the effect of the finite rigidity

resolution is reduced [1].

In addition, the selection presented in this section yields purities above 99% [76] for the three species and, therefore, no background is introduced in the anisotropy analysis.

	He	**C**	**O**
TOF	$Q_{Lower} > 1.4$	$Q_{Lower} > 5.4$	$Q_{Lower} > 7.4$
	$Q_{Upper} > 1.25$	$5.4 < Q_{Upper} < 7.5$	$7.4 < Q_{Upper} < 9.5$
Inner Tracker	$1.7 < Q_{Inn} < 2.5$	$5.5 < Q_{Inn} < 6.45$	$7.55 < Q_{Inn}$ 8.45
External Layers	$1.6 < Q_{L1} < 2.9$	$5.5 < Q_{L1} < 6.5$	$7.55 < Q_{L1} < 8.45$
	$1.6 < Q_{L9} < 2.9$	$5.5 < Q_{L9} < 7.7$	$7.5 < Q_{9} < 9.9$

Table 5.1: List of charge selection cuts applied for helium, carbon and oxygen.

	L1+Inner		
R_{min} (GV)	$N_{He}^{meas}(\times 10^3)$	$N_{C}^{meas}(\times 10^3)$	$N_{O}^{meas}(\times 10^3)$
18	112051.64	3674.25	3394.78
30	54430.99	1814.09	1707.60
45	25799.19	863.52	824.21
80	9926.68	327.50	318.47
150	3635.11	117.06	116.03
200	2311.30	74.60	73.48
300	1247.71	40.04	39.14
500	571.57	18.15	17.46
1000	201.36	5.95	6.04

Table 5.2: Number of measured helium, carbon and oxygen events in the 9 cumulative rigidity ranges and for the L1+Inner tracker pattern.

	Full Span		
R_{min} (GV)	$N_{He}^{meas}(\times 10^3)$	$N_{C}^{meas}(\times 10^3)$	$N_{O}^{meas}(\times 10^3)$
18	28523.09	785.58	686.09
30	12712.51	353.48	315.25
45	6502.27	179.69	162.69
80	2545.38	68.29	62.71
150	921.60	23.99	21.78
200	578.17	14.83	13.32
300	308.27	7.68	6.76
500	139.45	3.29	2.91
1000	47.00	1.04	0.91

Table 5.3: Number of measured helium, carbon and oxygen events in the 9 cumulative rigidity ranges and for the Full Span tracker pattern.

[1] It should be also noted that the last rigidity range of the analysis is below the MDR for the L1+Inner tracker pattern.

5.2 Light Primary Nuclei Efficiencies

The light primary nuclei efficiencies are determined directly on data and follow the same strategy as in electrons (see section 4.3). In this case, the main subdetector involved in the selection is the tracker and the efficiencies that will play a major role in the analysis are related to the reconstruction, selection, and quality criteria of the track as well as the hit association with the external layers (*L1 and L9 picking efficiencies*). The computation of the efficiencies is performed as a function of the rigidity and within the corresponding fiducial volume. Their evaluation is presented as follows: inner tracker efficiencies, picking efficiencies, and trigger efficiency.

5.2.1 Inner Tracker Efficiencies

The initial sample corresponds to downward-going particles ($\beta > 0.4$) fulfilling the physics trigger requirement and TOF charge consistent with He, C, and O (2, 6, and 8 respectively) [2].

The efficiencies are then computed sequentially requiring the following conditions:

- **Tracker reconstruction efficiency:** Reconstructed track exists in the inner tracker with at least 4 hits between L2-L8.
- **Tracker selection efficiency:** Inner Charge (Q_{Inn}) consistent with Z = 2, 6, 8 for helium, carbon and oxygen respectively.
- **Tracker quality criteria efficiency:** Inner track reconstruction good χ^2 in both bending (Y) and non-bending (X) planes.

5.2.2 Picking Efficiencies

After the evaluation of the inner tracker efficiencies, the layer 1 and layer 9 picking efficiencies [3] are computed separately on the sample of events satisfying all inner tracker cuts. Then, the efficiencies are computed requiring the following conditions:

- **L1 (L9) picking reconstruction efficiency:** Associated hit in L1 (L9) with L1+Inner (Inner+L9) reconstructed rigidity.
- **L1 (L9) picking selection efficiency:** L1 (L9) charge ($Q_{L1(L9)}$) consistent with Z = 2, 6, 8 for helium, carbon and oxygen respectively, and a good χ^2 in both bending (Y) and non-bending (X) planes for the L1 (L9).

5.2.3 Trigger Efficiency

As described in section 4.3, the trigger efficiency is evaluated on data from the sample of events satisfying all selection cuts with any physics trigger N_{phys} or any trigger unbiased N_{unb}. The latter requires that 3/4 TOF planes are fired instead of 4/4 and is prescaled by a factor 1/100 to reduce the sample size in the acquisition procedure. The trigger efficiency is estimated as the fraction of events with N_{phys} over the total sample and is expressed as

$$\varepsilon_{trig} = \frac{N_{phys}}{N_{phys} + 100\, N_{unb}} \tag{5.1}$$

5.3 Light Primary Nuclei Fluxes Computation

The flux in the jth rigidity bin (ΔR_j, $R_j + \Delta R_j$) was defined in equation 3.7 as

$$\Phi_j = \frac{N_j}{(A_{eff})_j\, (T_{exp})_j\, \Delta R_j} \tag{5.2}$$

[2] Since the track is not necessarily available at this stage the fiducial volume is determined with the extrapolation of the TOF track into layers 1 and 9 and the rigidity is estimated by means of the ECAL energy.

[3] The layer 9 picking efficiencies will only be computed when the Full Span sample is used.

where N_j is the number of selected events corrected for bin-to-bin migrations, $(A_{eff})_j$ the effective acceptance, and $(T_{exp})_j$ the exposure time (see section 3.2.1). For rigidities $R > 1$ TV (where the MDR is almost reached for the L1+Inner sample [76]) the Full Span tracker pattern is used, whereas for rigidities below the L1+Inner is applied. The bin-to-bin migrations are corrected using the *Folded Acceptance* unfolding procedure, which accounts for the resolution in the rigidity measurement. A detailed description of the effective acceptance computation and the unfolding procedure is presented in appendix B.

Results for 8.5 years of data taking together with the latest AMS-02 publications covering 5 years of data, are presented in figures 5.1a, 5.1b and 5.1c. The differences observed at low rigidities arise from a different solar modulation associated to the time period of the analyses. For rigidities above few tens of GV the solar modulation effect is negligible and the results are consistent with the AMS publication, as expected. For the anisotropy analysis, the contribution from the solar modulation is not relevant since the lowest cumulative rigidity range corresponds to 18 GV.

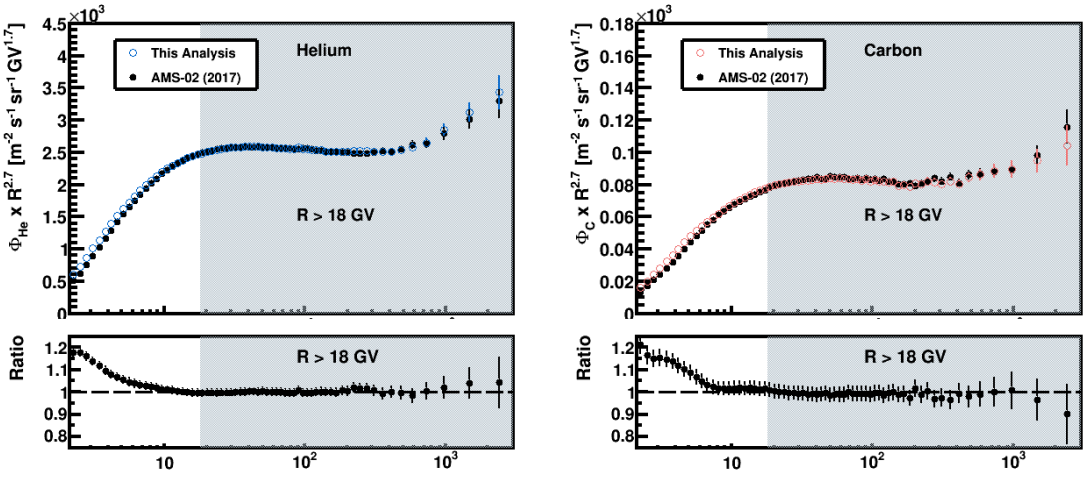

(a) (b)

(c)

Figure 5.1: Comparison of the helium, carbon and oxygen fluxes obtained with this analysis with the AMS-02 latest publication [76].

5.4 Parametrization of the Light Primary Nuclei Efficiencies for Anisotropies

The strategy followed to separate the efficiencies sequentially for each associated cut allows to obtain a precise determination of the detector dependences at the different geographical positions and, therefore, understand the origin of the instrumental effects in galactic coordinates.

This section will present the procedure followed to quantify the impact of the detector effects in the anisotropy analysis for the light primary helium, carbon and oxygen samples.

5.4.1 One-Dimensional Study in Geomagnetic Colatitude

The study of the one-dimensional efficiency distributions as a function of the geomagnetic colatitude provides valuable information about the behavior of the different subdetectors along the ISS orbit and serves as a first estimation to quantify the impact of the efficiency corrections in the multipolar analysis.

In the case of the light primary nuclei, the one-dimensional approach allows to compare the impact of the efficiency dependences for the different species used in this analysis. As an example, figure 5.2a shows the relative variation of the layer 1 picking selection efficiency (the most relevant in the anisotropy analysis) as a function of the geomagnetic colatitude for helium, carbon, and oxygen respectively and for rigidities $R > 18$ GV. Again, $cos(\theta_M) = +1$ corresponds to the northern geomagnetic pole and the $cos(\theta_M) = -1$ to the southern. The relative variation of the efficiencies is parametrized by a quadratic function (equation 4.6) where the p_1 quantifies the North-South asymmetry and p_2 the symmetric drop (the relevant directions when transforming to galactic coordinates according to the transformation matrix, figure A.1c). The parameters p_1 and p_2 for each species are displayed in figure 5.2b, where the carbon and oxygen parameter values show a consistent determination of the efficiency dependences within the uncertainties with respect to helium. This holds for all the efficiencies involved in the analysis. Therefore, in this work, the efficiency corrections determined on helium will be used for carbon and oxygen. This prescription provides a more precise determination of the corrections due to the larger size of the helium sample.

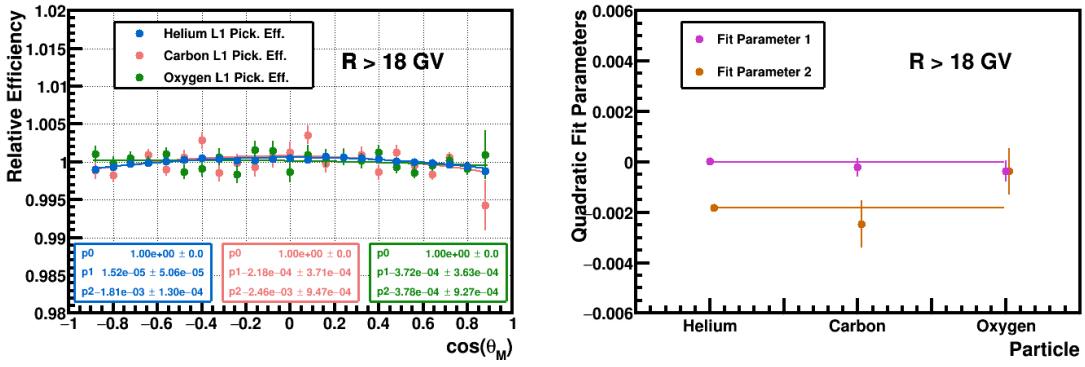

(a) (b)

Figure 5.2: (a) Comparison of the relative variation of the layer 1 picking selection efficiency as a function of the geomagnetic colatitude for helium, carbon and oxygen and for rigidities $R > 18GV$. (b) Comparison between helium, carbon and oxygen parameters of the fit to a quadratic function, p_1 and p_2, of the layer 1 picking selection efficiency as a function of the geomagnetic colatitude.

5.4.2 Spherical Harmonic Study in ISS Geographical Position Coordinates

The spherical harmonic parametrization of the skymap efficiency distributions in ISS geographical position provides the efficiency corrections $\Delta_{\ell m}$ by means of the relative analysis of anisotropies of the samples of rejected N_{ko} and accepted N_{ok} events for each cumulative rigidity range.

The rigidity dependence of the corrections is described with a first and second order polynomial parametrization as a function of the logarithm of the rigidity for the dipole ($\ell = 1$) and quadrupole ($\ell = 2$) components respectively. Special is the case of the Δ_{NS} for the layer 1 picking selection efficiency which shows a significant change in the amplitude for $R > 100$ GV, and a logistic function [4] is found to provide a better description of the data points (figure 5.3a). For the Δ_{2+0} the points are well described by a quadratic function (figure 5.3b). A detailed study of the variation of the layer 1 picking selection efficiency is shown in appendix C.

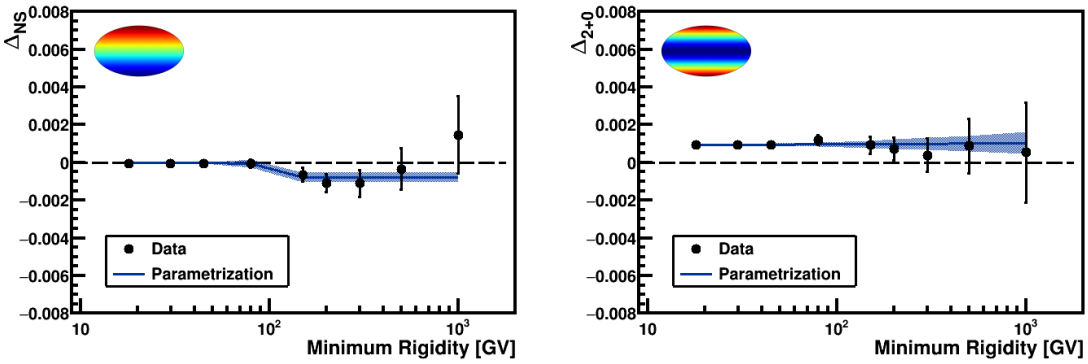

(a) (b)

Figure 5.3: Layer 1 picking selection efficiency corrections for the Δ_{NS} (a) and Δ_{2+0} (b) components. The data points are obtained from the relative analysis of the N_{ko} and N_{ok} samples. The correction is fitted to a logistic and quadratic parametrization for the $\ell = 1$ and $\ell = 2$ respectively.

The procedure presented in section 4.5 to determine the significant efficiencies is followed for helium. The distribution of pulls $(\Delta^i_{\ell m}/\sigma(\Delta^i_{\ell m}))$ for each rigidity range is obtained (figure 5.4). The effect of the scan for the sigma and mean values to determine the significant efficiencies are shown in figures 5.5a and 5.5b. Finally, the significant efficiency corrections in the lowest rigidity range are introduced with the aforementioned parametrizations.

Figure 5.6 shows the dipole and quadrupole components associated to each helium efficiency (top panel) as well as the total efficiency correction (bottom panel) for rigidities $R > 18$ GV. The total efficiency correction is computed as the sum of the individual corrections, where only those tagged as significant following the previous method are included. The biggest contributions come from the layer 1 picking reconstruction and selection efficiencies and they mainly affect the North-South direction, represented by the Δ_{NS} and Δ_{2+0}, which is explained by the drop at high latitudes, as observed in the one-dimensional study of the efficiencies. The Δ_{2-1} also has a minor contribution due to the asymmetry of the geomagnetic poles in ISS geographical position coordinates. Overall, the corrections are below the permil level and, therefore, even smaller contributions are expected in galactic coordinates due to the dilution of the Δ_{NS} and Δ_{2+0} through the effective coordinate transformations.

Figures 5.7a and 5.7b show the skymap of the spherical harmonic parametrization of the layer 1 picking selection efficiency as well as the total one up to $\ell = 2$ for rigidities $R > 18$ GV, where only significant corrections have been included. The North-South asymmetry is clearly observed in both

[4] Mathematically the logistic function is expressed as $g(R_{min}) = m_1 + m_2/\left(1 + e^{m_3 R_{min} + m_4}\right)$

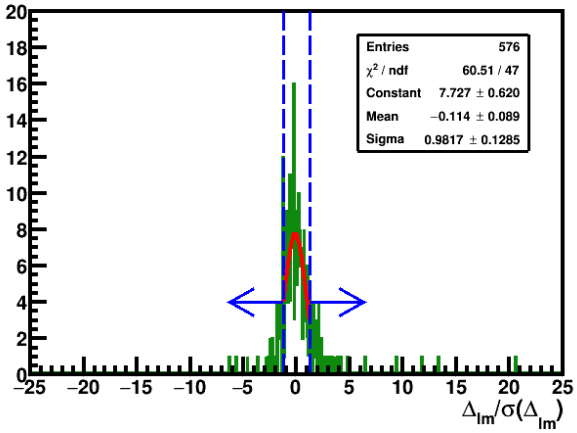

Figure 5.4: Distribution of the helium efficiency correction pulls for each efficiency (6), rigidity range (9), dipole, and quadrupole components (8). Efficiency corrections whose pull is below the threshold are consistent with statistical fluctuations and described by a normal distribution. Those corrections above the threshold are significant and include it in the analysis (indicated by an arrow).

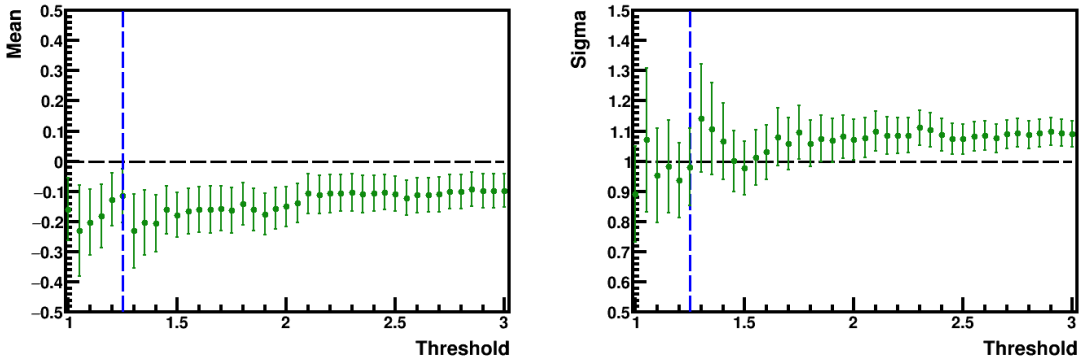

(a) Mean (b) Sigma

Figure 5.5: Scan in the mean (a) and sigma (b) parameters of the fit to a Gaussian function of the pulls distribution in figure 5.4 as a function of the threshold value. The optimum value of a threshold, which corresponds to mean ~ 0 and sigma ~ 1, ensures that the efficiency corrections with pull below that value are well described by a Gaussian distribution and, therefore, consistent with statistical fluctuations.

figures. The observed dependences of the total efficiency are used to correct the exposure time map and obtain the reference map for the analysis in ISS geographical position coordinates.

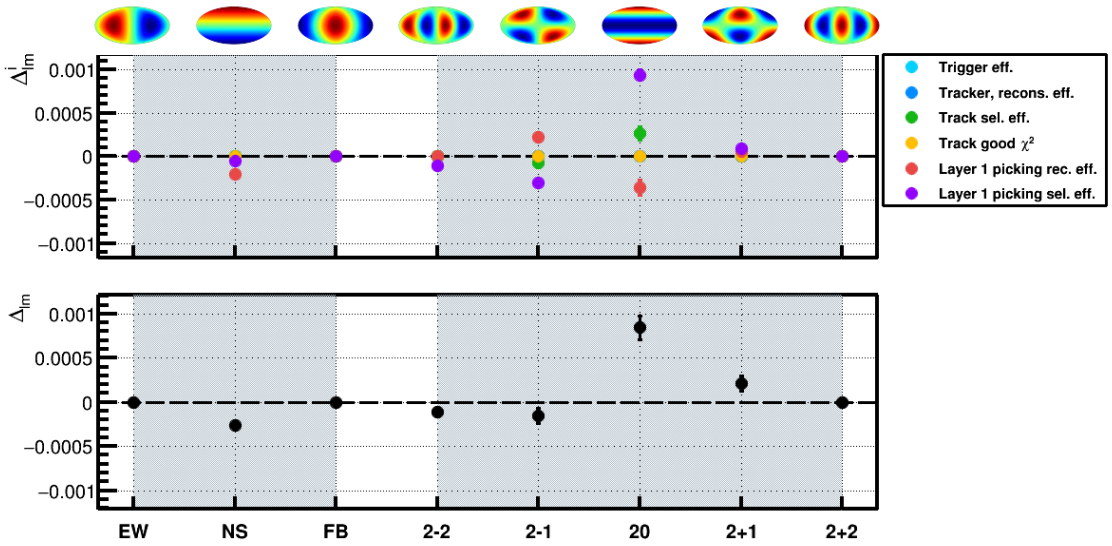

Figure 5.6: Individual (top) and total (bottom) helium efficiency corrections for the dipole ($\ell = 1$) and quadrupole ($\ell = 2$) components for $R > 18$ GV in ISS geographical position coordinates. The main direction affected is the North-South with the biggest contribution coming from the layer 1 picking selection efficiency.

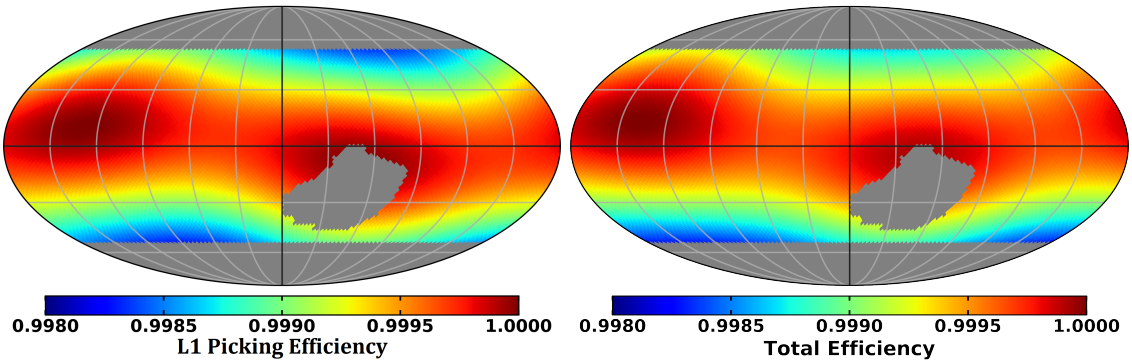

(a) L1 Picking Efficiency (b) Total Efficiency

Figure 5.7: ISS geographical position skymap of the spherical harmonic parametrization of the picking layer 1 selection efficiency (a) as well as the total one (b) up to $\ell = 2$ for rigidities $R > 18$ GV, where only significant corrections have been included.

5.4.3 Spherical Harmonic Study in Galactic Coordinates

Once the geographical dependences of the helium efficiencies are understood the same procedure can be followed in the reference system of analysis. The corrections are computed directly in galactic coordinates with the skymap distributions of the N_{ko} and N_{ok} samples for each rigidity range. The rigidity dependence of the efficiency corrections and the method to choose the significant efficiencies follow the same approach as in the previous section.

The dipole and quadrupole components associated to each efficiency correction (top panel) and for the total efficiency correction (bottom panel) for rigidities $R > 18$ GV are shown in figure 5.8. The North-South asymmetry observed in ISS geographical position coordinates, represented by the Δ_{NS} and Δ_{2+0}, is projected onto all directions in galactic coordinates and most of the components are now significant, with, again, a dominant contribution from the layer 1 picking reconstruction and selection efficiencies. In galactic coordinates, the amplitude of the corrections is much below

the permil level and, therefore, the measurement is not expected to be dominated by the systematic corresponding to the efficiency corrections.

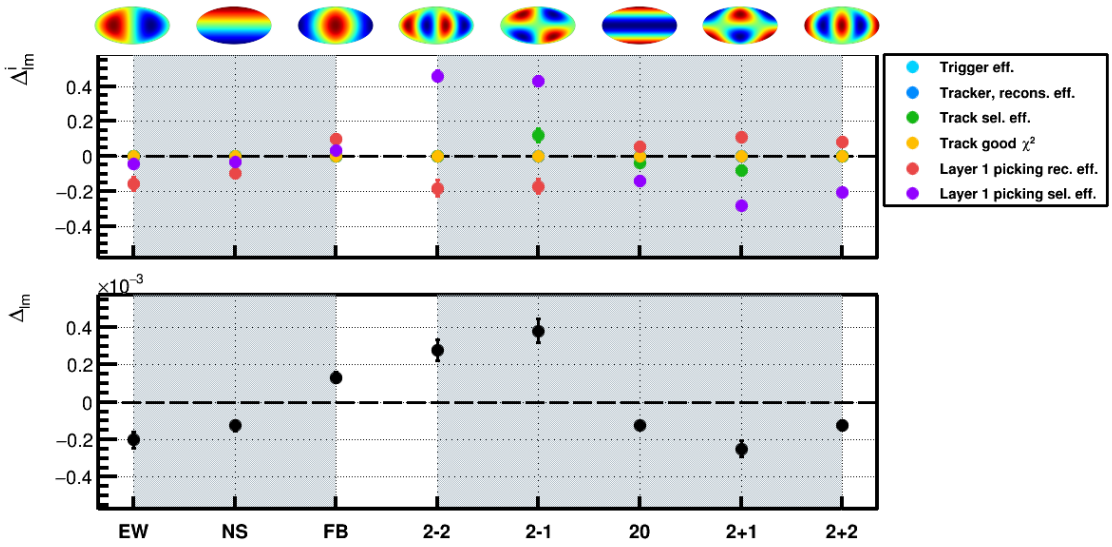

Figure 5.8: Individual (top) and total (bottom) helium efficiency corrections for the dipole ($\ell = 1$) and quadrupole ($\ell = 2$) components for $R > 18$ GV in galactic coordinates. Most of the components are now significant due to the projection of the Δ_{NS} and Δ_{2+0} from ISS geographical position coordinates into galactic coordinates. The main contribution comes from the layer 1 picking reconstruction and selection efficiencies.

The skymaps of the spherical harmonic parametrization of the layer 1 picking selection efficiency as well as the total one up to $\ell = 2$ for rigidities $R > 18$ GV in galactic coordinates are shown in figures 5.9a and 5.9b. For the total efficiency, only significant corrections have been included. The skymap of the total efficiency is used to correct the exposure time map and obtain the reference map for the anisotropy analysis in galactic coordinates.

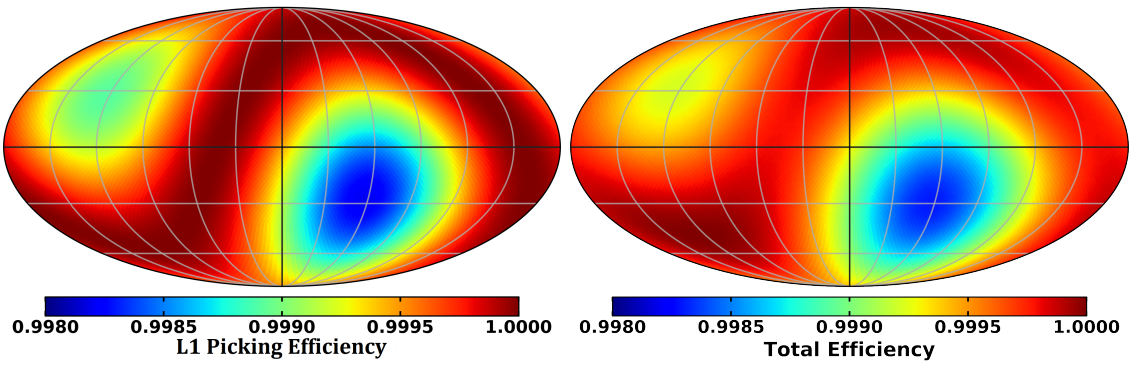

(a) L1 Picking Efficiency (b) Total Efficiency

Figure 5.9: Spherical harmonic parametrization of the layer 1 picking selection efficiency (a) as well as the total one (b) up to $\ell = 2$ for rigidities $R > 18$ GV in galactic coordinates, where only significant corrections have been included.

5.5 Rigidity Scale Effects

The measurement of the rigidity is a key ingredient in the anisotropy analysis for the light primary nuclei. In particular, the determination of the alignment of the different layers of the silicon tracker detector is crucial since small shifts in their positions can induce an intrinsic bias in the rigidity measurement and therefore affect its precision, especially when the trajectories are very straight (high rigidity particles).

In AMS, a static alignment was done during the test beam with protons which was further validated with ISS data to correct small displacements during the launch. In addition, a dynamic alignment takes care of correcting the small displacements of the outer layers produced by short-term variations of the temperature along the ISS orbit. Nevertheless, residual shifts in some tracker elements may still occur and give rise to an absolute rigidity scale, which will induce a systematic bias of the rigidity measurement $\Delta(1/R)$. The absolute value of the rigidity scale for helium, carbon and oxygen reported by AMS was found to be smaller than 1/29 TV^{-1} [173]. Results are presented first for helium, due to the larger size of the sample and, then, compared with carbon and oxygen at the end of the section.

The effect of a rigidity scale produces an increase or a decrease in the population of events above a certain measured rigidity. The calibration curve in figure 5.10 quantifies this effect when a positive or negative bias is applied, where five high rigidity ranges have been used: R_{min} = 150, 200, 300, 500 and 1000 GV. As expected, the amplitude of the effect to a rigidity scale increases at high rigidities.

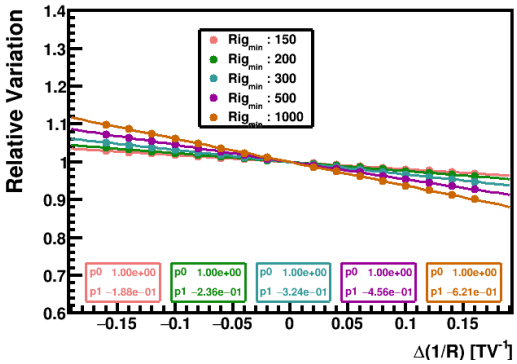

Figure 5.10: Calibration Curve for the effect of a rigidity scale on the number of selected helium events. A rigidity scale of $\Delta(1/R) = 0.1\ TV^{-1}$ for events with rigidities $R > 1000$ GV would produce a variation of $\sim 8\%$ in the number of helium events.

For the anisotropy analysis, any rigidity scale that depends on the ISS position will automatically produce variations in the number of selected events that could induce spurious effects. Therefore, the determination of the variation of the rigidity scale in the relevant reference systems is needed. For this work, results in ISS geographical position coordinates will be shown, since it is a system where the possible effects are enhanced and non-negligible contributions might appear.

The effect of $\Delta(1/R)$ is estimated from the fraction of spillover events, defined as the ratio of those reconstructed with $R < 0$ GV over those with $R > 45$ GV, figure 5.11a, which are very sensitive to a bias in the tracker rigidity reconstruction. The accuracy of this estimation is improved by extending the definition of spillover events to those with 1/R < 1/1.8 TV^{-1}.

The calibration curve in figure 5.11b shows the change in the fraction of spillover helium events induced by a $\Delta(1/R)$, where a negative bias ($\Delta(1/R) < 0$) increases the spillover ratio and vice versa.

The relative variation of the spillover ratio of helium events is investigated as a function of

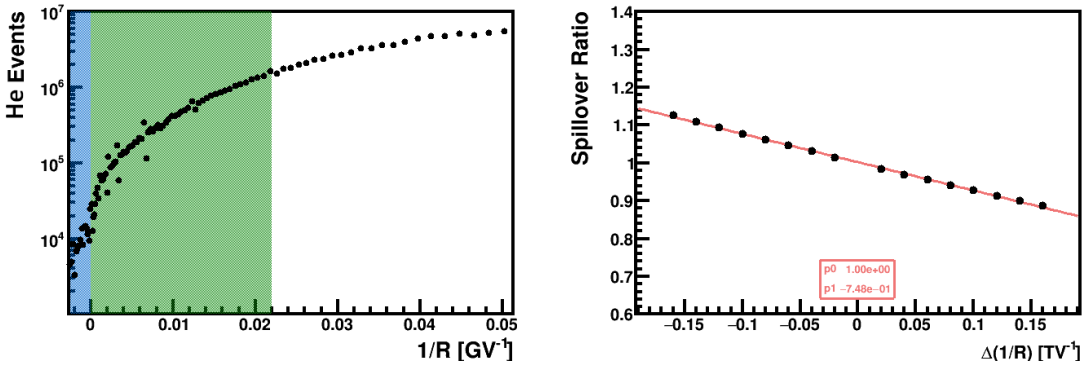

(a) (b)

Figure 5.11: (a) Distribution of selected helium events as a function of $1/R$. Events reconstructed with negative rigidity, R <0 GV are shown in a blue band and correspond to the spillover events, whereas those with rigidities R >45 GV are shown with a green band. (b) Calibration curve for the effect of a rigidity scale on the spillover fraction of helium events.

the cosine of the colatitude ($\cos(\theta)$) in ISS geographical coordinates where the same analysis performed for the one-dimensional approach is used. In particular, the variation with respect to ($\cos(\theta)$) is fitted to a quadratic function and the parameters of the fit are related with the a_{10} and a_{2+0} through the equation 4.7. Results are presented in figure 5.12a together with the fit to a quadratic function, where the p_2 parameter shows a significant amplitude. The variation in the spillover estimator can be translated into a rigidity scale $\Delta(1/R)$ by means of the calibration curve shown in figure 5.11b. The modulation of $\Delta(1/R)$ is presented in figure 5.12b where a similar functional behavior from figure 5.12a is inherited.

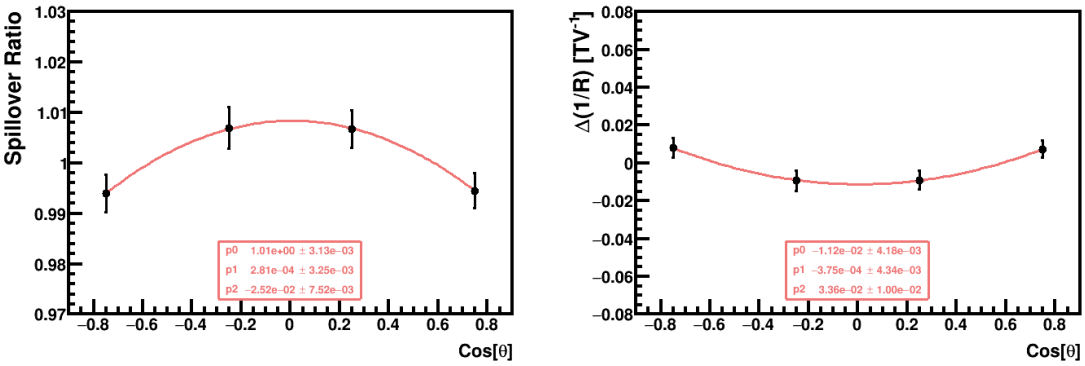

(a) (b)

Figure 5.12: Variation of the helium spillover ratio (a) and rigidity scale $\Delta(1/R)$ (b) as a function of the cosine of the colatitude ($cos(\theta)$) in ISS geographical position coordinates.

The bias $\Delta(1/R)$ as a function of $cos(\theta)$ is translated into variations in the number of selected events by means of the calibrations curves from 5.10 for each rigidity range. As an example, the modulation obtained for rigidities R > 200 GV and R > 1000 GV are shown in figures 5.13a and 5.13b. As can be seen, the effect of a rigidity scale modulation produces an increase in the amplitude of the p_2 parameter with the rigidity.

The parameters of the fit, p_1 and p_2, are related with the ρ_{NS} and ρ_{2+0} respectively. The effect of the rigidity scale in the multipole components of the anisotropy analysis is obtained by means

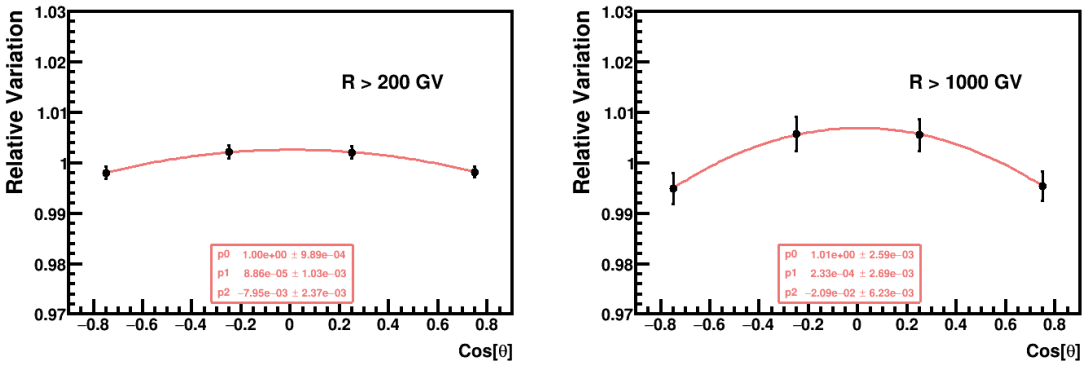

(a) (b)

Figure 5.13: (a) Relative variation in the number of selected helium events produced by the rigidity scale as a function of the cosine of the colatitude ($cos(\theta)$) for rigidities $R > 200$ GV (a) and $R > 1000$ GV (b).

of equation 4.7, allowing to obtain a rigidity scale correction. Figures 5.14a and 5.14b show the helium rigidity scale correction for the ρ_{NS} and ρ_{2+0} in ISS geographical position coordinates.

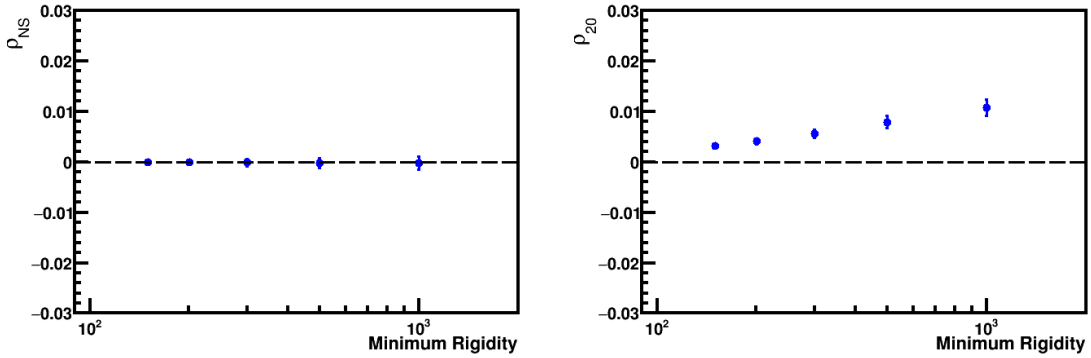

(a) (b)

Figure 5.14: Helium rigidity scale correction for the ρ_{NS} (a) and ρ_{2+0} (b) obtained with the spillover estimator in ISS geographical position coordinates.

In addition, the rigidity scale correction obtained in ISS geographical position coordinate is transformed into galactic coordinates by means of the transformation matrix from appendix A. Results are presented in figures 5.15a, 5.15b and 5.15c for the ρ_{EW}, ρ_{NS} and ρ_{FB} respectively.

Finally, the comparison of the parameters of the fit to a quadratic function, p_1 and p_2, of the rigidity scale obtained from helium, carbon, and oxygen in ISS geographical position coordinates is presented in 5.16. Carbon and oxygen rigidity scales are consistent with the helium one within the uncertainties and, therefore, the rigidity scale corrections determined for the helium sample will be used for the carbon and oxygen events. This prescription provides a more precise determination of the rigidity scale corrections due to the larger size of the spillover fraction of helium events.

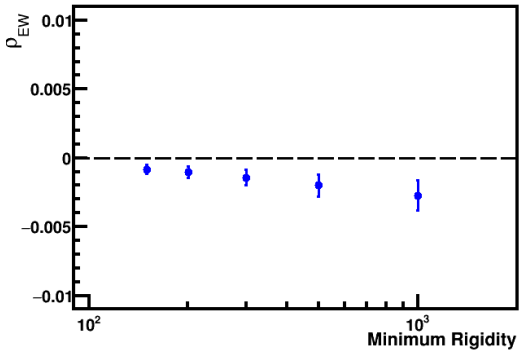

(a) East-West

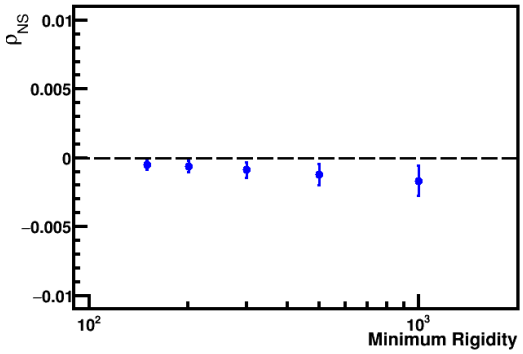

(b) North-South

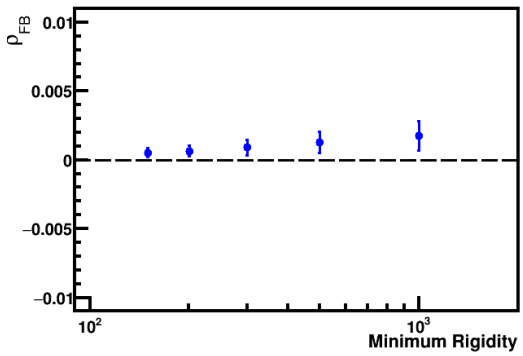

(c) Forward-Backward

Figure 5.15: Helium rigidity scale correction determined in ISS geographical position coordinates and transformed into galactic coordinates for the ρ_{EW} (a), ρ_{NS} (b) and ρ_{FB} (c).

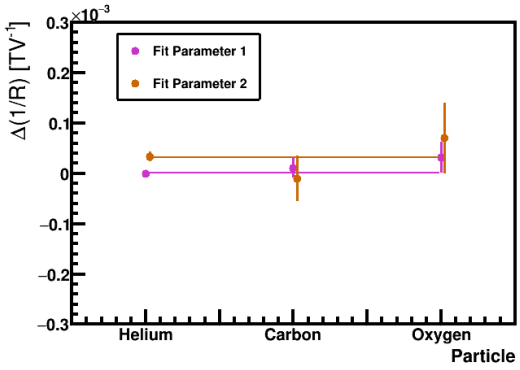

Figure 5.16: Comparison of the parameters of the fit to a quadratic function, p_1 and p_2 of the rigidity scale determined in helium, carbon and oxygen in ISS geographical position coordinates. Results are consistent with a common value within the uncertainties.

5.6 Results on the Light Primary Nuclei Anisotropy

The measurement of the light primary nuclei anisotropy is performed by correcting the exposure time map with the efficiency and rigidity scale corrections. As discussed in sections 5.4 and 5.5 the efficiency and rigidity scale corrections determined in helium will be applied to carbon and oxygen. A detailed description of the analysis and the impact of the corrections will be presented first for the helium events. Then, final results for carbon and oxygen events will be reported.

5.6.1 Helium

ISS Geographical Position Coordinates

As presented in section 4.6.1 the one-dimensional study provides a first estimation at the impact of the most relevant efficiency corrections required in the anisotropy analysis.

The helium relative variation of the raw rate together with the total efficiency as a function of the cosine of the geomagnetic colatitude for rigidities $R > 18$ GV is shown in figure 5.17a. The raw rate presents a drop at high latitudes of $\sim 0.2\%$ (much smaller than in the case of electrons). The fit to a quadratic function of the rate and total efficiency variation show consistent results, which is quantified with the p_1 and p_2 parameters. This is better observed in the ratio, figure 5.17b, where the fit parameters are consistent with zero and, therefore, the North-South direction is expected to be fully corrected by the efficiency corrections in positional coordinates.

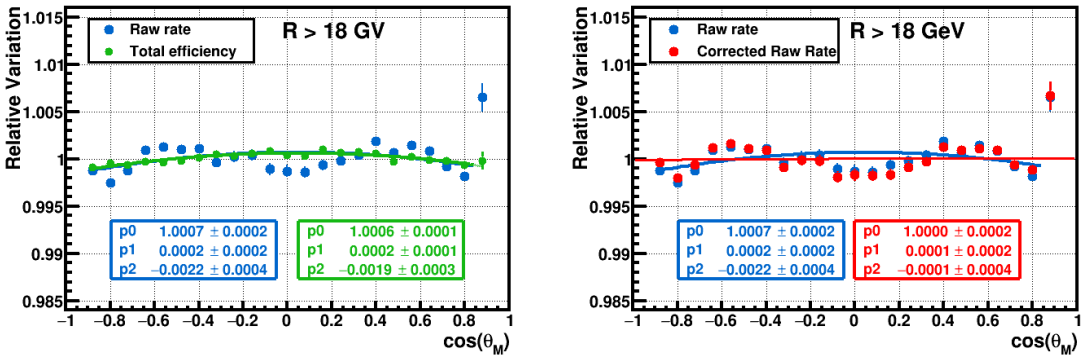

(a) (b)

Figure 5.17: (a) Helium relative variation of the raw rate (blue) together with the total efficiency (green) as a function of the geomagnetic colatitude (a) and corrected raw rate (b) for rigidities $R > 18$ GV. A small drop of ~ 0.2 % in the rate at high latitudes is observed. The fit to a quadratic function of both distributions show consistent results, which is quantified with the p_1 and p_2.

For the spherical harmonic analysis, the correction of the exposure time map by means of the total efficiency map determined in section 5.4.2 allows to compute the isotropic reference map. In addition, the effect of the rigidity scale determined in section 5.5 has been included to correct the exposure time.

The determination of the multipole components is carried out by using the binned-likelihood fit from equation 3.38 for the different rigidity ranges. In order to see the impact of the efficiency corrections in the components the corrected and uncorrected exposure time maps are used as a reference. The results are shown for the ρ_{NS} and ρ_{2+0} components in figure 5.18, which are the ones that mainly project into galactic coordinates. The top panel presents the components for the different rigidity ranges and the bottom panel the deviations with respect to isotropy in terms of standard deviations for each data point.

Significant deviations are observed for the uncorrected ρ_{NS} component, especially at high rigidities. The parametrization of the efficiency corrections and, in particular the use of a logistic function for the L1 picking selection efficiency (see section 5.4.2), reduces the deviations (figure 5.18a). In the case of the ρ_{2+0} component, figure 5.18b, the efficiency corrections completely account for the deviations at low rigidities whereas for high rigidities the rigidity scale correction fully corrects the observed data points.

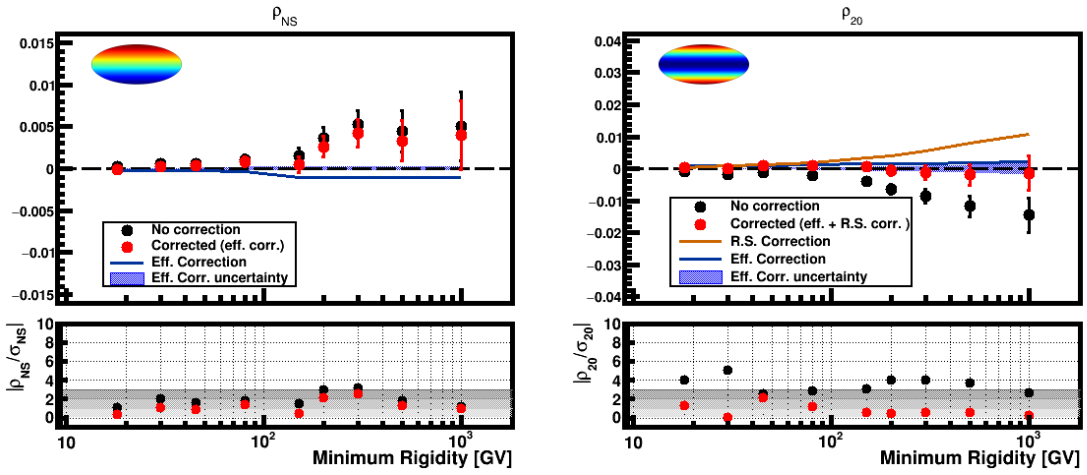

(a) (b)

Figure 5.18: Helium multipole components ρ_{NS} (a) and ρ_{2+0} (b) in ISS geographical position coordinates where no corrections (black dots), and efficiency + rigidity scale corrections (red dots) are included. The error bars in the dots stand for the statistical uncertainties. Efficiency corrections are shown as a blue line with its uncertainty displayed as a blue band and the rigidity scale corrections as a brown line. Finally, in the bottom panel the deviations from isotropy are evaluated in terms of standard deviations.

In order to quantify the possible contribution of higher multipoles in the analysis, the same significance estimator previously defined in equation 4.9 can be constructed. As an example, figure 5.19 shows the distribution in the sky of measured helium events, and the isotropic reference. The significance map for rigidities $R > 18$ GV is shown in figure 5.20a. In addition, figure 5.20b shows the significance histogram which is consistent with a normal distribution.

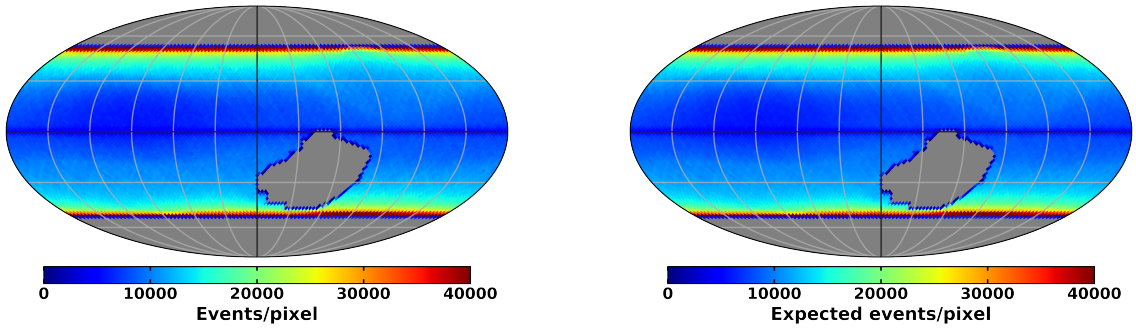

(a) (b)

Figure 5.19: Helium skymap distributions of measured (a) and expected events (b) for rigidities $R > 18$ GV in ISS geographical position coordinates.

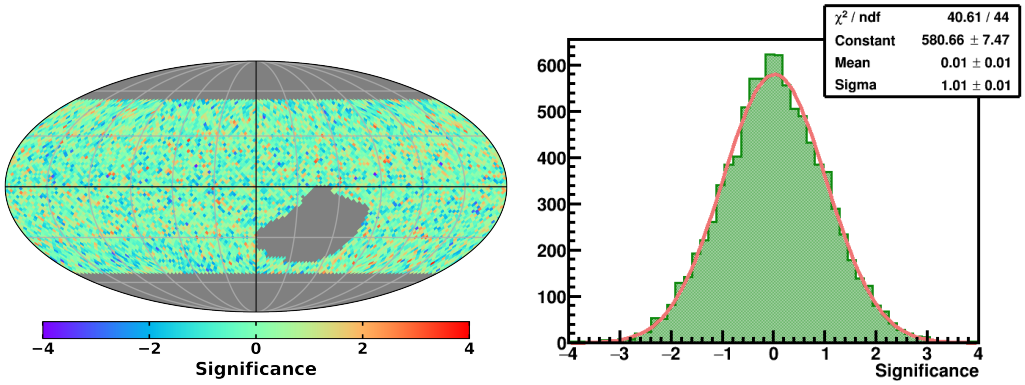

(a) (b)

Figure 5.20: Helium significance skymap (a) and distribution (b) for rigidities $R > 18$ GV in ISS geographical position coordinates.

Galactic Coordinates

The precise understanding of the analysis in ISS geographical position coordinate systems allows to extend the procedure to the physical reference system, where a signal could be measured. The skymap of measured events, as well as the corrected and uncorrected reference, are introduced in the binned-likelihood to retrieve the multipole components in galactic coordinates. The inclusion of the rigidity scale corrections is also considered for the corrected reference map, in particular, it is obtained by means of the matrix transformation from ISS geographical position to galactic coordinates, as stated in section 5.5.

Figure 5.21 shows the ρ_{EW} and ρ_{2-2} components which are the ones that receive the biggest contributions from the North-South direction in ISS geographical position. The top panel presents the components for the different rigidity ranges, and the bottom panel the deviations with respect to isotropy in terms of standard deviations for each data point. The uncorrected results show smaller deviations than those shown in the previous section from isotropy due to dilution of the components from geographical to galactic coordinates, especially in the quadrupole. The deviations at high rigidities in ρ_{EW} component are accounted with the corrections coming from the L1 picking selection efficiency parametrization and the rigidity scale corrections (figure 5.21a). In figure 5.21b, the rigidity scale correction also accounts for the small deviations at high rigidities. Therefore, the corrected components show consistent values with isotropy for all rigidity ranges.

Similar to the ISS geographical position, the same significance estimator can be used to confirm that there are no significant contributions from higher multipoles and the skymap is consistent with isotropy. Figure 5.22 shows the distributions in the sky of measured helium events, and the isotropic reference for rigidities $R > 18$ GV in galactic coordinates. No structures are found in the significance map, figure 5.23a, and figure 5.23b show consistent results with a normal distribution.

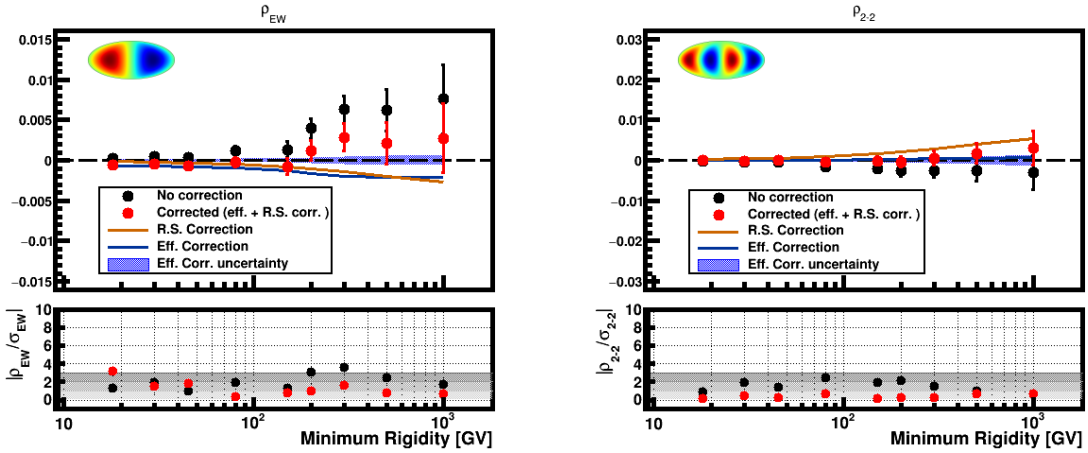

(a) (b)

Figure 5.21: Helium multipole components ρ_{EW} (a) and ρ_{2-2} (b), in galactic coordinates where no corrections (black dots), and efficiency + rigidity scale corrections (red dots) are included. The error bars in the dots stand for the statistical uncertainties. Efficiency corrections are shown as a blue line with its uncertainty displayed as a blue band and the rigidity scale corrections as a brown line. In the bottom panel the deviations from isotropy are evaluated in terms of standard deviations.

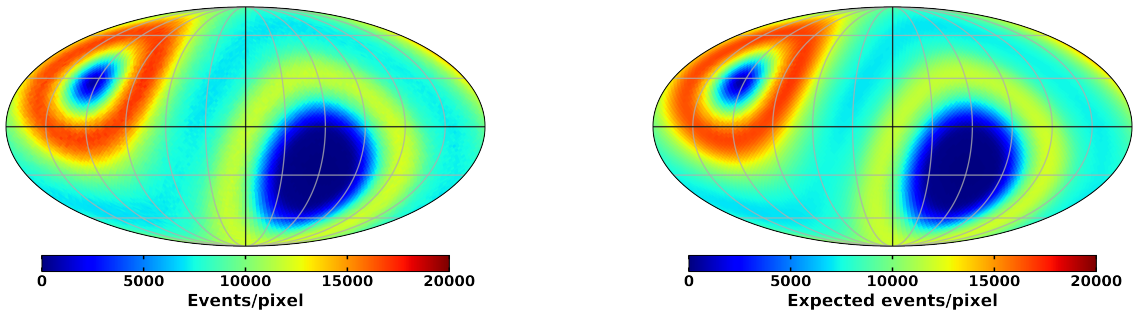

(a) (b)

Figure 5.22: Helium skymap distributions of measured (a) and expected events (b) for rigidities $R > 18$ GV in galactic coordinates.

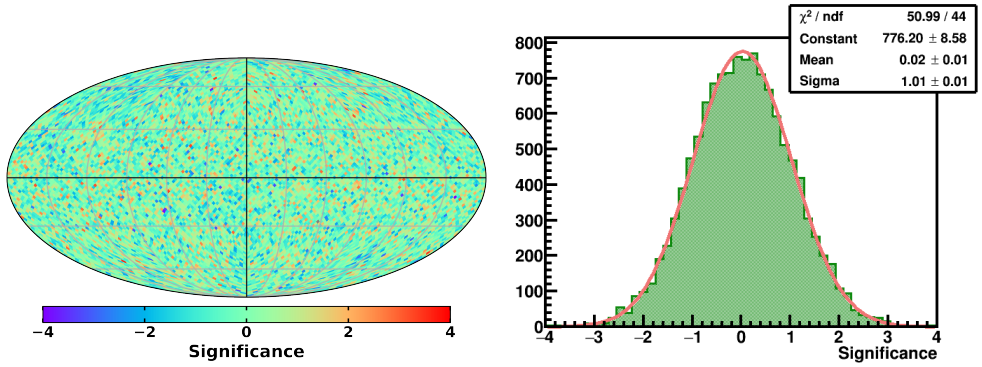

(a) (b)

Figure 5.23: Helium significance skymap (a) and distribution (b) for rigidities $R > 18$ GV in galactic coordinates.

Results on the Helium Dipole Components in Galactic Coordinates

The determination of the corrected dipole components for helium events follows the same procedure of the electron analysis. In particular, the skymap distributions of measured and expected events (exposure time map corrected by efficiency and rigidity scale corrections) are included in the binned-likelihood fit defined in equation 3.38 to obtain the corrected dipole components.

In this case, the sources of systematic uncertainties are the following:

- **Efficiency Corrections:** The statistical uncertainty of the contributing individual efficiency corrections are propagated.
- **Election of Significant Corrections:** As in the case of electrons, the effect that a variation of ± 0.2 around the threshold value in figure 5.4 has on the total efficiency correction is considered as an additional source of systematic uncertainties.
- **Rigidity Scale:** The uncertainty associated with the correction, obtained by means of the transformation from ISS geographical position, is propagated in the systematic uncertainties.

Figure 5.24a shows the total equivalent systematic uncertainty together with each contribution, where the uncertainty associated with the efficiency and the rigidity scale corrections are the dominant ones. In addition, the comparison between the statistical and the systematic uncertainties is shown in figure 5.24b. As can be seen, the statistical uncertainty dominates in the whole rigidity range.

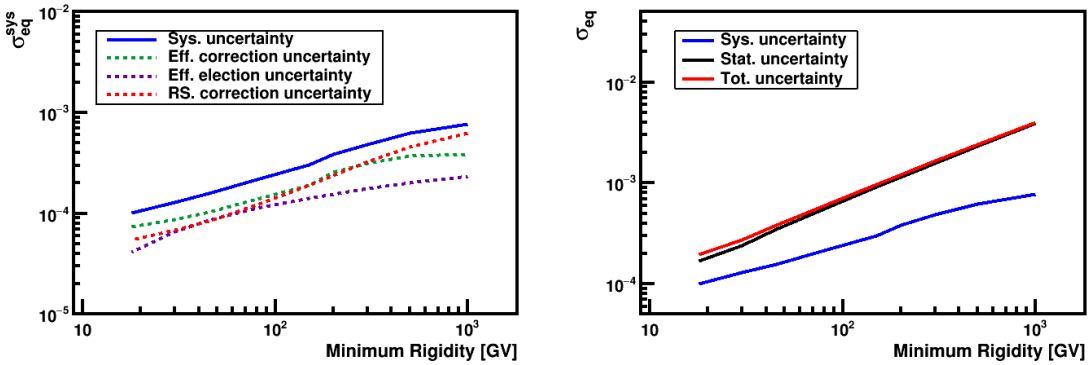

(a) (b)

Figure 5.24: (a) Different contributions to the total equivalent systematic uncertainties (blue solid line): efficiency corrections (green dotted line), efficiency election (purple dotted line), and rigidity scale correction (red dotted line). (b) Comparison of the statistical, systematic and total equivalent uncertainties on the helium dipole components.

The three dipole components, ρ_{EW}, ρ_{NS}, and ρ_{FB} as a function of the minimum rigidity are shown in figure 5.25 for helium events. No significant deviations from isotropy are observed. The dipole amplitude is computed using the three dipole components, figure 5.26a, and for rigidities $R > 200GV$ the dipole amplitude corresponds to $\delta_M(200GV) = 0.21$ %.

Since the results are consistent with isotropy the 95 % C.I. upper limits on the dipole amplitude can be established (figure 5.26b). For rigidities $R > 200GV$ the upper limit is $\delta_{UL}^{95\%}(200GV) = 0.35\%$.

The numerical results corresponding to the helium dipole anisotropy are presented in the table D.5 from appendix D.2.

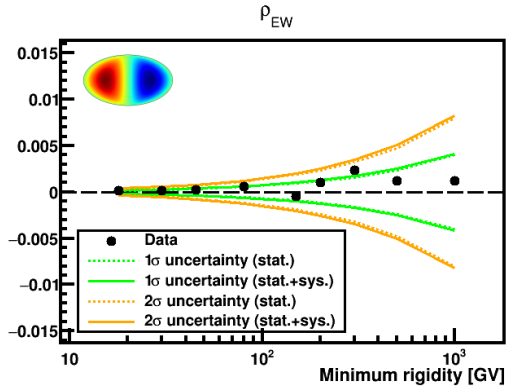

(a) East-West

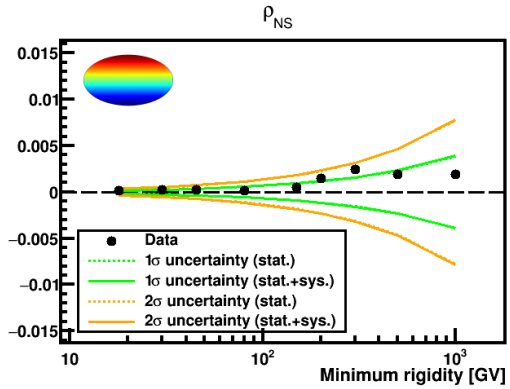

(b) North-South

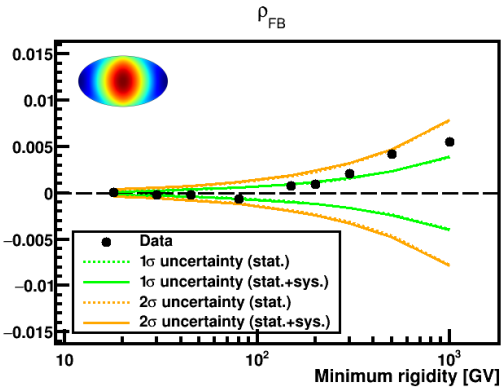

(c) Forward-Backward

Figure 5.25: Helium dipole components, EW, NS and FB in galactic coordinates where the 1 and 2-sigma deviations from isotropy (green and yellow, respectively) corresponding to the statistical (dotted line) and total (solid line) uncertainties are shown.

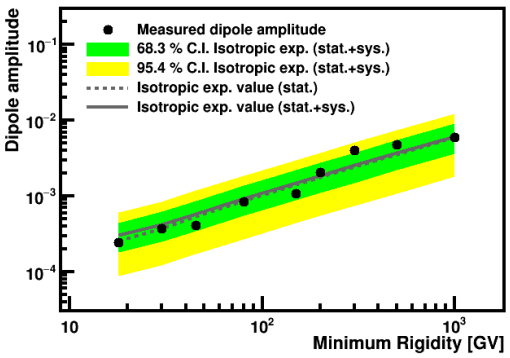

(a) Dipole Amplitude

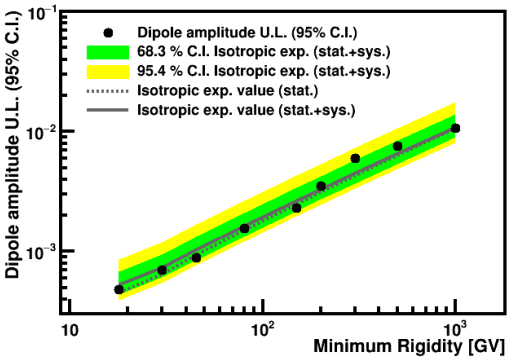

(b) Upper Limit

Figure 5.26: Helium measured dipole amplitude (a) and 95% C.I. upper limit (b) as a function of the minimum rigidity in galactic coordinates. The 1 and 2-sigma total uncertainty bands are shown in green and yellow respectively. The expected value from isotropy considering the statistical (dotted line) and the statistical + systematic (solid line) uncertainties is also displayed.

5.6.2 Carbon and Oxygen

As discussed in the introduction, the carbon and oxygen anisotropy will make use of the same corrections applied on helium. Then, the skymap distributions of measured and expected carbon and oxygen events are included in the binned-likelihood fit from equation 3.38 to obtain the corrected and uncorrected dipole components.

The impact of the helium corrections in the multipole components is less significant than for the helium anisotropy due to the large statistical errors associated to the smaller size of the carbon and oxygen samples. As in helium, the systematic uncertainties are much below the statistical uncertainties, which dominate in the whole rigidity range. Consequently, results on the dipole components including both statistical and systematic uncertainties are consistent with isotropy. The figures describing the aforementioned results can be found in appendix D.

The dipole amplitude for each rigidity range is computed using the dipole components and the results are found to be compatible with the isotropic expectation value within the statistical and systematic uncertainties, figures 5.27a and 5.27b. For rigidities $R > 200$ GV the measured dipole amplitude is $\delta_M(200GV) = 0.89$ % and $\delta_M(200GV) = 0.9$ % for carbon and oxygen respectively.

Since no deviation from isotropy are obseved, the 95 % C.I. upper limits on the dipole amplitude can be established, figures 5.28a and 5.28b. Again, for rigidities $R > 200$ GV the upper limit is $\delta_{UL}^{95\%}(200GV) = 1.66$ % and $\delta_{UL}^{95\%}(200GV) = 1.68$% for carbon and oxygen respectively.

The numerical results corresponding to the carbon and oxygen dipole anisotropy are presented in the tables D.6 and D.7 from appendix D.2.

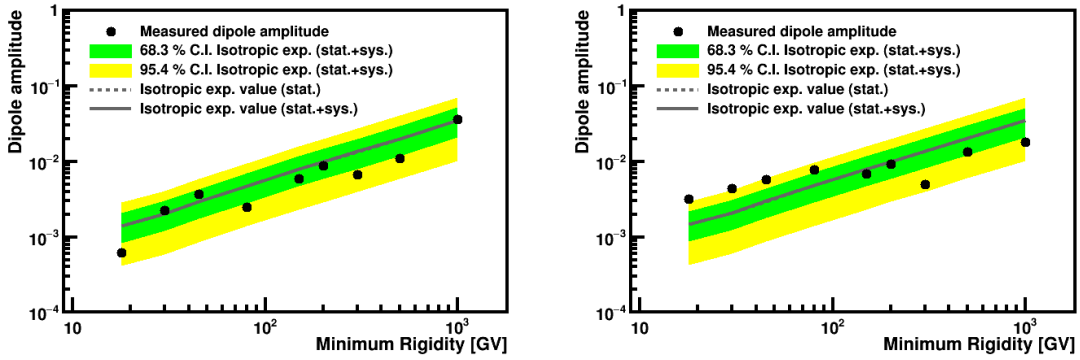

(a) Carbon Dipole Amplitude (b) Oxygen Dipole Amplitude

Figure 5.27: Carbon (a) and oxygen (b) measured dipole amplitude as a function of the minimum rigidity in galactic coordinates. The 1 and 2-sigma total uncertainty bands are shown in green and yellow respectively. The expected value from isotropy considering the statistical (dotted line) and the statistical + systematic (solid line) uncertainties is also displayed.

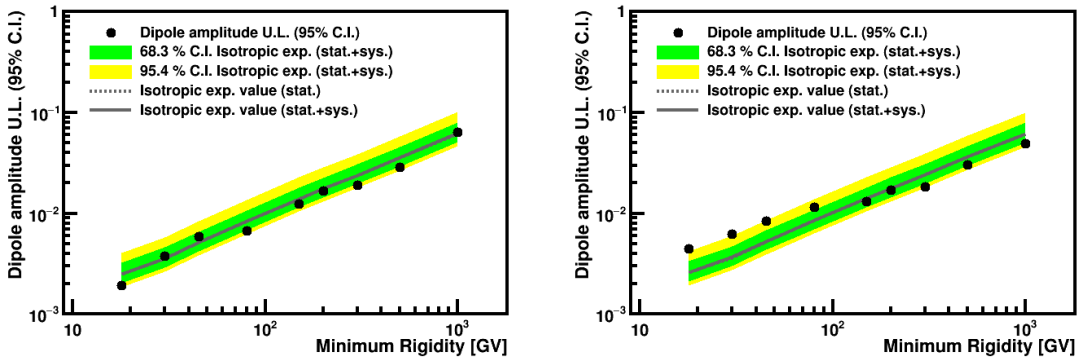

(a) Carbon Upper Limit (b) Oxygen Upper Limit

Figure 5.28: Carbon (a) and oxygen (b) 95% C.I. upper limit as a function of the minimum rigidity in galactic coordinates. The 1 and 2-sigma total uncertainty bands are shown in green and yellow respectively. The expected value from isotropy considering the statistical (dotted line) and the statistical + systematic (solid line) uncertainties is also displayed.

5.7 Updates on the Proton Anisotropy

Results on the proton anisotropy were reported in [228] for 5 years of data taking. In this section an update of the proton anisotropy analysis with 8.5 years of data is presented.

The analysis performed on protons is conceptually the same to the one shown for light nuclei, however, significant differences are observed and the one-dimensional approach can be used to illustrate them. Figure 5.29a shows the comparison between the proton and helium relative variation of the raw rates as a function of the cosine of the geomagnetic colatitude for rigidities $R > 18$ GV. Significant differences are observed in both the p_1 and p_2 parameters of the fit to a quadratic function, which are associated to a much bigger variation of the efficiencies at the different geographical locations for the proton sample. As an example, the relative variation of the two most relevant efficiencies for protons and helium are compared (trigger efficiency for protons and L1 picking selection efficiency for helium), figure 5.29b. As can be seen, the proton trigger efficiency shows a drop of ~ 3 % at high latitudes whereas the helium L1 picking selection efficiency shows a drop of the $\sim 0.2\%$ at high latitudes [5]. The trigger efficiency variation in protons is due to a higher sensitivity to accidentals firing the ACCs. This effect becomes more relevant at high latitudes where the rate of incoming particles increases. Light primary nuclei fire a different trigger which is less sensitive to this effect.

In order to minimize the effect of the trigger variation along the ISS orbit for protons two strategies have been followed. On the one hand, the Full Span sample has been used to avoid very inclined trajectories (so no ACCs are fired), and to increase the fraction of events firing the electron trigger, so that the ACC veto is disabled. On the other hand, the proton analysis can be improved by constraining the data sample between the geomagnetic locations $-0.8 < cos(\theta_M) < 0.8$. This allows to exclude regions where this effect is more important due to the high rate of incoming particles with a moderate reduction in the sample size (~ 8 %). As a consequence, the trigger efficiency corrections will be reduced together with the corresponding systematic uncertainty. As an illustration, figures 5.29a and 5.29b show the relative variation of the proton raw rate and trigger efficiency described by a quadratic function between $-0.8 < cos(\theta_M) < 0.8$. As can be observed, the limitation of the analysis to smaller latitudes reduces the amplitude in the p_1 and p_2 parameters.

The analysis of the proton dipole anisotropy for 8.5 years of data taking follows the same

[5] The trigger efficiency variation on protons is absence in helium.

procedure presented in the previous sections of this thesis. The impact of the efficiency corrections is first investigated in ISS geographical position coordinates, and then extended to galactic coordinates. Then, the skymap distributions of measured and expected events (corrected exposure time map) provides the information to obtain the corrected multipole components. Finally, the dipole components and dipole amplitude are calculated. For this work, only results on the dipole anisotropy are presented; the most relevant figures of the analysis can be found in appendix D.

Figures 5.30a, 5.30b and 5.30c components show the ρ_{EW}, ρ_{NS} and ρ_{FB} including statistical and systematic uncertainties respectively. The dipole amplitude is shown in figure 5.31a for each rigidity range. No deviations from isotropy are found. For rigidities $R > 200$ GV the dipole amplitude is $\delta_M(200GV) = 0.19\%$.

The compatibility with isotropy allows to establish 95 % C.I. upper limits to the dipole amplitude for each rigidity range, figure 5.31b. For rigidities $R > 200$ GV the limit is $\delta_{UL}^{95\%}(200GV) = 0.35\%$.

The numerical results corresponding to the proton dipole anisotropy are presented in the table D.8 from appendix D.2.

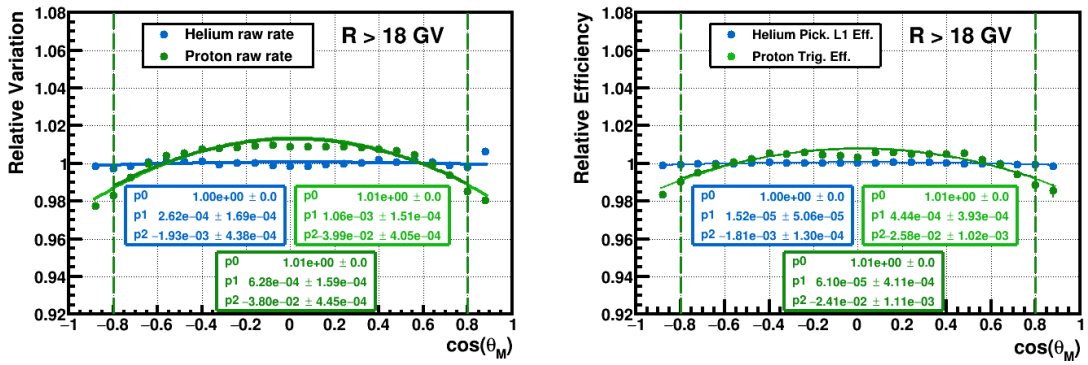

(a) (b)

Figure 5.29: (a) Comparison between the proton (light green) and helium (blue) relative variation of the raw rates as a function of the geomagnetic colatitude for rigidities $R > 18$ GV. (b) Comparison between the proton relative variation of the trigger efficiency (light green) and helium relative variation of the picking L1 selection efficiency (blue) as a function of the geomagnetic colatitude. Both figures also show the proton relative variation of the raw rate and trigger efficiency (dark green) constrained between $-0.8 < cos(\theta_M) < 0.8$. All distributions are fitted to a quadratic function and, in particular, a general improvement in the p_1 and p_2 parameters for the protons between $-0.8 < cos(\theta_M) < 0.8$ is observed.

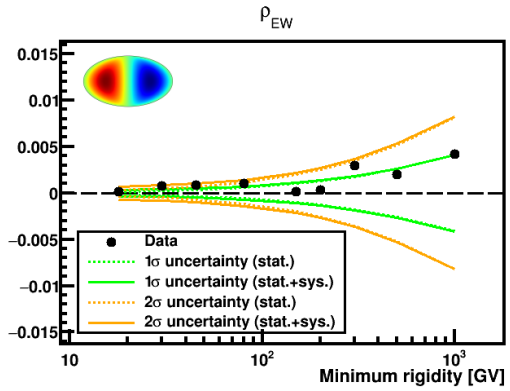

(a) East-West

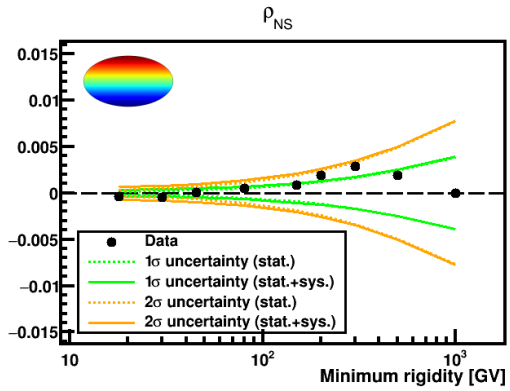

(b) North-South

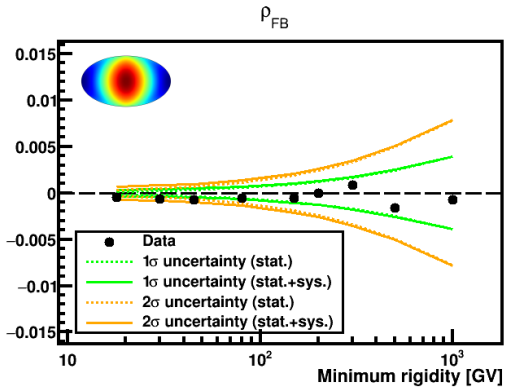

(c) Forward-Backward

Figure 5.30: Proton dipole components, *EW*, *NS* and *FB* in galactic coordinates where the 1 and 2-sigma deviations from isotropy (green and yellow, respectively) corresponding to the statistical (dotted line) and total (solid line) uncertainties are shown.

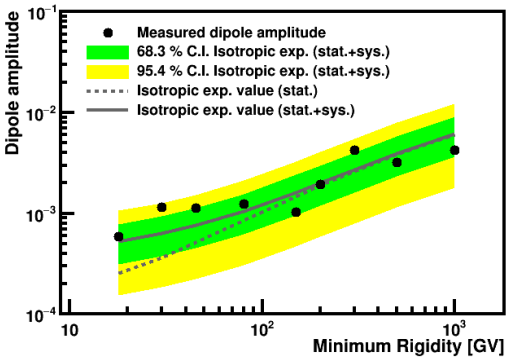

(a) Dipole Amplitude

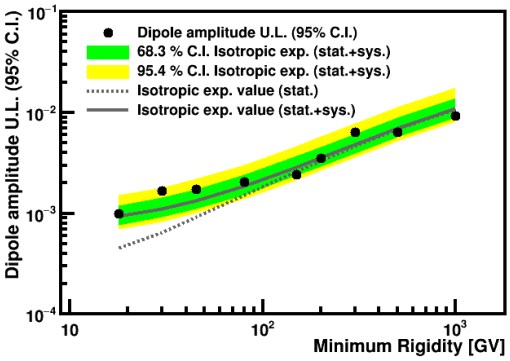

(b) Upper Limit

Figure 5.31: Proton measured dipole amplitude (a) and 95% C.I. upper limit (b) as a function of the minimum rigidity in galactic coordinates. The 1 and 2-sigma total uncertainty bands are shown in green and yellow respectively. The expected value from isotropy considering the statistical (dotted line) and the statistical + systematic (solid line) uncertainties is also displayed.

Conclusions and Outlook

"The important thing is to not stop questioning. Curiosity has its own reason for existing."

— Albert Einstein

The recent observations of AMS-02 have shown unexpected features in the energy spectrum of the cosmic ray fluxes that challenge the current understanding of the acceleration and propagation mechanisms. Among the many models proposed to explain the spectral features, those requiring the presence of nearby sources to account for the observed effects are of special interest. In particular, pulsars are the leading candidates for the positron excess and the models predict a dipole anisotropy up to 1% at 10 GeV. Therefore, the measurement of the directionality of cosmic rays provides an additional characterization to the energy dependence of the fluxes that may allow distinguishing among the different models.

The measurement of anisotropies with space-borne detectors, like AMS-02, profits from a nearly full sky coverage to recover the 3-dimensional dipole anisotropy. Furthermore, the excellent particle identification and energy reconstruction allow for a precise measurement of the directionality of the different cosmic ray species.

The determination of the directionality of the fluxes mainly relies on the construction of an isotropic reference map which is compared with the map of measured events. The observation of any significant deviation between these maps will be regarded as a signal.

In this thesis, the techniques developed to obtain the isotropic reference map in the search for anisotropies with AMS-02 and its application to different cosmic ray species have been presented. In particular, results on the dipole anisotropy for electrons, positrons, protons, helium, carbon, and oxygen for 8.5 years of data taking have been reported.

The method developed in this thesis relies on the division of the detector's field of view into small pixels, where each one provides an almost full sky coverage. This approach allows constructing individual exposure time and event maps for each pixel such that a binned-likelihood fit is used to compare both distributions and obtain the dipole components. The possible spurious effects arising from the geographical dependences of the detector's behavior are taken into account by means of the efficiency correction maps, which can be understood in the non-physical reference system ISS geographical positions. Once these effects are understood, the method is directly applied in galactic coordinates, where the measurement of the anisotropy is performed to investigate signals

of physical origin in the Galaxy.

For electrons and positrons, intermediate results obtained with a cut-based selection on a 6.5-year sample have been included in two recent AMS publications in Physical Review Letters.

The electron and positron measurement of the anisotropy for 8.5 years has been optimized in order to increase the available statistics and improve the sensitivity to pulsar predictions. The optimization is based on the inclusion of a template fit method to separate the leptons from the proton background as well as an improvement in the selection criteria. Results on the optimized analysis for electrons and positrons in galactic coordinates are consistent with isotropy and 95% C.I. upper limits are established. In the lowest energy range $16 < E < 500$ GeV the corresponding upper limits are:

$$\textbf{Electrons: } \delta_{e^-} < 0.37\%$$
$$\textbf{Positrons: } \delta_{e^+} < 1.70\%$$

The proton, as well as the light primary nuclei anisotropy, for 8.5 years of data taking have been also presented. The latter results constitute the first measurement of the anisotropy of individual cosmic ray species heavier than protons and provide additional constraints to the models. Results on the dipole anisotropy for the four species in galactic coordinates are consistent with isotropy and 95% C.I. upper limits to the dipole amplitude are established. For rigidities $R > 200$ GV, the corresponding limits are:

$$\textbf{Proton: } \delta_p < 0.35\%$$
$$\textbf{Helium: } \delta_{He} < 0.35\%$$
$$\textbf{Carbon: } \delta_C < 1.66\%$$
$$\textbf{Oxygen: } \delta_O < 1.68\%$$

The upper limits obtained in this work for all particle species are dominated by the available statistics and are, thus, expected to improve in the coming years thanks to the extended operation of AMS-02 on the ISS to at least 2028. For some of these measurements, this improvement will allow to challenge the model predictions. For instance, in the case of the positron anisotropy, figure 5.32, the expected sensitivity for the energy range $16 < E < 500$ GeV by the end of the ISS mission will allow distinguishing between the prediction of the pulsar model displayed in the figure and the isotropic model favored by the dark matter scenario for the positron excess.

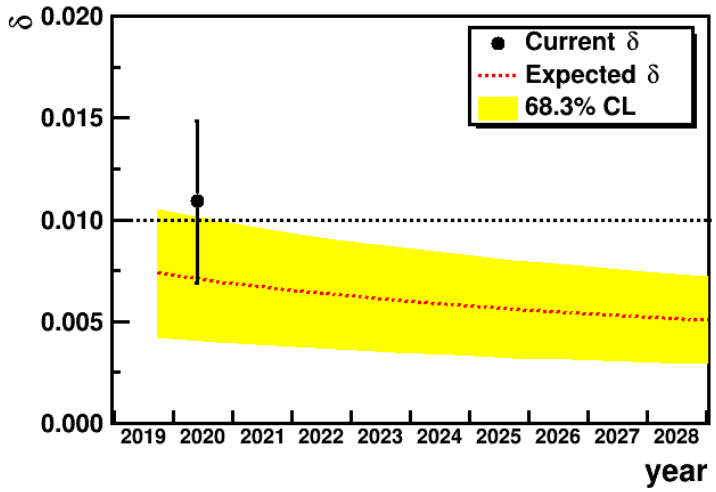

Figure 5.32: Projection of the expected positron dipole amplitude for $16 < E < 500$ GeV up to the end of the ISS (currently scheduled in 2028). The dipole amplitude (black dot) together with the isotropic expectation (dashed red line) and the one sigma band (yellow band) are displayed. Predictions from a pulsar model are also shown [145].

Conclusiones y Perspectivas de Futuro

"Los imposibles de hoy serán posibles mañana."

— Konstantin Tsiolkovsky

Las observaciones más recientes presentadas por AMS-02 muestran características inesperadas en los flujos que desafían el entendimiento de los actuales mecanismos de aceleración y propagación. Entre los muchos modelos propuestos para explicar las características espectrales, aquellos que requieren la presencia de fuentes cercanas para dar cuenta de los efectos observados son de especial interés. En concreto, los púlsares son los candidatos favoritos para el exceso de positrones y los modelos predicen una anisotropía dipolar de hasta un 1% a 10 GeV. Por tanto, la medida de la direccionalidad de los rayos cósmicos proporciona una caracterización adicional a la dependencia energética de los flujos que podría permitir distinguir entre las distintas predicciones.

La medida de la anisotropía con detectores en el espacio, como AMS-02, se beneficia de su cobertura casi completa para recuperar la anisotropía dipolar tridimensional. Además, la excelente identificación de las partículas y su reconstrucción de la energía permite realizar una medida precisa de la direccionalidad de las distintas especies de rayos cósmicos.

La determinación de la direccionalidad de los flujos se basa principalmente en la construcción de un mapa de referencia isótropo que se compara con el mapa de sucesos medidos. La observación de cualquier desviación significativa entre los mapas se interpretará como una señal.

En esta tesis, se han presentado las técnicas desarrolladas para obtener el mapa de referencia isótropo en la búsqueda de anisotropías y su aplicación a distintas especies de rayos cósmicos. En concreto, se han mostrado los resultados de la anisotropía dipolar para electrones, positrones, protones, helio, carbono, y oxígeno para 8.5 años de toma de datos.

El método desarrollado en esta tesis se basa en la división del campo de visión del detector en pequeños píxeles, donde cada uno proporciona una cobertura casi completa del cielo. Esta estrategia permite construir mapas de tiempo de exposición y sucesos individuales para cada uno de los píxeles, de tal modo, que un ajuste binned-likelihood se usa para comparar ambas distribuciones y obtener las componentes dipolares. Los posibles efectos espurios procedentes de las dependencias geográficas del comportamiento del detector se tienen en cuenta mediante los mapas de eficiencias, que se pueden entender en el sistema de referencia no físico asociado a la posición geográfica de la ISS. Una vez estos efectos se han entendido, el método se aplica directamente en coordenadas

galácticas, donde la medida de la anisotropía se realiza para investigar señales con origen físico galáctico.

Para electrones y positrones, los resultados intermedios obtenidos con una selección basada en cortes sobre una muestra de 6.5 años han sido incluidos en dos recientes publicaciones de AMS en Physical Review Letters.

La medida de la anisotropía de electrones y positrones para 8.5 años ha sido optimizada para aumentar la estadística disponible y poder mejorar la sensibilidad a las predicciones de los púlsares. La optimización se basa tanto en la inclusión de un método basado en ajustes a patrones para separar a los leptones del fondo de protones como en la mejora de los criterios de la selección. Los resultados del análisis optimizado para electrones y positrones en coordenadas galácticas son consistentes con isotropía y se establecen límites superiores al 95% de nivel de confianza. En el rango más bajo de energía $16 < E < 500$ GeV los correspondientes límites superiores son:

Electrones: $\delta_{e^-} < 0.37\%$
Positrones: $\delta_{e^+} < 1.70\%$

También, se ha presentado la anisotropía de tanto los protones como los núcleos primarios ligeros. Los resultados de los últimos constituyen la primera medida de la anisotropía de las especies individuales de rayos cósmicos más pesadas que protones y proporcionan restricciones adicionales a los modelos. Los resultados de la anisotropía dipolar para las cuatro especies en coordenadas galácticas son consistentes con isotropía y se establecen límites superiores al 95% de nivel de confianza. Para el rango de rigidez $R > 200$ GV, los correspondientes límites son:

Protones: $\delta_p < 0.35\%$
Helio: $\delta_{He} < 0.35\%$
Carbono: $\delta_C < 1.66\%$
Oxígeno: $\delta_O < 1.68\%$

Los límites superiores obtenidos para todas las especies de partículas están dominados por la estadística disponible y se espera que mejoren en los siguientes años gracias a la prolongación de la toma de datos de AMS-02 en la ISS hasta al menos 2028. Por ejemplo, en el caso de los positrones, figura 5.33, la sensibilidad esperada en el rango de energía $16 < E < 500$ GeV al final de la misión de la ISS permitirá distinguir entre la predicción del modelo de púlsar mostrado en la figura y el modelo de isotropía favorecido por el escenario de materia oscura en el exceso de positrones.

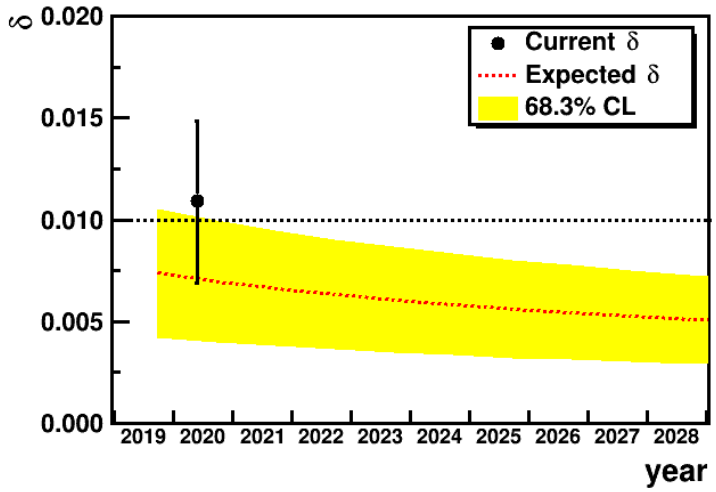

Figure 5.33: Proyección de la amplitud dipolar esperada en positrones para $16 < E < 500$ GeV hasta el final de la ISS (actualmente programado en 2028). Se muestra la amplitud dipolar (punto negro) junto con el valor esperado por isotropía (línea roja discontinua) y la banda de una sigma (banda amarilla). La predicción de un modelo de púlsares también se incluye [145].

Acknowledgements

"The good times of today are the sad thoughts of tomorrow."

— Bob Marley

El trabajo que se presenta en estas páginas no es más que el cúmulo de un montón de traspiés, tropiezos, caídas, batacazos y, si se me permite decirlo, más traspiés, tropiezos, caídas y batacazos. Pero no es solo eso, es una historia de superación, progreso y aprendizaje. Una historia de enseñanzas más allá del propio tema sobre el que esta obra versa. Honestamente, miro atrás y todavía veo al nervioso y recién incorporado Miguel dando sus primeros pasos en la que sería una de las mayores aventuras hasta la fecha. De hecho, mi perspectiva desde el presente me trae recuerdos de cortos fotogramas con todas las experiencias pasando a gran velocidad (tal vez la de la luz). Por un momento, se siente como si las mismísimas ecuaciones de Einstein hubiesen actuado sobre mi persona. Es una sensación extraña, difícil de explicar. Al final, un proyecto de tales dimensiones trae muchas vivencias y sentimientos acumulados que, en gran parte, se deben a todas aquellas personas que me han acompañado durante este tiempo. Personas que han contribuido a que todo haya desembocado en buen cauce. Por todo esto, me gustaría dedicar este espacio para agradecéroslo. En fin, que ya me dejo de rollos. ¡Allá voy!

Antes de todo, me gustaría empezar agradeciendo al COVID-19 (sin olvidarme y lamentando todas las desgracias que ha desencadenado) haber aparecido justo en mi año de escritura. Sin ninguna duda, tu aparición y las consecuentes restricciones me han permitido concentrarme en un proyecto que, de otro modo, me hubiese costado muchísimo más. Sin ti, la procrastinación me hubiese invadido.

Dejando las tonterías, me gustaría comenzar agradeciendo a mis directores de tesis, Jorge y Miguel Ángel. Jorge, te agradezco que hayas compartido tus conocimientos, tu tiempo, y hayas puesto tanto esfuerzo y dedicación en mi trabajo. Miguel Ángel, muchas facetas he compartido contigo, has sido compañero estudiante de travesía, mentor, maestro, director y, ante todo, amigo. Sin ninguno de los dos, esto no hubiese sido posible.

También, agradecer al grupo de AMS todo su apoyo y sabiduría, los cuales me han servido para ser un mejor profesional y persona. Javier, Carlitos, Carlos Mañá, Manuel, Alberto (aunque ahora seas Bolonia) y Francesca.

Una parte muy importante de estos años ha sido toda aquella gente de la que me he rodeado y

con la que he compartido momentos en el CIEMAT. Primero, me gustaría dedicar unas pequeñas palabras a Héctor, Iker y Lourdes. Héctor, gracias por todos los buenos momentos en escuelas, conferencias, escalando y, sobre todo, por estar ahí escuchándome este último año. Iker, nunca olvidaré tu piedra, los caballeros tomatines de la mesa redonda, los secuestros de bebidas, tu infinidad de visitas en horario de trabajo, tu inestimable ayuda con el edificio 1, y las interesantes conversaciones sobre política internacional y Russians affairs. Lourdes, fichaje de último año (aunque nos conociésemos de antes) que ha resultado un éxito, mucha suerte en tu plan de este año. Finalmente, muchas gracias al resto: Edgar, José, Sergio, Martín, Irenes, Ana, Diana, Chiara, Adri, Julia y Rodrigo (los dos últimos recientemente incorporados a lo cuales les deseo lo mejor).

Como socio fundador del despachito, me enorgullece poder agradecer tanto a mis compañeros fundadores como a los nuevos fichajes su presencia durante la tesis. Me gustaría agradecer a Carlitos y Salvatore por dejarnos desocupada la cristalera, lo cual nos permitió construir la famosa área recreativa. Nunca olvidaré aquellos momentos jugando al ping-pong después de comer. Carmen que has sido compañera de infinidad de aventuras (conferencias, escuelas, reuniones, festivales de vino, festivales de música, investigaciones criminales, investigaciones de holgazanería y un gran etc.). Mab por soportarme desde los comienzos y aguantar mis innumerables preguntas con el papeleo de la autónoma. Lallena, por crear una gran piña en el CIEMAT. Juaaaaaaaaaaaaaaaaaaaaan, eres un crack. David y Pepe, no os he conocido mucho, pero espero dejar el despachito en buenas manos. Miguel Ángel, en demasiados párrafos quieres aparecer.

Igualmente, me gustaría agradecer a mis compañeros españoles de la colaboración Alejandro, Mónica y Ramón. En concreto, Alejandro te agradezco tu compañía en infinidad de eventos, tu disponibilidad para seguir mis planes de loco (tanto en Tenerife como en Ginebra) y, por supuesto, tu particular sentido del humor.

I would also like to thank my friends from the collaboration Mat, Huy and Maura. Mat, thank you for hosting me and sharing your time while I was in Boston. Maura, thank you for making my stays at CERN an amazing experience with your barbeques, picnics etc. Huy, you are the best lead, even Russians tell us off when you are in charge.

Me gustaría dedicar unas líneas a mis amigos de la complu. Dolado, hemos pasado juntos por las distintas etapas del doctorado, incluida la deposición. Gracias por esos desayunos y espero que continúes escalando con nosotros. Pablo, Alex y Oli, compañeros de carrera, máster y doctorado, siempre me alegra poder veros. Lucía y Jen, me alegro mucho de que hayamos conservado la relación hasta ahora, vuestros chats me han ayudado mucho. Lordén y Fran, aunque nos veamos con menos frecuencia, siempre me hace ilusión veros y, por supuesto, matar unos zombis ya que estamos.

Sin duda, mis amigos de infancia han jugado un papel muy importante y tienen que aparecer en estas páginas. Sergio, amigo íntimo, hermano, consejero y apoyo siempre que lo necesito; llegaremos a los 97 y bailaremos en la tumba de Lizi. Pallas, inestimable amigo que representa un foco de admiración y superación. Irene, madre que siempre cuida de todo el grupo. Charly, tu sonrisa y presencia siempre alegra nuestros corazones, pero, por favor, la próxima vez que hagamos una pelea de dinosaurios intenta no romperme el dedo. Alvariwi, siempre estás dispuesto a escuchar y ayudar, pero me gustaría verte más.

Me gustaría mencionar a mis compañeros de la Tríada Diego y Héctor. Con vosotros he conocido una naturaleza distinta a la del Universo, pero más cercana, más tangible; la naturaleza de la Madre Tierra. Infinidad de aventuras, experiencias, y recuerdos se acumulan durante estos años. También, muchos proyectos juntos, unos que han resultado más satisfactorios (b..at), y otros que menos. Espero que sigamos por muchos años descubriendo nuestro planeta.

Este párrafo está dedicado a mis amigos roleros con los cuales he pasado grandes momentos. Gayu, nos conocemos de hace muchos años y siempre has estado ahí cuando te he necesitado. Te considero una parte importante en mi vida. Artu, siempre alegre, motivado, ilusionado y dispuesto

a alegrarnos con tus historias. Fredy, estos años has estado un poco más ausente, pero te quiero igual y te deseo mucha suerte con el futuro.

Por supuesto, más gente ha ayudado a que este proyecto sea posible. Alba, nos conocemos de hace muchos años y siempre hemos tenido una gran relación; espero que esto continúe. Andrea y Paco, he disfrutado mucho vuestra presencia y cada paso nuevo que dais en vuestras vidas me llena de alegría. Espero que este paso que doy yo os la proporcione a vosotros también. Cristina, nos conocemos desde hace bastante poco, pero preveo una gran amistad. Gracias por brindarme tu compañía en un verano genial antes de empezar la escritura.

Благодарю матушку Россию за то влияние, которое она оказала на мою личность. Прежде всего мне хотелось бы поблагодарить Анну, которая всегда была рядом и с кем я пережил множество хороших моментов. Более того, я благодарю ее за поддержку, оказанную мне в самые трудные моменты, без нее весь процесс написания этой работы был бы намного тяжелее. Спасибо за то, что ты была со мной. Так же, я хотел бы поблагодарить Романа за все время, что мы были в России и не только. Так же нельзя не упомянуть Сибирь за то, что наслала своих слуг на мои ягодицы, они несомненно преподали мне незабываемый урок.

Finalmente, este libro se lo dedico a mi madre, mis hermanos, mis abuelos y mis perros Tyr y Rolo. Gracias por ser la mejor familia.

Appendices

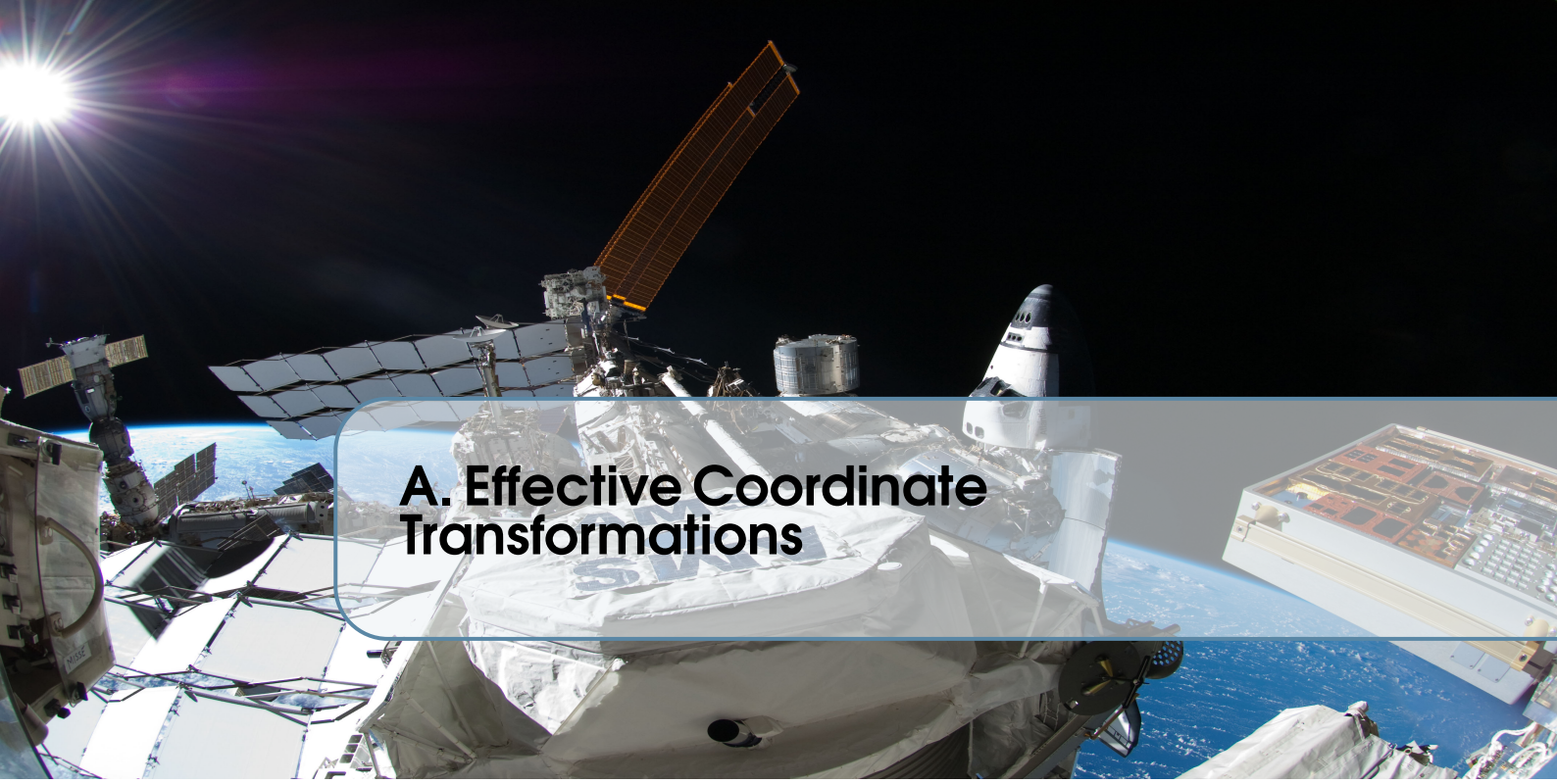

A. Effective Coordinate Transformations

The coordinate transformation between reference systems not only have an impact on the skymap, but also affects how a signal projects from one system into another. For this purpose, a Toy Monte Carlo simulation for an ideal AMS-like detector can be used. Summarizing, the simulated detector is a cylinder of 25º half-opening onboard the ISS and tilted 12º with respect to the local zenith. The orbital parameters of the ISS (position, velocity, and attitude) as well as the livetime are taken from the RTI database, more details can be found in [228].

The transformation of the multipole components of a signal from one coordinate system, i, into another, j, can be quantified by means of the matrix transformation, m_{ij}, such that $\rho^i_{lm} = m_{ij}\,\rho^j_{lm}$. We shall remark that the coordinate transformations depend on the specific characteristics of the detector and, thus, the ones presented here only apply for an AMS-like experiment.

The transformation between a signal injected in the dipole and quadrupole components in ISS geographical positions (GPos) and ISS geomagnetic positions (MPos) shows the relation between two positional systems and is displayed in figure A.1a. An additional term for the isotropic component is also considered (ρ_{ISO}), that quantifies the dilution of a signal because of the coordinate transformation assuming that $\rho_{ISO} = \sqrt{1 - \sum_{lm} m^2_{lm}}$. The matrix shows an almost complete conversion in the North-South direction, ρ_{NS} and ρ_{2+0}, and a rotation in the Forward-Backward and the East-West components. The quadrupoles transform without loss of signal, therefore, both positional systems are equivalent from the point of view of a signal transformation.

On the other hand, the transformation between ISS geographical positions and GTOD (both geographic coordinates) illustrates the differences between positional and directional systems. The matrix is diagonal for the dipole and has a partial dilution in the quadrupole components (figure A.1b).

Finally, figure A.1c shows the transformation between ISS geographical position and galactic coordinates (Gal). In particular, only the North-South direction in ISS geographical position (ρ_{NS} and ρ_{2+0}) transform into galactic coordinates, with a bigger contribution to the dipole ρ_{EW} and the quadrupole ρ_{2-2} and ρ_{2-1}. The rest of the dipole and quadrupole components are diluted due to the Earth's rotation.

The effective coordinate transformation matrices provide a quantitative description about the

transformation of a signal between the different reference systems, in particular, from the non-physical to the physical one. In our case, it provides information on which components in ISS geographical positions are relevant to understand the detector effects.

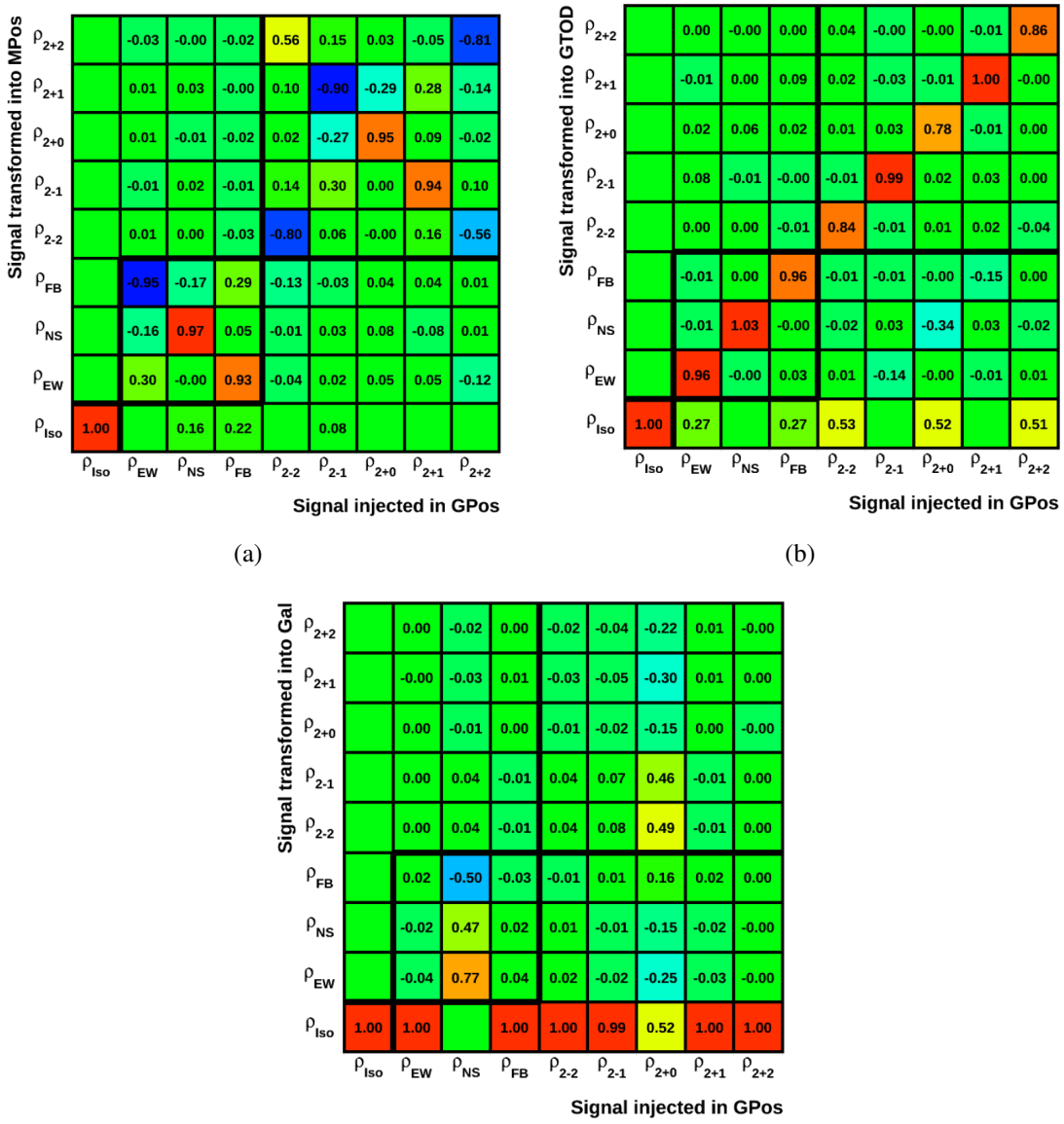

(a) (b)

(c)

Figure A.1: Effective matrix coordinate transformation from ISS geographical position to ISS geomagnetic positions (a), GTOD (b) and galactic coordinates (c).

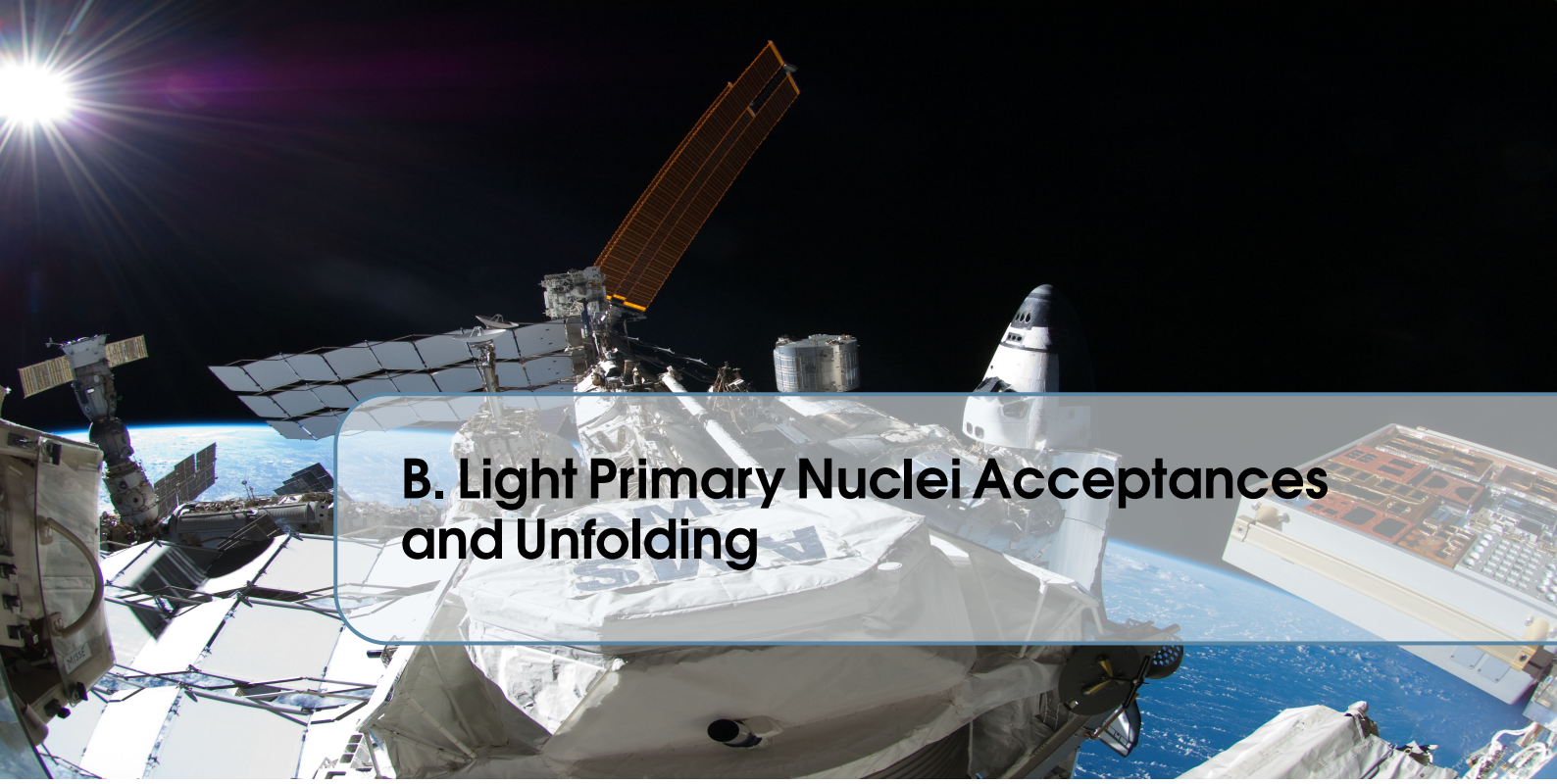

B. Light Primary Nuclei Acceptances and Unfolding

B.1 Acceptances

The effective acceptance was defined in equation 3.5 as

$$A_{eff}(R) = \int d\Omega_g \int d\Omega_d \, \beta(R, \hat{r}_d) \tag{B.1}$$

where $\beta(R, \hat{r}_d)$ stands for the detector response in local coordinates $\hat{r_d} = (\theta_d, \phi_d)$. In the ideal case of $\beta(R, \hat{r}_d) = 1$, the geometrical factor is determined as

$$G = \int d\Omega_g \int d\Omega_d = \int_0^{\pi} cos(\theta)\, dcos(\theta) \int_0^{2\pi} d\phi \int_S \hat{r_d} \cdot d\vec{S} = \pi S \, [m^2 sr] \tag{B.2}$$

with S the surface of the detector.

The way to compute $\beta(R, \hat{r}_d)$ will be discussed below.

B.1.1 MC Acceptances

The MC simulation described in section 2.13 provides the exact number of generated events (n_{gen}) within the rigidity range of interest and also the number of accepted events with the same selection used in data (n_{sel}). These two distributions describe the response of the detector, and thus account for the $\beta(R, \hat{r}_d)$ factor. In this sense, the MC acceptance is defined as

$$A_{MC}(R) = G \, \frac{n_{sel}(R)}{n_{gen}(R)} \tag{B.3}$$

where G is the geometrical factor, $G = \pi l^2 = 47.78 \; m^2 sr$, where $l = 3.9 \; m$ corresponds to the side of the simulation cube.

The rigidity dependence of the A_{MC} is shown in figure B.1 for helium, carbon and oxygen in Full Span and L1+Inner. Results are presented for rigidities upto $R = 3000$ GV and $R = 1000$ GV for the Full Span and L1+Inner samples respectively, where the range of the latter is limited by the MDR. The acceptance decreases as the charge Z increases due to the probability of interaction of

the nuclei with the material of the detector that increases with the charge. In the lowest rigidity part a sharp drop is observed for all the species due to energy losses of low energy nuclei when they go through the material of AMS-02. In order to avoid such a drop in the measurement the results are presented above 1.9 GV for helium and carbon and 2.15 GV for Oxygen, which is the limit where the acceptance starts to drop.

The A_{MC} corresponds to the maximum acceptance of the detector assuming that the simulation describes perfectly the response of the detector. This is usually not the case and therefore a correction factor $\kappa(R)$ has to be introduced to account for this effect.

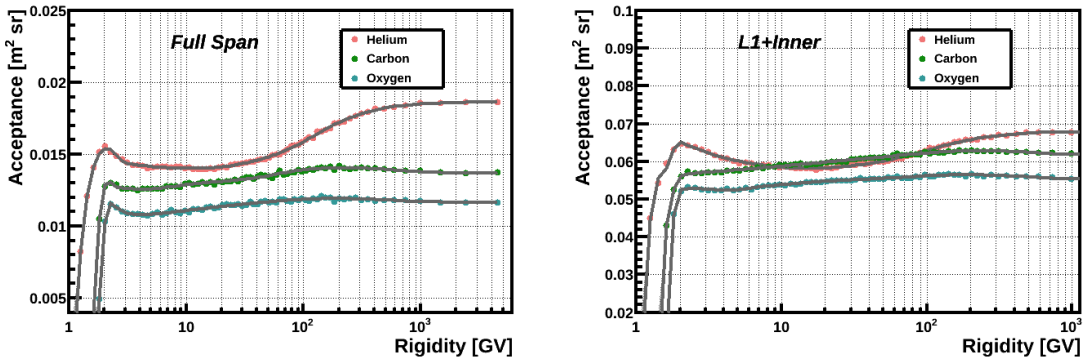

(a) Full Span (b) L1+Inner

Figure B.1: MC acceptances for helium, carbon and oxygen as a function of the generated rigidity for Full Span (a) and L1+Inner (b) tracker patterns.

B.1.2 Corrections Data-MC

The A_{MC} does not take into account the small differences that might exist between the reconstruction and selection efficiencies in Data and MC. Thus, by comparing these discrepancies the simulation can be corrected to reproduce better the real response of the detector. The factor $\kappa(R)$ can be defined as

$$\kappa(R) = \prod_i \frac{\varepsilon^i_{Data}}{\varepsilon^i_{MC}} \tag{B.4}$$

where ε^i_{Data} and ε^i_{MC} are the corresponding efficiencies for data and MC respectively. The light nuclei efficiencies were defined in 5.2 sequentially for each of the cuts applied in the selection. This procedure was followed to account for variations at the permil level or even lower in the anisotropy searches, however, for the purpose of the fluxes calculations, where variations at the percent level are significant, there is no need to compute the efficiency for each of the cuts. For this reason, the efficiencies are grouped as follows: *trigger efficiency*, *tracker innner efficiency*, *picking L1 efficiency* and *picking L9 efficiency* (only for Full Span tracker pattern).

The contribution of the different efficiencies to $\kappa(R)$ is shown in the figure B.2. In particular, the most relevant efficiencies for all species are the tracker inner, the picking L1 and picking L9 (only for the Full Span sample) showing a rather flat dependence with the rigidity for most of the efficiencies.

B.1.3 Effective Acceptances

Finally, taking into account the correction factor $\kappa(R)$ the effective acceptance of the detector is then written as follows

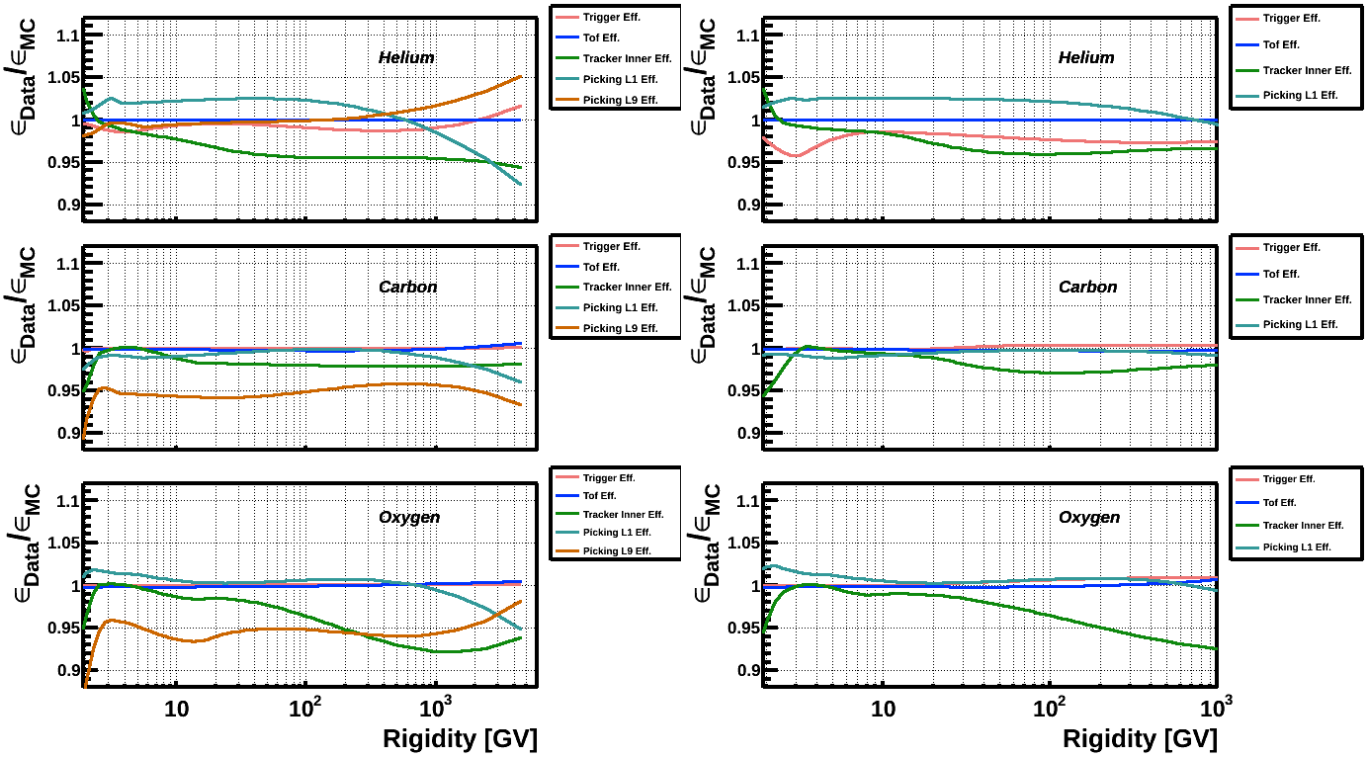

(a) Full Span (b) L1+Inner

Figure B.2: Helium, carbon and oxygen ratio of each reconstruction and selection efficiencies for Data and MC. All results are presented for Full Span (a) and L1+Inner (b) tracker pattern.

$$A_{eff}(R) = A_{MC}(R)\ \kappa(R) \tag{B.5}$$

Figure B.3 shows the A_{eff} as a function of the rigidity for helium, carbon and oxygen in Full Span and L1+Inner.

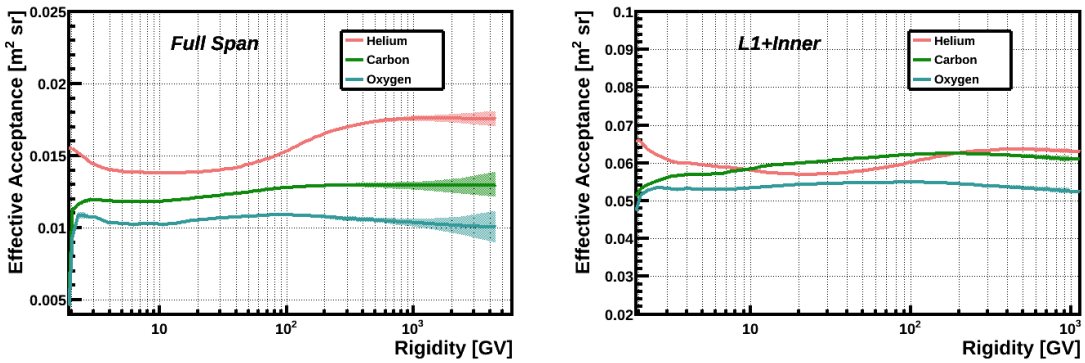

(a) Full Span (b) L1+Inner

Figure B.3: Effective acceptances for helium, carbon and oxygen as a function of the rigidity for Full Span (a) and L1+Inner (b) tracker patterns.

B.2 Unfolding

In order to compute the light nuclei fluxes the number of selected events has to be corrected with the bin-to-bin migrations. In general, a particle with a true rigidity R is measured by the detector with a different reconstructed rigidity R_{rec} due to the limited rigidity resolution. This effect becomes relevant specially in the high rigidity part where the resolution steadily worsens as approaching the MDR. In particular, due to the shape of the cosmic rays spectra more low rigidity particles are assigned with high rigidity than vice-versa. The unfolding takes into account these effects and relies in a precise knowledge of the rigidity resolution function.

The resolution function can be evaluated following different methods, for this work the iterative procedure called folded acceptance will be used [234; 235] and the evaluation will be made in the MC simulation. The method can be divided in the following steps:

1. The procedure starts by defining a weight function for the first iteration i = 0 to give the correct shape to the MC spectrum. For this work, the parametrization of the flux described in [76] is used and evaluated in each rigidity bin

$$W_0(R) = f(R)\, R \tag{B.6}$$

   where the factor R is added to the equation to compensate the spectral shape of the MC ($dN_{MC}/dR \sim R^{-1}$).
2. The number of events measured as a function of the reconstructed rigidity $N_{rec}(R_{rec})$ are weighted for each bin and for each iteration with the weight function $W_i(R)$.
3. The folded acceptance $(A_{fold})_i$ defined as

$$(A_{fold})_i(R) = \frac{N_{rec}(R_{rec})W_i(R)}{N_{gen}} \tag{B.7}$$

   is computed for each bin of rigidity and iteration.
4. The flux is calculated for each bin and iteration with the folded acceptance and the number of reconstructed events

$$\Phi_i(R) = \frac{N_{rec}(R_{rec})}{(A_{fold})_i(R)} \tag{B.8}$$

   The parametrization of Φ_i to a spiline is used as the weight function $W_i(R)$ for the next iteration.

The iterative procedure is repeated until the convergence condition is satisfied: the comparison between the last and previous iteration is $\Phi_n/\Phi_{n-1} < 0.1\%$ for each rigidity bin.

Finally, the unfolding factor is computed as the ratio of events before and after the unfolding procedure Φ_0/Φ_n. The results are presented in figure B.4, where the high rigidity part have the most relevant contributions. In particular in the L1+Inner sample there are corrections at 1 TV of 20 % whereas for Full Span is 10 %. This is mainly due to a better rigidity resolution when a good hit in the L9 is associated for the Full Span sample.

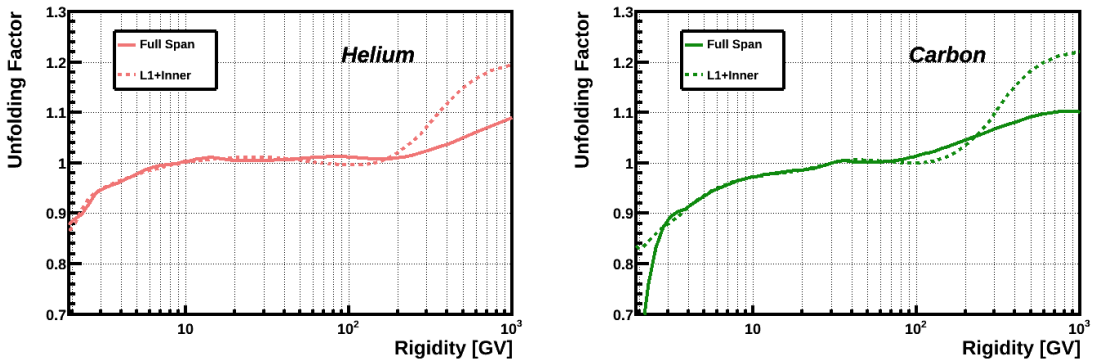

(a) Helium

(b) Carbon

(c) Oxygen

Figure B.4: Unfolding factors for helium (a), carbon (b) and oxygen (b) as a function of the rigidity for the Full Span and L1+Inner tracker patterns.

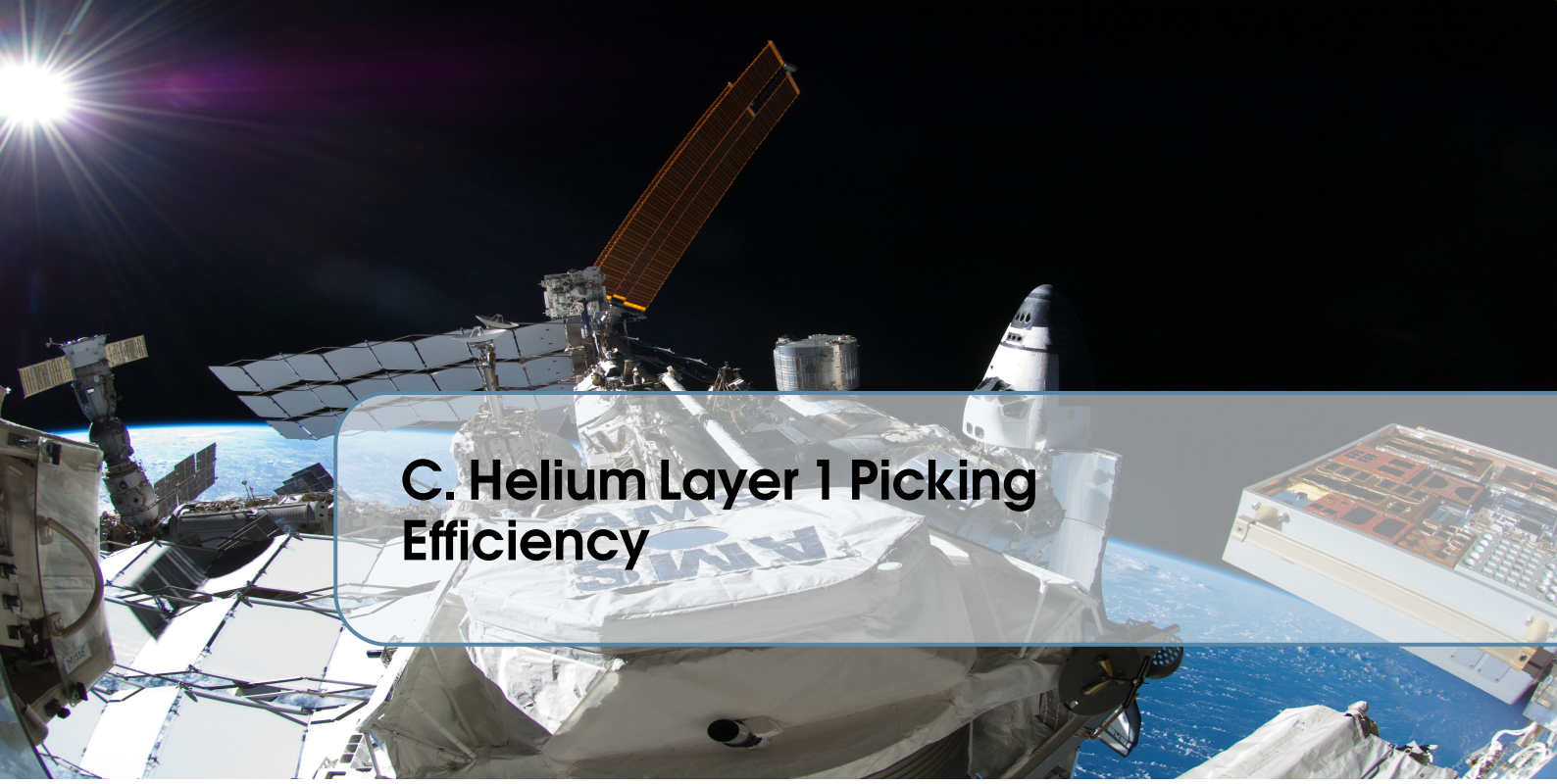

C. Helium Layer 1 Picking Efficiency

The standard method to describe the rigidity dependence of the efficiency corrections uses a first and second order polynomial parametrization for the dipole ($\ell = 1$) and quadrupole ($\ell = 2$) components respectively. Nevertheless, the Δ_{NS} helium layer 1 picking efficiency in ISS geographical position coordinates (see section 5.4.2) showed a special behavior with a significant change in the amplitude for rigidities $R > 100$ GV with respect to the low rigidity ranges. A logistic function was used instead of a linear fit to achieve a better description of the data points. This parametrization allowed to further correct the deviations observed at high rigidities in the helium anisotropy. The objective of this appendix is to perform a detailed study of the geographical variation of this efficiency and, for this purpose, the one-dimensional approach provides the necessary tools.

Three set of figures are shown: the first one, figure C.1a, corresponds to the comparison of the relative variation of the helium layer 1 picking selection efficiency as a function of the geomagnetic colatitude for two low rigidity ranges (one for $R > 18$ GV and the other one $R > 30$ GV). The second one, figure C.2a, compares two intervals at high rigidities (one for $R > 200$ GV and the one for $R > 300$ GV). Finally, figure C.3a, shows the comparison for one range at low rigidities, $R > 18$ GV, and the other one at high rigidities, $R > 200$ GV. The relative variation of the efficiency is described with a quadratic function, where the p_1 and p_2 parameters are related with Δ_{NS} and Δ_{2+0} of the spherical harmonic study. In addition, the ratios, figures C.1b, C.2b and C.3b, are displayed for completeness.

Figures C.1a and C.2a show an identical variation with respect to the geomagnetic colatitude, which is further confirmed by the parameters p_1 and p_2 of the fit to a quadratic function. The ratios, figures C.1b and C.2b, and the corresponding parameters of the fit corroborate the observations. On the contrary, the comparison for $R > 18$ GV with $R > 200$ GV, figure C.3a, shows a significant change in the p_1, which is verified with the ratio.

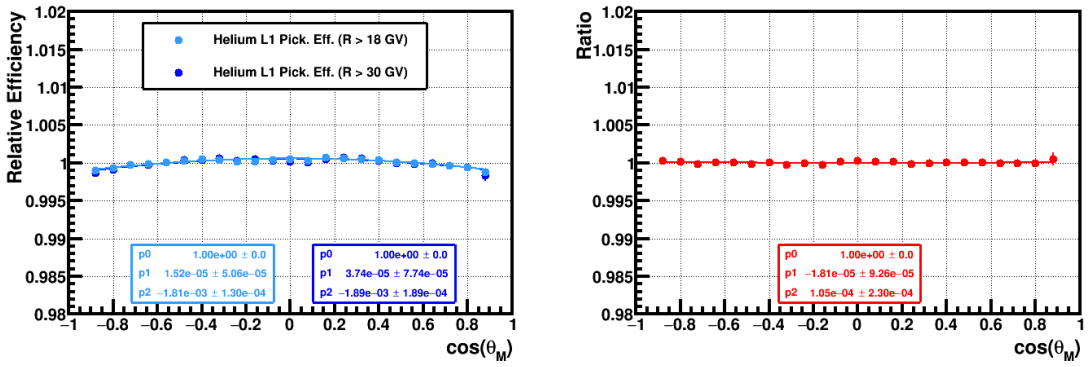

(a) (b)

Figure C.1: (a) Comparison of the relative variation of the helium layer 1 picking selection efficiency as a function of the geomagnetic colatitude for rigidities $R > 18GV$ and $R > 30$ GV, showing a significant change in the slope for the latter. This effect can be also observed in the ratio (b).

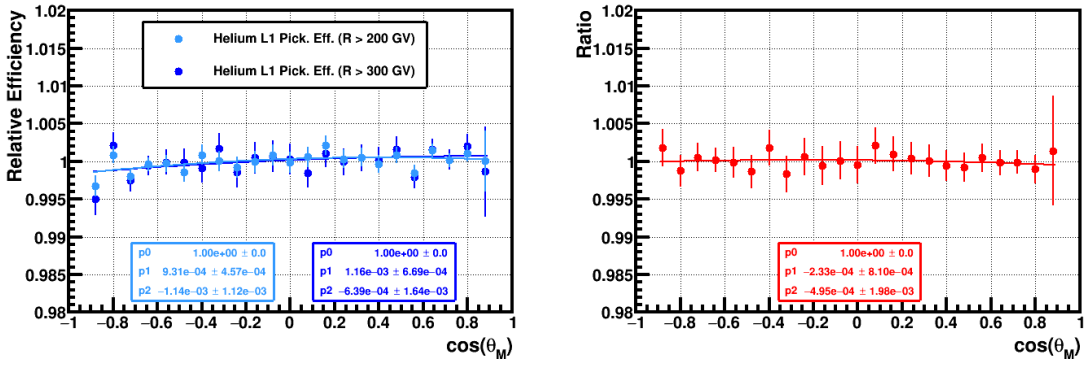

(a) (b)

Figure C.2: (a) Comparison of the relative variation of the helium picking layer 1 selection efficiency as a function of the geomagnetic colatitude for rigidities $R > 200GV$ and $R > 300$ GV, showing a significant change in the slope for the latter. This effect can be also observed in the ratio (b).

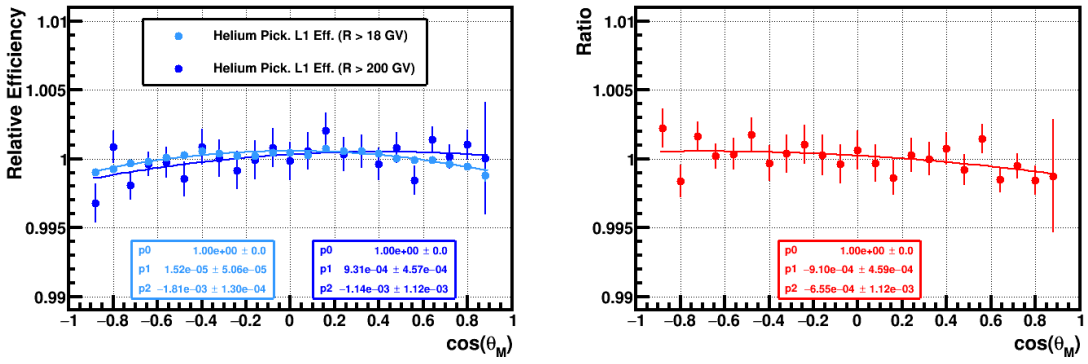

(a) (b)

Figure C.3: (a) Comparison of the relative variation of the helium picking layer 1 selection efficiency as a function of the geomagnetic colatitude for rigidities $R > 18GV$ and $R > 200$ GV, showing a significant change in the slope for the latter. This effect can be also observed in the ratio (b).

D. Supplemental Material

This appendix provides further details on the carbon, oxygen and proton anisotropy as well as the tables of the numerical results for 8.5 years of data taking.

D.1 Figures

D.1.1 Carbon and Oxygen

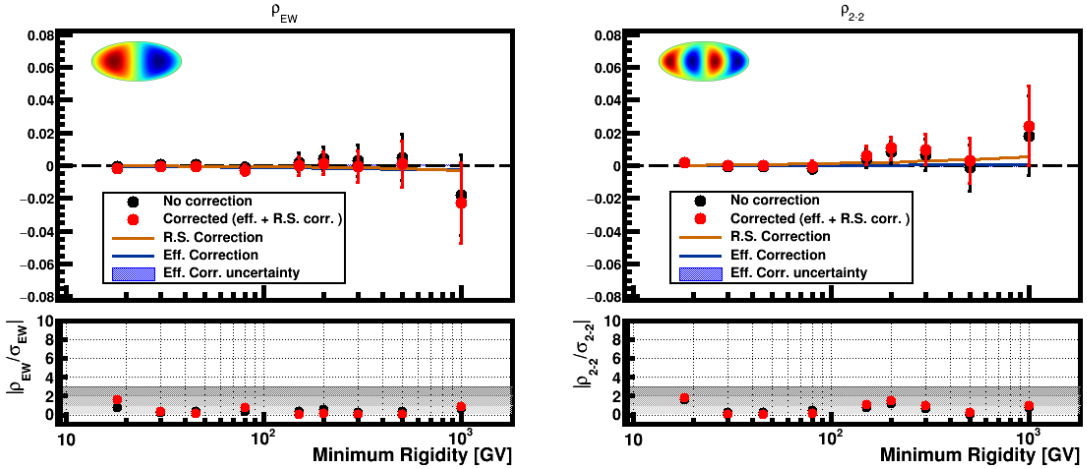

(a) (b)

Figure D.1: Carbon multipole components ρ_{EW} (a) and ρ_{2-2} (b), in galactic coordinates where no corrections (black dots), and efficiency + rigidity scale corrections (red dots) are included. The error bars in the dots stand for the statistical uncertainties. Efficiency corrections are shown as a blue line with its uncertainty displayed as a blue band and the rigidity scale corrections as a brown line. Finally, in the bottom panel the deviations from isotropy are evaluated in terms of standard deviations.

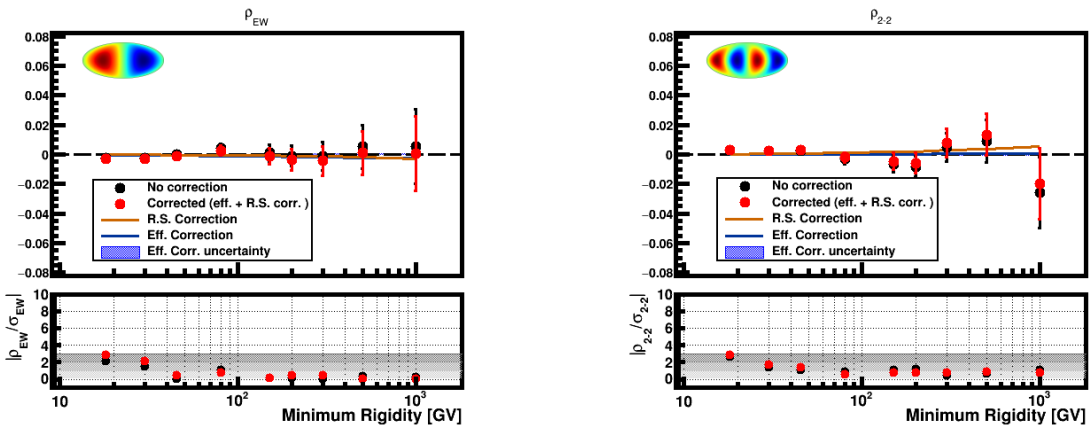

(a) (b)

Figure D.2: Oxygen multipole components ρ_{EW} (a) and ρ_{2-2} (b), in galactic coordinates where no corrections (black dots), efficiency and rigidity scale corrections (red dots) are included. The error bars in the dots stand for the statistical uncertainties. Efficiency corrections are shown as a blue line with its uncertainty displayed as a blue band and the rigidity scale corrections as a brown line. Finally, in the bottom panel the deviations from isotropy are evaluated in terms of the sigmas.

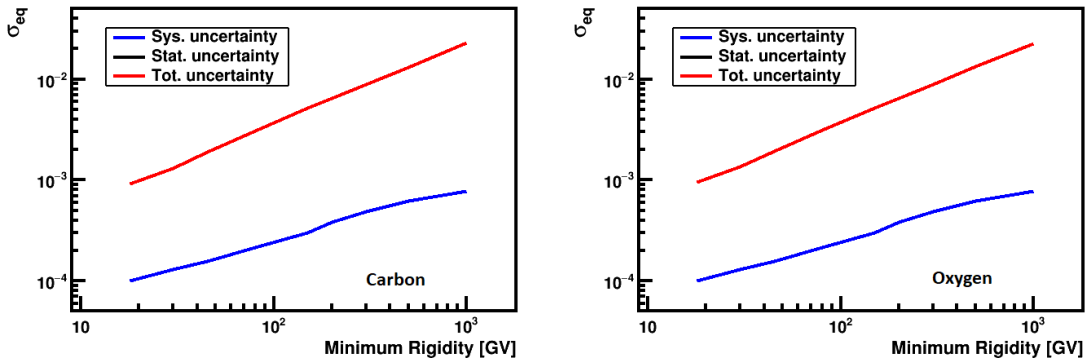

(a) (b)

Figure D.3: Comparison of the statistical, systematic and total equivalent uncertainties on the carbon (a) and oxygen (b) dipole components. The measurement is dominated by the statistical errors in the entire rigidity range.

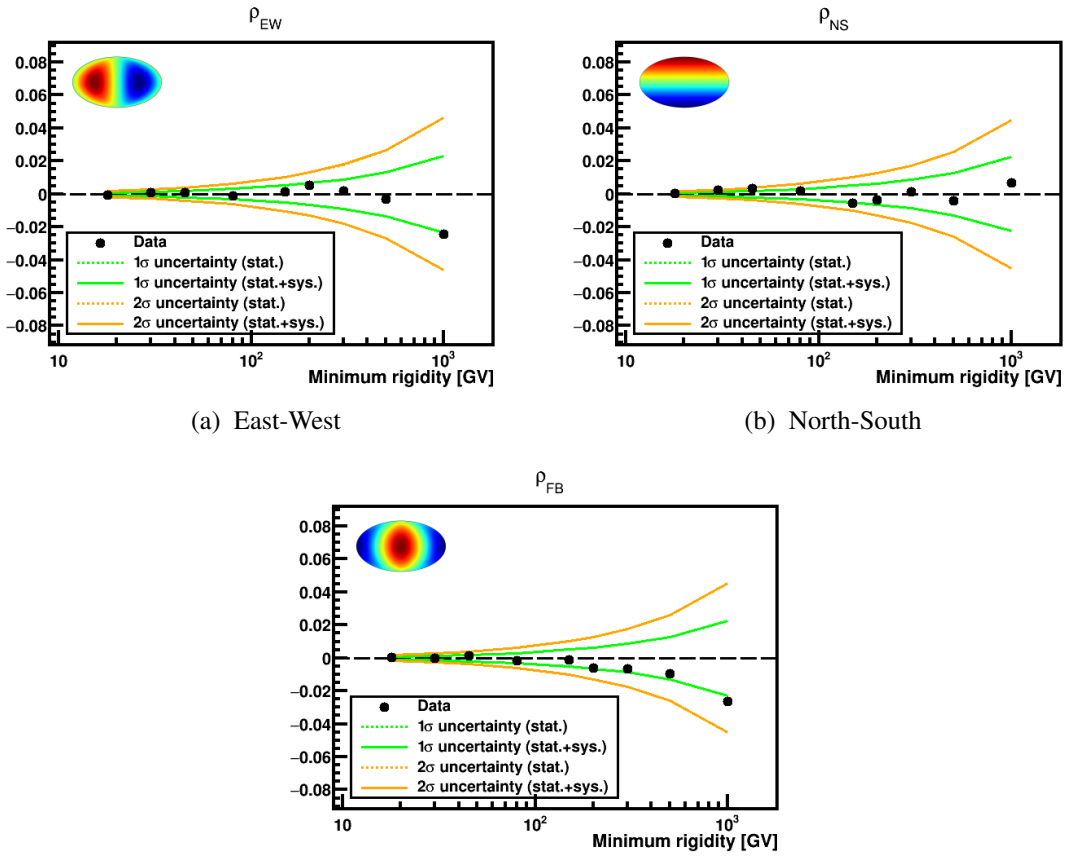

(a) East-West (b) North-South

(c) Forward-Backward

Figure D.4: Carbon dipole components, EW, NS and FB in galactic coordinates where the 1 and 2-sigma deviations from isotropy (green and yellow, respectively) corresponding to the statistical (dotted line) and total (solid line) uncertainties are shown.

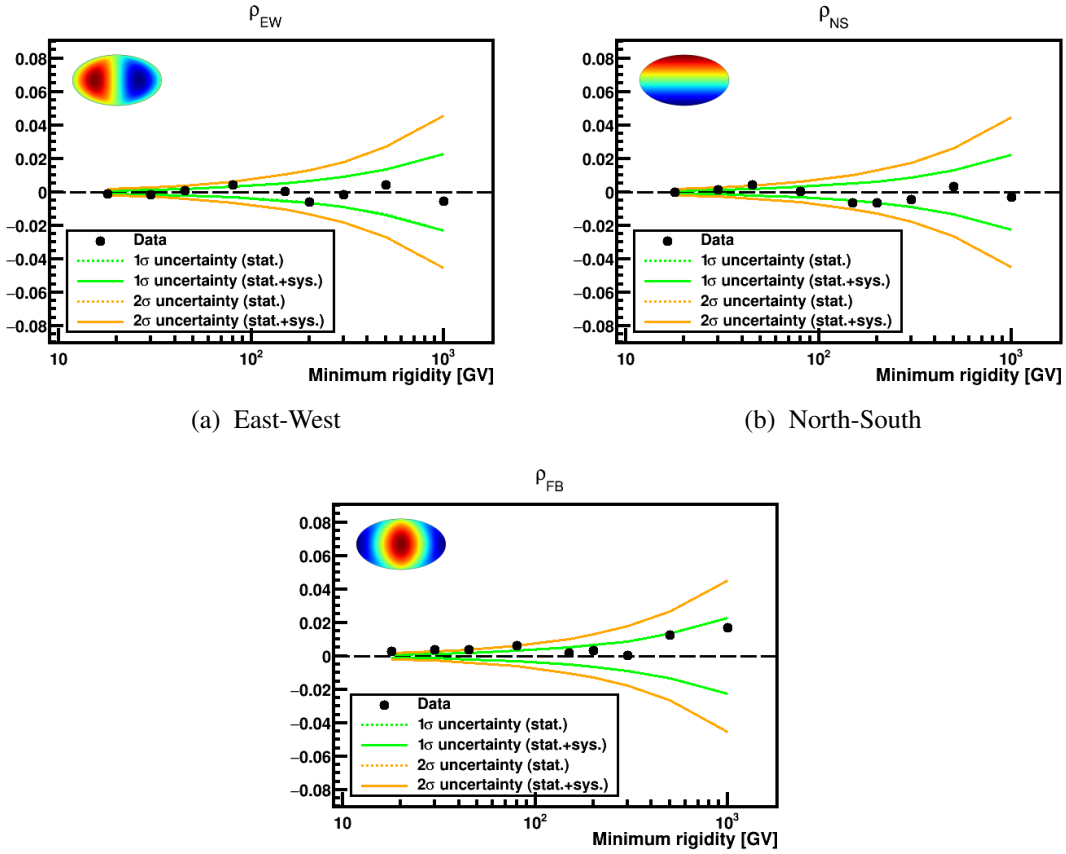

(a) East-West

(b) North-South

(c) Forward-Backward

Figure D.5: Oxygen dipole components, EW, NS and FB in galactic coordinates where the 1 and 2-sigma deviations from isotropy (green and yellow, respectively) corresponding to the statistical (dotted line) and total (solid line) uncertainties are shown.

D.1.2 Protons

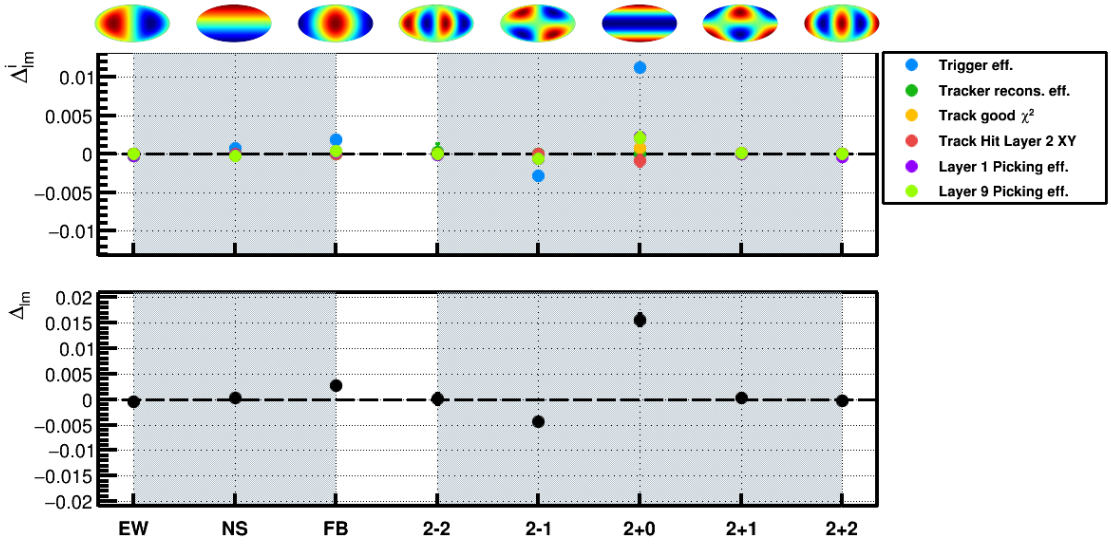

Figure D.6: Individual (top) and total (bottom) proton efficiency corrections for the dipole ($\ell = 1$) and quadrupole ($\ell = 2$) components for $R > 18$ GV in ISS Geographical Position coordinates. The main direction affected is the North-South with the biggest contribution coming from the trigger efficiency.

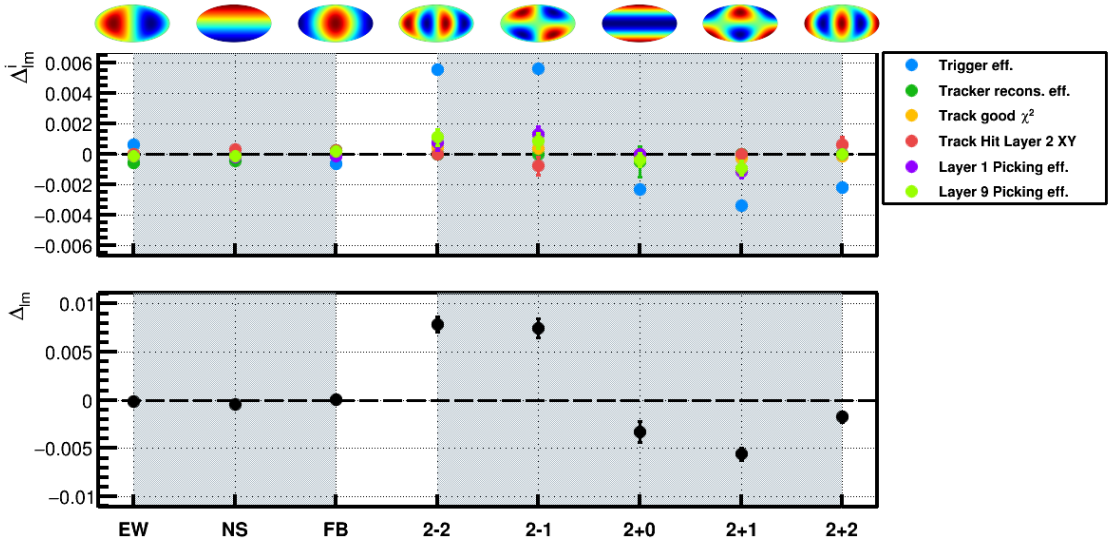

Figure D.7: Individual (top) and total (bottom) proton efficiency corrections for the dipole ($\ell = 1$) and quadrupole ($\ell = 2$) components for $R > 18$ GV in galactic coordinates. Most of the components are now significant due to the projection of the Δ^i_{NS} and Δ^i_{2+0} from ISS geographical position coordinates into galactic coordinates. The main contribution comes from the trigger efficiency.

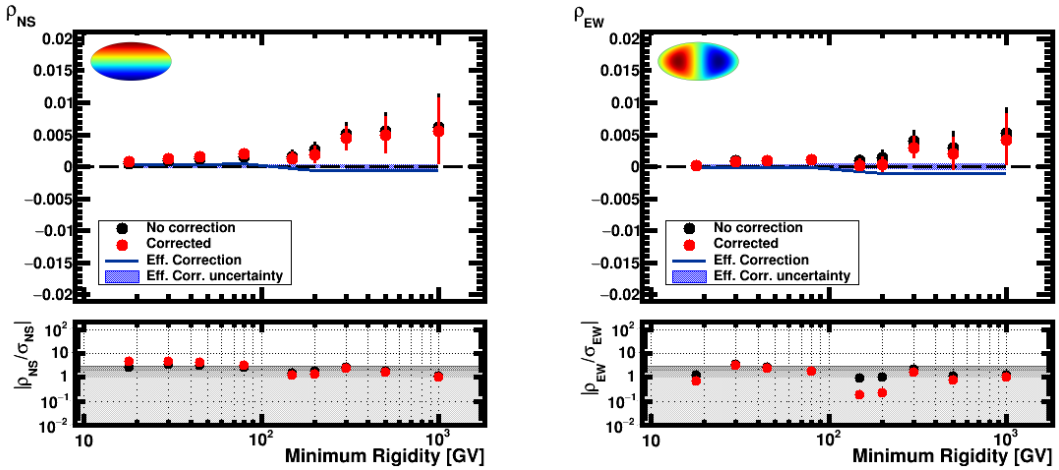

(a) (b)

Figure D.8: Proton multipole components ρ_{NS} (a) and ρ_{EW} (b) in ISS geographical position and galactic coordinates respectively, where no corrections (black dots), and efficiency corrections (red dots) are included. The error bars in the dots stand for the statistical uncertainties. Efficiency corrections are shown as a blue line with its uncertainty displayed as a blue band. Finally, in the bottom panel the deviations from isotropy are evaluated in terms of standard deviations.

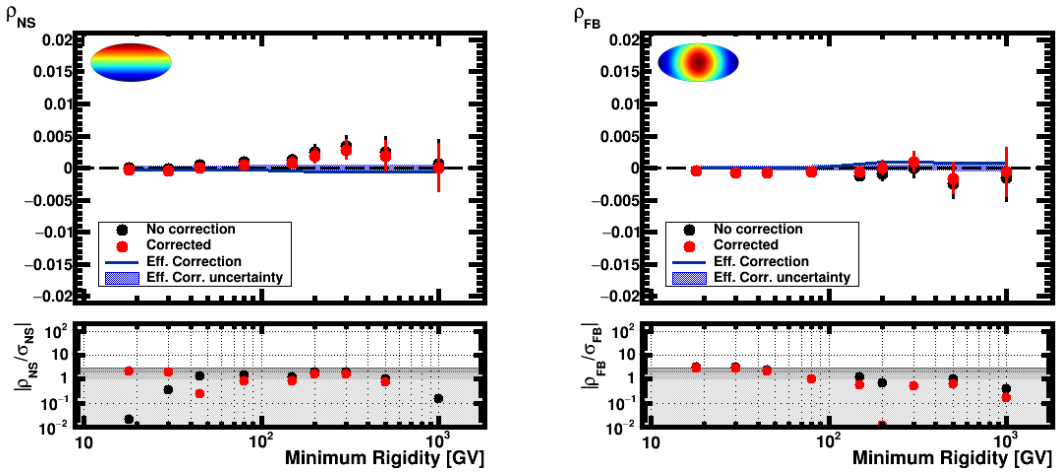

(a) (b)

Figure D.9: Proton multipole components ρ_{NS} (a) and ρ_{FB} (b) in galactic coordinates where no corrections (black dots), and efficiency corrections (red dots) are included. The error bars in the dots stand for the statistical uncertainties. Efficiency corrections are shown as a blue line with its uncertainty displayed as a blue band. Finally, in the bottom panel the deviations from isotropy are evaluated in terms of standard deviations.

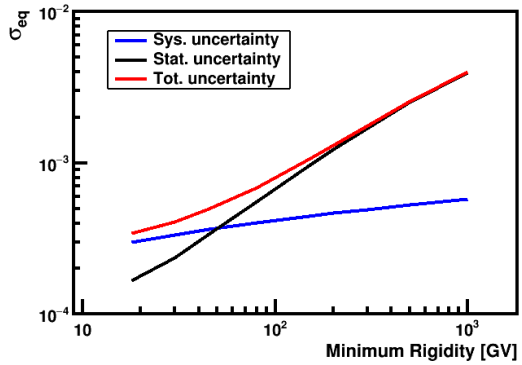

Figure D.10: Comparison of the statistical, systematic and total equivalent uncertainties on the proton dipole components. The measurement is dominated by the statistical error for rigidities above $R > 80$ GV.

D.2 Tables

D.2.1 Electron Anisotropy

Table D.1: Results on the electron dipole anisotropy in galactic coordinates for 6.5 years.

E_{min} [GeV]	$N_{e^-}^{meas}$	$N_{e^-}^{eq}$	ρ_{EW} (%)	σ_{EW}^{stat} (%)	σ_{EW}^{sys} (%)	$\rho_{EW}/\sigma_{EW}^{tot}$	ρ_{NS} (%)	σ_{NS}^{stat} (%)	σ_{NS}^{sys} (%)	$\rho_{NS}/\sigma_{NS}^{tot}$	ρ_{FB} (%)	σ_{FB}^{stat} (%)	σ_{FB}^{sys} (%)	$\rho_{FB}/\sigma_{FB}^{tot}$	δ_M(%)	$\delta_{U.L.}^{95\%\ C.L.}$(%)
16	1304252	1304252	0.146	0.153	0.162	+0.66	0.029	0.154	0.103	+0.16	-0.224	0.153	0.124	-1.14	0.268	0.512
25	572977	572977	0.075	0.237	0.180	+0.25	0.149	0.229	0.125	+0.57	-0.367	0.229	0.158	-1.32	0.402	0.736
40	190954	190954	-0.127	0.410	0.203	-0.28	0.036	0.397	0.156	+0.08	-0.340	0.397	0.200	-0.77	0.365	0.968
65	59612	59612	-0.577	0.735	0.230	-0.75	0.235	0.709	0.191	+0.32	-0.343	0.710	0.248	-0.46	0.711	1.696
100	20630	20630	-0.491	1.247	0.256	-0.39	0.395	1.210	0.224	+0.32	0.296	1.202	0.291	+0.24	0.696	2.571

Table D.2: Results of the optimized analysis on the electron dipole anisotropy in galactic coordinates for 8.5 years.

E_{min} [GeV]	$N_{e^-}^{meas}$	$N_{e^-}^{eq}$	ρ_{EW} (%)	σ_{EW}^{stat} (%)	σ_{EW}^{sys} (%)	$\rho_{EW}/\sigma_{EW}^{tot}$	ρ_{NS} (%)	σ_{NS}^{stat} (%)	σ_{NS}^{sys} (%)	$\rho_{NS}/\sigma_{NS}^{tot}$	ρ_{FB} (%)	σ_{FB}^{stat} (%)	σ_{FB}^{sys} (%)	$\rho_{FB}/\sigma_{FB}^{tot}$	δ_M(%)	$\delta_{U.L.}^{95\%\ C.L.}$(%)
16	2267410	2267410	0.048	0.118	0.062	+0.36	0.006	0.117	0.065	+0.04	-0.206	0.117	0.072	-1.50	0.212	0.371
25	896181	896181	-0.061	0.192	0.105	-0.28	0.180	0.185	0.112	+0.83	-0.171	0.185	0.064	-0.87	0.256	0.514
40	297648	297648	-0.217	0.332	0.152	-0.59	-0.319	0.321	0.163	-0.88	-0.076	0.322	0.083	-0.23	0.393	0.835
65	92893	92893	-0.582	0.594	0.200	-0.93	0.195	0.574	0.217	+0.32	0.572	0.575	0.119	+0.97	0.839	1.571
100	31949	31949	-0.561	1.011	0.243	-0.54	0.507	0.982	0.265	+0.50	1.412	0.979	0.156	+1.42	1.602	2.803

D.2.2 Positron Anisotropy

Table D.3: Results on the positron dipole anisotropy in galactic coordinates including background contamination for 6.5 years.

E_{min} [GeV]	$N_{e^+}^{meas}$	$N_{e^+}^{eq}$	ρ_{EW} (%)	σ_{EW}^{stat} (%)	σ_{EW}^{sys} (%)	$\rho_{EW}/\sigma_{EW}^{tot}$	ρ_{NS} (%)	σ_{NS}^{stat} (%)	σ_{NS}^{sys} (%)	$\rho_{NS}/\sigma_{NS}^{tot}$	ρ_{FB} (%)	σ_{FB}^{stat} (%)	σ_{FB}^{sys} (%)	$\rho_{FB}/\sigma_{FB}^{tot}$	$\delta_M(\%)$	$\delta_{U.L.}^{95\%\ C.L.}(\%)$
16	98904	90485	0.980	0.583	0.162	+1.62	-0.122	0.582	0.103	-0.21	-0.638	0.582	0.124	-1.07	1.175	1.886
25	50048	45924	0.921	0.845	0.180	+1.07	-0.167	0.813	0.125	-0.20	-1.185	0.809	0.158	-1.44	1.510	2.498
40	20463	18688	0.887	1.324	0.203	+0.66	-0.679	1.274	0.156	-0.53	-1.489	1.270	0.200	-1.16	1.861	3.417
65	7924	7045	-0.264	2.150	0.230	-0.12	-0.119	2.083	0.191	-0.06	0.003	2.053	0.248	+0.00	0.289	4.144
100	3324	2785	-2.740	3.400	0.256	-0.80	-0.214	3.282	0.224	-0.07	3.604	3.253	0.291	+1.10	4.532	8.524

Table D.4: Results of the optimized analysis on the positron dipole anisotropy in galactic coordinates including background contamination for 8.5 years.

E_{min} [GeV]	$N_{e^+}^{meas}$	$N_{e^+}^{eq}$	ρ_{EW} (%)	σ_{EW}^{stat} (%)	σ_{EW}^{sys} (%)	$\rho_{EW}/\sigma_{EW}^{tot}$	ρ_{NS} (%)	σ_{NS}^{stat} (%)	σ_{NS}^{sys} (%)	$\rho_{NS}/\sigma_{NS}^{tot}$	ρ_{FB} (%)	σ_{FB}^{stat} (%)	σ_{FB}^{sys} (%)	$\rho_{FB}/\sigma_{FB}^{tot}$	$\delta_M(\%)$	$\delta_{U.L.}^{95\%\ C.L.}(\%)$
16	153931	153931	0.677	0.456	0.062	+1.47	-0.374	0.447	0.065	-0.83	-0.826	0.448	0.072	-1.82	1.131	1.700
25	70905	70905	1.049	0.686	0.105	+1.51	-0.192	0.658	0.112	-0.29	-1.291	0.658	0.064	-1.95	1.674	2.517
40	28588	28588	1.377	1.075	0.152	+1.27	-0.812	1.041	0.163	-0.77	-0.918	1.036	0.083	-0.88	1.844	3.094
65	10974	10974	0.670	1.728	0.200	+0.39	-1.534	1.690	0.217	-0.90	0.255	1.659	0.119	+0.15	1.693	3.891
100	4483	4483	0.077	2.688	0.243	+0.03	-1.308	2.637	0.265	-0.49	5.551	2.585	0.156	+2.14	5.704	8.901

D.2.3 Helium Anisotropy

Table D.5: Results on the helium dipole anisotropy in galactic coordinates for 8.5 years.

E_{min} [GeV]	N_{He}^{meas}	ρ_{EW} (%)	σ_{EW}^{stat} (%)	σ_{EW}^{sys} (%)	$\rho_{EW}/\sigma_{EW}^{tot}$	ρ_{NS} (%)	σ_{NS}^{stat} (%)	σ_{NS}^{sys} (%)	$\rho_{NS}/\sigma_{NS}^{tot}$	ρ_{FB} (%)	σ_{FB}^{stat} (%)	σ_{FB}^{sys} (%)	$\rho_{FB}/\sigma_{FB}^{tot}$	δ_M(%)	$\delta_{U.L.}^{95\%\ C.L.}$(%)
18	112051641	0.019	0.017	0.009	+0.98	0.011	0.017	0.008	+0.60	0.011	0.017	0.010	+0.55	0.024	0.047
29	54430999	0.015	0.024	0.012	+0.56	0.026	0.024	0.010	+1.03	-0.022	0.024	0.014	-0.79	0.037	0.069
45	25799190	0.022	0.035	0.015	+0.58	0.025	0.034	0.011	+0.69	-0.023	0.034	0.018	-0.59	0.041	0.088
80	9926682	0.056	0.057	0.024	+0.90	0.012	0.055	0.015	+0.21	-0.061	0.056	0.023	-1.00	0.083	0.155
150	3635117	-0.044	0.094	0.037	-0.43	0.055	0.091	0.020	+0.59	0.081	0.092	0.031	+0.84	0.107	0.229
201	2311304	0.105	0.118	0.051	+0.82	0.152	0.114	0.024	+1.30	0.096	0.115	0.035	+0.79	0.208	0.352
300	1247713	0.237	0.160	0.066	+1.36	0.245	0.156	0.030	+1.54	0.207	0.156	0.042	+1.28	0.399	0.604
500	571568	0.124	0.237	0.085	+0.49	0.192	0.230	0.040	+0.82	0.418	0.231	0.053	+1.76	0.476	0.763
1000	201360	0.121	0.400	0.102	+0.29	0.194	0.388	0.053	+0.50	0.551	0.389	0.068	+1.40	0.597	1.071

D.2.4 Carbon Anisotropy

Table D.6: Results on the carbon dipole anisotropy in galactic coordinates for 8.5 years.

E_{min} [GeV]	N_C^{meas}	ρ_{EW} (%)	σ_{EW}^{stat} (%)	σ_{EW}^{sys} (%)	$\rho_{EW}/\sigma_{EW}^{tot}$	ρ_{NS} (%)	σ_{NS}^{stat} (%)	σ_{NS}^{sys} (%)	$\rho_{NS}/\sigma_{NS}^{tot}$	ρ_{FB} (%)	σ_{FB}^{stat} (%)	σ_{FB}^{sys} (%)	$\rho_{FB}/\sigma_{FB}^{tot}$	δ_M(%)	$\delta_{U.L.}^{95\%\ C.L.}$(%)
18	3674254	-0.048	0.092	0.009	-0.51	0.034	0.091	0.008	+0.38	0.017	0.091	0.010	+0.19	0.061	0.194
29	1814089	0.071	0.133	0.012	+0.53	0.208	0.129	0.010	+1.60	-0.011	0.130	0.014	-0.09	0.220	0.374
45	863515	0.096	0.192	0.015	+0.49	0.312	0.187	0.011	+1.67	0.151	0.188	0.018	+0.80	0.360	0.585
80	327504	-0.130	0.312	0.024	-0.41	0.145	0.304	0.015	+0.48	-0.139	0.305	0.023	-0.45	0.239	0.665
150	117059	0.096	0.523	0.037	+0.18	-0.601	0.509	0.020	-1.18	-0.105	0.510	0.031	-0.21	0.618	1.252
201	74603	0.545	0.655	0.051	+0.83	-0.341	0.637	0.024	-0.53	-0.612	0.640	0.035	-0.95	0.887	1.662
300	40037	0.145	0.896	0.066	+0.16	0.159	0.870	0.030	+0.18	-0.632	0.873	0.042	-0.72	0.668	1.894
500	18151	-0.330	1.337	0.085	-0.25	-0.449	1.287	0.040	-0.35	-0.976	1.295	0.053	-0.75	1.124	2.882
1000	5952	-2.453	2.318	0.102	-1.06	0.527	2.254	0.053	+0.23	-2.629	2.267	0.068	-1.16	3.634	6.329

D.2.5 Oxygen Anisotropy

Table D.7: Results on the oxygen dipole anisotropy in galactic coordinates for 8.5 years.

E_{min} [GeV]	N_O^{meas}	ρ_{EW} (%)	σ_{EW}^{stat} (%)	σ_{EW}^{sys} (%)	$\rho_{EW}/\sigma_{EW}^{tot}$	ρ_{NS} (%)	σ_{NS}^{stat} (%)	σ_{NS}^{sys} (%)	$\rho_{NS}/\sigma_{NS}^{tot}$	ρ_{FB} (%)	σ_{FB}^{stat} (%)	σ_{FB}^{sys} (%)	$\rho_{FB}/\sigma_{FB}^{tot}$	δ_M(%)	$\delta_{U.L.}^{95\%\ C.L.}$(%)
18	3394783	-0.132	0.096	0.009	-1.37	-0.011	0.095	0.008	-0.12	0.286	0.095	0.010	+3.00	0.315	0.444
29	1707605	-0.178	0.137	0.012	-1.30	0.115	0.133	0.010	+0.86	0.381	0.134	0.014	+2.84	0.436	0.618
45	824218	0.095	0.197	0.015	+0.48	0.429	0.192	0.011	+2.24	0.368	0.192	0.018	+1.90	0.573	0.828
80	318467	0.430	0.316	0.024	+1.35	0.027	0.308	0.015	+0.09	0.628	0.310	0.023	+2.02	0.761	1.149
150	116030	-0.012	0.524	0.037	-0.02	-0.680	0.510	0.020	-1.33	0.198	0.513	0.031	+0.39	0.709	1.329
201	73476	-0.554	0.658	0.051	-0.84	-0.630	0.640	0.024	-0.98	0.324	0.646	0.035	+0.50	0.900	1.678
300	39140	-0.188	0.902	0.066	-0.21	-0.460	0.877	0.030	-0.52	0.032	0.886	0.042	+0.04	0.498	1.836
500	17462	0.386	1.351	0.085	+0.29	0.264	1.315	0.040	+0.20	1.237	1.327	0.053	+0.93	1.323	3.044
1000	6037	-0.552	2.282	0.102	-0.24	-0.481	2.240	0.053	-0.21	1.707	2.264	0.068	+0.75	1.858	4.938

D.2.6 Proton Anisotropy

Table D.8: Results on the proton dipole anisotropy in galactic coordinates for 8.5 years.

E_{min} [GeV]	N_{Pr}^{meas}	ρ_{EW} (%)	σ_{EW}^{stat} (%)	σ_{EW}^{sys} (%)	$\rho_{EW}/\sigma_{EW}^{tot}$	ρ_{NS} (%)	σ_{NS}^{stat} (%)	σ_{NS}^{sys} (%)	$\rho_{NS}/\sigma_{NS}^{tot}$	ρ_{FB} (%)	σ_{FB}^{stat} (%)	σ_{FB}^{sys} (%)	$\rho_{FB}/\sigma_{FB}^{tot}$	δ_M(%)	$\delta_{U.L.}^{95\%\ C.L.}$(%)
18	113248936	0.012	0.017	0.030	+0.36	-0.038	0.017	0.030	-1.12	-0.043	0.017	0.030	-1.27	0.059	0.100
29	56577806	0.080	0.024	0.034	+1.91	-0.046	0.023	0.033	-1.14	-0.068	0.023	0.033	-1.66	0.114	0.167
45	27887341	0.088	0.035	0.037	+1.75	0.007	0.033	0.036	+0.15	-0.071	0.033	0.036	-1.45	0.114	0.174
80	10189797	0.103	0.057	0.041	+1.46	0.048	0.055	0.040	+0.70	-0.053	0.055	0.040	-0.77	0.125	0.206
150	3434285	0.019	0.099	0.045	+0.17	0.083	0.094	0.044	+0.80	-0.059	0.095	0.044	-0.56	0.103	0.240
201	2094187	0.030	0.127	0.047	+0.22	0.191	0.120	0.046	+1.48	-0.004	0.121	0.046	-0.03	0.193	0.350
300	1090391	0.299	0.176	0.050	+1.64	0.285	0.167	0.049	+1.64	0.085	0.168	0.049	+0.48	0.422	0.641
500	500336	0.197	0.259	0.054	+0.74	0.190	0.246	0.052	+0.76	-0.164	0.248	0.052	-0.65	0.320	0.633
1000	203245	0.419	0.408	0.058	+1.02	0.002	0.385	0.057	+0.00	-0.069	0.389	0.057	-0.18	0.424	0.929

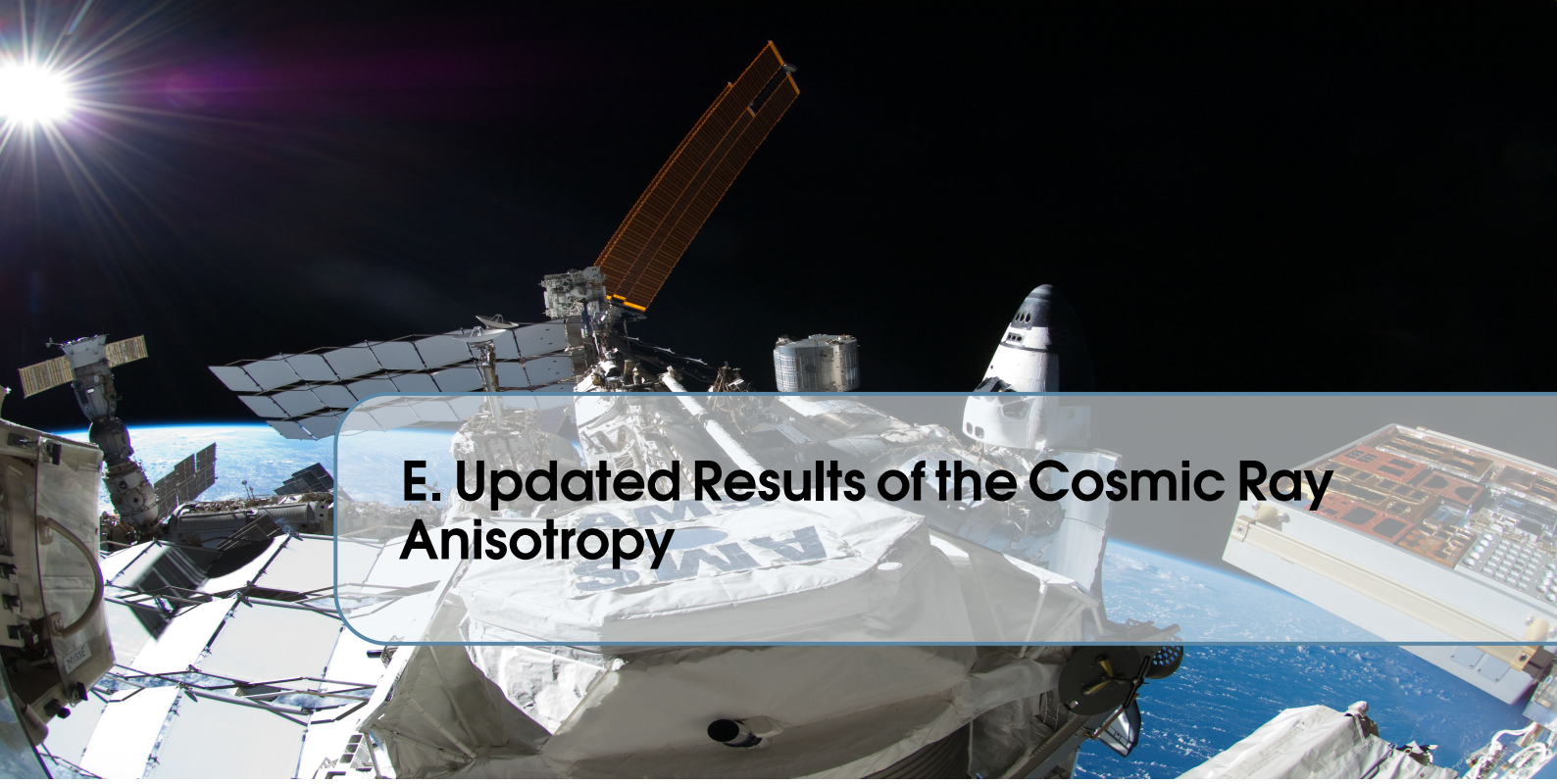

E. Updated Results of the Cosmic Ray Anisotropy

All the results presented in this work corresponded to 8.5 years of data taking with AMS-02. In addition, following exactly the same procedure explained in chapters 4 and 5 this appendix presents an update for the 9 years of data taking, which corresponds to an exposure time of 1.91×10^8 s.

Figures E.1, E.3, E.5, E.7, E.9 and E.11 present the dipole components including both statistical and systematic uncertainties for electrons, positrons, helium, carbon, oxygen, and proton respectively.

The dipole amplitude for each cumulative energy and rigidity range is computed using the dipole components and the results are shown in figures E.2a, E.4a, E.6a, E.8a, E.10a and E.12a. In the lowest energy range, $E_{min} = 16$ GeV, the measured dipole amplitude is $\delta_M^{e^-}(16GeV) = 0.20\%$ and $\delta_M^{e^+}(16GeV) = 1.09\%$ for electrons and positrons. In the case of light primary nuclei and protons and for rigidities $R > 200$ GV the measured dipole amplitude is $\delta_M^{He}(200GV) = 0.18\%$, $\delta_M^{C}(200GV) = 0.85\%$, $\delta_M^{O}(200GV) = 0.93\%$, and $\delta_M^{p}(200GV) = 0.15\%$.

No deviations from isotropy are found for any of the species and the 95 % C.I. limit on the dipole amplitude is established for each of the energy and rigidity ranges (figures E.2b, E.4b, E.6b, E.8b, E.10b, and E.12b). In the lowest energy range, $E_{min} = 16$ GeV, the upper limit is $(\delta_{UL}^{95\%})^{e^-}(16GeV) = 0.36\%$ and $(\delta_{UL}^{95\%})^{e^+}(16GeV) = 1.65\%$ for electrons and positrons. For rigidities $R > 200$ GV the upper limit is $(\delta_{UL}^{95\%})^{He}(200GV) = 0.32\%$, $(\delta_{UL}^{95\%})^{C}(200GV) = 1.62\%$, $(\delta_{UL}^{95\%})^{O}(200GV) = 1.69\%$ and $(\delta_{UL}^{95\%})^{p}(200GV) = 0.32\%$.

The numerical results corresponding to the 9 years electron, positron, helium, carbon, oxygen and proton dipole anisotropy are presented in the tables E.1, E.2, E.3, E.4, E.5 and E.6 from section E.2.

E.1 Figures

E.1.1 Electron Anisotropy

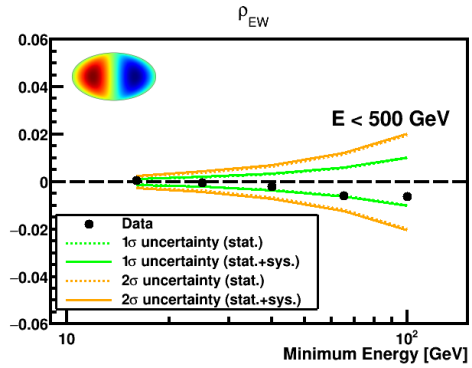

(a) East-West

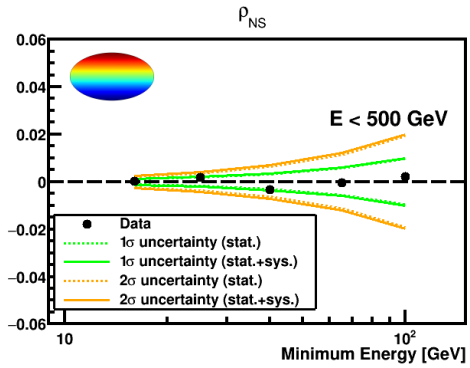

(b) North-South

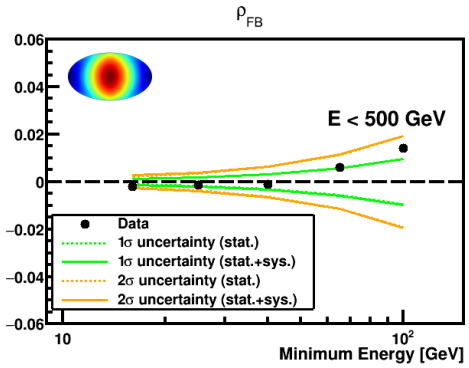

(c) Forward-Backward

Figure E.1: Electron dipole components, EW, NS and FB in galactic coordinates where the 1 and 2-sigma deviations from isotropy (green and yellow, respectively) corresponding to the statistical (dotted line) and total (solid line) uncertainties are shown.

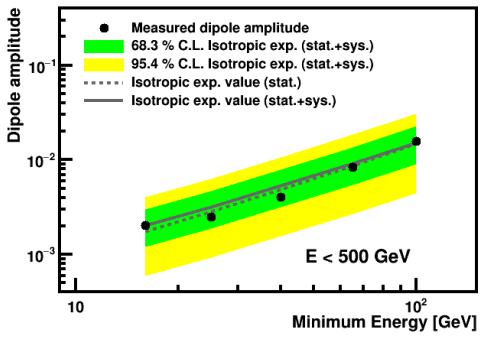

(a) Dipole Amplitude

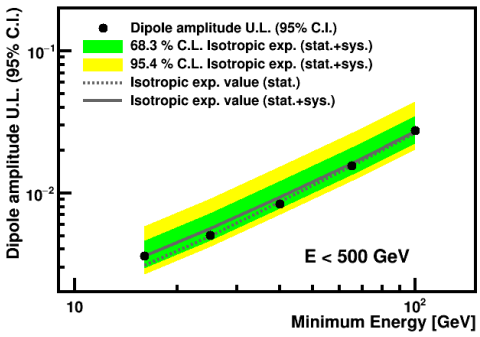

(b) Upper Limit

Figure E.2: Electron measured dipole amplitude (a) and 95% C.I. upper limit (b) as a function of the minimum energy in galactic coordinates. The 1 and 2-sigma total uncertainty bands are shown in green and yellow respectively. The expected value from isotropy considering the statistical (dotted line) and the statistical + systematic (solid line) uncertainties is also displayed.

E.1.2 Positron Anisotropy

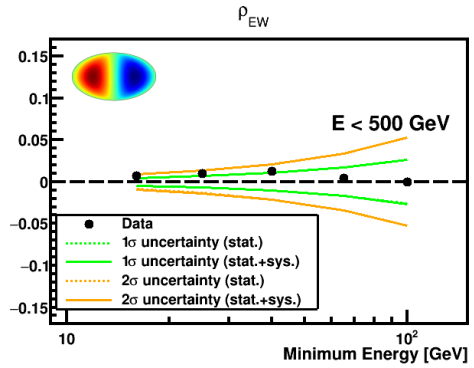

(a) East-West

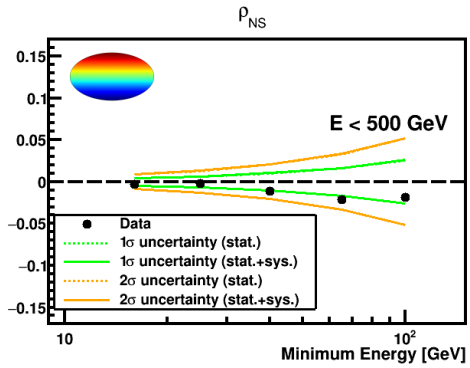

(b) North-South

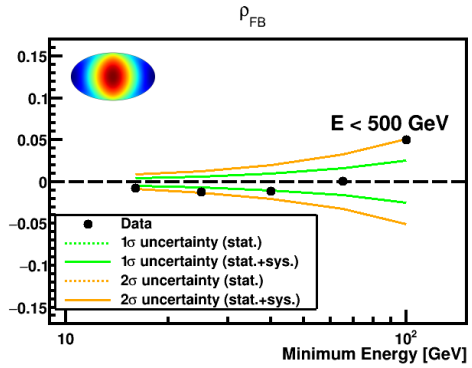

(c) Forward-Backward

Figure E.3: Positron dipole components, EW, NS and FB in galactic coordinates where the 1 and 2-sigma deviations from isotropy (green and yellow, respectively) corresponding to the statistical (dotted line) and total (solid line) uncertainties are shown.

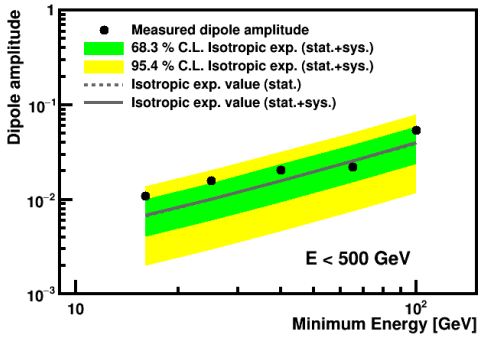

(a) Dipole Amplitude

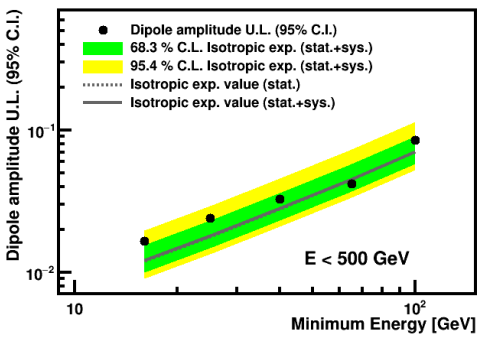

(b) Upper Limit

Figure E.4: Positron measured dipole amplitude (a) and 95% C.I. upper limit (b) as a function of the minimum energy in galactic coordinates. The 1 and 2-sigma total uncertainty bands are shown in green and yellow respectively. The expected value from isotropy considering the statistical (dotted line) and the statistical + systematic (solid line) uncertainties is also displayed.

E.1.3 Helium Anisotropy

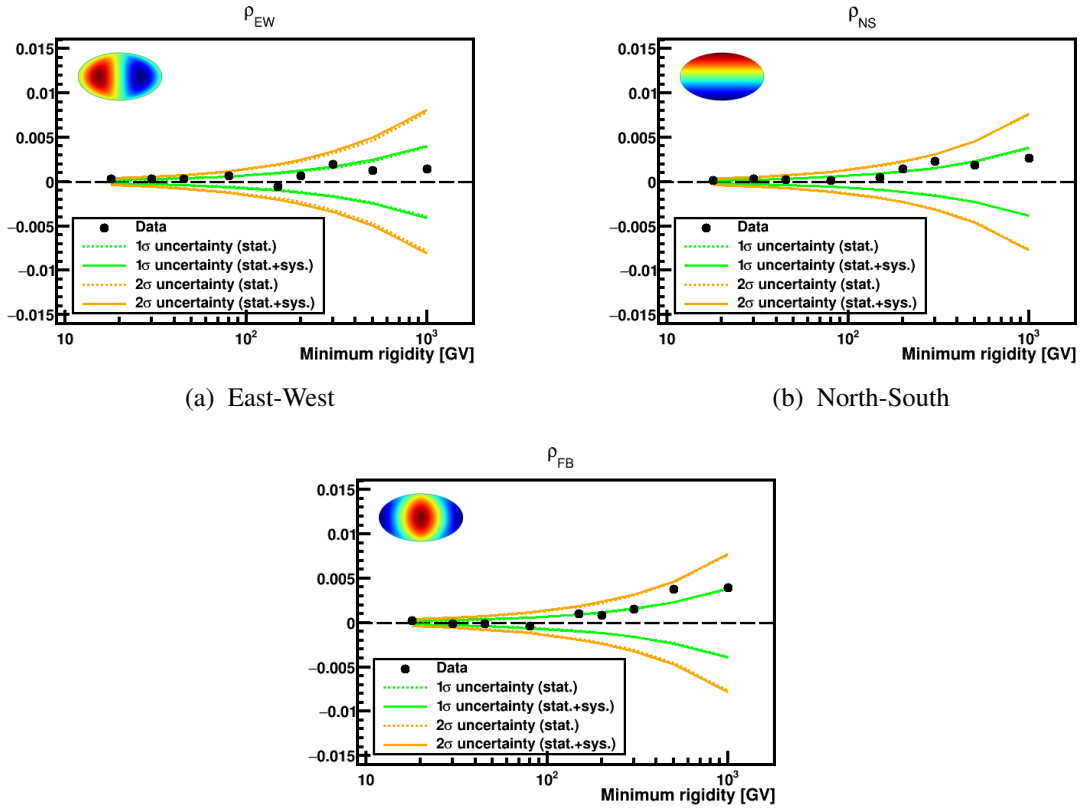

(a) East-West (b) North-South

(c) Forward-Backward

Figure E.5: Helium dipole components, *EW*, *NS* and *FB* in galactic coordinates where the 1 and 2-sigma deviations from isotropy (green and yellow, respectively) corresponding to the statistical (dotted line) and total (solid line) uncertainties are shown.

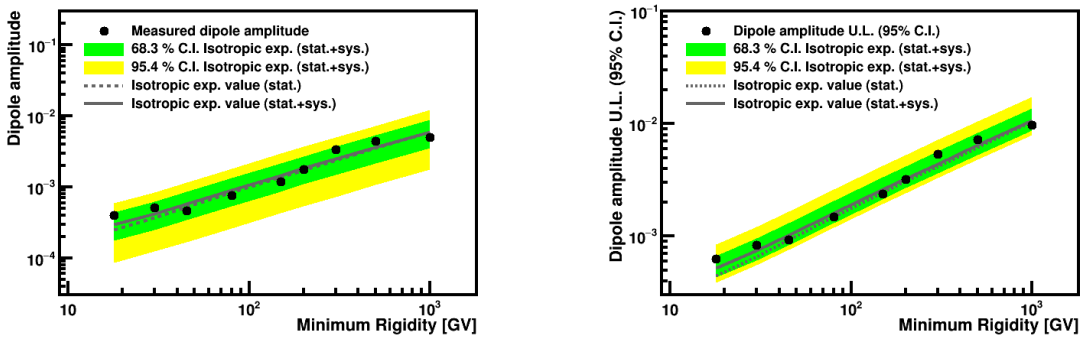

(a) Dipole Amplitude (b) Upper Limit

Figure E.6: Helium measured dipole amplitude (a) and 95% C.I. upper limit (b) as a function of the minimum rigidity in galactic coordinates. The 1 and 2-sigma total uncertainty bands are shown in green and yellow respectively. The expected value from isotropy considering the statistical (dotted line) and the statistical + systematic (solid line) uncertainties is also displayed.

E.1.4 Carbon Anisotropy

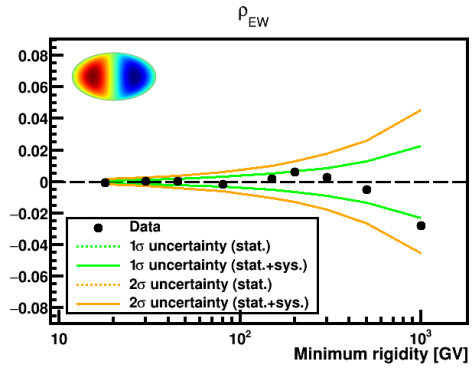

(a) East-West

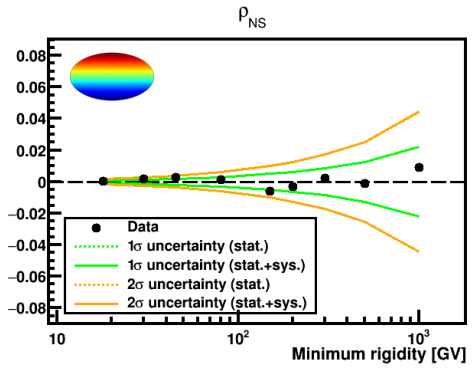

(b) North-South

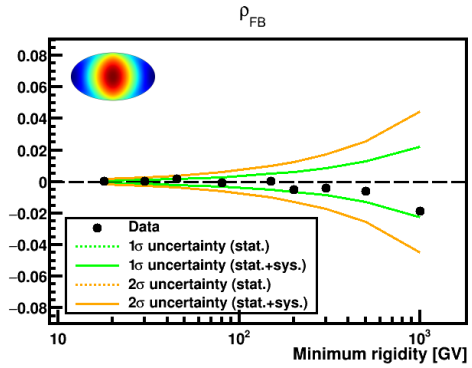

(c) Forward-Backward

Figure E.7: Carbon dipole components, *EW*, *NS* and *FB* in galactic coordinates where the 1 and 2-sigma deviations from isotropy (green and yellow, respectively) corresponding to the statistical (dotted line) and total (solid line) uncertainties are shown.

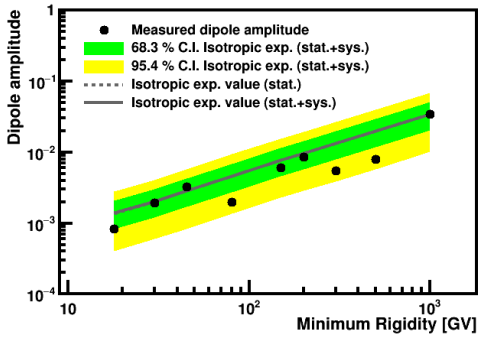

(a) Dipole Amplitude

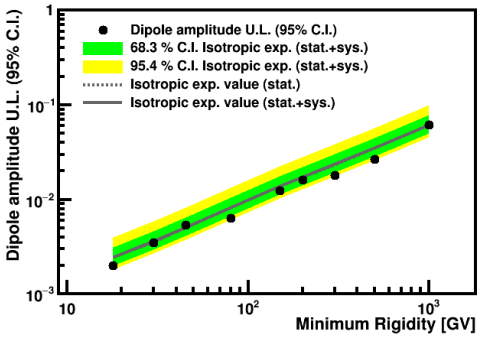

(b) Upper Limit

Figure E.8: Carbon measured dipole amplitude (a) and 95% C.I. upper limit (b) as a function of the minimum rigidity in galactic coordinates. The 1 and 2-sigma total uncertainty bands are shown in green and yellow respectively. The expected value from isotropy considering the statistical (dotted line) and the statistical + systematic (solid line) uncertainties is also displayed.

E.1.5 Oxygen Anisotropy

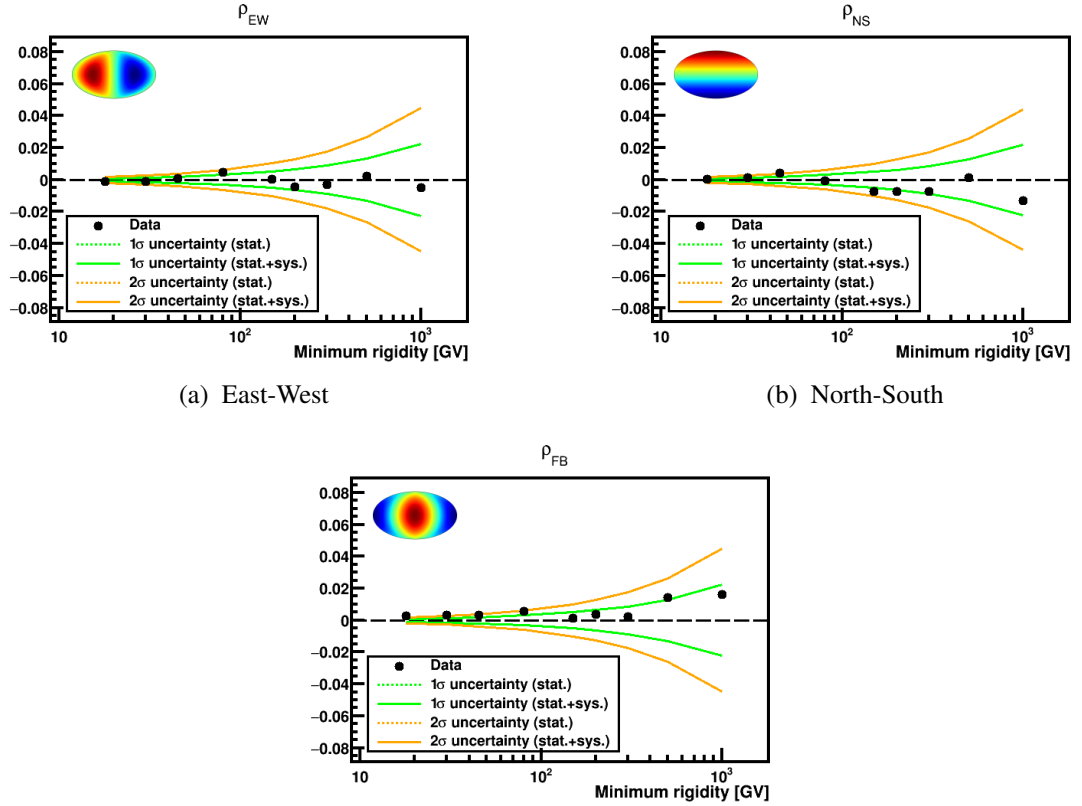

(a) East-West (b) North-South

(c) Forward-Backward

Figure E.9: Oxygen dipole components, *EW*, *NS* and *FB* in galactic coordinates where the 1 and 2-sigma deviations from isotropy (green and yellow, respectively) corresponding to the statistical (dotted line) and total (solid line) uncertainties are shown.

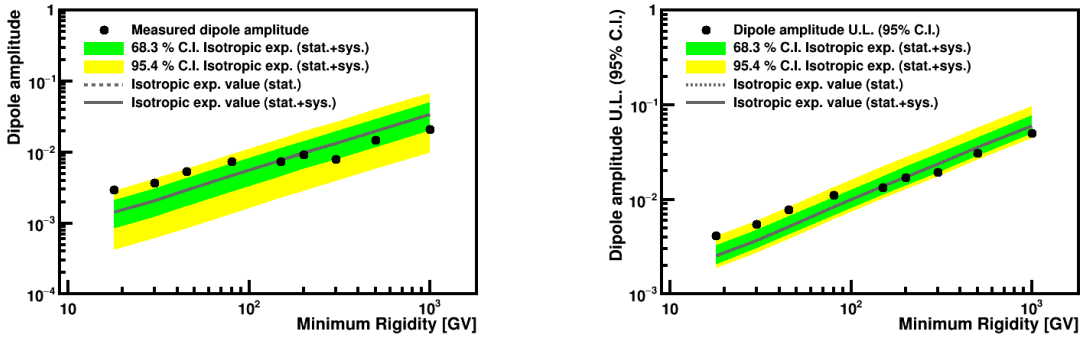

(a) Dipole Amplitude (b) Upper Limit

Figure E.10: Oxygen measured dipole amplitude (a) and 95% C.I. upper limit (b) as a function of the minimum rigidity in galactic coordinates. The 1 and 2-sigma total uncertainty bands are shown in green and yellow respectively. The expected value from isotropy considering the statistical (dotted line) and the statistical + systematic (solid line) uncertainties is also displayed.

E.1.6 Proton Anisotropy

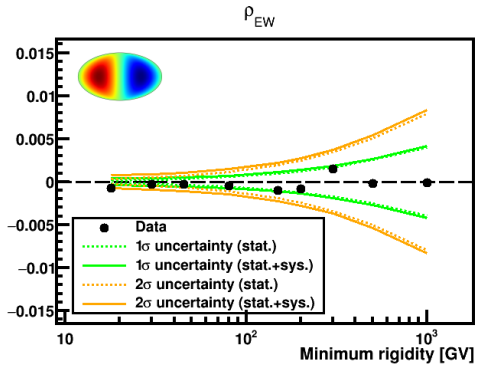

(a) East-West

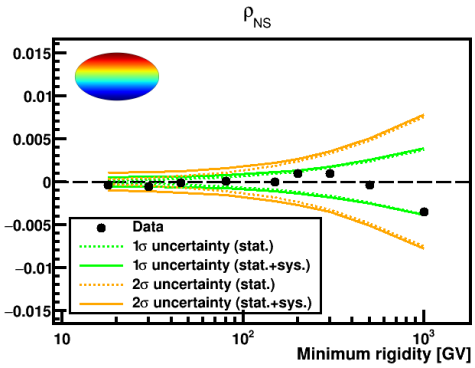

(b) North-South

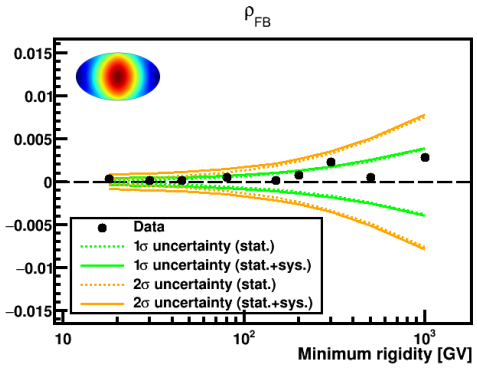

(c) Forward-Backward

Figure E.11: Proton dipole components, *EW*, *NS* and *FB* in galactic coordinates where the 1 and 2-sigma deviations from isotropy (green and yellow, respectively) corresponding to the statistical (dotted line) and total (solid line) uncertainties are shown.

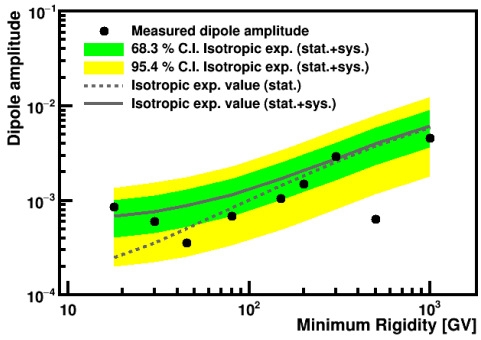

(a) Dipole Amplitude

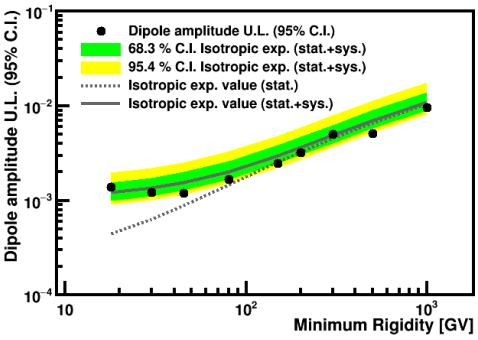

(b) Upper Limit

Figure E.12: Proton measured dipole amplitude (a) and 95% C.I. upper limit (b) as a function of the minimum rigidity in galactic coordinates. The 1 and 2-sigma total uncertainty bands are shown in green and yellow respectively. The expected value from isotropy considering the statistical (dotted line) and the statistical + systematic (solid line) uncertainties is also displayed.

E.2 Tables

E.2.1 Electron Anisotropy

Table E.1: Results of the optimized analysis on the electron dipole anisotropy in galactic coordinates for 9 years.

E_{min} [GeV]	$N_{e^-}^{meas}$	$N_{e^-}^{eq}$	ρ_{EW} (%)	σ_{EW}^{stat} (%)	σ_{EW}^{sys} (%)	$\rho_{EW}/\sigma_{EW}^{tot}$	ρ_{NS} (%)	σ_{NS}^{stat} (%)	σ_{NS}^{sys} (%)	$\rho_{NS}/\sigma_{NS}^{tot}$	ρ_{FB} (%)	σ_{FB}^{stat} (%)	σ_{FB}^{sys} (%)	$\rho_{FB}/\sigma_{FB}^{tot}$	δ_M(%)	$\delta_{U.L.}^{95\%\ C.L.}$(%)
16	2375405	2375405	0.060	0.115	0.062	+0.46	0.024	0.114	0.065	+0.18	-0.192	0.114	0.071	-1.43	0.202	0.359
25	938534	938534	-0.050	0.187	0.105	-0.23	0.190	0.181	0.112	+0.89	-0.151	0.181	0.060	-0.79	0.248	0.502
40	311617	311617	-0.194	0.324	0.151	-0.54	-0.344	0.314	0.163	-0.97	-0.101	0.315	0.077	-0.31	0.408	0.835
65	97200	97200	-0.575	0.580	0.199	-0.94	-0.050	0.562	0.217	-0.08	0.611	0.563	0.111	+1.06	0.840	1.554
100	33387	33387	-0.632	0.987	0.242	-0.62	0.230	0.961	0.265	+0.23	1.419	0.959	0.147	+1.46	1.571	2.746

E.2.2 Positron Anisotropy

Table E.2: Results of the optimized analysis on the positron dipole anisotropy in galactic coordinates including background contamination for 9 years.

E_{min} [GeV]	$N_{e^+}^{meas}$	$N_{e^+}^{eq}$	ρ_{EW} (%)	σ_{EW}^{stat} (%)	σ_{EW}^{sys} (%)	$\rho_{EW}/\sigma_{EW}^{tot}$	ρ_{NS} (%)	σ_{NS}^{stat} (%)	σ_{NS}^{sys} (%)	$\rho_{NS}/\sigma_{NS}^{tot}$	ρ_{FB} (%)	σ_{FB}^{stat} (%)	σ_{FB}^{sys} (%)	$\rho_{FB}/\sigma_{FB}^{tot}$	$\delta_M(\%)$	$\delta_{U.L.}^{95\%\ C.L.}(\%)$
16	160953	160953	0.681	0.445	0.062	+1.51	-0.291	0.437	0.065	-0.66	-0.802	0.438	0.071	-1.81	1.091	1.646
25	74126	74126	0.984	0.669	0.105	+1.45	-0.169	0.645	0.112	-0.26	-1.241	0.644	0.060	-1.92	1.593	2.411
40	29879	29879	1.253	1.049	0.151	+1.18	-1.127	1.020	0.163	-1.09	-1.143	1.014	0.077	-1.12	2.036	3.270
65	11467	11467	0.402	1.687	0.199	+0.24	-2.170	1.653	0.217	-1.30	0.107	1.623	0.111	+0.07	2.209	4.219
100	4676	4676	-0.054	2.625	0.242	-0.02	-1.881	2.580	0.265	-0.73	5.055	2.535	0.147	+1.99	5.394	8.504

E.2.3 Helium Anisotropy

Table E.3: Results on the helium dipole anisotropy in galactic coordinates for 9 years.

E_{min} [GeV]	N_{He}^{meas}	ρ_{EW} (%)	σ_{EW}^{stat} (%)	σ_{EW}^{sys} (%)	$\rho_{EW}/\sigma_{EW}^{tot}$	ρ_{NS} (%)	σ_{NS}^{stat} (%)	σ_{NS}^{sys} (%)	$\rho_{NS}/\sigma_{NS}^{tot}$	ρ_{FB} (%)	σ_{FB}^{stat} (%)	σ_{FB}^{sys} (%)	$\rho_{FB}/\sigma_{FB}^{tot}$	δ_M(%)	$\delta_{U.L.}^{95\%\ C.L.}$(%)
18	116638283	0.033	0.017	0.011	+1.64	0.012	0.016	0.009	+0.66	0.020	0.016	0.010	+1.04	0.040	0.063
29	53146785	0.035	0.025	0.013	+1.24	0.036	0.024	0.010	+1.38	-0.009	0.024	0.014	-0.32	0.051	0.083
45	26795443	0.036	0.035	0.017	+0.95	0.028	0.034	0.012	+0.77	-0.010	0.034	0.018	-0.26	0.047	0.093
80	10303855	0.067	0.056	0.025	+1.10	0.012	0.054	0.015	+0.22	-0.036	0.055	0.024	-0.60	0.077	0.148
150	3771855	-0.051	0.092	0.037	-0.51	0.048	0.090	0.020	+0.52	0.097	0.090	0.031	+1.02	0.120	0.236
201	2397420	0.071	0.116	0.051	+0.56	0.142	0.112	0.024	+1.24	0.081	0.113	0.035	+0.68	0.178	0.321
300	1293662	0.194	0.157	0.066	+1.14	0.233	0.153	0.030	+1.50	0.152	0.154	0.042	+0.95	0.340	0.534
500	592365	0.130	0.233	0.085	+0.52	0.192	0.226	0.040	+0.84	0.377	0.227	0.053	+1.62	0.443	0.724
1000	208651	0.142	0.392	0.102	+0.35	0.268	0.381	0.053	+0.70	0.395	0.383	0.068	+1.02	0.498	0.976

E.2.4 Carbon Anisotropy

Table E.4: Results on the carbon dipole anisotropy in galactic coordinates for 9 years.

E_{min} [GeV]	N_C^{meas}	ρ_{EW} (%)	σ_{EW}^{stat} (%)	σ_{EW}^{sys} (%)	$\rho_{EW}/\sigma_{EW}^{tot}$	ρ_{NS} (%)	σ_{NS}^{stat} (%)	σ_{NS}^{sys} (%)	$\rho_{NS}/\sigma_{NS}^{tot}$	ρ_{FB} (%)	σ_{FB}^{stat} (%)	σ_{FB}^{sys} (%)	$\rho_{FB}/\sigma_{FB}^{tot}$	δ_M(%)	$\delta_{U.L.}^{95\%\ C.L.}$(%)
18	3819427	-0.071	0.091	0.011	-0.78	0.012	0.089	0.009	+0.14	0.039	0.090	0.010	+0.43	0.082	0.202
29	1768990	0.017	0.134	0.013	+0.13	0.191	0.131	0.010	+1.46	0.029	0.131	0.014	+0.22	0.194	0.352
45	894260	0.033	0.189	0.017	+0.18	0.266	0.184	0.012	+1.44	0.178	0.185	0.018	+0.96	0.322	0.542
80	338860	-0.141	0.307	0.025	-0.46	0.127	0.299	0.015	+0.43	-0.049	0.300	0.024	-0.16	0.196	0.635
150	121027	0.170	0.514	0.037	+0.33	-0.586	0.500	0.020	-1.17	0.053	0.502	0.031	+0.10	0.612	1.235
201	77048	0.610	0.644	0.051	+0.94	-0.309	0.628	0.024	-0.49	-0.503	0.631	0.035	-0.80	0.849	1.615
300	41332	0.279	0.881	0.066	+0.32	0.244	0.857	0.030	+0.28	-0.398	0.860	0.042	-0.46	0.544	1.812
500	18739	-0.516	1.313	0.085	-0.39	-0.108	1.267	0.040	-0.09	-0.602	1.276	0.053	-0.47	0.800	2.686
1000	6145	-2.788	2.276	0.102	-1.22	0.912	2.217	0.053	+0.41	-1.852	2.233	0.068	-0.83	3.469	6.124

E.2.5 Oxygen Anisotropy

Table E.5: Results on the oxygen dipole anisotropy in galactic coordinates for 9 years.

E_{min} [GeV]	N_O^{meas}	ρ_{EW} (%)	σ_{EW}^{stat} (%)	σ_{EW}^{sys} (%)	$\rho_{EW}/\sigma_{EW}^{tot}$	ρ_{NS} (%)	σ_{NS}^{stat} (%)	σ_{NS}^{sys} (%)	$\rho_{NS}/\sigma_{NS}^{tot}$	ρ_{FB} (%)	σ_{FB}^{stat} (%)	σ_{FB}^{sys} (%)	$\rho_{FB}/\sigma_{FB}^{tot}$	δ_M(%)	$\delta_{U.L.}^{95\%\ C.L.}$(%)
18	3524895	-0.118	0.094	0.011	-1.25	0.016	0.093	0.009	+0.17	0.266	0.093	0.010	+2.84	0.291	0.416
29	1665404	-0.116	0.138	0.013	-0.84	0.118	0.135	0.010	+0.87	0.330	0.135	0.014	+2.42	0.369	0.544
45	852774	0.079	0.193	0.017	+0.41	0.410	0.189	0.012	+2.17	0.329	0.189	0.018	+1.73	0.532	0.778
80	329174	0.473	0.311	0.025	+1.52	-0.046	0.304	0.015	-0.15	0.567	0.305	0.024	+1.85	0.740	1.120
150	119971	0.042	0.515	0.037	+0.08	-0.729	0.502	0.020	-1.45	0.140	0.505	0.031	+0.28	0.744	1.349
201	76011	-0.450	0.647	0.051	-0.69	-0.713	0.630	0.024	-1.13	0.393	0.635	0.035	+0.62	0.930	1.690
300	40486	-0.278	0.886	0.066	-0.31	-0.708	0.862	0.030	-0.82	0.230	0.871	0.042	+0.26	0.795	1.952
500	18091	0.228	1.326	0.085	+0.17	0.126	1.290	0.040	+0.10	1.449	1.305	0.053	+1.11	1.473	3.109
1000	6222	-0.479	2.246	0.102	-0.21	-1.298	2.199	0.053	-0.59	1.595	2.238	0.068	+0.71	2.111	5.027

E.2.6 Proton Anisotropy

Table E.6: Results on the proton dipole anisotropy in galactic coordinates for 9 years.

E_{min} [GeV]	N_{Pr}^{meas}	ρ_{EW} (%)	σ_{EW}^{stat} (%)	σ_{EW}^{sys} (%)	$\rho_{EW}/\sigma_{EW}^{tot}$	ρ_{NS} (%)	σ_{NS}^{stat} (%)	σ_{NS}^{sys} (%)	$\rho_{NS}/\sigma_{NS}^{tot}$	ρ_{FB} (%)	σ_{FB}^{stat} (%)	σ_{FB}^{sys} (%)	$\rho_{FB}/\sigma_{FB}^{tot}$	δ_M(%)	$\delta_{U.L.}^{95\%\ C.L.}$(%)
18	118567211	-0.072	0.016	0.034	-1.89	-0.037	0.016	0.049	-0.72	0.029	0.016	0.039	+0.69	0.086	0.139
29	59201280	-0.026	0.024	0.038	-0.59	-0.052	0.023	0.051	-0.92	0.016	0.023	0.042	+0.34	0.060	0.122
45	29177661	-0.031	0.034	0.041	-0.59	-0.009	0.032	0.054	-0.15	0.013	0.033	0.045	+0.24	0.035	0.119
80	10663002	-0.047	0.056	0.047	-0.64	0.003	0.053	0.057	+0.04	0.049	0.054	0.049	+0.68	0.068	0.167
150	3595607	-0.104	0.096	0.055	-0.94	-0.000	0.092	0.062	-0.00	0.016	0.093	0.055	+0.15	0.105	0.248
201	2193321	-0.083	0.124	0.061	-0.60	0.100	0.118	0.065	+0.75	0.074	0.119	0.058	+0.56	0.150	0.318
300	1142557	0.152	0.171	0.072	+0.82	0.093	0.163	0.070	+0.53	0.228	0.164	0.064	+1.29	0.290	0.502
500	524643	-0.023	0.253	0.092	-0.08	-0.035	0.240	0.080	-0.14	0.048	0.242	0.075	+0.19	0.064	0.512
1000	213518	-0.007	0.398	0.129	-0.02	-0.354	0.376	0.099	-0.91	0.286	0.380	0.097	+0.73	0.455	0.953

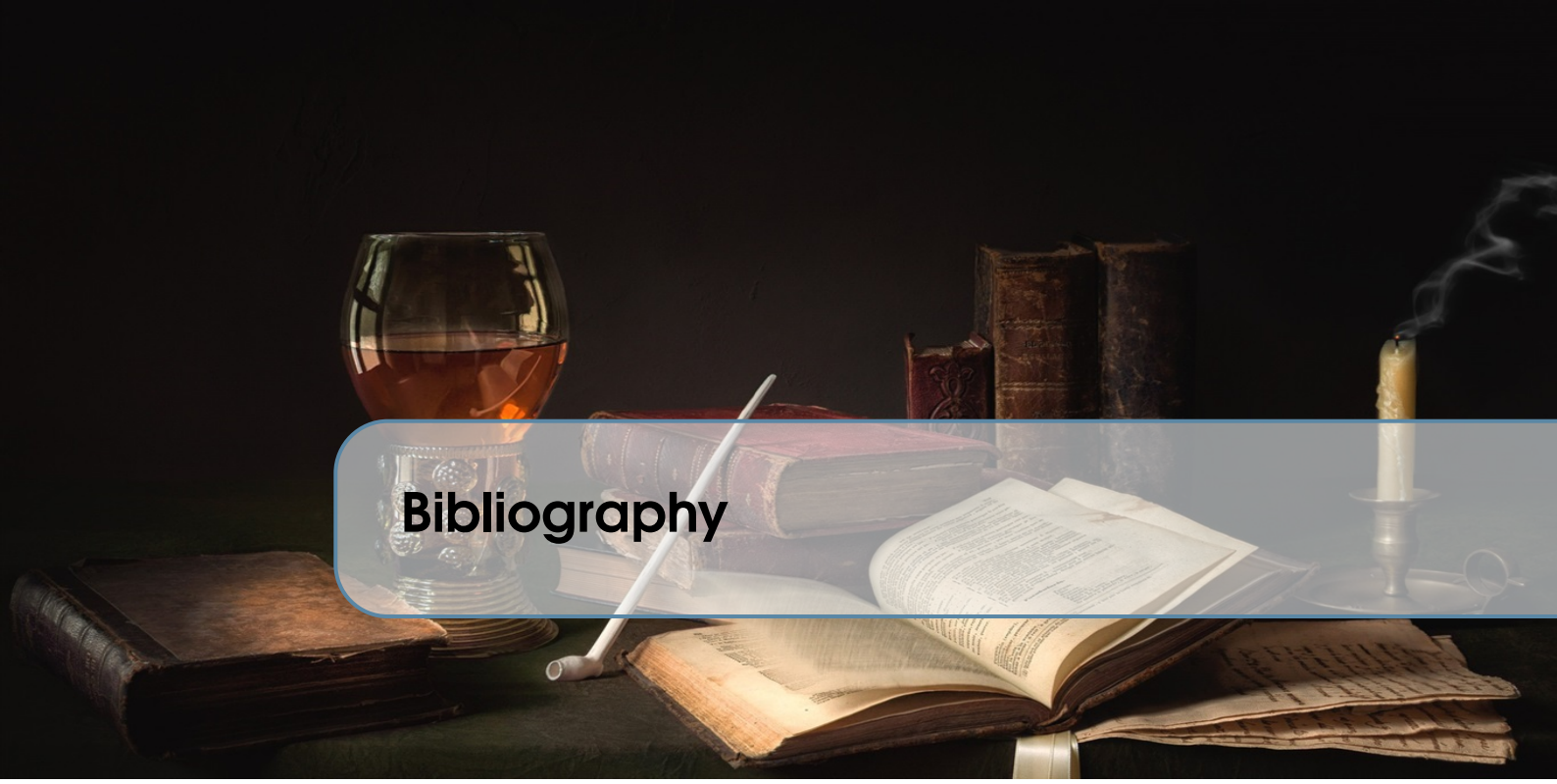

Bibliography

[1] H. Becquerel. “On the rays emitted by phosphorescence”. In: *Comptes Rendus* 122.420 (1896) (cited on page 1).

[2] H. Becquerel. “On the invisible rays emitted by phosphorescent bodies”. In: *Comptes Rendus* 122.501 (1896) (cited on page 1).

[3] T. Wulf. “Über die in der atmosphäre vorhandene strahlung von hoher durchdringungsfähigkeit”. In: *Phys. Zeit.* 10.5 (1909), pages 152–157 (cited on page 1).

[4] D. Pacini. “La radiazione penetrante alla superficie ed in seno alle acque”. In: *Il Nuovo Cimento* 3 (Dec. 1912), pages 93–100. DOI: 10.1007/BF02957440 (cited on page 1).

[5] V. F. Hess. “Über Beobachtungen der durchdringenden Strahlung bei sieben Freiballonfahrten”. In: *Phys. Zeit.* 13 (1912), pages 1084–1091 (cited on page 1).

[6] V. F. Hess. *The Nobel Prize in Physics 1936*. https://www.nobelprize.org/prizes/physics/1936/summary/ (cited on page 1).

[7] R. A. Millikan and G. Harvey Cameron. “High Frequency Rays of Cosmic Origin III. Measurements in Snow-Fed Lakes at High Altitudes”. In: *Phys. Rev.* 28 (5 Nov. 1926), pages 851–868. DOI: 10.1103/PhysRev.28.851. URL: https://link.aps.org/doi/10.1103/PhysRev.28.851 (cited on page 1).

[8] J. Clay. “Penetrating Radiation”. In: *Proceedings of the Section of Sciences, Koninklijke Akademie van Wetenschappen Te Amsterdam* 30 (Dec. 1927), pages 1115–1127. URL: https://www.dwc.knaw.nl/DL/publications/PU00011919.pdf (cited on page 1).

[9] Bruno Rossi. “On the Magnetic Deflection of Cosmic Rays”. In: *Phys. Rev.* 36 (3 Aug. 1930), pages 606–606. DOI: 10.1103/PhysRev.36.606. URL: https://link.aps.org/doi/10.1103/PhysRev.36.606 (cited on page 2).

[10] Thomas H. Johnson. “The Azimuthal Asymmetry of the Cosmic Radiation”. In: *Phys. Rev.* 43 (10 May 1933), pages 834–835. DOI: 10.1103/PhysRev.43.834. URL: https://link.aps.org/doi/10.1103/PhysRev.43.834 (cited on page 2).

[11] Luis Alvarez and Arthur H. Compton. "A Positively Charged Component of Cosmic Rays". In: *Phys. Rev.* 43 (10 May 1933), pages 835–836. DOI: 10.1103/PhysRev.43.835. URL: https://link.aps.org/doi/10.1103/PhysRev.43.835 (cited on page 2).

[12] Bruno Rossi. "Directional Measurements on the Cosmic Rays Near the Geomagnetic Equator". In: *Phys. Rev.* 45 (3 Feb. 1934), pages 212–214. DOI: 10.1103/PhysRev.45.212. URL: https://link.aps.org/doi/10.1103/PhysRev.45.212 (cited on page 2).

[13] Carl D. Anderson. "The Positive Electron". In: *Phys. Rev.* 43 (6 Mar. 1933), pages 491–494. DOI: 10.1103/PhysRev.43.491. URL: https://link.aps.org/doi/10.1103/PhysRev.43.491 (cited on page 2).

[14] J. C. Street and E. C. Stevenson. "New Evidence for the Existence of a Particle of Mass Intermediate Between the Proton and Electron". In: *Phys. Rev.* 52 (9 Nov. 1937), pages 1003–1004. DOI: 10.1103/PhysRev.52.1003. URL: https://link.aps.org/doi/10.1103/PhysRev.52.1003 (cited on page 2).

[15] G.P.S. Occhialini and C.F. Powell. "Nuclear disintegration produced by slow charged particles of small mass". In: *Nature* 159 (1947), pages 186–190. DOI: 10.1038/159186a0 (cited on page 2).

[16] G. D. Rochester and C. C. Butler. "Evidence for the Existence of New Unstable Elementary Particles". In: *Nature* 160 (1947), pages 855–857. DOI: 10.1038/160855a0. URL: https://doi.org/10.1038/160855a0 (cited on page 2).

[17] M. Wiedenbeck et al. "An Overview of the Origin of Galactic Cosmic Rays as Inferred from Observations of Heavy Ion Composition and Spectra". In: *Space Science Reviews* 130 (June 2007). DOI: 10.1007/s11214-007-9198-y (cited on page 3).

[18] J. W. Cronin, T. K. Gaisser, and S. P. Swordy. "Cosmic Rays at the Energy Frontier". In: *Scientific American* 276 (Jan. 1997), pages 44–49. DOI: 10.1038/scientificamerican0197-44 (cited on page 4).

[19] Jörg R. Hörandel. "Cosmic-ray composition and its relation to shock acceleration by supernova remnants". In: *Advances in Space Research* 41.3 (2008), pages 442–463. ISSN: 0273-1177. DOI: https://doi.org/10.1016/j.asr.2007.06.008. URL: http://www.sciencedirect.com/science/article/pii/S0273117707006308 (cited on page 4).

[20] Jörg R Höorandel. "A review of experimental results at the knee". In: *Journal of Physics: Conference Series* 47 (Oct. 2006), pages 41–50. DOI: 10.1088/1742-6596/47/1/005. URL: https://doi.org/10.1088/1742-6596/47/1/005 (cited on page 4).

[21] Andrew M. Taylor. "Cosmic rays beyond the knees". In: *Nature* 531 (2016), pages 43–44. DOI: 10.1038/531043a (cited on page 4).

[22] Kenneth Greisen. "End to the cosmic ray spectrum?" In: *Phys. Rev. Lett.* 16 (1966), pages 748–750. DOI: 10.1103/PhysRevLett.16.748 (cited on page 4).

[23] Vitor de Souza. "Testing the agreement between the $X_{\max}$ distributions measured by the Pierre Auger and Telescope Array Observatories". In: *PoS* ICRC2017 (2018), page 522. DOI: 10.22323/1.301.0522 (cited on page 4).

[24] Oliver Deligny. "The energy spectrum of ultra-high energy cosmic rays measured at the Pierre Auger Observatory and at the Telescope Array". In: *PoS* ICRC2019 (2018). DOI: https://pos.sissa.it/358/234/pdf (cited on page 4).

[25] Particle Data Group et al. “Review of Particle Physics”. In: *Progress of Theoretical and Experimental Physics* 2020.8 (Aug. 2020). ISSN: 2050-3911. DOI: 10.1093/ptep/ptaa104. eprint: https://academic.oup.com/ptep/article-pdf/2020/8/083C01/34673722/ptaa104.pdf. URL: https://doi.org/10.1093/ptep/ptaa104 (cited on page 5).

[26] V. L. Ginzburg and S. I. Syrovatskii. *The Origin of Cosmic Rays*. 1964 (cited on page 5).

[27] ENRICO Fermi. “On the Origin of the Cosmic Radiation”. In: *Phys. Rev.* 75 (8 Apr. 1949), pages 1169–1174. DOI: 10.1103/PhysRev.75.1169. URL: https://link.aps.org/doi/10.1103/PhysRev.75.1169 (cited on page 5).

[28] E.G. Berezhko, V.K. Yelshin, and L.T. Ksenofontov. “Numerical investigation of cosmic ray acceleration in supernova remnants”. In: *Astroparticle Physics* 2.2 (1994), pages 215–227. ISSN: 0927-6505. DOI: https://doi.org/10.1016/0927-6505(94)90043-4. URL: http://www.sciencedirect.com/science/article/pii/0927650594900434 (cited on page 5).

[29] Andrew W. Strong, Igor V. Moskalenko, and Vladimir S. Ptuskin. “Cosmic-Ray Propagation and Interactions in the Galaxy”. In: *Annual Review of Nuclear and Particle Science* 57.1 (2007), pages 285–327. DOI: 10.1146/annurev.nucl.57.090506.123011. eprint: https://doi.org/10.1146/annurev.nucl.57.090506.123011. URL: https://doi.org/10.1146/annurev.nucl.57.090506.123011 (cited on page 6).

[30] E.N. Parker. “The passage of energetic charged particles through interplanetary space”. In: *Planetary and Space Science* 13.1 (1965), pages 9–49. ISSN: 0032-0633. DOI: https://doi.org/10.1016/0032-0633(65)90131-5. URL: http://www.sciencedirect.com/science/article/pii/0032063365901315 (cited on page 6).

[31] V.S. Berezinsky et al. *Astrophysics of cosmic rays*. Edited by V.L. Ginzburg. 1990 (cited on pages 6, 20).

[32] A. N. Kolmogorov. “The Local Structure of Turbulence in Incompressible Viscous Fluid for Very Large Reynolds Numbers”. In: *Proceedings: Mathematical and Physical Sciences* 434.1890 (1991), pages 9–13. ISSN: 09628444. URL: http://www.jstor.org/stable/51980 (cited on page 6).

[33] Robert H. Kraichnan. “Inertial Range Spectrum of Hydromagnetic Turbulence”. In: *The Physics of Fluids* 8.7 (1965), pages 1385–1387. DOI: 10.1063/1.1761412. eprint: https://aip.scitation.org/doi/pdf/10.1063/1.1761412. URL: https://aip.scitation.org/doi/abs/10.1063/1.1761412 (cited on page 6).

[34] Beck R. “Galactic and extragalactic magnetic fields - A concise review”. In: *Astrophysics and Space Sciences Transactions (ASTRA)* 5 (Oct. 2009). DOI: 10.5194/astra-5-43-2009 (cited on pages 6, 17).

[35] *GALPROP*. http://galprop.stanford.edu,1998 (cited on page 7).

[36] *DRAGON*. http://dragon.hepforge.org/DRAGON/Home.html,1992 (cited on page 7).

[37] D. Maurin. “USINE:. a new public cosmic ray propagation code Basic phenomenology, sample results, and a bit of USINE”. In: edited by S. Giani, C. Leroy, and P. G. Rancoita. June 2011, pages 420–434. DOI: 10.1142/9789814329033_0053 (cited on page 7).

[38] E. N. Parker. “Dynamics of the Interplanetary Gas and Magnetic Fields.” In: *Astrophysical Journal* 128 (Nov. 1958), page 664. DOI: 10.1086/146579 (cited on page 7).

[39] L. J. Gleeson and W. I. Axford. “Solar Modulation of Galactic Cosmic Rays”. In: *Astrophysical Journal* 154 (Dec. 1968), page 1011. DOI: 10.1086/149822 (cited on page 8).

[40] Rolf Kappl. “SOLARPROP: Charge-sign dependent solar modulation for everyone”. In: *Computer Physics Communications* 207 (2016), pages 386–399. ISSN: 0010-4655. DOI: https://doi.org/10.1016/j.cpc.2016.05.025. URL: http://www.sciencedirect.com/science/article/pii/S001046551630159X (cited on page 8).

[41] M.S. Potgieter. “The charge-sign dependent effect in the solar modulation of cosmic rays”. In: *Advances in Space Research* 53.10 (2014). Cosmic Ray Origins: Viktor Hess Centennial Anniversary, pages 1415–1425. ISSN: 0273-1177. DOI: https://doi.org/10.1016/j.asr.2013.04.015. URL: http://www.sciencedirect.com/science/article/pii/S0273117713002275 (cited on page 8).

[42] C. Størmer. “On the Trajectories of Electric Particles in the Field of a Magnetic Dipole with Applications to the theory of Cosmic Radiation. First Communication”. In: *Publications of the Oslo Observatory, vol. 1, pp.Ji-JPIX* () (cited on page 9).

[43] Thebault Erwan et al. “International Geomagnetic Reference Field: the 12th generation”. In: *Earth, Planets and Space* 67 (May 2015), page 79. DOI: 10.1186/s40623-015-0228-9 (cited on page 10).

[44] J A Van Allen et al. “OBSERVATION OF HIGH INTENSITY RADIATION BY SATELLITES 1958 ALPHA AND GAMMA”. In: *Jet Propulsion* 28 (Sept. 1958). DOI: 10.2514/8.7396 (cited on page 10).

[45] J. A. Van Allen. “Geomagnetically-Trapped Corpuscular Radiation”. In: *Proceedings of the Royal Society of London. Series A, Mathematical and Physical Sciences* 253.1275 (1959), pages 525–529. ISSN: 00804630. URL: http://www.jstor.org/stable/100702 (cited on page 10).

[46] N. Chiba et al. “Akeno Giant Air Shower Array (AGASA) covering 100 km2 area”. In: *Nuclear Instruments and Methods in Physics Research Section A: Accelerators, Spectrometers, Detectors and Associated Equipment* 311.1 (1992), pages 338–349. ISSN: 0168-9002. DOI: https://doi.org/10.1016/0168-9002(92)90882-5. URL: http://www.sciencedirect.com/science/article/pii/0168900292908825 (cited on page 11).

[47] T Antoni et al. “The cosmic-ray experiment KASCADE”. In: *Nuclear Instruments and Methods in Physics Research Section A: Accelerators, Spectrometers, Detectors and Associated Equipment* 513.3 (2003), pages 490–510. ISSN: 0168-9002. DOI: https://doi.org/10.1016/S0168-9002(03)02076-X. URL: http://www.sciencedirect.com/science/article/pii/S016890020302076X (cited on page 11).

[48] G. Navarra et al. “KASCADE-Grande: a large acceptance, high-resolution cosmic-ray detector up to 1018eV”. In: *Nuclear Instruments and Methods in Physics Research Section A: Accelerators, Spectrometers, Detectors and Associated Equipment* 518.1 (2004). Frontier Detectors for Frontier Physics: Proceedin, pages 207–209. ISSN: 0168-9002. DOI: https://doi.org/10.1016/j.nima.2003.10.061. URL: http://www.sciencedirect.com/science/article/pii/S0168900203027748 (cited on page 11).

[49] R.W. Springer. “The High Altitude water Cherenkov (HAWC) Observatory”. In: *Nuclear and Particle Physics Proceedings* 279-281 (2016). Proceedings of the 9th Cosmic Ray International Seminar, pages 87–94. ISSN: 2405-6014. DOI: https://doi.org/10.1016/j.nuclphysbps.2016.10.013. URL: http://www.sciencedirect.com/science/article/pii/S2405601416301948 (cited on page 11).

[50] Daniel Ferenc. "The MAGIC gamma-ray observatory". In: *Nuclear Instruments and Methods in Physics Research Section A: Accelerators, Spectrometers, Detectors and Associated Equipment* 553.1 (2005). Proceedings of the fifth International Workshop on Ring Imaging Detectors, pages 274–281. ISSN: 0168-9002. DOI: https://doi.org/10.1016/j.nima.2005.08.085. URL: http://www.sciencedirect.com/science/article/pii/S0168900205016098 (cited on page 11).

[51] J.A Hinton. "The status of the HESS project". In: *New Astronomy Reviews* 48.5 (2004). 2nd VERITAS Symposium on the Astrophysics of Extragalactic Sources, pages 331–337. ISSN: 1387-6473. DOI: https://doi.org/10.1016/j.newar.2003.12.004. URL: http://www.sciencedirect.com/science/article/pii/S1387647303003555 (cited on page 11).

[52] T.C Weekes et al. "VERITAS: the Very Energetic Radiation Imaging Telescope Array System". In: *Astroparticle Physics* 17.2 (2002), pages 221–243. ISSN: 0927-6505. DOI: https://doi.org/10.1016/S0927-6505(01)00152-9. URL: http://www.sciencedirect.com/science/article/pii/S0927650501001529 (cited on page 11).

[53] J. Abraham et al. "Properties and performance of the prototype instrument for the Pierre Auger Observatory". In: *Nuclear Instruments and Methods in Physics Research Section A: Accelerators, Spectrometers, Detectors and Associated Equipment* 523.1 (2004), pages 50–95. ISSN: 0168-9002. DOI: https://doi.org/10.1016/j.nima.2003.12.012. URL: http://www.sciencedirect.com/science/article/pii/S0168900203033497 (cited on page 11).

[54] G. Cataldi. "Towards AugerPrime: the upgrade of the Pierre Auger Observatory". In: *Nuclear and Particle Physics Proceedings* 291-293 (2017). "New eyes on the Universe" CRIS 2016 Cosmic Rays International Seminars Proceedings of the Cosmic Rays International Seminars, pages 96–101. ISSN: 2405-6014. DOI: https://doi.org/10.1016/j.nuclphysbps.2017.06.019. URL: http://www.sciencedirect.com/science/article/pii/S240560141730398X (cited on page 11).

[55] H. Kawai et al. "Telescope Array Experiment". In: *Nuclear Physics B - Proceedings Supplements* 175-176 (2008). Proceedings of the XIV International Symposium on Very High Energy Cosmic Ray Interactions, pages 221–226. ISSN: 0920-5632. DOI: https://doi.org/10.1016/j.nuclphysbps.2007.11.002. URL: http://www.sciencedirect.com/science/article/pii/S0920563207007992 (cited on page 11).

[56] M. A. DuVernois et al. "Cosmic-Ray Electrons and Positrons from 1 to 100 GeV: Measurements with HEAT and Their Interpretation". In: *The Astrophysical Journal* 559.1 (Sept. 2001), pages 296–303. DOI: 10.1086/322324 (cited on page 11).

[57] A. S. Beach et al. "Measurement of the Cosmic-Ray Antiproton-to-Proton Abundance Ratio between 4 and 50 GeV". In: *Phys. Rev. Lett.* 87 (27 Dec. 2001), page 271101. DOI: 10.1103/PhysRevLett.87.271101. URL: https://link.aps.org/doi/10.1103/PhysRevLett.87.271101 (cited on page 11).

[58] S. Haino et al. "Measurements of primary and atmospheric cosmic-ray spectra with the BESS-TeV spectrometer". In: *Physics Letters B* 594.1 (2004), pages 35–46. ISSN: 0370-2693. DOI: https://doi.org/10.1016/j.physletb.2004.05.019. URL: http://www.sciencedirect.com/science/article/pii/S0370269304007567 (cited on page 11).

[59] S. Orito et al. "Precision Measurement of Cosmic-Ray Antiproton Spectrum". In: *Phys. Rev. Lett.* 84 (6 Feb. 2000), pages 1078–1081. DOI: 10.1103/PhysRevLett.84.1078. URL: https://link.aps.org/doi/10.1103/PhysRevLett.84.1078 (cited on page 11).

[60] M. Boezio et al. “The Cosmic-Ray Electron and Positron Spectra Measured at 1 AU during Solar Minimum Activity”. In: *The Astrophysical Journal* 532.1 (Mar. 2000), pages 653–669. DOI: 10.1086/308545. URL: https://doi.org/10.1086/308545 (cited on page 11).

[61] M. Boezio et al. “The cosmic-ray proton and helium spectra measured with the CAPRICE98 balloon experiment”. In: *Astroparticle Physics* 19.5 (2003), pages 583–604. ISSN: 0927-6505. DOI: https://doi.org/10.1016/S0927-6505(02)00267-0. URL: http://www.sciencedirect.com/science/article/pii/S0927650502002670 (cited on page 11).

[62] M. Boezio et al. “The Cosmic-Ray Antiproton Flux between 3 and 49 GeV”. In: *The Astrophysical Journal* 561.2 (Nov. 2001), pages 787–799. DOI: 10.1086/323366. URL: https://doi.org/10.1086/323366 (cited on page 11).

[63] K. Abe et al. “Measurement of the cosmic-ray low-energy antiproton spectrum with the first BESS-Polar Antarctic flight”. In: *Physics Letters B* 670.2 (2008), pages 103–108. ISSN: 0370-2693. DOI: https://doi.org/10.1016/j.physletb.2008.10.053. URL: http://www.sciencedirect.com/science/article/pii/S0370269308013270 (cited on pages 11, 15).

[64] Jin Chang et al. “An excess of cosmic ray electrons at energies of 300–800 GeV”. In: *Nature* 456 (Dec. 2008), pages 362–5. DOI: 10.1038/nature07477 (cited on page 11).

[65] A.D. Panov et al. “Energy Spectra of Abundant Nuclei of Primary Cosmic Rays from the Data of ATIC-2 Experiment: Final Results”. In: *Bull. Russ. Acad. Sci. Phys.* 73.5 (2009), pages 564–567. DOI: 10.3103/S1062873809050098. arXiv: 1101.3246 [astro-ph.HE] (cited on page 11).

[66] H. S. Ahn et al. “DISCREPANT HARDENING OBSERVED IN COSMIC-RAY ELEMENTAL SPECTRA”. In: *The Astrophysical Journal* 714.1 (Apr. 2010), pages L89–L93. DOI: 10.1088/2041-8205/714/1/l89. URL: https://doi.org/10.1088/2041-8205/714/1/l89 (cited on page 12).

[67] V. V. Akimov et al. “Measurements of the primary cosmic ray spectra in the 10^{11}-10^{14} eV energy range from Proton-1, 2, 3 satellites”. In: *International Cosmic Ray Conference*. Volume 1. International Cosmic Ray Conference. Jan. 1970, page 517 (cited on page 12).

[68] J. J. Engelmann et al. “Charge composition and energy spectra of cosmic-ray nuclei for elements from Be to Ni - Results from HEAO-3-C2.” In: *Astronomy and Astrophysics* 233 (July 1990), pages 96–111 (cited on page 12).

[69] P Meyer et al. “Cosmic Ray Nuclei (CRN) detector investigation. Final Report”. In: (Jan. 1991) (cited on page 12).

[70] M. Green et al. “ASTROMAG: A superconducting particle astrophysics magnet facility for the space station”. In: *IEEE Transactions on Magnetics* 23.2 (1987), pages 1240–1243. DOI: 10.1109/TMAG.1987.1064905 (cited on page 12).

[71] S. Ahlen et al. “An antimatter spectrometer in space”. In: *Nuclear Instruments and Methods in Physics Research Section A: Accelerators, Spectrometers, Detectors and Associated Equipment* 350.1 (1994), pages 351–367. ISSN: 0168-9002. DOI: https://doi.org/10.1016/0168-9002(94)91184-3. URL: http://www.sciencedirect.com/science/article/pii/0168900294911843 (cited on pages 12, 23).

[72] O. Adriani et al. “PAMELA Measurements of Cosmic-Ray Proton and Helium Spectra”. In: *Science* 332.6025 (2011), pages 69–72. ISSN: 0036-8075. DOI: 10.1126/science.1199172. eprint: https://science.sciencemag.org/content/332/6025/69.full.pdf. URL: https://science.sciencemag.org/content/332/6025/69 (cited on page 13).

[73] Q. An et al. “Measurement of the cosmic ray proton spectrum from 40 GeV to 100 TeV with the DAMPE satellite”. In: *Science Advances* 5.9 (2019). DOI: 10.1126/sciadv.aax3793 (cited on page 13).

[74] O. Adriani et al. “Direct Measurement of the Cosmic-Ray Proton Spectrum from 50 GeV to 10 TeV with the Calorimetric Electron Telescope on the International Space Station”. In: *Phys. Rev. Lett.* 122 (18 May 2019), page 181102. DOI: 10.1103/PhysRevLett.122.181102. URL: https://link.aps.org/doi/10.1103/PhysRevLett.122.181102 (cited on page 13).

[75] M. Aguilar et al. “Precision Measurement of the Proton Flux in Primary Cosmic Rays from Rigidity 1 GV to 1.8 TV with the Alpha Magnetic Spectrometer on the International Space Station”. In: *Phys. Rev. Lett.* 114 (17 Apr. 2015), page 171103. DOI: 10.1103/PhysRevLett.114.171103. URL: https://link.aps.org/doi/10.1103/PhysRevLett.114.171103 (cited on page 13).

[76] M. Aguilar et al. “Observation of the Identical Rigidity Dependence of He, C, and O Cosmic Rays at High Rigidities by the Alpha Magnetic Spectrometer on the International Space Station”. In: *Phys. Rev. Lett.* 119 (25 Dec. 2017), page 251101. DOI: 10.1103/PhysRevLett.119.251101. URL: https://link.aps.org/doi/10.1103/PhysRevLett.119.251101 (cited on pages 13, 102, 103, 105, 144).

[77] M. Aguilar et al. “The Alpha Magnetic Spectrometer (AMS) on the international space station: Part II — Results from the first seven years”. In: *Physics Reports* (2020). ISSN: 0370-1573. DOI: https://doi.org/10.1016/j.physrep.2020.09.003. URL: http://www.sciencedirect.com/science/article/pii/S0370157320303434 (cited on pages 14, 16, 25, 27, 28, 30, 32, 37).

[78] M. Aguilar et al. “Observation of New Properties of Secondary Cosmic Rays Lithium, Beryllium, and Boron by the Alpha Magnetic Spectrometer on the International Space Station”. In: *Phys. Rev. Lett.* 120 (2 Jan. 2018), page 021101. DOI: 10.1103/PhysRevLett.120.021101. URL: https://link.aps.org/doi/10.1103/PhysRevLett.120.021101 (cited on page 13).

[79] G. Bernard et al. “TeV cosmic-ray proton and helium spectra in the myriad model”. In: *Astronomy and Astrophysics* 555 (June 2013), A48. ISSN: 1432-0746. DOI: 10.1051/0004-6361/201321202. URL: http://dx.doi.org/10.1051/0004-6361/201321202 (cited on page 13).

[80] Vladimir Ptuskin, Vladimir Zirakashvili, and Eun-Suk Seo. “Spectra of Cosmic-Ray Protons and Helium Produced in Supernova Remnants”. In: *Astrophysical Journal* 763.1, 47 (Jan. 2013), page 47. DOI: 10.1088/0004-637X/763/1/47. arXiv: 1212.0381 [astro-ph.HE] (cited on page 13).

[81] Pasquale Blasi and Elena Amato. “Diffusive propagation of cosmic rays from supernova remnants in the Galaxy. II: anisotropy”. In: *Journal of Cosmology and Astroparticle Physics* 2012.01 (Jan. 2012), pages 011–011. DOI: 10.1088/1475-7516/2012/01/011. URL: https://doi.org/10.1088/1475-7516/2012/01/011 (cited on page 13).

[82] Roberto Aloisio, Pasquale Blasi, and Pasquale Serpico. "Nonlinear cosmic ray Galactic transport in the light of AMS-02 and Voyager data". In: *Astron. Astrophys.* 583 (2015), A95. DOI: 10.1051/0004-6361/201526877. arXiv: 1507.00594 [astro-ph.HE] (cited on page 13).

[83] Pasquale Blasi, Elena Amato, and Pasquale D. Serpico. "Spectral Breaks as a Signature of Cosmic Ray Induced Turbulence in the Galaxy". In: *Phys. Rev. Lett.* 109 (6 Aug. 2012), page 061101. DOI: 10.1103/PhysRevLett.109.061101. URL: https://link.aps.org/doi/10.1103/PhysRevLett.109.061101 (cited on page 13).

[84] P. Blasi. "Non-linear Cosmic Ray Propagation". In: *Nuclear and Particle Physics Proceedings* 297-299 (2018). Cosmic Ray Origin - Beyond the Standard Models, pages 115–124. ISSN: 2405-6014. DOI: https://doi.org/10.1016/j.nuclphysbps.2018.07.018. URL: http://www.sciencedirect.com/science/article/pii/S2405601418301056 (cited on page 13).

[85] O. Adriani et al. "Cosmic-Ray Positron Energy Spectrum Measured by PAMELA". In: *Phys. Rev. Lett.* 111 (8 Aug. 2013), page 081102. DOI: 10.1103/PhysRevLett.111.081102. URL: https://link.aps.org/doi/10.1103/PhysRevLett.111.081102 (cited on page 15).

[86] M. Ackermann et al. "Measurement of Separate Cosmic-Ray Electron and Positron Spectra with the Fermi Large Area Telescope". In: *Phys. Rev. Lett.* 108 (1 Jan. 2012), page 011103. DOI: 10.1103/PhysRevLett.108.011103. URL: https://link.aps.org/doi/10.1103/PhysRevLett.108.011103 (cited on page 15).

[87] S. Abdollahi et al. "Cosmic-ray electron-positron spectrum from 7 GeV to 2 TeV with the Fermi Large Area Telescope". In: *Phys. Rev. D* 95 (8 Apr. 2017), page 082007. DOI: 10.1103/PhysRevD.95.082007. URL: https://link.aps.org/doi/10.1103/PhysRevD.95.082007 (cited on page 15).

[88] M. Aguilar et al. "Towards Understanding the Origin of Cosmic-Ray Electrons". In: *Phys. Rev. Lett.* 122 (10 Mar. 2019), page 101101. DOI: 10.1103/PhysRevLett.122.101101. URL: https://link.aps.org/doi/10.1103/PhysRevLett.122.101101 (cited on pages 15, 16, 61, 62, 67, 78, 91).

[89] M. Aguilar et al. "Towards Understanding the Origin of Cosmic-Ray Positrons". In: *Phys. Rev. Lett.* 122 (4 Jan. 2019), page 041102. DOI: 10.1103/PhysRevLett.122.041102. URL: https://link.aps.org/doi/10.1103/PhysRevLett.122.041102 (cited on pages 15, 16, 61, 62, 82).

[90] DAMPE Collaboration et al. "Direct detection of a break in the teraelectronvolt cosmic-ray spectrum of electrons and positrons". In: *Nature* 552.7683 (Dec. 2017), pages 63–66. DOI: 10.1038/nature24475. arXiv: 1711.10981 [astro-ph.HE] (cited on page 15).

[91] O. Adriani et al. "Extended Measurement of the Cosmic-Ray Electron and Positron Spectrum from 11 GeV to 4.8 TeV with the Calorimetric Electron Telescope on the International Space Station". In: *Phys. Rev. Lett.* 120 (26 June 2018), page 261102. DOI: 10.1103/PhysRevLett.120.261102. URL: https://link.aps.org/doi/10.1103/PhysRevLett.120.261102 (cited on page 15).

[92] Kathrin Egberts. "The spectrum of cosmic-ray electrons measured with H.E.S.S." In: *Nuclear Instruments and Methods in Physics Research Section A: Accelerators, Spectrometers, Detectors and Associated Equipment* 630.1 (2011). Proceedings of the 2nd Roma International Conference on Astroparticle Physics (RICAP 2009), pages 36–39. ISSN: 0168-9002. DOI: https://doi.org/10.1016/j.nima.2010.06.022. URL:

http://www.sciencedirect.com/science/article/pii/S016890021001212X (cited on page 15).

[93] M. Aguilar et al. "Precision Measurement of the $(e^+ + e^-)$ Flux in Primary Cosmic Rays from 0.5 GeV to 1 TeV with the Alpha Magnetic Spectrometer on the International Space Station". In: *Phys. Rev. Lett.* 113 (22 Nov. 2014), page 221102. DOI: 10.1103/PhysRevLett.113.221102. URL: https://link.aps.org/doi/10.1103/PhysRevLett.113.221102 (cited on page 15).

[94] O. Adriani et al. "PAMELA Results on the Cosmic-Ray Antiproton Flux from 60 MeV to 180 GeV in Kinetic Energy". In: *Phys. Rev. Lett.* 105 (12 Sept. 2010), page 121101. DOI: 10.1103/PhysRevLett.105.121101. URL: https://link.aps.org/doi/10.1103/PhysRevLett.105.121101 (cited on page 15).

[95] M. Aguilar et al. "Antiproton Flux, Antiproton-to-Proton Flux Ratio, and Properties of Elementary Particle Fluxes in Primary Cosmic Rays Measured with the Alpha Magnetic Spectrometer on the International Space Station". In: *Phys. Rev. Lett.* 117 (9 Aug. 2016), page 091103. DOI: 10.1103/PhysRevLett.117.091103. URL: https://link.aps.org/doi/10.1103/PhysRevLett.117.091103 (cited on page 15).

[96] Kfir Blum, Boaz Katz, and Eli Waxman. "AMS-02 Results Support the Secondary Origin of Cosmic Ray Positrons". In: *Phys. Rev. Lett.* 111 (21 Nov. 2013), page 211101. DOI: 10.1103/PhysRevLett.111.211101. URL: https://link.aps.org/doi/10.1103/PhysRevLett.111.211101 (cited on page 17).

[97] R. Cowsik, B. Burch, and T. Madziwa-Nussinov. "THE ORIGIN OF THE SPECTRAL INTENSITIES OF COSMIC-RAY POSITRONS". In: *The Astrophysical Journal* 786.2 (Apr. 2014), page 124. DOI: 10.1088/0004-637x/786/2/124. URL: https://doi.org/10.1088/0004-637x/786/2/124 (cited on page 17).

[98] Rolf Kappl and Martin Wolfgang Winkler. "The cosmic ray antiproton background for AMS-02". In: *Journal of Cosmology and Astroparticle Physics* 2014.09 (Sept. 2014), pages 051–051. DOI: 10.1088/1475-7516/2014/09/051. URL: https://doi.org/10.1088/1475-7516/2014/09/051 (cited on page 17).

[99] Rolf Kappl, Annika Reinert, and Martin Wolfgang Winkler. "AMS-02 antiprotons reloaded". In: *Journal of Cosmology and Astroparticle Physics* 2015.10 (Oct. 2015), pages 034–034. DOI: 10.1088/1475-7516/2015/10/034. URL: https://doi.org/10.1088/1475-7516/2015/10/034 (cited on page 17).

[100] Gaëlle Giesen et al. "AMS-02 antiprotons, at last! Secondary astrophysical component and immediate implications for Dark Matter". In: *Journal of Cosmology and Astroparticle Physics* 2015.09 (Sept. 2015), pages 023–023. DOI: 10.1088/1475-7516/2015/09/023. URL: https://doi.org/10.1088/1475-7516/2015/09/023 (cited on page 17).

[101] Carmelo Evoli, Daniele Gaggero, and Dario Grasso. "Secondary antiprotons as a Galactic Dark Matter probe". In: *Journal of Cosmology and Astroparticle Physics* 2015.12 (Dec. 2015), pages 039–039. DOI: 10.1088/1475-7516/2015/12/039. URL: https://doi.org/10.1088/1475-7516/2015/12/039 (cited on page 17).

[102] ELENA AMATO. "THE THEORY OF PULSAR WIND NEBULAE". In: *International Journal of Modern Physics: Conference Series* 28 (Jan. 2014), page 1460160. ISSN: 2010-1945. DOI: 10.1142/s2010194514601604. URL: http://dx.doi.org/10.1142/S2010194514601604 (cited on page 17).

[103] Pasquale D. Serpico. "Astrophysical models for the origin of the positron "excess"". In: *Astroparticle Physics* 39-40 (2012). Cosmic Rays Topical Issue, pages 2–11. ISSN: 0927-6505. DOI: https://doi.org/10.1016/j.astropartphys.2011.08.007. URL: http://www.sciencedirect.com/science/article/pii/S0927650511001654 (cited on page 17).

[104] Tim Linden and Stefano Profumo. "PROBING THE PULSAR ORIGIN OF THE ANOMALOUS POSITRON FRACTION WITH AMS-02 AND ATMOSPHERIC CHERENKOV TELESCOPES". In: *The Astrophysical Journal* 772.1 (July 2013), page 18. DOI: 10.1088/0004-637x/772/1/18. URL: https://doi.org/10.1088/0004-637x/772/1/18 (cited on page 17).

[105] Ilias Cholis and Dan Hooper. "Dark matter and pulsar origins of the rising cosmic ray positron fraction in light of new data from the AMS". In: *Phys. Rev. D* 88 (2 July 2013), page 023013. DOI: 10.1103/PhysRevD.88.023013. URL: https://link.aps.org/doi/10.1103/PhysRevD.88.023013 (cited on page 17).

[106] A.D. Erlykin and A.W. Wolfendale. "Cosmic ray positrons from a local, middle-aged supernova remnant". In: *Astroparticle Physics* 49 (2013), pages 23–27. ISSN: 0927-6505. DOI: https://doi.org/10.1016/j.astropartphys.2013.08.001. URL: http://www.sciencedirect.com/science/article/pii/S0927650513001229 (cited on page 17).

[107] Peng-Fei Yin et al. "Pulsar interpretation for the AMS-02 result". In: *Phys. Rev. D* 88 (2 July 2013), page 023001. DOI: 10.1103/PhysRevD.88.023001. URL: https://link.aps.org/doi/10.1103/PhysRevD.88.023001 (cited on page 17).

[108] N. Fornengo. "Astrophysical interpretation of the ASM-02 leptonic data". In: *Nuclear and Particle Physics Proceedings* 265-266 (2015). Proceedings of the Neutrino Oscillation Workshop, pages 248–250. ISSN: 2405-6014. DOI: https://doi.org/10.1016/j.nuclphysbps.2015.06.064. URL: http://www.sciencedirect.com/science/article/pii/S240560141500406X (cited on page 17).

[109] F. Zwicky. "Die Rotverschiebung von extragalaktischen Nebeln". In: *Helv. Phys. Acta* 6 (1933), pages 110–127. DOI: 10.1007/s10714-008-0707-4 (cited on page 17).

[110] Vera C. Rubin and Jr. Ford W. Kent. "Rotation of the Andromeda Nebula from a Spectroscopic Survey of Emission Regions". In: *Astrophysical Journal* 159 (Feb. 1970), page 379. DOI: 10.1086/150317 (cited on page 17).

[111] V. C. Rubin, Jr. Ford W. K., and N. Thonnard. "Extended rotation curves of high-luminosity spiral galaxies. IV. Systematic dynamical properties, Sa -> Sc." In: *Astrophysical Journal* 225 (Nov. 1978), pages L107–L111. DOI: 10.1086/182804 (cited on page 17).

[112] Henk Hoekstra and Bhuvnesh Jain. "Weak Gravitational Lensing and Its Cosmological Applications". In: *Annual Review of Nuclear and Particle Science* 58.1 (2008), pages 99–123. DOI: 10.1146/annurev.nucl.58.110707.171151. URL: https://doi.org/10.1146/annurev.nucl.58.110707.171151 (cited on page 17).

[113] C Chang et al. "Dark Energy Survey Year 1 results: curved-sky weak lensing mass map". In: *Monthly Notices of the Royal Astronomical Society* 475.3 (Jan. 2018), pages 3165–3190. ISSN: 0035-8711. DOI: 10.1093/mnras/stx3363. URL: https://doi.org/10.1093/mnras/stx3363 (cited on page 17).

[114] E. Komatsu et al. “SEVEN-YEAR WILKINSON MICROWAVE ANISOTROPY PROBE (WMAP) OBSERVATIONS: COSMOLOGICAL INTERPRETATION”. In: 192.2 (Jan. 2011), page 18. DOI: 10.1088/0067-0049/192/2/18. URL: https://doi.org/10.1088/0067-0049/192/2/18 (cited on page 17).

[115] P. A. R. Ade et al. “Planck2015 results”. In: *Astronomy and Astrophysics* 594 (Sept. 2016), A13. ISSN: 1432-0746. DOI: 10.1051/0004-6361/201525830. URL: http://dx.doi.org/10.1051/0004-6361/201525830 (cited on page 17).

[116] Jonathan L. Feng. “Dark Matter Candidates from Particle Physics and Methods of Detection”. In: *Annual Review of Astronomy and Astrophysics* 48.1 (2010), pages 495–545. DOI: 10.1146/annurev-astro-082708-101659. URL: https://doi.org/10.1146/annurev-astro-082708-101659 (cited on page 17).

[117] Troy A. Porter, Robert P. Johnson, and Peter W. Graham. “Dark Matter Searches with Astroparticle Data”. In: *Annual Review of Astronomy and Astrophysics* 49.1 (2011), pages 155–194. DOI: 10.1146/annurev-astro-081710-102528. URL: https://doi.org/10.1146/annurev-astro-081710-102528 (cited on page 17).

[118] Joachim Kopp. “Constraints on dark matter annihilation from AMS-02 results”. In: *Phys. Rev. D* 88 (7 Oct. 2013), page 076013. DOI: 10.1103/PhysRevD.88.076013. URL: https://link.aps.org/doi/10.1103/PhysRevD.88.076013 (cited on page 17).

[119] Lars Bergstrom et al. “New Limits on Dark Matter Annihilation from Alpha Magnetic Spectrometer Cosmic Ray Positron Data”. In: *Phys. Rev. Lett.* 111 (17 Oct. 2013), page 171101. DOI: 10.1103/PhysRevLett.111.171101. URL: https://link.aps.org/doi/10.1103/PhysRevLett.111.171101 (cited on page 17).

[120] M. Cirelli et al. “Addendum including AMS 2013 data to "Model-independent implications of the $e^{\pm}$, $\bar{p}$ cosmic ray spectra on properties of Dark Matter"[Nucl. Phys. B 813 (1-2) (2009) 1-21]”. In: *Nuclear Physics B* 873.3 (Aug. 2013), pages 530–533. DOI: 10.1016/j.nuclphysb.2013.05.002 (cited on page 17).

[121] Keith R. Dienes, Jason Kumar, and Brooks Thomas. “Dynamical Dark Matter and the positron excess in light of AMS results”. In: *Phys. Rev. D* 88 (10 Nov. 2013), page 103509. DOI: 10.1103/PhysRevD.88.103509. URL: https://link.aps.org/doi/10.1103/PhysRevD.88.103509 (cited on page 17).

[122] Lei Feng et al. “AMS-02 positron excess: New bounds on dark matter models and hint for primary electron spectrum hardening”. In: *Physics Letters B* 728 (2014), pages 250–255. ISSN: 0370-2693. DOI: https://doi.org/10.1016/j.physletb.2013.12.012. URL: http://www.sciencedirect.com/science/article/pii/S0370269313009878 (cited on page 17).

[123] Yuji Kajiyama, Hiroshi Okada, and Takashi Toma. “New Interpretation of the Recent Result of AMS-02 and Multi-component Decaying Dark Matters with non-Abelian Discrete Flavor Symmetry”. In: *Eur. Phys. J. C* 74 (2014), page 2722. DOI: 10.1140/epjc/s10052-014-2722-9. arXiv: 1304.2680 [hep-ph] (cited on page 17).

[124] Chuan-Hung Chen, Cheng-Wei Chiang, and Takaaki Nomura. “Dark matter for excess of AMS-02 positrons and antiprotons”. In: *Physics Letters B* 747 (2015), pages 495–499. ISSN: 0370-2693. DOI: https://doi.org/10.1016/j.physletb.2015.06.035. URL: http://www.sciencedirect.com/science/article/pii/S0370269315004578 (cited on page 17).

[125] R. Cowsik. "Positrons and Antiprotons in Galactic Cosmic Rays". In: *Annual Review of Nuclear and Particle Science* 66.1 (2016), pages 297–319. DOI: 10.1146/annurev-nucl-102115-044851. URL: https://doi.org/10.1146/annurev-nucl-102115-044851 (cited on page 17).

[126] Leila Ali Cavasonza et al. "Constraints on Leptophilic Dark Matter from the AMS-02 Experiment". In: *The Astrophysical Journal* 839.1 (Apr. 2017), page 36. DOI: 10.3847/1538-4357/aa624d. URL: https://doi.org/10.3847/1538-4357/aa624d (cited on page 17).

[127] Arthur H. Compton and Ivan A. Getting. "An Apparent Effect of Galactic Rotation on the Intensity of Cosmic Rays". In: *Phys. Rev.* 47 (11 June 1935), pages 817–821. DOI: 10.1103/PhysRev.47.817. URL: https://link.aps.org/doi/10.1103/PhysRev.47.817 (cited on page 18).

[128] Marco Aglietta et al. "A Measurement of the Solar and Sidereal Cosmic-Ray Anisotropy at E 0 approximately 10 14 eV". In: *The Astrophysical Journal* 470 (Sept. 1996), page 501. DOI: 10.1086/177881 (cited on page 18).

[129] M. Amenomori et al. "Observation by an Air-Shower Array in Tibet of the Multi-TeV Cosmic-Ray Anisotropy due to Terrestrial Orbital Motion Around the Sun". In: *Physical Review Letters* 93.6 (Aug. 2004). ISSN: 1079-7114. DOI: 10.1103/physrevlett.93.061101. URL: http://dx.doi.org/10.1103/PhysRevLett.93.061101 (cited on page 18).

[130] Abdo Abdo et al. "The Large-Scale Cosmic-Ray Anisotropy as Observed with Milagro". In: *The Astrophysical Journal* 698 (June 2009), page 2121. DOI: 10.1088/0004-637X/698/2/2121 (cited on page 18).

[131] R. Abbasi et al. "MEASUREMENT OF THE ANISOTROPY OF COSMIC-RAY ARRIVAL DIRECTIONS WITH ICECUBE". In: *The Astrophysical Journal* 718.2 (July 2010), pages L194–L198. ISSN: 2041-8213. DOI: 10.1088/2041-8205/718/2/l194. URL: http://dx.doi.org/10.1088/2041-8205/718/2/L194 (cited on page 18).

[132] K. Nagashima, K. Fujimoto, and R. M. Jacklyn. "Galactic and heliotail-in anisotropies of cosmic rays as the origin of sidereal daily variation in the energy region < 104 GeV". In: *Journal of Geophysical Research: Space Physics* 103.A8 (1998), pages 17429–17440. DOI: https://doi.org/10.1029/98JA01105. URL: https://agupubs.onlinelibrary.wiley.com/doi/abs/10.1029/98JA01105 (cited on page 18).

[133] K. Nagashima, K. Fujimoto, and R. M. Jacklyn. "Solar modulation of galactic and heliotail-in anisotropies of cosmic rays at Sakashita underground station (320 $\sim$ 650 GeV)." In: *Earth Planet* 56 (2004), pages 479–483. DOI: https://doi.org/10.1186/BF03352501 (cited on page 18).

[134] A. Aab et al. "Observation of a large-scale anisotropy in the arrival directions of cosmic rays above 8.10^{18} eV". In: *Science* 357.6357 (Sept. 2017), pages 1266–1270. ISSN: 1095-9203. DOI: 10.1126/science.aan4338. URL: http://dx.doi.org/10.1126/science.aan4338 (cited on page 19).

[135] John Linsley. "Fluctuation Effects on Directional Data". In: *Phys. Rev. Lett.* 34 (24 June 1975), pages 1530–1533. DOI: 10.1103/PhysRevLett.34.1530. URL: https://link.aps.org/doi/10.1103/PhysRevLett.34.1530 (cited on page 20).

[136] V. Savchenko, M. Kachelrieß, and D. V. Semikoz. "IMPRINT OF A 2 MILLION YEAR OLD SOURCE ON THE COSMIC-RAY ANISOTROPY". In: *The Astrophysical Journal* 809.2 (Aug. 2015), page L23. DOI: 10.1088/2041-8205/809/2/l23. URL: https://doi.org/10.1088/2041-8205/809/2/l23 (cited on page 20).

[137] Wei Liu, Yi-Qing Guo, and Qiang Yuan. "Indication of nearby source signatures of cosmic rays from energy spectra and anisotropies". In: *Journal of Cosmology and Astroparticle Physics* 2019.10 (Oct. 2019), pages 010–010. DOI: 10.1088/1475-7516/2019/10/010. URL: https://doi.org/10.1088/1475-7516/2019/10/010 (cited on page 20).

[138] G. Di Sciascio and R. Iuppa. *On the Observation of the Cosmic Ray Anisotropy below 10^{15} eV*. 2014. arXiv: 1407.2144 [astro-ph.HE] (cited on page 20).

[139] Antonella Castellina and Fiorenza Donato. "Astrophysics of Galactic Charged Cosmic Rays". In: *Planets, Stars and Stellar Systems. Volume 5: Galactic Structure and Stellar Populations*. Edited by Terry D. Oswalt and Gerard Gilmore. Volume 5. 2013, page 725. DOI: 10.1007/978-94-007-5612-0_14 (cited on page 20).

[140] Markus Ahlers and Philipp Mertsch. "Origin of small-scale anisotropies in Galactic cosmic rays". In: *Progress in Particle and Nuclear Physics* 94 (2017), pages 184–216. ISSN: 0146-6410. DOI: https://doi.org/10.1016/j.ppnp.2017.01.004. URL: http://www.sciencedirect.com/science/article/pii/S0146641017300054 (cited on page 20).

[141] Miguel Pato, Massimiliano Lattanzi, and Gianfranco Bertone. "Discriminating the source of high-energy positrons with AMS-02". In: *Journal of Cosmology and Astroparticle Physics* 2010.12 (Dec. 2010), pages 020–020. DOI: 10.1088/1475-7516/2010/12/020. URL: https://doi.org/10.1088/1475-7516/2010/12/020 (cited on page 21).

[142] Ignacio Cernuda. "Cosmic-ray electron anisotropies as a tool to discriminate between exotic and astrophysical sources". In: *Astroparticle Physics* 34.2 (Sept. 2010), pages 59–69. ISSN: 0927-6505. DOI: 10.1016/j.astropartphys.2010.05.003. URL: http://dx.doi.org/10.1016/j.astropartphys.2010.05.003 (cited on page 21).

[143] Enrico Borriello, Luca Maccione, and Alessandro Cuoco. "Electron anisotropy: A tool to discriminate dark matter in cosmic rays". In: *J. Phys. Conf. Ser.* 375 (2012). Edited by Lothar Oberauer, Georg Raffelt, and Robert Wagner, page 012031. DOI: 10.1088/1742-6596/375/1/012031 (cited on page 21).

[144] Stefano Profumo. "An observable electron-positron anisotropy cannot be generated by dark matter". In: *Journal of Cosmology and Astroparticle Physics* 2015.02 (Feb. 2015), pages 043–043. DOI: 10.1088/1475-7516/2015/02/043. URL: https://doi.org/10.1088/1475-7516/2015/02/043 (cited on page 21).

[145] Dan Hooper, Pasquale Blasi, and Pasquale Dario Serpico. "Pulsars as the sources of high energy cosmic ray positrons". In: *Journal of Cosmology and Astroparticle Physics* 2009.01 (Jan. 2009), pages 025–025. DOI: 10.1088/1475-7516/2009/01/025. URL: https://doi.org/10.1088/1475-7516/2009/01/025 (cited on pages 21, 127, 131).

[146] Tim Linden and Stefano Profumo. "PROBING THE PULSAR ORIGIN OF THE ANOMALOUS POSITRON FRACTION WITH AMS-02 AND ATMOSPHERIC CHERENKOV TELESCOPES". In: *The Astrophysical Journal* 772.1 (July 2013), page 18. DOI: 10.1088/0004-637x/772/1/18. URL: https://doi.org/10.1088/0004-637x/772/1/18 (cited on page 21).

[147] S. Manconi, M. Di Mauro, and F. Donato. "Dipole anisotropy in cosmic electrons and positrons: inspection on local sources". In: *Journal of Cosmology and Astroparticle Physics* 2017.01 (Jan. 2017), pages 006–006. DOI: 10.1088/1475-7516/2017/01/006. URL: https://doi.org/10.1088/1475-7516/2017/01/006 (cited on page 21).

[148] Kun Fang, Xiao-Jun Bi, and Peng-Fei Yin. "Discriminating local sources of high-energy cosmic electrons and positrons by current and future anisotropy measurements". In: *Monthly Notices of the Royal Astronomical Society* 478.4 (June 2018), pages 5660–5670. ISSN: 0035-8711. DOI: 10.1093/mnras/sty1463. URL: https://doi.org/10.1093/mnras/sty1463 (cited on page 21).

[149] Wei Liu, Yi-Qing Guo, and Qiang Yuan. "Indication of nearby source signatures of cosmic rays from energy spectra and anisotropies". In: *JCAP* 10 (2019), page 010. DOI: 10.1088/1475-7516/2019/10/010. arXiv: 1812.09673 [astro-ph.HE] (cited on page 21).

[150] Yi-Qing Guo and Qiang Yuan. "Understanding the spectral hardenings and radial distribution of Galactic cosmic rays and Fermi diffuse γ rays with spatially-dependent propagation". In: *Phys. Rev. D* 97 (6 Mar. 2018), page 063008. DOI: 10.1103/PhysRevD.97.063008. URL: https://link.aps.org/doi/10.1103/PhysRevD.97.063008 (cited on page 21).

[151] Bing Zhao et al. *Geminga SNR: Possible candidate of local cosmic-ray factory*. 2021. arXiv: 2104.07321 [astro-ph.HE] (cited on page 21).

[152] O. Adriani et al. "SEARCH FOR ANISOTROPIES IN COSMIC-RAY POSITRONS DETECTED BY THE PAMELA EXPERIMENT". In: *The Astrophysical Journal* 811.1 (Sept. 2015), page 21. DOI: 10.1088/0004-637x/811/1/21. URL: https://doi.org/10.1088/0004-637x/811/1/21 (cited on page 21).

[153] U. Giaccari et al. "Anisotropy studies in the cosmic ray proton flux with the PAMELA experiment". In: *Nuclear Physics B - Proceedings Supplements* 239-240 (2013). Proceedings of the 9th workshop on Science with the New Generation of High Energy Gamma-ray Experiments: From high energy gamma sources to cosmic rays, one century after their discovery, pages 123–128. ISSN: 0920-5632. DOI: https://doi.org/10.1016/j.nuclphysbps.2013.05.020. URL: http://www.sciencedirect.com/science/article/pii/S0920563213003976 (cited on page 21).

[154] S. Abdollahi et al. "Search for Cosmic-Ray Electron and Positron Anisotropies with Seven Years of Fermi Large Area Telescope Data". In: *Phys. Rev. Lett.* 118 (9 Mar. 2017), page 091103. DOI: 10.1103/PhysRevLett.118.091103. URL: https://link.aps.org/doi/10.1103/PhysRevLett.118.091103 (cited on page 21).

[155] LAT Collaboration. *A Search for Cosmic-ray Proton Anisotropy with the Fermi Large Area Telescope*. 2019. arXiv: 1903.02905 [astro-ph.HE] (cited on page 21).

[156] Maria Munoz Salinas et al. "Anisotropy Searches with DAMPE". In: *PoS* ICRC2019 (2020), page 113. DOI: 10.22323/1.358.0113 (cited on page 21).

[157] Holger Motz and Yoichi Asaoka. "Analysis of CALET Data for Anisotropy in Electron+Positron Cosmic Rays". In: *PoS* ICRC2019 (2020), page 112. DOI: 10.22323/1.358.0112 (cited on page 21).

[158] Miguel Velasco and Jorge Casaus. "Measurement of anisotropies in cosmic ray arrival directions with the AMS Detector on the Space Station". In: Dec. 2017, page 621. DOI: 10.22323/1.314.0621 (cited on pages 21, 61, 101).

[159] J. Alcaraz et al. “Search for antihelium in cosmic rays”. In: *Physics Letters B* 461.4 (1999), pages 387–396. ISSN: 0370-2693. DOI: https://doi.org/10.1016/S0370-2693(99)00874-6. URL: http://www.sciencedirect.com/science/article/pii/S0370269399008746 (cited on page 23).

[160] J. Alcaraz et al. “Helium in near Earth orbit”. In: *Physics Letters B* 494.3 (2000), pages 193–202. ISSN: 0370-2693. DOI: https://doi.org/10.1016/S0370-2693(00)01193-X. URL: http://www.sciencedirect.com/science/article/pii/S037026930001193X (cited on page 23).

[161] J. Alcaraz et al. “Cosmic protons”. In: *Physics Letters B* 490.1 (2000), pages 27–35. ISSN: 0370-2693. DOI: https://doi.org/10.1016/S0370-2693(00)00970-9. URL: http://www.sciencedirect.com/science/article/pii/S0370269300009709 (cited on page 23).

[162] J. Alcaraz et al. “Leptons in near earth orbit”. In: *Physics Letters B* 484.1 (2000), pages 10–22. ISSN: 0370-2693. DOI: https://doi.org/10.1016/S0370-2693(00)00588-8. URL: http://www.sciencedirect.com/science/article/pii/S0370269300005888 (cited on page 23).

[163] J. Alcaraz et al. “Protons in near earth orbit”. In: *Physics Letters B* 472.1 (2000), pages 215–226. ISSN: 0370-2693. DOI: https://doi.org/10.1016/S0370-2693(99)01427-6. URL: http://www.sciencedirect.com/science/article/pii/S0370269399014276 (cited on page 23).

[164] M. Aguilar et al. “A study of cosmic ray secondaries induced by the Mir space station using AMS-01”. In: *Nuclear Instruments and Methods in Physics Research Section B: Beam Interactions with Materials and Atoms* 234.3 (2005), pages 321–332. ISSN: 0168-583X. DOI: https://doi.org/10.1016/j.nimb.2005.01.015. URL: http://www.sciencedirect.com/science/article/pii/S0168583X05000030 (cited on page 23).

[165] M. Aguilar et al. “Cosmic-ray positron fraction measurement from 1 to 30 GeV with AMS-01”. In: *Physics Letters B* 646.4 (2007), pages 145–154. ISSN: 0370-2693. DOI: https://doi.org/10.1016/j.physletb.2007.01.024. URL: http://www.sciencedirect.com/science/article/pii/S0370269307001104 (cited on page 23).

[166] M. Aguilar et al. “Relative composition and energy spectra of light nuclei in cosmic rays: Results from AMS-01”. In: *The Astrophysical Journal* 724.1 (), pages 329–340. DOI: 10.1088/0004-637x/724/1/329. URL: https://doi.org/10.1088/0004-637x/724/1/329 (cited on page 23).

[167] M. Aguilar et al. “The Alpha Magnetic Spectrometer (AMS) on the International Space Station: Part I – results from the test flight on the space shuttle”. In: *Physics Reports* 366.6 (2002), pages 331–405. ISSN: 0370-1573. DOI: https://doi.org/10.1016/S0370-1573(02)00013-3. URL: http://www.sciencedirect.com/science/article/pii/S0370157302000133 (cited on pages 23, 25).

[168] NASA. *Reference Guide to the International Space Station*. Nov. 2010. ISBN: 0-16-086517-4. URL: https://www.nasa.gov/pdf/508318main_ISS_ref_guide_nov2010.pdf (cited on page 24).

[169] K. Lübelsmeyer et al. “Upgrade of the Alpha Magnetic Spectrometer (AMS-02) for long term operation on the International Space Station (ISS)”. In: *Nuclear Instruments and Methods in Physics Research Section A: Accelerators, Spectrometers, Detectors and Associated Equipment* 654.1 (2011), pages 639–648. ISSN: 0168-9002. DOI: https://doi.org/10.1016/j.nima.2011.06.051. URL: http://www.sciencedirect.com/science/article/pii/S0168900211011752 (cited on pages 25, 26).

[170] Chen Hesheng. “Permanent magnet system of alpha magnetic spectrometer”. In: *Science in China Series A: Mathematics* 43 (2000/09/01), pages 996–1008. ISSN: 1862-2763. DOI: https://doi.org/10.1007/BF02879806 (cited on page 25).

[171] Samuel Ting. “The Alpha Magnetic Spectrometer on the International Space Station”. In: *Nuclear Physics B - Proceedings Supplements* 243-244 (2013). Proceedings of the IV International Conference on Particle and Fundamental Physics in Space, pages 12–24. ISSN: 0920-5632. DOI: https://doi.org/10.1016/j.nuclphysbps.2013.09.028. URL: http://www.sciencedirect.com/science/article/pii/S0920563213005525 (cited on page 25).

[172] G. Ambrosi et al. “The spatial resolution of the silicon tracker of the Alpha Magnetic Spectrometer”. In: *Nuclear Instruments and Methods in Physics Research Section A: Accelerators, Spectrometers, Detectors and Associated Equipment* 869 (2017), pages 29–37. ISSN: 0168-9002. DOI: https://doi.org/10.1016/j.nima.2017.07.014. URL: http://www.sciencedirect.com/science/article/pii/S0168900217307258 (cited on page 26).

[173] J. Berdugo et al. “Determination of the rigidity scale of the Alpha Magnetic Spectrometer”. In: *Nuclear Instruments and Methods in Physics Research Section A: Accelerators, Spectrometers, Detectors and Associated Equipment* 869 (2017), pages 10–14. ISSN: 0168-9002. DOI: https://doi.org/10.1016/j.nima.2017.07.012. URL: http://www.sciencedirect.com/science/article/pii/S0168900217307234 (cited on pages 27, 111).

[174] Paolo Zuccon. “AMS-02 Track reconstruction and rigidity measurement”. In: *33rd International Cosmic Ray Conference*. 2013, page 1064 (cited on page 27).

[175] C. Höppner et al. “A novel generic framework for track fitting in complex detector systems”. In: *Nuclear Instruments and Methods in Physics Research Section A: Accelerators, Spectrometers, Detectors and Associated Equipment* 620.2 (2010), pages 518–525. ISSN: 0168-9002. DOI: https://doi.org/10.1016/j.nima.2010.03.136. URL: http://www.sciencedirect.com/science/article/pii/S0168900210007473 (cited on page 27).

[176] Y. Jia et al. “Nuclei charge measurement by the Alpha Magnetic Spectrometer silicon tracker”. In: *Nuclear Instruments and Methods in Physics Research Section A: Accelerators, Spectrometers, Detectors and Associated Equipment* 972 (2020), page 164169. ISSN: 0168-9002. DOI: https://doi.org/10.1016/j.nima.2020.164169. URL: http://www.sciencedirect.com/science/article/pii/S0168900220305659 (cited on page 28).

[177] Th. Kirn and Th. Siedenburg. “The AMS-02 transition radiation detector”. In: *Nuclear Instruments and Methods in Physics Research Section A: Accelerators, Spectrometers, Detectors and Associated Equipment* 535.1 (2004). Proceedings of the 10th International Vienna Conference on Instrumentation, pages 165–170. ISSN: 0168-9002. DOI: https://doi.org/10.1016/j.nima.2004.07.273. URL: http://www.sciencedirect.com/science/article/pii/S0168900204015955 (cited on page 28).

[178] P. von Doetinchem et al. “Performance of the AMS-02 Transition Radiation Detector”. In: *Nucl. Instrum. Meth. A* 558 (2006), pages 526–535. DOI: 10.1016/J.NIMA.2005.12.187. arXiv: astro-ph/0608641 (cited on page 28).

[179] Th Kirn. “Threshold transition radiation detectors in astroparticle physics”. In: *Nuclear Instruments and Methods in Physics Research Section A-accelerators Spectrometers Detectors and Associated Equipment* 563 (July 2006), pages 338–342. DOI: 10.1016/j.nima.2006.02.190 (cited on page 28).

[180] Michael L. Cherry and Dietrich Müller. “Measurements of the Frequency Spectrum of Transition Radiation”. In: *Phys. Rev. Lett.* 38 (1 Jan. 1977), pages 5–8. DOI: 10.1103/PhysRevLett.38.5. URL: https://link.aps.org/doi/10.1103/PhysRevLett.38.5 (cited on page 30).

[181] Michael L. Cherry et al. “Transition radiation from relativistic electrons in periodic radiators”. In: *Phys. Rev. D* 10 (11 Dec. 1974), pages 3594–3607. DOI: 10.1103/PhysRevD.10.3594. URL: https://link.aps.org/doi/10.1103/PhysRevD.10.3594 (cited on page 30).

[182] A. Andronic and J. Wessels. “Transition radiation detectors”. In: *Nuclear Instruments and Methods in Physics Research Section A Accelerators Spectrometers Detectors and Associated Equipment* 666 (Feb. 2012), pages 130–147. DOI: 10.1016/j.nima.2011.09.041 (cited on page 30).

[183] Henning Gast et al. “Identification of cosmic-ray positrons with the transition radiation detector of the AMS experiment on the International Space Station”. In: *33rd International Cosmic Ray Conference*. 2013, page 0359 (cited on page 30).

[184] T. Räihä et al. “Monte Carlo simulations of the transition radiation detector of the AMS-02 experiment”. In: *Nuclear Instruments and Methods in Physics Research Section A: Accelerators, Spectrometers, Detectors and Associated Equipment* 868 (2017), pages 10–14. ISSN: 0168-9002. DOI: https://doi.org/10.1016/j.nima.2017.06.042. URL: http://www.sciencedirect.com/science/article/pii/S0168900217306952 (cited on page 30).

[185] https://ams02.space (cited on pages 30, 35, 38).

[186] V. Bindi et al. “Calibration and performance of the AMS-02 time of flight detector in space”. In: *Nuclear Instruments and Methods in Physics Research Section A: Accelerators, Spectrometers, Detectors and Associated Equipment* 743 (2014), pages 22–29. ISSN: 0168-9002. DOI: https://doi.org/10.1016/j.nima.2014.01.002. URL: http://www.sciencedirect.com/science/article/pii/S0168900214000102 (cited on page 31).

[187] Veronica Bindi et al. “The scintillator detector for the fast trigger and time-of-flight (TOF) measurement of the space experiment AMS-02”. In: *Nuclear Instruments and Methods in Physics Research Section A: Accelerators, Spectrometers, Detectors and Associated Equipment* 623 (Nov. 2010), pages 968–981. DOI: 10.1016/j.nima.2010.08.019 (cited on page 31).

[188] A. Basili et al. “The TOF-ACC flight electronics for the fast trigger and time of flight of the AMS-02 cosmic ray spectrometer”. In: *Nuclear Instruments and Methods in Physics Research Section A: Accelerators, Spectrometers, Detectors and Associated Equipment* 707 (Apr. 2013), pages 99–113. DOI: 10.1016/j.nima.2012.12.089 (cited on page 31).

[189] Nicolò Masi. “The AMS-02 time of flight (TOF) system: construction and overall performances in space”. In: May 2013 (cited on page 32).

[190] Ph. von Doetinchem et al. “The AMS-02 Anticoincidence Counter”. In: *Nuclear Physics B - Proceedings Supplements* 197.1 (2009). 11th Topical Seminar on Innovative Particle and Radiation Detectors (IPRD08), pages 15–18. ISSN: 0920-5632. DOI: https://doi.org/10.1016/j.nuclphysbps.2009.10.025. URL: http://www.sciencedirect.com/science/article/pii/S0920563209007464 (cited on page 33).

[191] T. Bruch and W. Wallraff. “The Anti-Coincidence Counter shield of the AMS tracker”. In: *Nuclear Instruments and Methods in Physics Research Section A: Accelerators, Spectrometers, Detectors and Associated Equipment* 572.1 (2007). Frontier Detectors for Frontier Physics, pages 505–507. ISSN: 0168-9002. DOI: https://doi.org/10.1016/j.nima.2006.10.376. URL: http://www.sciencedirect.com/science/article/pii/S016890020602119X (cited on page 33).

[192] Philip Doetinchem et al. “The Anticoincidence Counter System of AMS-02”. In: (June 2009) (cited on page 33).

[193] R. Pereira. “The AMS-02 RICH detector: Performance during ground-based data taking at CERN”. In: *Nuclear Instruments and Methods in Physics Research Section A: Accelerators, Spectrometers, Detectors and Associated Equipment* 639.1 (2011). Proceedings of the Seventh International Workshop on Ring Imaging Cherenkov Detectors, pages 37–41. ISSN: 0168-9002. DOI: https://doi.org/10.1016/j.nima.2010.09.036. URL: http://www.sciencedirect.com/science/article/pii/S0168900210020292 (cited on page 33).

[194] Hu Liu et al. “The RICH detector of AMS-02: 5 years of operation in space”. In: *Nuclear Instruments and Methods in Physics Research Section A: Accelerators, Spectrometers, Detectors and Associated Equipment* 876 (2017). The 9th international workshop on Ring Imaging Cherenkov Detectors (RICH2016), pages 5–8. ISSN: 0168-9002. DOI: https://doi.org/10.1016/j.nima.2016.12.011. URL: http://www.sciencedirect.com/science/article/pii/S016890021631258X (cited on page 33).

[195] P. A. Čerenkov. “Visible Radiation Produced by Electrons Moving in a Medium with Velocities Exceeding that of Light”. In: *Phys. Rev.* 52 (4 Aug. 1937), pages 378–379. DOI: 10.1103/PhysRev.52.378. URL: https://link.aps.org/doi/10.1103/PhysRev.52.378 (cited on page 33).

[196] William Gillard. “High precision measurement of the AMS-RICH aerogel refractive index with cosmic-ray”. In: *33rd International Cosmic Ray Conference*. 2013, page 0742 (cited on page 34).

[197] F. Giovacchini. “Performance in space of the AMS-02 RICH detector”. In: *Nuclear Instruments and Methods in Physics Research Section A: Accelerators, Spectrometers, Detectors and Associated Equipment* 766 (2014). RICH2013 Proceedings of the Eighth International Workshop on Ring Imaging Cherenkov Detectors Shonan, Kanagawa, Japan, December 2-6, 2013, pages 57–60. ISSN: 0168-9002. DOI: https://doi.org/10.1016/j.nima.2014.04.036. URL: http://www.sciencedirect.com/science/article/pii/S0168900214004410 (cited on pages 34, 35).

[198] I.M. Frank and I.E. Tamm. “Coherent visible radiation of fast electrons passing through matter”. In: *Compt. Rend. Acad. Sci. URSS* 14.3 (1937), pages 109–114. DOI: 10.3367/UFNr.0093.196710o.0388 (cited on page 34).

[199] C. Adloff et al. “The AMS-02 lead-scintillating fibres Electromagnetic Calorimeter”. In: *Nuclear Instruments and Methods in Physics Research Section A: Accelerators, Spectrometers, Detectors and Associated Equipment* 714 (2013), pages 147–154. ISSN: 0168-9002. DOI: https://doi.org/10.1016/j.nima.2013.02.020. URL: http://www.sciencedirect.com/science/article/pii/S016890021300199X (cited on page 35).

[200] Manuela Vecchi et al. “The electromagnetic calorimeter of the AMS-02 experiment”. In: (Oct. 2012) (cited on page 35).

[201] F. Cervelli et al. “A reduced scale e.m. calorimeter prototype for the AMS-02 experiment”. In: *Nuclear Instruments and Methods in Physics Research Section A: Accelerators, Spectrometers, Detectors and Associated Equipment* 490.1 (2002), pages 132–139. ISSN: 0168-9002. DOI: https://doi.org/10.1016/S0168-9002(02)00915-4. URL: http://www.sciencedirect.com/science/article/pii/S0168900202009154 (cited on page 35).

[202] F. Cadoux et al. “The AMS-02 electromagnetic calorimeter”. In: *Nuclear Physics B - Proceedings Supplements* 113.1 (2002), pages 159–165. ISSN: 0920-5632. DOI: https://doi.org/10.1016/S0920-5632(02)01836-4. URL: http://www.sciencedirect.com/science/article/pii/S0920563202018364 (cited on page 35).

[203] A. Kounine et al. “Precision measurement of 0.5 GeV–3 TeV electrons and positrons using the AMS Electromagnetic Calorimeter”. In: *Nuclear Instruments and Methods in Physics Research Section A: Accelerators, Spectrometers, Detectors and Associated Equipment* 869 (2017), pages 110–117. ISSN: 0168-9002. DOI: https://doi.org/10.1016/j.nima.2017.07.013. URL: http://www.sciencedirect.com/science/article/pii/S0168900217307246 (cited on page 35).

[204] Stefano Di Falco. “Performance of the AMS-02 Electromagnetic Calorimeter in Space”. In: *33rd International Cosmic Ray Conference*. 2013, page 0855 (cited on pages 35, 37).

[205] C. H. Lin. “Trigger Logic Design Specifications”. In: *Internal Note* (2008) (cited on page 36).

[206] C. Lin. “Trigger Logic Design Specifications”. In: *Internal AMS-02 Note* (2005) (cited on page 36).

[207] A. Sabellek. “The Space Qualified Data Acquisition for the Transition Radiation Detector of the AMS-02 Experiment on the International Space Station”. In: 2016 (cited on page 37).

[208] X Cai. “On board computing system for AMS-02 mission”. In: (2005). URL: https://cds.cern.ch/record/962442 (cited on page 37).

[209] A. Kounine and V. Koutsenko. “Flight Software for xDR and JINx nodes in AMS-02”. In: *AMS Internal Notes* (2011) (cited on page 37).

[210] Vitali Choutko and the Ams Collaboration. “Parallelization of the event processing in the AMS experiment”. In: *Journal of Physics: Conference Series* 219.3 (Apr. 2010), page 032032. DOI: 10.1088/1742-6596/219/3/032032. URL: https://doi.org/10.1088/1742-6596/219/3/032032 (cited on page 41).

[211] V. Choutko et al. “Computing Strategy of the AMS Experiment”. In: *Journal of Physics: Conference Series* 664.3 (Dec. 2015), page 032029. DOI: 10.1088/1742-6596/664/3/032029. URL: https://doi.org/10.1088/1742-6596/664/3/032029 (cited on page 41).

[212] R. Brun. *Root Web page*. http://http://root.cern.ch/. 2001 (cited on page 41).

[213] J. Allison et al. “Geant4 Developments and Applications”. In: *IEEE Transactions on Nuclear Science* 53 (Feb. 2006), pages 270–278. DOI: 10.1109/TNS.2006.869826 (cited on page 41).

[214] J. Allison *et al*. “Recent developments in Geant4”. In: *Nucl. Instrum. Methods Phys., Sect A* 835 (Nov. 2016), pages 186–225. DOI: https://doi.org/10.1016/j.nima.2016.06.125 (cited on page 41).

[215] J.d. Sullivan. “Geometric factor and directional response of single and multi-element particle telescopes”. In: *Nuclear Instruments and Methods* 95.1 (1971), pages 5–11. DOI: 10.1016/0029-554x(71)90033-4 (cited on page 43).

[216] D.E. Alexandreas et al. “Point source search techniques in ultrahigh-energy gamma-ray astronom”. In: *Nucl. Instrum. Meth. A* 328 (1993), pages 570–577. DOI: 10.1016/0168-9002(93)90677-A (cited on page 43).

[217] Peter Duffett-Smith and Jonathan Zwart. “Practical Astronomy with your Calculator or Spreadsheet”. In: *Cambridge University Press, 2010. ISBN: 9780521146548* (Jan. 2011). DOI: 10.1017/CBO9780511861161 (cited on page 46).

[218] K.R. Lang. *Astrophysical formulae: Vol. 1: Radiation, gas processes and high-energy astrophysics. Vol. 2: Space, time, matter and cosmology*. Springer, Aug. 1999 (cited on page 46).

[219] M.A. Hapgood. “Space physics coordinate transformations: A user guide”. In: *Planetary and Space Science* 40.5 (1992), pages 711–717. ISSN: 0032-0633. DOI: https://doi.org/10.1016/0032-0633(92)90012-D (cited on page 46).

[220] C. Consolandi S. Della Torre and D. Grandi. “Coordinates and Sun Position for AMS-02,” in: *Planetary and Space Science* (). Internal note (cited on page 46).

[221] George B Arfken and Hans J Weber. *Mathematical methods for physicists; 4th ed.* San Diego, CA: Academic Press, 1995. URL: https://cds.cern.ch/record/379118 (cited on page 47).

[222] Prey. “The theory of spherical and ellipsoidal harmonics”. In: *Monatshefte für Mathematik und Physik* 41.1 (1934). DOI: 10.1016/0029-554x(71)90033-4 (cited on page 47).

[223] E.O. Steinborn and K. Ruedenberg. “Rotation and Translation of Regular and Irregular Solid Spherical Harmonics”. In: edited by Per-Olov Löwdin. Volume 7. Advances in Quantum Chemistry. Academic Press, 1973, pages 1–81. DOI: https://doi.org/10.1016/S0065-3276(08)60558-4. URL: http://www.sciencedirect.com/science/article/pii/S0065327608605584 (cited on page 47).

[224] J. Berdugo et al. *On the upper limits for dipole anisotropies in cosmic-ray positrons*. 2015. arXiv: 1510.01221 [astro-ph.IM] (cited on page 49).

[225] G. L. Cassiday et al. “Evidence for 10^{18}-eV Neutral Particles from the Direction of Cygnus X-3”. In: *Phys. Rev. Lett.* 62 (4 Jan. 1989), pages 383–386. DOI: 10.1103/PhysRevLett.62.383. URL: https://link.aps.org/doi/10.1103/PhysRevLett.62.383 (cited on page 50).

[226] G.L. Cassiday et al. “Mapping the U.H.E. sky in search of point sources”. In: *Nuclear Physics B - Proceedings Supplements* 14.1 (1990), pages 291–298. ISSN: 0920-5632. DOI: https://doi.org/10.1016/0920-5632(90)90434-V. URL: http://www.sciencedirect.com/science/article/pii/092056329090434V (cited on page 50).

[227] R. Atkins et al. “Observation of TeV Gamma Rays from the Crab Nebula with Milagro Using a New Background Rejection Technique”. In: *The Astrophysical Journal* 595.2 (Oct. 2003), pages 803–811. DOI: 10.1086/377498. URL: https://doi.org/10.1086/377498 (cited on page 50).

[228] M. A. Velasco. *Measurement of the large scale anisotropy in cosmic ray electrons, positrons and protons with the AMS-02 detector on the ISS*. June 2019. URL: https://eprints.ucm.es/51172/1/T40853.pdf (cited on pages 50, 59, 60, 63, 69, 122, 139).

[229] K. M. Gorski et al. “HEALPix: A Framework for High-Resolution Discretization and Fast Analysis of Data Distributed on the Sphere”. In: *The Astrophysical Journal* 622.2 (Apr. 2005), pages 759–771. DOI: 10.1086/427976. URL: https://doi.org/10.1086/427976 (cited on page 51).

[230] T. -P. Li and Y. -Q. Ma. “Analysis methods for results in gamma-ray astronomy.” In: *Astrophysical Journa* 272 (Sept. 1983), pages 317–324. DOI: 10.1086/161295 (cited on page 56).

[231] J. Neyman and Harold Jeffreys. “Outline of a Theory of Statistical Estimation Based on the Classical Theory of Probability”. In: *Philosophical Transactions of the Royal Society of London. Series A, Mathematical and Physical Sciences* 236.767 (1937), pages 333–380. DOI: 10.1098/rsta.1937.0005. eprint: https://royalsocietypublishing.org/doi/pdf/10.1098/rsta.1937.0005. URL: https://royalsocietypublishing.org/doi/abs/10.1098/rsta.1937.0005 (cited on page 57).

[232] Gary J. Feldman and Robert D. Cousins. “Unified approach to the classical statistical analysis of small signals”. In: *Phys. Rev. D* 57 (7 Apr. 1998), pages 3873–3889. DOI: 10.1103/PhysRevD.57.3873. URL: https://link.aps.org/doi/10.1103/PhysRevD.57.3873 (cited on page 57).

[233] James O. Berger, Jose M. Bernardo, and Dongchu Sun. “Objective Priors for Discrete Parameter Spaces”. In: *Journal of the American Statistical Association* 107.498 (2012), pages 636–648. DOI: 10.1080/01621459.2012.682538. eprint: https://doi.org/10.1080/01621459.2012.682538. URL: https://doi.org/10.1080/01621459.2012.682538 (cited on page 58).

[234] A. Kondor. “Method of convergent weights — An iterative procedure for solving Fredholm’s integral equations of the first kind”. In: *Nuclear Instruments and Methods in Physics Research* 216.1-2 (1983), pages 177–181. DOI: https://doi.org/10.1016/0167-5087(83)90348-4 (cited on page 144).

[235] G. D’ Agostini. “A multidimensional unfolding method based on Bayes’ theorem”. In: *Nuclear Instruments and Methods in Physics Research Section A: Accelerators, Spectrometers, Detectors and Associated Equipment* 362.2-3 (1994), pages 487–498. DOI: https://doi.org/10.1016/0168-9002(95)00274-X (cited on page 144).